

Synthesis of heparin conjugated silica nanoparticles for nanomedicine applications

Abdolelah Jaradat; MSc

Thesis submitted to the University of Nottingham for the degree of Doctor of Philosophy

January 2020

Abstract

Heparin has been extensively explored for cancer metastasis treatment owing to its ability to competitively inhibit metastatic cancer cells adhesion to P-selectin which is overexpressed on vascular endothelium and its inhibitory activity of platelet-tumour cells interaction. Moreover, heparin plays a key role in inhibiting the heparanase that is overexpressed during the early stage of metastasis process. However, heparin polymer is rapidly excreted through renal filtration. Detection of metastasis is of a paramount importance as it allows an early clinical intervention which could increase the survival rate of cancer patients.

In the first part of this thesis, heparin was conjugated to silica NPs surfaces in order to investigate its P-selectin blocking activity simultaneously exploiting the prolonged circulation of the NPs. Moreover, two structurally related polymers; chondroitin sulphate and sodium alginate were grafted onto the surface of silica NPs in order to be used as controls. Heparin, chondroitin sulphate and alginate were attached to NPs' surface by coupling of the EDC-activated polymers to amine functionalised NPs. TGA, azure A and DMMB assays confirmed the attachment of these polymers to the NPs surfaces. Polymer grafted NPs had a particle diameter *circa* 200 nm and negative zeta potential values (~ -56 mV). Heparin, chondroitin sulphate and alginate conjugated NPs were fluorescently labelled with different fluorophores; TAMRA, FAM and Alexa 633 respectively, in order to monitor their cell surface binding under flow conditions that mimic the *in vivo* circulation. The study revealed that heparin and chondroitin sulphate conjugated NPs were more bound to the surface of human umbilical vein endothelial cells (HUVECs) compared to alginate conjugated NPs as indicated by fluorescence microscopy. Furthermore, silica microparticles with mean size of ~ 1.4 µm were also synthesised and cellular uptake study was conducted which has shown that heparin conjugated microparticles exhibited less cellular internalisation compared to heparin conjugated NPs. However, the latter exhibited greater P-selectin dependent binding to

HUVECs' surface under flow conditions. To conclude, heparin conjugated NPs can interfere/bind with P-selectin receptors as the competitive assay showed that these NPs were blocked by anti-P-selectin antibodies. Consequently, this could suggest that heparin conjugated NPs could be further investigated and observed in the future as potential tools to reduce the dissemination of circulating tumour cells.

In the second part of this thesis, heparin was chemically modified to produce desulphated heparin and glycol split heparin for the inhibition of heparanase as they have been reported to have less side effects and greater heparanase inhibitory activity compared to unmodified heparin. Successful synthesis of the modified heparin derivatives was confirmed by ^{1}H-NMR. An anticoagulant assay (Anti Xa), which measures heparin activity by indirectly measuring its ability to activate antithrombin III, had indicated that glycol split heparin polymer exhibited lower anticoagulant activity compared with native heparin and thus it would have lower adverse reactions e.g. haemorrhage. Desulphated heparin is expected to have an additional clinical advantage compared to heparin such as higher antiangiogenic activity. Both heparin derivatives were attached to the surface of silica NPs using EDC coupling reaction. Heparin analogues conjugated NPs had a particle diameter around 200 nm so the EPR effect, which is a phenomenon that hypothesises a preferential accumulation of the NPs in the tumour interstitial fluid, could be exploited to accumulate the modified heparins in the extracellular space of the tumour where heparanase is overexpressed. Anti Xa assay also showed that glycol split heparin conjugated NPs exhibited lower anticoagulant activity compared with heparin conjugated NPs. Desulphated heparin conjugated NPs showed both significantly less blue shift effect on azure A λ_{max} and lower zeta potential value compared to heparin conjugated NPs. The data together indicate successful conjugation of the modified heparin polymers to the surface of silica NPs that could be further employed to inhibit heparanase.

In the final part of this thesis, different FRET based models were designed to detect heparinase which is the bacterial form of mammalian heparanase overexpressed during

metastasis, in order to enable the early diagnosis of cancer. In model I, both FRET pair were attached to heparin chain to attain fluorescence quenching using EDC/NHS coupling reaction. The fluorophore was either attached to the end or within the chain of heparin; however, the probe prepared by intrachain conjugation of the fluorophore showed significantly higher fluorescence quenching. This model showed promising results with respect to quenching efficiency (QE), unfortunately the restoration of the fluorescence signal after heparinase treatment was minimal compared with the chemical depolymerisation. Model II was then developed which adopts the use of core-shell NPs composed of 12 nm thick shell containing a fluorophore (TAMRA) and a black hole quencher conjugated heparin (BHQ2-Heparin) probe attached to NPs surfaces. Where the thinnest possible shell was used in order to maintain the FRET pair close to each other to achieve an optimum FRET energy transfer and maximal QE. The QE of this system was measured with either blank core or with a core containing 7-methoxy coumarin, however a discrepancy between the QE measurements of the core-shell nanosensors was observed with dramatically lower value obtained by coumarin based system. Due to the inconsistency of QE measurements of model II, model III was developed which comprises BHQ1 incorporated silica NPs and fluorescently labelled heparin appended to the NPs surfaces. In summation, Model III showed the best potential for bacterial heparinase detection and thus it could be further improved and utilised for detection of mammalian heparanase sampled from the blood of cancer patients for metastasis diagnosis. In conclusion, the results highlight that heparin conjugated nanoparticles could be manipulated for versatile nanomedicine applications, thus they could be further investigated as novel potential therapeutics and diagnostics for cancer metastasis.

Acknowledgement

I would like to express my sincere appreciations and gratitude to my supervisors Prof. Cameron Alexander, Prof. Jonathan Aylott and Dr. Kenton Arkill for their guidance and inspiration throughout my studies.

Also, I would like to thank all my colleagues in D38 lab including Dr. Veeren Chauhan, Dr. Mohammad Elsutohy, Dr. Mohammad Yousif Dr.Amjad Abouselo and Dr.Shehnaz Ahmad for their helpful company and useful discussion.

I would also like to thank Al-Isra University in Jordan for granting me the
PhD Scholarship and sponsoring my study.

Many thanks to my friends, Anas Gharaibeh, Dr. Ali-Al Azzo, Dr. Abdullah Naser, Ismail Boujnane, Dr. Hussein Aied, Dr. Abdulrahman Al-Natour and Dr. Mohammad Bayan for their incredible support and help

Most importantly, I would like to express my appreciation and thanks to my Dad Ali, my mum Afaf, my brothers and sister for all their love and continuous support. None of this work would have been done without my parents, I really dedicate this thesis to them with my heartfelt appreciation and gratitude.

Contents

Abstract III

Acknowledgement VI

Contents VII

List of Figures XV

List of Tables XXXIII

List of Abbreviations XXXIII

1 Chapter one: General Introduction 1

1.1 Nanomedicine 2

1.2 Cancer 2

1.3 Metastasis 3

1.3.1 Role and function of GAGs in cancer progression and cell signalling 4

1.3.1.1 GAGs family and categorisation 4

1.3.1.2 Differential characteristics of heparin and heparan sulphate 5

1.3.1.3 Heparan sulphate role in cell signalling and metastasis 7

1.3.1.4 Metastatic cascade inhibition by heparin 9

1.4 Nanoparticles 11

1.4.1 Ligand decorated nanoparticles and targeted drug delivery 14

1.4.2 Silica nanoparticles 16

1.5 Circulating tumour cells: Diagnosis, detection and treatment 16

1.5.1 Liquid biopsy ` 16

1.5.2 Approaches used for Inhibition of circulating tumour cells dissemination ... 18

1.5.3 Approaches used for detection of circulating tumour cells and early diagnosis of metastasis 21

1.6 Aim of the thesis 22

2 Chapter two: Synthesis of heparin conjugated nanoparticles to target cell surface P-selectin of endothelial cells to Inhibit metastasis 24

2.1 Introduction 25

2.1.1 P-selectin, heparin and metastasis 25

2.1.1.1 P-selectin role in metastasis 25

2.1.1.2 Inhibition of metastasis by heparin through blocking of cell adhesion receptors 26

2.1.2 Flow conditions use in systemic circulation simulators 28

2.2 Aim 29

2.3 Experimental 30

2.3.1 Materials 30

2.3.2 Methods 31

2.3.2.1 Synthesis of labelled amine functionalised nanoparticles 31

2.3.2.2 Synthesis of heparin, chondroitin and alginate conjugated nanoparticles 32

2.3.2.3 Synthesis of heparin conjugated microparticles 32

2.3.2.4 Nanoparticles characterisation 33

2.3.2.5 Thermogravimetric analysis (TGA) 34

2.3.2.6 Azure A and DMMB assays 34

2.3.2.7 Anticoagulant assay (Anti Xa assay) 34

2.3.2.8 Cell culture and maintenance 35

2.3.2.9 Immunofluorescence assay of P-selectin expression 35

2.3.2.10 Basal P-selectin expression by flow cytometry 36

2.3.2.11 Competitive assay of heparin conjugated NPs P-selectin dependent adhesion under static conditions 36

2.3.2.12 Flow assays 36

2.4 Results and discussion 37

2.4.1 Synthesis of heparin, chondroitin and alginate conjugated silica NPs 37

2.4.2 Characterisation 42

2.4.3 Particle Size 42

2.4.4 Zeta potential 44

2.4.5 Fluorescence of the NPs 44

2.4.6 Determination of the polymers grafted onto the NPs' surface 45

2.4.6.1 Confirmation of heparin grafting using TGA 45

2.4.6.2 Confirmation of heparin grafting using Azure A assay 46

2.4.6.3 Determination of the percentage of heparin grafted to NPs surfaces using azure A assay and TGA analysis 47

2.4.6.4 Confirmation of chondroitin and alginate grafting using DMMB assay 48

2.4.7 Anticoagulant activity of the modified NPs 50

2.4.8 Synthesis of heparin conjugated silica microparticles 52

2.4.9 Particle Size 52

2.4.10 Cellular uptake of heparin conjugated microparticles compared to NPs 53

2.4.11 Monitoring of heparin, chondroitin and alginate conjugated NPs-cellular binding under flow conditions 54

2.4.12 P-selectin dependent heparin conjugated NPs-HUVECs binding 59

2.4.12.1 Confirmation of P-selectin dependent heparin conjugated NPs-HUVECs binding using competitive assay 59

2.4.12.2 Monitoring of heparin conjugated particles-HUVECs binding under flow conditions 61

2.5 Conclusions 62

3 Chapter Three: Synthesis of heparin analogues conjugated NPs for heparanase inhibition 64

3.1 Introduction 65

3.1.1 Heparanase role in metastasis 65

1.1.1 Heparin analogues 66

1.1.2 Passive targeting of cancer using NPs 70

3.2 Aim 71

3.3 Materials and methods 72

3.3.1 Materials and equipment 72

3.3.2 Methods 72

3.3.2.1 NMR measurements of the prepared polymers 72

3.3.2.2 Particle size and zeta potential measurements 73

1.1.2.1 Heparin characterisation 74

1.1.2.2 Synthesis of glycol split heparin 75

1.1.2.3 Synthesis of desulphated heparin 75

1.1.2.4 Anticoagulant activity of glycol split heparin 76

1.1.2.5 Metachromatic assay of Desulphated heparin 76

1.1.2.6 Synthesis of glycol split conjugated and desulphated conjugated NPs 77

1.1.2.7 Characterisation of glycol split conjugated and desulphated conjugated NPs 77

3.4 Results and discussion 77

3.4.1 Synthesis of glycol split heparin 77

3.4.2 Polymer characterisation using ^{1}H-NMR 79

3.4.3 Anticoagulant assay 80

3.4.4 Synthesis of glycol split heparin conjugated NPs 82

3.4.5 Characterisation of glycol split heparin conjugated NPs 83

3.4.6 Anticoagulant properties of glycol split heparin conjugated NPs 84

3.4.7 Synthesis of desulphated heparin polymer 85

3.4.8 H^{1} NMR spectrum of desulphated heparin 86

3.4.9 Determination of heparin desulphation using Azure A assay 87

3.4.10 Characterisation of desulphated heparin conjugated NPs 89

3.4.11 Synthesis of desulphated heparin conjugated NPs 90

3.4.12 Identification of desulphated heparin grafted onto NPs surfaces 91

3.5 Conclusions and future work 92

4 Chapter Four: Development of FRET based heparinase nanosensors 94

4.1 Introduction 95

4.1.1 Heparanase use in cancer detection 95

4.1.2 Fluorescence quenching 95

4.1.3 Forester (fluorescence) resonance energy transfer (FRET) quenching 97

4.1.4 Dexter energy transfer mechanism 103

4.1.5 Static Quenching (contact quenching) 103

4.1.6 Heparinase and Heparanase differences 103

4.1.6.1 Heparinases 103

4.1.6.2 Heparanases 106

4.2 Aim 107

4.3 Materials and methods 109

4.3.1 Materials and equipment 109

4.3.2 Synthesis and characterisation of model I sensing probe 110

4.3.2.1 Synthesis of the dual-labelled heparin probe by intrachain conjugation of the FRET pair 110

4.3.2.2 Preparation of the physical mixtures of the FRET pair and heparin 111

4.3.2.3 Synthesis of dual-labelled heparin by end-chain conjugation of the fluorophore 111

4.3.2.4 Fluorescence quenching measurement 112

4.3.2.5 Chemical depolymerisation using nitrous acid and fluorescence signal recovery 113

4.3.2.6 Azure A assay for heparin degradation monitoring 113

4.3.2.7 Heparinase assay 114

4.3.3 Preparation of nanosensors using model II 114

4.3.3.1 Synthesis of core-shell NPs 114

4.3.3.2 Preparation of BHQ2-Heparin conjugated 12 nm-shell NPs 116

4.3.3.3 Synthesis of coumarin based core-shell system 117

4.3.3.4 Fluorescence measurements of core-shell NPs 118

4.3.3.5 Monitoring of spectral overlap of the donor-acceptor system in the core-shell NPs 118

4.3.4 Development of FRET based nanosensors using model III 118

4.3.4.1 Synthesis of the nanosensors 118

4.3.4.2 Characterisation of the nanosensors 120

4.3.4.2.1 Absorbance 120

4.3.4.2.2 Fluorescence 120

4.3.4.2.3 Particle Size 120

4.3.4.3 Quenching efficiency 121

4.3.4.4 Fluorescence signal recovery after heparinase treatment 121

4.4 Results and discussion 123

4.4.1 Synthesis of heparinase sensing probe using model I 123

4.4.1.1 Fluorescence quenching efficiency of the dual labelled heparin prepared by intrachain conjugation method 125

4.4.1.2 Fluorescence quenching efficiency of the dual labelled heparin prepared by end-chain conjugation method 126

4.4.1.3 Comparison study between end-chain and intrachain conjugation of the fluorophore 127

4.4.1.4 Study the role of covalent binding and inter/intra-molecular interaction between the FRET pair 130

4.4.1.5 Fluorescence signal recovery of dual labelled heparin probe using chemical degradation 132

4.4.1.6 Fluorescence signal recovery of dual labelled heparin probe after heparinase treatment 134
4.4.2 Development of heparinase nanosensors using model II 135
4.4.2.1 Synthesis of core-shell NPs containing unmodified core 135
4.4.2.1.1 Optimisation and characterisation of the core-shell NPs 135
4.4.2.1.2 Fluorescence spectra of the optimised core-shell NPs 138
4.4.2.1.3 Preparation of core-shell FRET based NPs 138
4.4.2.1.4 Spectral overlap and fluorescence quenching of the donor-acceptor pair in the prepared nanosensors 140
4.4.2.2 Design of coumarin based core-shell system 142
4.4.3 Development of heparinase nanosensors using model III 145
4.4.3.1 Preparation of fluorescein labelled heparin 145
4.4.3.2 Binding of fluorescein labelled heparin probe to the surface of BHQ1 incorporated NPs 146
4.4.3.3 Characterisation of BHQ1/Fluorescein FRET pair based nanosensors 148
4.4.3.3.1 Particle size 148
4.4.3.3.2 Absorption spectra of the nanosensors 148
4.4.3.4 Fluorescence quenching of the nanosensors 149
4.4.3.5 Fluorescence signal recovery after heparinase treatment 150
4.5 Conclusions 153
5 Chapter five: Conclusion and future work 156
5.1 Conclusions 157
5.2 Future work 161

6 References 164

List of Figures

Figure 1.1 Schematic representation of the metastatic process which can take place at two different stages. The first stage is the physical movement of the metastatic tumour cells from the primary site to distant organ and the second stage is colonisation of the metastasised cells at the secondary site. A: Cancer cells start to change their phenotype to a more motile and invasive form. B: tumour cells create a path through ECM aided by heparanase and other matrix degrading enzymes in order to enter the systemic circulation. C: Circulating tumour cell (CTCs) travel through blood vessels. D: CTCs extravasate and exit the circulatory system via rolling adhesion process. E: Tumour cells evade and escape the Immune system in order to survive at the secondary site and form a premetastatic niche. F: Tumour cells adapt and change the microenvironment for further growth and proliferation. Figure was taken from Chaffer et al. [13] 4

Figure 1.2 Illustration shows the possible patterns of sugar moieties making up heparin and heparan sulphate (HS) including the major and variable disaccharide repeating units. X= SO_3 or H. Y = Ac or H or SO_3. SO_3 = Sulphate group. H= Hydrogen atom, Ac= Acetyl group. Figure adapted from Nelson et al.[36] 6

Figure 1.3 **Schematics showing the role of heparan-sulphate in tumour metastasis.** Heparan-sulphate in the free form (HS; green lines) or attached to the proteoglycans (Red lines) mediates metastasis. **a:** cell surface HS on tumour cells can act as a ligand for P-selectin (**P**) receptor, which mediates adhesion either to platelets to create a protective clotting aggregates around tumour cells or to the endothelial cells lining the vascular capillaries. Enabling cancer cells to extravasate and metastasise to secondary organs. **b:** Heparanase cleaves heparan sulphate in the extracellular matrix; not only releasing the bound growth factors that promote further tumour cell proliferation but also creating a passage to facilitate

tumour cell movement to blood vessels. **c:** Heparan sulphate proteoglycans acts as a co-receptor for integrin receptors (**I**) thus mediating tumour cell adhesion to blood vessels to facilitate the extravasation of the circulating tumour cells. **d:** heparan sulphate mediates the microclimate-coagulation through modulating a coagulation factor thrombin (Factor IIa) in order to initiate the formation of fibronectin protective layer around tumour cells. e: cell surface HSPG interact with growth factors (FGF and VEGF) facilitating their binding to the cell surface receptors forming a ternary complex thus regulating the signalling pathway of further tumour cell growth. Exogenous heparin can inhibit heparan sulphate action at stages a, b, c and d. Figure was taken from Sasisekharan et al.[47] 9

Figure 1.4 Schematic shows metastatic cascade inhibition by native heparin polymer. Heparin blocks the metastasis at various stages. At stage (2), heparin inhibits the action of heparanase. At stage (3); heparin blocks the interaction between circulating tumour cells and P-selectin on overexpressed on the surface of platelets and vascular endothelial cells. 10

Figure 1.5 Schematics shows the accumulation of the NPs at the tumour site due to the EPR effect. NPs can only pass through porous blood vessels surrounding tumour tissues whilst they cannot cross through the endothelial barrier of the healthy vasculatures supplying the normal cells. Adapted from Abdalla et al.[67] 13

Figure 2.1 The structure of the most commonly occurring disaccharide repeating unit in heparin chain (left) and Sialyl Lewis x (sLe^x) (right).The structural similarities between the two ligands include the presence of amino sugar residue; D-glucosamine and the presence of L-idopyranuronic acid in heparin chain that resembles N-acetylneuraminic acid in sLe^x. ... 29

Figure 2.2 illustrative diagram shows stages of metastatic process and the aim of this study in utilising heparin conjugated NPs to disrupt metastasis at stage number (3). Metastasis starts at EMT (epithelial mesenchymal transition) stage where cells start to change morphology and become more metastatic. Heparanase degrades ECM (extracellular matrix) to create a path for metastatic cells to enter systemic circulation, then they bind to certain

receptors (P-selectin) upregulated on endothelial cells, which enhance the rolling adhesion of metastatic cells to extravasate and invade distance organs. 30

Figure 2.3 Schematics showing the synthesis of bare silica NPs. Steps of silica NPs formation, 1) Hydrolysis of TEOS in presence of NH_4OH to form silanol groups. 2) Condensation of silanol groups to form siloxane bonds (Si-O-Si). 38

Figure 2.4 The mechanism of fluorophore incorporation within the matrix of silica NPs which comprises two steps; the first step involves the covalent conjugation of the fluorophore to APTES linker and the second step encompasses the incorporation of the APTES-fluorophore conjugate within the silica matrix of the NPs during the polycondensation reaction between APTES and TEOS during the formation of silica NPs. **A:** Synthesis of TAMRA labelled silica NPs. **B:** Synthesis of FAM labelled silica NPs. **C:** Synthesis of Alexa 633 labelled silica NPs. 39

Figure 2.5 Schematic illustration of organosilane molecules (APTES) attachment to the surface of bare silica NPs (SiO_2 NPs) in order to form amine functionalised silica NPs (NH_2-SiO_2). Ethoxy groups of APTES were hydrolysed in presence of NH_4OH, subsequently reacted with free hydroxyl groups on the surface of bare silica NPs to form a covalent siloxane bonds (red)..... 40

Figure 2.6 Schematic representation of synthesis of heparin, chondroitin sulphate and alginate conjugated silica NPs labelled with TAMRA, FAM and Alexa 633 respectively using EDC as a zero length linker that activates the carboxylate groups of these polymers. A: coupling of heparin to amine functionalised TAMRA labelled silica NPs (NH_2-SiO_2) to produce heparin conjugated NPs (HP-SiO_2), B: coupling of chondroitin sulphate to amine functionalised FAM labelled silica NPs (NH_2-SiO_2) to produce chondroitin conjugated NPs (CH-SiO_2), C: coupling of sodium alginate to amine functionalised Alex 633 labelled silica NPs (NH_2-SiO_2) to produce alginate conjugated NPs (ALG-SiO_2). 41

Figure 2.7 Schematic representation of heparin conjugation to the surface of amine functionalised NPs using **A:** end-chain immobilisation method and **B:** Intrachain conjugation method..... 41

Figure 2.8 . Size of the non-grafted and polymer grafted NPs measured by dynamic light scattering (DLS). **A:** Particle size distribution of heparin conjugated NPs (HP-Si), alginate conjugated NPs (ALG-Si), chondroitin conjugated NPs (CH-Si) and non-grafted amine functionalised NPs (NH2-Si). **B:** Quantitative measurement of the average particle size of the NPs shown in A. **C:** Polydispersity index values of the NPs shown in A. Data was analysed using one way ANOVA test (column analyses), multiple comparison by comparing the mean of each column to the mean of the control column (NH2-Si). Error bars indicate SD (n = 3), ** is P ≤ 0.01, *** is P ≤ 0.001**** is P ≤ 0.0001. 43

Figure 2.9 TEM images (left) and corresponding histograms (right) of amine functionalised NPs (a) heparin conjugated NPs (b), chondroitin conjugated NPs (c) and alginate conjugated NPs (d) (scale bar = 500 nm). Histograms were generated by calculating the diameter of n numbers for each type of the NPs (n = 40). 43

Figure 2.10 Zeta potential measurements of negatively charged heparin conjugated NPs (HP-Si), alginate conjugated NPs (ALG-Si), and chondroitin conjugated NPs (CH-Si) and positively charged amine functionalised NPs (NH2-Si). Error bars indicate SD (n = 3). 44

Figure 2.11 Fluorescence spectra of TAMRA labelled heparin conjugated NPs (HP-Si), Alexa 633 labelled alginate conjugated NPs (ALG-Si), FAM labelled chondroitin conjugated NPs (CH-Si), showing the maximum emission wavelengths of the fluorophore incorporated NPs. Fluorescence intensity was normalised to maximum intensity..... 45

Figure 2.12 TGA curves of heparin alone, heparin conjugated NPs (HP-Si), amine functionalised NPs (NH_2-Si) and bare silica NPs (Blank-Si). 46

Figure 2.13 Schematic representation of possible electrostatic interaction between heparin and two molecules of azure A to form a dimer. 47

Figure 2.14 Effect of heparin polymer, heparin conjugated NPs and non-grafted amine functionalised NPs on maximum absorption wavelength of azure A dye. **A:** UV-visible absorption wavelength spectra of 0.0125mg/mL azure A alone (Blue), and after addition of 20 µg/mL heparin (Red), 0.5 mg/mL heparin conjugated NPs (Green), and 0.5 mg/mL amine functionalised NPs (Purple). **B:** Quantitative measurements of azure A lambda max change upon addition of heparin polymer, heparin conjugated NPs (HP-Si), and non-grafted amine functionalised NPs (NH2-Si). Data was analysed using one way ANOVA test (column analyses), multiple comparison by comparing the mean of each column to the mean of the control column (NH_2-Si). Error bars indicate SD (n = 3). **** is P ≤ 0.0001. 47

Figure 2.15 Percentage of heparin attached to the surface of silica NPs through EDC coupling reaction. Error bars indicate SD (n=3). Data was analysed using t test. ** is P ≤ 0.01. 48

Figure 2.16 Effect of sodium alginate, chondroitin sulphate polymers, alginate conjugated NPs and chondroitin conjugated NPs on the maximum absorption wavelength of DMMB dye at various pH values. A: UV-visible absorption wavelength of DMMB dye alone, and after addition of chondroitin sulphate polymer (CH-DMMB), sodium alginate polymer (ALG-DMMB), chondroitin conjugated NPs (CH-Si-DMMB) and alginate conjugated NPs (ALG-Si-DMMB) at pH 7.2. B: Quantitative measurements of DMMB lambda max change upon addition of the polymers and NPs shown in A at pH 7.2. C: UV-visible absorption wavelength of DMMB dye alone, and after addition of chondroitin sulphate polymer (CH-DMMB), sodium alginate polymer (ALG-DMMB), chondroitin conjugated NPs (CH-Si-DMMB), alginate conjugated NPs (ALG-Si-DMMB) at pH 1.5. D: Quantitative measurements of DMMB lambda max change upon addition of the polymers and NPs shown in A at pH 1.5. Data was analysed using t test. Error bars indicate SD (n = 3), ns is P > 0.05, ** is P ≤ 0.01, **** is P ≤ 0.0001. 49

Figure 2.17 Schematic illustrates the electrostatic interaction between negatively charged sodium alginate and positively charged cationic DMMB. **A:** Electrostatic Interaction between

the polymer and the dye at pH = 7.2 due to complete ionisation of sodium alginate carboxylate groups. **B:** Absence of electrostatic interaction between the polymer and the cationic dye at pH 1.5 due to protonation of the alginate carboxylate groups..... 50
Figure 2.18 Visual monitoring of the effect of chondroitin sulphate, sodium alginate polymers and their corresponding NPs on DMMB colour. **A:** Colour change of DMMB after addition of chondroitin sulphate polymer (CH), sodium alginate polymer (ALG), chondroitin conjugated NPs (CH-Si), alginate conjugated NPs (ALG-Si) at pH 7.2. **B:** Colour change of DMMB after addition of chondroitin sulphate polymer (CH), sodium alginate polymer (ALG), chondroitin conjugated NPs (CH-Si), alginate conjugated NPs (ALG-Si) at pH 1.5. 50
Figure 2.19 Anticoagulant activity represented by the optical density of the released pNA that is inversely proportional to anticoagulant activity of heparin and its derivatives. **A:** Schematic representation of anti Xa assay mechanism showing that the measurable chromophore pNA is only released by the residual (Heparin-unbound) active factor Xa, **B:** Anticoagulant activity of native heparin polymer (HP), **C:** Anticoagulant activity of heparin conjugated NPs (HP-Si), alginate conjugated NPs (ALG-Si) and chondroitin conjugated NPs (CH-Si). Data was analysed using two way ANOVA test (grouped analyses), p-value of the multiple comparison is < 0.0001 for HP-Si vs CH-Si, HP-Si vs ALG-Si and > 0.05 for CH-Si vs ALG-Si. Error bars indicate SD (n = 3). 52
Figure 2.20 Particle characterisation. **A:** Bright field images **B:** fluorescence image of 1.4 µm size heparin conjugated particles (HP-MPs) **C:** Histogram showing particles distribution. **D:** Polydispersity index (PDI) of heparin conjugated microparticles (HP-MPs) estimated using the equation: PDI = $SD^2/mean^2$. Histogram was generated using GraphPad Prism by measuring the diameters of n numbers of particles (n=700). Scale bar= 100 µm. 53
Figure 2.21 **A:** Confocal microscopy images of HUVECs cellular uptake of heparin conjugated NPs with 200 nm size (left) and heparin conjugated microparticles with 1.4 µm size (right). **B:** Quantitative measurement of different sizes of heparin particles internalisation by HUVECs

treated with 25 µg/mL particles. Data was analysed using unpaired t test. Error bars indicate SD (n = 3, 3 different random regions were taken). ** is P ≤ 0.01. Scale bar = 40 µm..... 54
Figure 2.22 HUVECs grown in ibidi µ-channel slide (left) for 72 hours and corresponding fluorescence images of the cells having nuclei stained with Hoechst showing near confluency growing. Images were taken from three different regions of the slide. Scale bar = 40 µm.. 55
Figure 2.23 Fluorescence microscopy images of HUVECs treated with mixture of 200 nm heparin conjugated NPs labelled with TAMRA (red), chondroitin conjugated NPs labelled with FAM (green) and alginate conjugated NPs labelled with Alexa 633 (magenta) under flow conditions. Images were taken from three different regions of µ-channel slide. Shear stress = 1.16 dyn/cm^2. Scale bar = 40 µm. 56
Figure 2.24 Time lapse fluorescence images of HUVECs treated with mixture of 200 nm heparin conjugated NPs labelled with TAMRA (red), chondroitin conjugated NPs labelled with FAM (green) and alginate conjugated NPs labelled with Alexa 633 (magenta) under flow conditions. Images were taken every 10 seconds. Shear stress = 1.16 dyne/cm^2. Scale bar = 40 µm. 57
Figure 2.25 P-selectin expression on the surface of HUVEC cells. **A:** Fluorescence image of HUVECs treated with FITC labelled anti CD62 antibody (immunostaining). **B:** percentage of basal P-selectin expression on HUVEC cell surface using flow cytometry. Scale bar = 20 µm. n=3, Error bars indicate SD (n = 3). % of P-selectin was represented by the percentage of labelled cells with FITC anti-P-selectin antibodies relative to the whole population of treated cells. 57
Figure 2.26 **A:** Fluorescence microscopy images of HUVECs incubated with Anti P-selectin antibody for 1 hour under static conditions followed by treatment with mixture of 200 nm heparin conjugated NPs labelled with TAMRA (red), chondroitin conjugated NPs labelled with FAM (green) and alginate conjugated NPs labelled with Alexa 633 (magenta) under flow conditions. Images were taken from three different regions of the µ-channel slide. Shear

stress = 1.16 dyn/cm^2. Scale bar = 40 µm. **B:** Schematic representation showing that P-selectin dependent binding of heparin and chondroitin conjugated NPs to HUVECs surface is disrupted by anti P-selectin antibodies. 58

Figure 2.27 **A:** Immunofluorescence assay showing fluorescence images of HUVECS treated with FITC-Anti CD62P antibody displaying P-selectin receptor expression before and after histamine stimulation. **B:** Quantitative analysis of heparin conjugated NPs (50 µg/mL) internalisation/ cell surface binding to HUVEC cells stimulated by histamine (0.1 mM) to upregulate P-selectin before and after addition of free heparin (1 mg/mL). Data was analysed using one way ANOVA test (column analyses), multiple comparison. Error bars indicate SD (n = 3). *** is P ≤ 0.001. 60

Figure 2.28 Cartoon showing that heparin conjugated NPs (HP-Si) outcompeted by heparin ligands that are already occupying P-selectin receptors expressed on the surface of endothelial cells (competitive assay). 61

Figure 2.29 Confocal microscopy images of HUVECs treated with 200 nm-heparin conjugated NPs (HP-Si NPs) and 1.4 µm-heparin conjugated microparticles (HP-Si MPs) under flow conditions. Shear stress = 1.16 dyn/cm^2. n=3. Scale bar = 40 µm. 62

Figure 3.1 Chemical structure of heparin monomer modifications carried out to produce different modified heparin derivatives; namely 2-O, 6-O desulphation, N-desulphation, Glycol splitting of non-sulphated iduronic acid or glucuronic acid. 67

Figure 3.2 Chemical structure of glycol split heparin derivatives prepared by sodium periodate. Gs-HP (NHR): is a glycol split heparin with either N-sulphate or NH2 (R = SO_3^- or H) group in the glucose amine residue. Gs-HP (NAC): is a glycol split heparin with either N-Acetyl the glucose amine residue. Adapted from Naggi et al.[226] 68

Figure 3.3 Chemical structure of 2-O (Iduronic acid), 3-O (Glucosamine) sulphated heparin repeated units (A) and 2-O (Iduronic acid), 3-O (Glucosamine) desulphated heparin repeated

units (B). Purple arrows indicate the 2-O sulphation and desulphation in A and B respectively, red arrows indicate 3-O sulphation and desulphation in A and B respectively..... 70

Figure 3.4 Schemtic reperesentation of metastatic stages. Heparin derivatives conjugated silica NPs are supposed to inhibit heparnase at stage 2. Conseqently reducing the degradation of the exctracellaular matrix surrounding the tumour cells and metastatic cencer progression. 72

Figure 3.5 schematic illustration of glycol split heparin synthesis. Step 1 involves periodate oxidation of 2,3 oxygen atoms to produce heparin periodate intermdiate. Step 2 involves the reduction of aldhyde groups formed at C2 and C3 of glucuronic acid residues using sodium borohydride as a reducing agent to produce hydroxyl groups at the same postions. 78

Figure 3.6 Illustration showing A**:** 3D chemical structure of heparin tetrasaccharide ligand bound to the active site of heparanase (Sticks represent covalent bonds, balls represent atoms. grey= carbon, red= oxygen, blue= nitrogen, yellow= sulphur)**. B:** 3D view of the ligand (Iduronic acid)-active site interaction (Grey dashed lines represent hydrophobic interaction, blue dashed lines represent hydrogen bonds, IDR606: Iduronic acid ligand. The following abbreviations represent the amino acids of heparanase at active site; N224: Asparagine. E225, E343: Glutamic acid. T97: Threonine. D62: Aspartic acid. A347: Alanine. K98: Lysine. G49, G350, G349, G96: Glycine. Y348, Y298, Y391: Tyrosine. **C:** Simplified 2D view of the ligand –active site interaction (Black dashed lines indicate hydrogen bonds, Asn : Asparagine, Glu: Glutamic acid, Thr: Threonine, Asp: Aspartic acid, Tyr: Tyrosine, Gly: Glycine), Experimental data was obtained by X-ray diffraction method. Figure was adapted from Wu et al.[243] 79

Figure 3.7 H^1 NMR spectra of native heparin and glycol split heparin. Red arows show the major peak of glucuronic acid protons at C2 and C3 of the ring, where some have disapeared in glycol split heparin. Heparin chemical shift (400 MHz, D2O); δ(ppm) = 1.15-1.1 (t, GlcNS6S, –CH2), 1.97 (s, GlcNAc6S, -CO-CH3, α to carbonyl), 3.22-3.2 (m, GlcNS6S H2), 3.41-3.29 (m,

GlcA H2, H3), 3.63-3.58 (m, GlcNS6S H3), 3.77-3.67 (m, GlcNS6S H4), 3.89-3.87 (m, GlcNS6S H5), 3.97-3.92 (m, IdoA2S H4), 4.037 (s, IdoA2S H3), 4.21-4.13(m, GlcNS6S H6), 4.27 (s, IdoA2S H2), 4.46-4.33 (m, GlcA H1),4.94-4.86 (m, IdoA2S H5), 5.23-5.10 (m, IdoA2S H1), 5.51-5.34 (m, GlcNS6S3S H1). Glycol split heparin chemical shift; δ(ppm) = 1.97 (s, GlcNAc6S, -CO-CH3, α to carbonyl), 3.23-3.20 (m, GlcNS6S H2), 3.63-3.59 (m, GlcNS6S H3), 3.79-3.69 (m, GlcNS6S H4), 3.90-3.88 (m, GlcNS6S H5), 3.98-3.94 (m, IdoA2S H4), 4.04 (s, IdoA2S H3), 4.21-4.14 (m, GlcNS6S H6), 4.28 (s, IdoA2S H2), 4.45-4.33 (m, GlcA H1), 5.05-4.85 (m, IdoA2S H5), 5.25-5.12 (m, IdoA2S H1), 5.48-5.31 (m, GlcNS6S3S H1). 80

Figure 3.8 Anticoagulant activity of intact heparin polymer (HP) and glycol split heparin (GS-HP) represented by the optical density of the released pNA that is inversely proportional to anticoagulant activity of heparin and its derivatives. Data was analysed using two way ANOVA test (grouped analyses), Error bars indicate SD (n = 3). P value <0.0001. 81

Figure 3.9 Schematic reperesentation of glycol splitting of heparin pentasahraide sequence; consisiting of the antithrombin binding residues showing that splitting of glucuronic acid residue might be responsile for the disruption of the binding ability of this sequence with its antithrombin binding site. 82

Figure 3.10 Schematic representation of synthesis of glycol heparin conjugated silica NPs by coupling of amine functionalised silica NPs (NH_2-SiO_2) to glycol split heparin using EDC to produce heparin conjugated NPs (GS.HP-SiO_2). 83

Figure 3.11 Characterisation of glycol split heparin conjugated NPs. **A:** Particle diemeter of glycol split heparin conjugated NPs (GS-HP) compared to amine functionalised NPs (NH_2-Si). **B:** Polydispersity index (PDI) of the NPs shown in A. **C:** Zeta potential values of glycol split heparin conjugated NPs (GS-HP) and heparin conjugated NPs (HP-Si) compared to amine functionalised NPs (NH_2-Si) showing surface charge conversion. 84

Figure 3.12 Optical density of the released pNA measured at 405 nm representing the Anticoagulant activity of heparin conjugated NPs (HP-Si) and glycol split NPs (GS.HP-Si). Data

was analysed using two way ANOVA test (grouped analyses), Error bars indicate SD (n = 3). P value <0.0001..... 85

Figure 3.13 Schematic of O-desulphated heparin synthesis. Step 1 reperesents alkalinasation of heparin in order to form C2-C3 epoxy intermediate. Step 2 reperesents the lyophylisation of the prodeced epoxy intermediate resulting in hydrolysis of epoxy group and formation of hydroxyl groups at the same positions to produce 2-O desulphated heparin. 86

Figure 3.14 H^1 NMR spectra of native heparin and desulphated heparin Red arrows show the peak of iduronic acid proton at C1 of the ring where a dramatic shift occurred in desulphated heparin compared to the same peak in intact heparin. Heparin chemical shift (400 MHz, D2O); δ(ppm) = 1.15-1.1 (t, GlcNS6S, –CH2), 1.97 (s, GlcNAc6S, -CO-CH3, α to carbonyl), 3.22-3.2 (m, GlcNS6S H2), 3.41-3.29 (m, GlcA H2, H3), 3.63-3.58 (m, GlcNS6S H3), 3.77-3.67 (m, GlcNS6S H4), 3.89-3.87 (m, GlcNS6S H5), 3.97-3.92 (m, IdoA2S H4), 4.037 (s, IdoA2S H3), 4.21-4.13(m, GlcNS6S H6), 4.27 (s, IdoA2S H2), 4.46-4.33 (m, GlcA H1),4.94-4.86 (m, IdoA2S H5), 5.23-5.10 (m, IdoA2S H1), 5.51-5.34 (m, GlcNS6S3S H1). δ(ppm) = 1.98 (s, GlcNAc6S, -CO-CH3, α to carbonyl), 3.18-3.16 (m, GlcNS6S H2), 3.37-3.28 (m, GlcA H2, H3), 3.70-3.58 (m, GlcNS6S H3), 3.74-3.71 (m, GlcNS6S H4), 3.86-3.84 (m, GlcNS6S H5), 3.98-3.94 (m, IdoA2S H4), 4.06 (s, IdoA2S H3), 4.10-4.03(m, GlcNS6S H6), 4.12 (s, IdoA2S H2), 4.41-4.26 (m, GlcA H1), 4.90-4.87 (m, IdoA2S H5), 5.01-4.96 (m, IdoA2S H1), 5.53-5.26 (m, GlcNS6S3S H1). 87

Figure 3.15 Effect of O-desulpated heparin polymer on maximum absorption wavelength of azure A dye. **A:** UV-visible absorption wavelength spectra oF azure A alone (green), after addition of O-desulpated heparin polymer (red), and after addition of intact heparin sulpate (green),. **B:** Quantitative measurements of azure A lambda max change upon addition O-desulpated heparin polymer compared to that upon addition of intact heparin polymer. Data was analysed using unpaired t test. Error bars indicate SD (n = 3). *** is P ≤ 0.001. 88

Figure 3.16 Visual monitoring of the effect of O-desulphated heparin (Des.HP) and intact heparin (HP) polymers on Azure A dye colour using diferent concentrations ranging from 0 to 20 μg/mL. 89

Figure 3.17 Characterisation of desulphated heparin conjugated NPs. **A:** Particle diemeter of desuphated heparin conjugated NPs (Des-HP) compared to amine functionalised NPs (NH_2-Si).B: Polydispersity index (PDI) of the NPs shown in A. **C:** Zeta potential values of desulphated heparin conjugated NPs (Des-HP) and heparin conjugated NPs (HP-Si) compared to amine functionalised NPs (NH_2-Si) showing surface charge conversion. 90

Figure 3.18 Schematic representation of synthesis of desulphated heparin conjugated silica NPs by coupling of amine functionalised silica NPs (NH_2-SiO_2) to glycol split heparin using EDC to produce heparin conjugated NPs (Des.HP-SiO_2). 91

Figure 3.19 Effect of O-desulphated heparin conjugated NPs maximum absorption wavelength of azure A dye. **A:** UV-visible absorption wavelength spectra of azure A alone (green), after addition of O-desulphated heparin conjugated NPs (red), and after addition of unmodified heparin conjugated NPs (blue), **B:** Quantitative measurements of azure A lambda max change upon addition O-desulphated heparin conjugated NPs (Des.HP-Si) and heparin conjugated NPs (HP-Si),. Data was analysed using unpaired t test. Error bars indicate SD (n = 3). ** is $P \leq 0.01$. 92

Figure 4.1 Modified form of Jablonski diagram showing intersystem crossing (ISC) between singlet excited state of the donor and triplet excited state of the acceptor.[252] 96

Figure 4.2 The Jablonski diagram showing the mechanism of Förster Resonance Energy Transfer (FRET). Electrons transition from the ground state to an excited state in both donor and acceptor when they are excited, and they lose energy by both fluorescence with rate constant $k_{f(D)}$ for donor or $k_{f(A)}$ for acceptor non-fluorescence mechanisms with rate constant $k_{nf(D)}$ for donor or $k_{nf(A)}$ for acceptor. Throughout FRET, excited energy of the donor is also transferred to an acceptor with rate constant k_{FRET}. [255] 98

Figure 4.3 Effect of distance which separates the donor–acceptor pair on the efficiency of energy transfer attained by FRET process.[258] 99

Figure 4.4 Schematic visualizes the angles that are used to determine the relative orientation of the donor and acceptor transition moment.[260] 100

Figure 4.5 Dexter energy transfer enables diffusion of triplet excitons. Donor (D) and acceptor (A) molecules; the asterisk denotes excited state. The dashed arrows demonstrate simultaneous electronic configuration rearrangement of the electron transfer from the excited state of the donor molecule (D*) to a neutral acceptor (A).[278] 103

Figure 4.6 Diagram shows heparinase I, II and III specificities toward heparin and heparan sulphate. **A:** Heparinase I specificity, Y= SO_3^- or H, Z= SO_3^- or H. **B:** Heparinase II specificity, X= SO_3^- or H (Iduronic or glucuronic acid), R= SO_3^- or CH_3CO, Y= SO_3^- or H. **C:** Heparinase III: Y= SO_3^- or H, R= SO_3^- or CH_3CO. ∿∿ = Covalent bond is either above or below the ring plane, figure was adapted form Desai et al.[285] 104

Figure 4.7 β elimination mechanism of heparin degraded by heparinase II. The degradation mechanism involves C5 proton abstraction by deprotonated basic amino acid; Cysteine (Cys135) and subsequent proton donation by protonated acidic amino acid Histidine; (His 203) to stabilise the negative oxygen leaving group producing OH. Divalent ions (Ca^{+2}) work as a Lewis acid attracting the electrons of C5-Carboxyl groups consequently facilitating the abstraction of C5-proton by cystein. M^{*+}= Lysine or Ca^{+2}, M^+= Ca^{+2}. Figure was adapted from Sasisekharan et al.[291] 105

Figure 4.8 Hydrolysis mechanism of heparan glyosidic linkage cleavage by heparanase involving glutamic acid amino acid residue deprotonation in aqueous environment to provide water molecules necessary for hydrolysis, figure was adapted from Rivara et al.[294] 107

Figure 4.9 Schematic representation of Dual labelled heparin sensing probe synthesised by (A) intrachain conjugation of aminomethyl fluorescein and black hole quencher 1 (BHQ1) to heparin using EDC/NHS coupling agents, and dual labelled heparin sensing probe synthesised

by end-chain conjugation of fluoresceinamine using reductive amination method and intrachain conjugation of black hole quencher 1 (BHQ-Amine) to heparin using EDC/NHS coupling agents. 124

Figure 4.10 Florescence quenching of the dual labelled heparin probe. A: Fluorescence spectrum, B: Fluorescence Intensity of dual labelled heparin prepared by intrachain conjugation of fluorescein and BHQ1 to heparin carboxylate groups (Dual labelled HP) compared to fluorescein labelled heparin(Flu-HP)prepared by intrachain conjugation of fluorescein. Data was analysed using unpaired t test. Error bars indicate SD (n = 3), ** is P ≤ 0.01, *** is P ≤ 0.001**** is P ≤ 0.0001. 125

Figure 4.11 Quenching efficiency of the dual labelled heparin prepared using intrachain conjugation of the FRET pair at different molar ratio of BHQ1 to heparin showing that the maximum quenching efficiency has been achieved at 1:20 molar ratio. Data was analysed using unpaired t test. Error bars indicate SD (n = 3), ns is non-significant difference (P-value ≥ 0.05). 126

Figure 4.12 Fluorescence quenching of the dual labelled heparin probe. A: Fluorescence spectrum, B: Fluorescence intensity of dual labelled heparin prepared by end-chain conjugation of fluorescein to heparin carboxylate groups (Dual labelled HP) compared to fluorescein labelled heparin (Flu-HP) prepared by end-chain conjugation of fluorescein. Data was analysed using unpaired t test. Error bars indicate SD (n = 3), ** is P ≤ 0.01, *** is P ≤ 0.001, **** is P ≤ 0.0001. 127

Figure 4.13 3D chemical structure of dual labelled heparin probe. A: 3D structure of dual labelled heparin prepared by intrachain conjugation of fluorescein and BHQ1. B: 3D structure of dual labelled heparin prepared by end-chain conjugation of fluorescein while attaching the BHQ1 within heparin chain. Data was analysed by MM2 energy minimization calculations using ChemBio3D software. 129

Figure 4.14 Effect of intermolecular dimerization of the FRET pairs. A: The fluorescence of fluoresceinamine in combination with positively charged BHQ1-Amine and negatively charged heparin (Physical mix) compared to physical mix of heparin and aminomethyl-fluorescein and the corresponding chemical structures of the physical mixture. B: The fluorescence of negatively charged carboxyfluorescein in combination with negatively charged BHQ1 and negatively charged heparin (Physical mix) compared to physical mixture of heparin and fluorescein (HP+FAM) and the corresponding chemical structures of the physical mixture. 131

Figure 4.15 Schematic representation of dual labelled heparin probe depolymerisation by nitrous acid. Deaminative cleavage of dual labelled heparin probe to produce 2, 5-anhydromannose derivatives releasing the quenched fluorescein into the solution to recover the fluorescence signal. 133

Figure 4.16 Complete degradation of heparin by Nitrous acid at pH 1.5. Azure A absorption spectrum after addition of depolymerised heparin by nitrous acid (Azure A + Depolymerised HP) and intact heparin (Azure A + Intact HP). 133

Figure 4.17 Fluorescence signal recovery of dual labelled heparin depolymerisation using nitrous acid at pH 1.5. Emission spectra (A) and emission intensity (B) of dual labelled heparin after depolymerisation by nitrous acid. Data was analysed using unpaired t test. Error bars indicate SD (n = 3), ** is $P \leq 0.01$. 134

Figure 4.18 Fluorescence signal recovery of dual labelled heparin probe after incubation with heparinase I and II for 24 hours. Fluorescence spectra (A) and Fluorescence intensity (B) of heparinase treated dual labelled heparin probe (HEP-treated dual labelled HP) compared to untreated dual labelled heparin probe (Untreated dual labelled HP). Data was analysed using unpaired t test. Error bars indicate SD (n = 3), * is $P \leq 0.05$. 135

Figure 4.19 Illustrative diagram of core-shell NPs with different shell thicknesses ranging from 12 nm to 70 nm and their corresponding particles size distribuations relative to blank silica core size distribution measured by dynamic light scattering (DLS). 137

Figure 4.20 Fluorescence spectra of TAMRA incorprated within the outer layer of different core-shell silica NPs containing blank core silica matrix having diffeent thicknesses of their shells ranging from 12 nm to 70 nm. 138

Figure 4.21 Schematic of A: BHQ2 conjugated heparin probe synthesis using EDC/NHS coupling reaction , B: BHQ2 conjugated heparin (BHQ2-HP) probe grafting onto the surface of TAMRA containing 12 nm shell NPs (TAMRA-Si) to produce FRET based TAMRA-BHQ2, donor-acceptor system (BHQ2-HP-Si) using EDC/NHS reaction. 139

Figure 4.22 A: Spectral overlap of the absorption spectra of black hole quencher (BHQ2), black hole quencher conjugated heparin probe (BHQ2-HP) and black hole quencher conjugated heparin grafted onto the surface of core-shell silica NPs (BHQ2-HP-Si) and the fluorescence spectrum of TAMRA-labelled core-shell NPs. Fluorescence spectra (B), and fluorescence intensity (C) heparin conjugated core-shell NPs containing TAMRA incorporated within the shell (HP-Si) compared to black hole quencher–heparin conjugated core-shell NPs containing TAMRA incorporated within the shell (BHQ2-HP-Si). Data was analysed using unpaired t test. Error bars indicate SD (n = 3), ** is P ≤ 0.01, *** is P ≤ 0.001**** is P ≤ 0.0001. 141

Figure 4.23 A: Illustrative diagram of a ratiometric core-shell NPs composed of an inert nanoparticle core, encapsulating BHQ2-insensitive fluorophore; 7-Methoxycoumarin as a reference dye and shell containing BHQ2-sensitive fluorophore; TAMRA. B: Fluorescence spectra of coumarin dye and coumarin incorporated NPs (Coumarin-Si) alongside the absorption spectra of black hole quencher 2- heparin conjugate (BHQ2-HP conjugate) and black hole quencher 2-heparin conjugated core-shell silica NPs (BHQ2-HP-Si). Fluorescence spectra and fluorescent ratio of core-shell NPs containing shell modified with either heparin

(HP-Si) or black hole quencher-heparin conjugate (BHQ2-HP-Si) and core consisting of coumarin as a reference fluorophore incorporated within the silica matrix. C: emission spectra of the BHQ2-insensitive fluorophore (7 methoxy coumarin), recorded on a spectrofluorometer after excitation at 360 nm. D: Emission spectra of the BHQ2-responsive dye incorporated in the nanoparticle shell (TAMRA) recodred on spectrophotometer after excitation at 540 nm, E: Fluorescent ratio of TAMRA to coumarin measured at emission wavelngths; 575 nm and 385 nm respectively. Data was analysed using unpaired t test. Error bars indicate SD (n = 3), ** is P ≤ 0.01. 144

Figure 4.24 **A:** Schematics showing a 12 nm core-shell NPs after appending of either native heparin (HP) or black hole quencher 2 linked heparin (BHQ2-HP). After weighing the same mass of each NPs type the number of BHQ2-HP conjugated NPs is speculated to be lower than the number of heparin conjugated NPs owing to the higher estimated particle-weight of BHQ2-HP conjugated NPs. **B:** Total Particles weight difference between BHQ2-HP conjugated NPs and heparin conjugated NPs having the same amount of the precursor blank NPs before the conjugation process and treated under exactly the same washing conditions. Data was analysed using unpaired t test. Error bars indicate SD (n = 3), ** is P ≤ 0.01. 145

Figure 4.25 A: Schematic diagram of heparin conjugation with aminomethyl fluorescein through EDC/NHS coupling reaction to produce fluorescent heparin conjugate. B: Fluorescence spectrum of fluorescent heparin; aminomethyl fluorescein-heparin probe compared to free aminomethyl fluorescein dye. 146

Figure 4.26 Schematic diagram of BHQ1 incorporation within the silica matrix of the NPs by attaching BHQ1-SE to APTES linker and subsequent BHQ1-APTES conjugate incorporation through formation of siloxane bonds (red) between APTES AND TEOS during the formation of silica NPs to produce BHQ1 incorporated silica NPs (BHQ1-Si). 147

Figure 4.27 Schematic representing fluorescent heparin; aminomethyl fluorescein-heparin grafting onto the surface of black hole quenher1 (BHQ1) incorporated silica NPs using EDC/NHS coupling reaction to produce heparinase nanosensors (Flu-HP-Si-BHQ1). 147
Figure 4.28 Particle size distribution of BHQ1 incorpotaed silica NPs (red) compared to blank silica marix NPs (black) meaured by DLS. 148
Figure 4.29 Absorption spectra of black hole quencher-1 (BHQ1) incorporated silica NPs (BHQ1-Si) compared to black hole quencher-1 (BHQ1) covalently attached to aminopropyltriethoxysilane; APTES (BHQ1-APTES conjugate). 149
Figure 4.30 Fluorescence spectra (A) and fluorescence intensity (B) of fluorescent heparin (Flu-HP) conjugated to the surface of blank silica NPs (red) compared to fluorescent heparin labelled with aminomethyl fluorescein (Flu-HP) conjugated to the surface of black hole quencher-1 incorporated NPs (blue). 150
Figure 4.31 Fluorescence signal recovery of model III nanosensors. A: Fluorescence spectra(left) and intensity (right) of fluorescein labelled heparin probe (Flu-HP) grafted onto the surface of BHQ1 incorporatde NPs with heparinase treatment (red) and without heparinase treatment (blue) at pH 7. B: Fluorescence spectra (left) and intensity (right) of fluorescein labelled heparin probe grafted onto the surface of BHQ1 incorporatde NPs with heparinase (red) and without heparinase (blue) after adjustment the pH of the buffer solution from 7 to 11 after enzyme treatment. Data was analysed using unpaired t test. Error bars indicate SD (n = 3), ns (nonsignificant) is $P > 0.05$, *** is $P \leq 0.001$. 152
Figure 4.32 schematic representation the role of pH adjustment in releasing of heparin fragments after treating heparinase nanosensors with heparinase I & II. A: Ionically bound heparin fragments remaining close to the surface of black hole quencher incorporated NPs at pH 7. B: Unbound heparin fragments released away from the surface of the black hole quencher incorporated NPs after adjusting the pH of the suspension from 7 to 11. 153

List of Tables

Table 1 Commonly used fluorophores and their corresponding black hole quenchers (BHQs) which make up the donor-acceptor FRET pair system. Some of the fluorophores listed below such as CAL Fluor and Quasar dyes produced by Biosearch are used for multiplex real-time quantitative PCR. Where they have a wide range of emission maximum wavelengths (540 nm to 705 nm), these dyes are considered as a low cost alternative for fluorophores commonly used on real-time thermocyclers (TET, JOE, VIC, HEX, Texas Red, Cy3, Cy5, and Cy5.5).Where they can be coupled with the corresponding black hole quencher and used for qPCR.[256] 101

Table 2 Illustrative diagrams of the FRET based models designed for studying of heparinase sensing and detection. 109

List of Abbreviations

NH_4OH	Ammonium hydroxide
SiO_2	Silicon dioxide
NPs	Nanoparticles
TEOS	Tetraethylorthosilicate
APTES	(3-Aminopropyl)triethoxysilane
EDC	N-(3-Dimethylaminopropyl)-N’-ethylcarbodiimide hydrochloride
EDTA	Ethylenediaminetetraacetic acid
DMMB	1,9-Dimethyl Methylene Blue zinc chloride double salt
Trizma base	Tris(hydroxymethyl)aminomethan
MES	2-(N-morpholino)ethane sulfonic acid
TAMRA, SE	Carboxytetramethylrhodamine Succinimidyl Ester
5(6)-FAM, SE	5-(and-6)-Carboxyfluorescein Succinimidyl Ester mixed isomers

Alexa 633, SE	Alexa fluor 633-Succinimidyl Ester
HUVECs	Human umbilical vein endothelial cells
PFA	Paraformaldehyde
CD62P	Cluster of differentiation 62; P-Selectin
FITC	Fluorescein isothiocyanate
TEM	Transmission electron microscope
DLS	Dynamic light scattering
EPR	Enhanced permeability and retention
D_2O	Deuterium oxide
EGF	Epidermal growth factor
FGF	Fibroblast growth factor
VEGF	Vascular endothelial growth factor
EpCAM	Epithelial cell adhesion molecule
mAb	Monoclonal antibody
Fab	Antigen-binding fragments
DNA	Deoxyribonucleic acid
ctDNA	Circulating tumour DNA
CTCs	Circulating tumour cells
CECs	Circulating endothelial cells
Anti-Xa	Anti-factor Xa
AT	Antithrombin
IL-1β	Interleukin 1 beta (Leukocytic pyrogen)
NF-κB	Nuclear factor kappa B light chain
RES	Reticuloendothelial system
HEPI	Heparinase I from flavobacterium heparinum
HEPII	Heparinase II from flavobacterium heparinum

Coumarin-SE	7-methoxycoumarin-Succinimidyl ester
Sulfo-NHS	N-hydroxysulfosuccinimide
BHQ1-Carboxylate	Black hole quencher 1-Carbxylate
BHQ1-Amine	Black hole quencher 1-Amine
BHQ1-SE	Black hole quencher 1-Succinimidyl ester
BHQ2-Amine	Black hole quencher 2-Amine
NaOH	Sodium hydroxide
NMR	Nuclear magnetic resonance
FRET	Förster (Flourescence) resonance energy transfer
cP	Centipoise
nm	Nanometre
TGA	Thermogravimetric analysis
QE	Quenching efficiency
PCR	Polymerase chain reaction
NGS	Next generation sequencing
VCAM-1	Vascular adhesion molecule 1
ICAM-1	Intercellular adhesion molecule 1
TNF-α	Tumour necrosis factor alpha

1 Chapter one: General Introduction

1.1 Nanomedicine

Nanomedicines are the products of nanotechnology applied to therapy, and include the use of nanomaterials for drug delivery, biosensing and bioimaging, blood purification and tissue engineering.[1] Amongst the many nanotechnology platforms, nanoparticles have been extensively investigated as potential nanomedicines, primarily for their ability to act as carriers to enhance the site-selective delivery of therapeutic agents. Of particular note have been nanoparticles (NPs) for malignant cancer therapy, with the key design aim being to generate NPs which can act as "magic bullets" for enhanced transport of cytotoxic drugs to a desired site of action while minimising systemic exposure.[2] Accordingly, there have been many examples of investigational cancer nanomedicines, but while some have been adopted clinically (Doxil/Caelyx)[3] and Abraxane,[4] cancers as a disease class remain inadequately treated.

1.2 Cancer

Cancer is an uncontrollable division of normal cells to produce immature and less specialised cells which are less able to perform the functions of normal cells,[5-6] where cells evade the apoptosis process and become insensitive to anti-growth signals.[7] Cancer occurs due to genetic mutation of cell cycle controllable genes.[8] This could be also influenced by environmental factors.[9]

The high mortality rate ~ 90% in cancer patients, who are diagnosed with highly metastatic cancer types e.g. melanoma, pancreatic adenocarcinoma and small cell lung cancer, is attributed to metastasis.[10-12] Metastasis is a complex process that involves several distinct stages. The spread of cancer requires the entry of the tumour cells into the systemic circulation; a process called intravasation followed by endothelial cell adhesion and extravasation in order to form a premetastatic niche in distant organs.[13-14]

Understanding the mechanism by which the tumour cells metastasise is crucial for improving the outcomes and achieving better prognosis in cancer patients treatment.[15]

1.3 Metastasis

Metastasis is defined as the spread of a primary tumour to other surrounding tissues and to distant organs. The metastatic process starts with epithelial-mesenchymal transition, where tumour cells become more motile at this stage. This happens when cancerous cells evade the immune system, consequently bypassing the immune system checkpoints. In the epithelial-mesenchymal transition, mutation of gene expression is accumulated in step-wise manner is known to contribute to the transition of normal epithelial cells to mesenchymal tumour cells. These tumour cells adapt to independently induce growth and confer invasive morphology. For instance, neoplastic cells are formed as a result of mutation in cell-cell adhesion genes, which is accompanied by downregulation of certain receptors such as tight junctions which hold the cells together at the solid tumour. The dysmorphic shape of cancerous cells enables their extravasation from the capillaries and invading the cells in distant organs, consequently spread of tumour.[16-17] One of the key events that also occurs at early metastatic stage when tumour cells become mobile is upregulation of heparanase enzymes. Heparanases facilitate the movement of metastatic cells from the tumour site to the blood vessels by degrading extracellular matrix components namely heparan sulphate which hinders the movement of metastatic cells. Once metastatic cells have reached the systemic circulation, they start to attach to vascular endothelium by rolling adhesion process which is quite similar to the rolling adhesion of leukocytes during the inflammation process.[18-19] Metastatic cells hijack vascular endothelium receptors used by immune cells for rolling adhesion and extravasation. Thus, circulating tumour cells overexpress a tetrasaccharide ligand called Sialyl Lewis x (sLe^x) that binds to selectin type receptors; namely P- and E- selectin receptors overexpressed by endothelial cells lining the blood vessels, subsequently cancerous cells extravasate from the

capillary beds and invade normal cells in distant organs, thus colonising into secondary tumour.[20-24] Various stages of metastasis process are depicted in Figure 1.1.

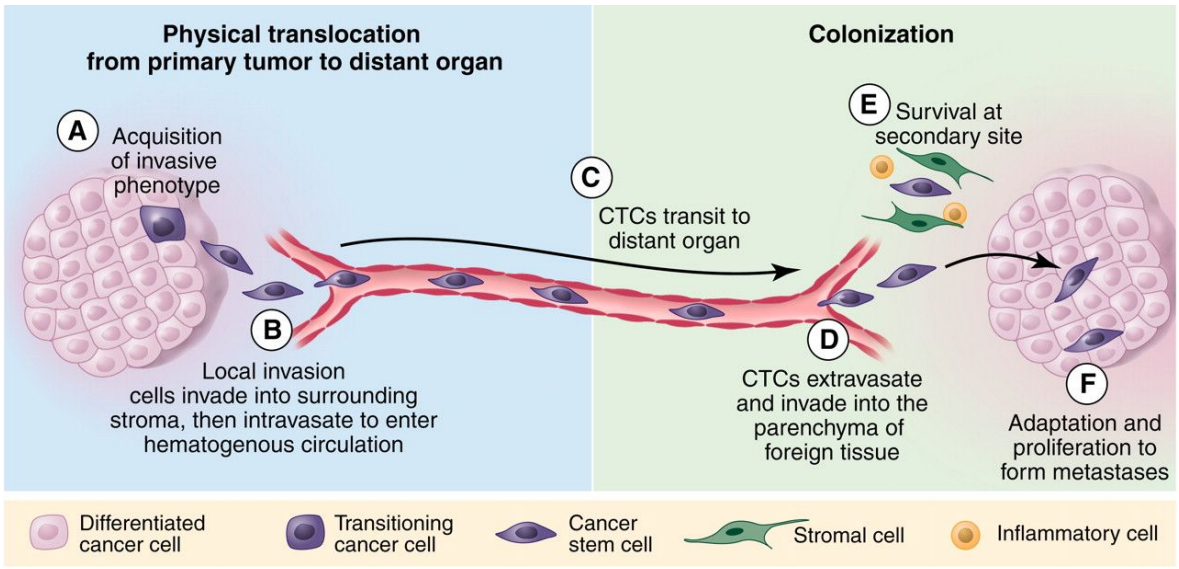


Figure 1.1 Schematic representation of the metastatic process which can take place at two different stages. The first stage is the physical movement of the metastatic tumour cells from the primary site to distant organ and the second stage is colonisation of the metastasised cells at the secondary site. A: Cancer cells start to change their phenotype to a more motile and invasive form. B: tumour cells create a path through ECM aided by heparanase and other matrix degrading enzymes in order to enter the systemic circulation. C: Circulating tumour cell (CTCs) travel through blood vessels. D: CTCs extravasate and exit the circulatory system via rolling adhesion process. E: Tumour cells evade and escape the Immune system in order to survive at the secondary site and form a premetastatic niche. F: Tumour cells adapt and change the microenvironment for further growth and proliferation. Figure was taken from Chaffer et al. [13]

1.3.1 Role and function of GAGs in cancer progression and cell signalling

1.3.1.1 GAGs family and categorisation

Glycosaminoglycans (GAGs) are linear negatively charged heteropolysaccharides composed of repeating disaccharide units of hexosamine and hexuronic acid. Depending on the variability monosaccharides occurrence within the polymer chain and their sulphation pattern, GAGs are categorised into either sulphated or non-sulphated polysaccharides. Sulphated GAGs include heparin, heparan sulphate, chondroitin sulphate, dermatan sulphate and keratan sulphate. While non-sulphated GAG encompasses hyaluronan.[25-26] GAGs are known as major macromolecules in regulating physiology and pathology of many conditions in the human body.[27-28] They modulate cellular properties and function by acting directly on cell receptors and interacting with growth factors to enhance the downstream signalling pathway for cellular proliferation which is necessary for wound healing and tissue repair.[29]

Researchers have also reported that the occurrence of GAG with altered structures in several diseases indicating their importance as biomarkers for diagnostic procedures.[30]

1.3.1.2 Differential characteristics of heparin and heparan sulphate

Heparin is stored in the mast cells of connective tissues; the only cells of human body that can produce heparin.[31] While, Heparan sulphate (HS) is a natural polysaccharide present in most mammalian cells. It is predominantly present on cell surfaces and in the extracellular matrix (ECM). Thus, heparan sulphate functions as a regulator to normal and pathological conditions.[32-33]

Heparin and HS are made of repeating disaccharide units of glucosamine (GlcN) and hexuronic acid residues consisting of either glucuronic acid (GlcA) and/ or iduronic acid (IdoA). Where these sugar moieties are covalently attached through a glyosidic bond called α 1-4 linkage, thus forming a negatively charged heteropolysaccharides of heparin and HS. Heparin and HS differ in the number of these repeating units, consequently the molecular weight and in proportion of the major units that occur within the chain of the polysaccharides. HS could either be free or bound to a protein core, specifically the serglycin (a protein that is primarily expressed in hematopoietic and endothelial cells), to form Heparan sulphate proteoglycan (HSPG). In contrast heparin is present in free form.[34-35] The structure of each monomer; the major and minor units that form either heparin or HS chain is illustrated in Figure 1.2.

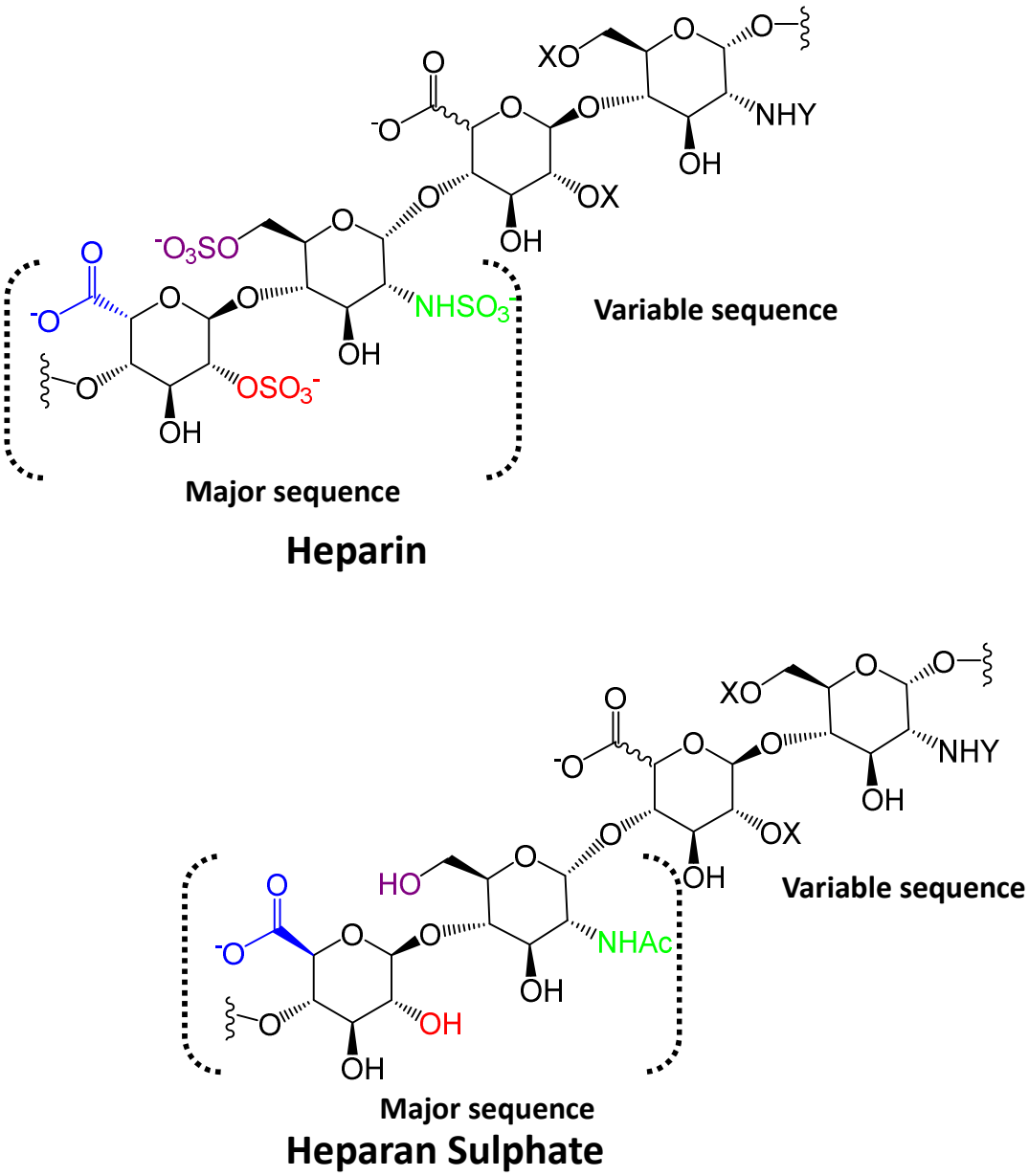


Figure 1.2 Illustration shows the possible patterns of sugar moieties making up heparin and heparan sulphate (HS) including the major and variable disaccharide repeating units. X= SO_3 or H. Y = Ac or H or SO_3. SO_3 = Sulphate group. H= Hydrogen atom, Ac= Acetyl group. Figure adapted from Nelson et al.[36]

Heparin and heparan sulphate are not entirely similar. Heparan sulphate consists of a different primary structure of disaccharide subunits. Where it has longer chains and higher average molecular weight (around 30kDa) that is two times the molecular weight of heparin chain. Due to its long chain, heparan sulphate is known to confer to have high susceptibility of variations on in its minor disaccharide monomer, therefore comprising a significant structural heterogeneity. Modification of the structure of the sugar moieties forming HS,

such as changing or removing the acetyl group or sulphate group at the N-position of glucosamine, sulphation at the 2O-position of uronic acid or 6O- and 3O-position of glucosamine and epimerization of C-5 position of uronic acid could all contribute to the variability and complexity of the sequence pattern.[37]

Heparin and HS have a distinctive 3-O sulpho group on the internal D-glucosamine (GlcNS (3S)) residue which enables the high binding affinity to antithrombin. The 3 O-sulphation had been claimed to be a useful biomarker for identifying sequences in HS chains required for viral entry[38] and bridging of growth factor-receptor in the ternary complex.[39] Heparin and heparan sulphate possess a unique pentasaccharide sequence which binds to antithrombin, subsequently inducing a blood thinning effect. Consequently, Heparin is widely used as an anticoagulant.[40]

1.3.1.3 Heparan sulphate role in cell signalling and metastasis

According to their cellular localisation, HS chains are either cell surface bound proteoglycans or basement membrane proteoglycans (Extracellular matrix based). HSPG present abundantly on cell surfaces and in the extracellular matrix, therefore it enables reorganisation of the extracellular matrix binding to collagen I, collagen IV, fibronectin and laminin; structural formation and consistency of the matrix with basement membrane. This implicating the role of HSPG in regulating cell-cell adhesion and cell-extracellular matrix interaction. Therefore, in absence of HSPG, malignant cells are triggered and begin to invade and metastasise to distant organs.[41]

Furthermore, cell surface HSPGs with its sulphation pattern on HS chain can interact with various growth factors, cytokines and chemokines thus possessing different biological roles.[42-43] Thus the sulphation pattern of HS chain in HSPGs could modulate various pathological and biological functions. For instance, Tetramer to hexamer sequence of 2O-sulphated iduronic acid with 6O-sulphated glucosamine enables HS chain to bind to basic fibroblast growth factor (FGF-2), thus modulating the cell proliferation and metastasis. In

turn, FGF-2 binds to fibroblast growth factor receptor (FGFR) in order to induce cell signalling, subsequently cell division and growth.[44] In this sense, cell surface HSPG plays a crucial role in progression cancer and cell signalling.[45]

On the other hand, cell free HS chains could also interact with growth factors such as FGF-2 and vascular endothelial growth factor (VEGF), creating a reservoir of protected growth factors which enables promotion or inhibition of tumour growth and angiogenesis.[46] Moreover, cell surface heparan sulphate bind to P-selectin receptors expressed on the surface of the platelets and mediates the coagulation process through thrombin in order to create a protective layer around the tumour cells, enabling CTCs to evade the immune system.[47]

Figure 1.3 shows a schematic diagram representing the role of HS/ HSPG in modulating various pathological mechanisms in metastasis and invasion of tumour cells and the ability of heparin to compete HS at these cellular effects.

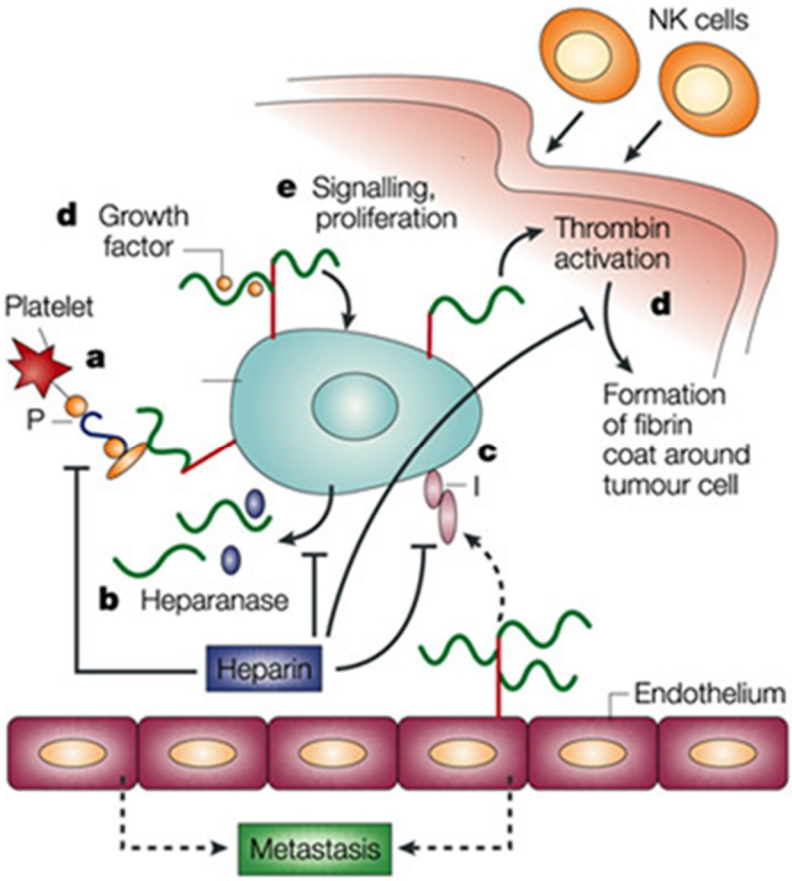


Figure 1.3 ***Schematics showing the role of heparan sulphate in tumour metastasis.*** *Heparan-sulphate in the free form (HS; green lines) or attached to the proteoglycans (Red lines) mediates metastasis.* ***a:*** *cell surface HS on tumour cells can act as a ligand for P-selectin (**P**) receptor, which mediates adhesion either to platelets to create a protective clotting aggregates around tumour cells or to the endothelial cells lining the vascular capillaries. Enabling cancer cells to extravasate and metastasise to secondary organs.* ***b:*** *Heparanase cleaves heparan sulphate in the extracellular matrix; not only releasing the bound growth factors that promote further tumour cell proliferation but also creating a passage to facilitate tumour cell movement to blood vessels.* ***c:****Heparan sulphate proteoglycans acts as a co-receptor for integrin receptors (**I**) thus mediating tumour cell adhesion to blood vessels to facilitate the extravasation of the circulating tumour cells.* ***d:*** *heparan sulphate mediates the microclimate-coagulation through modulating a coagulation factor thrombin (Factor IIa) in order to initiate the formation of fibronectin protective layer around tumour cells. e: cell surface HSPG interact with growth factors (FGF and VEGF) facilitating their binding to the cell surface receptors forming a ternary complex thus regulating the signalling pathway of further tumour cell growth. Exogenous heparin can inhibit heparan sulphate action at stages a, b, c and d. Figure was taken from Sasisekharan et al.*[47]

1.3.1.4 Metastatic cascade inhibition by heparin

Heparin interferes with the metastatic process throughout its different stages. Heparin reduces the movement of the highly motile metastatic cells through extracellular matrix (ECM), a prerequisite step for intravasation process. Thanks to heparanase inhibitory activity of heparin, the penetration of the metastatic cells through ECM could be reduced as heparanase is responsible for cleavage of heparan sulphate; a major component of ECM that

facilitates tumour cells movement away from the primary tumour toward the blood vessels.[48] Heparin can also block certain receptors overexpressed on the surface of vascular endothelium namely P-selectin receptors that are exploited by circulating tumour cells through the extravasation process.[49] Furthermore, the anti-platelet activity of heparin prevents the formation of microclots surrounding the circulating tumour cells by disrupting the P-selectin mediated interaction between platelet and circulating tumour cells. The formation of microclots helps circulating tumour cells escape the immune system components such as microphages due to the covering of the recognition antigens on tumour cell surface, where tumour cells hoax the immune system.[50] Figure 1.4 shows the inter-play role of heparin in metastatic cascade inhibition.

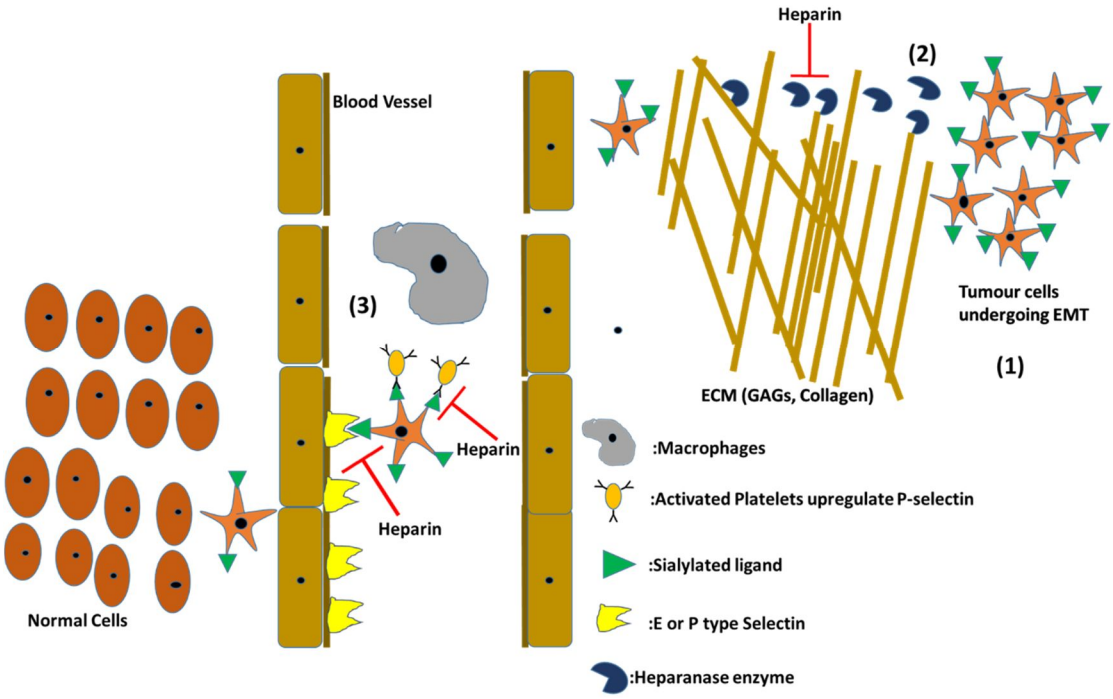


Figure 1.4 Schematic shows metastatic cascade inhibition by native heparin polymer. Heparin blocks the metastasis at various stages. At stage (2), heparin inhibits the action of heparanase. At stage (3); heparin blocks the interaction between circulating tumour cells and P-selectin on overexpressed on the surface of platelets and vascular endothelial cells.

Furthermore, Exosomes are nanovesicles secreted by cancer cells, carrying certain proteins and onco-micro RNAs required for modulation of recipient cells microenvironment at the secondary tumour site, thus facilitating the metastasis. Heparin had shown its ability to interfere with the transfer of microRNA from cancer cells to the recipient cells in the

metastatic niche of the secondary tumour. For instance, It has been confirmed that heparin; but not structurally related sugar chondroitin sulphate, could decrease exosome uptake by glioblastoma cells. The inhibition of exosome uptake was highly dependent on the degree of sulphation (charge density) and the dose of heparin.[51]

In light of these observations, heparin plays a key role in inhibiting the metastatic cascade, subsequently it can prevent tumour cells dissemination through blocking the underlying mechanisms of metastasis.

1.4 Nanoparticles

NPs have long been used to deliver chemotherapeutic drugs to specific target sites in a controlled manner, thus reducing the off-target effects and non-desirable side reactions that are usually accompanied with cytotoxic drugs.[52-53] Particles are considered to be in the 'nano' range if they have particle diameters less than 1000 nm, although most investigational NPs have diameters of 200 nm or less.[54] The targeting effect of the nanocarriers is attributed to the EPR (enhanced permeability and retention) effect as illustrated in Figure 1.5. It is hypothesised that the nanoparticles are passively targeted to the active site by virtue of their size (larger than that of normal small drug molecules).[55-56] Nanoparticles are thought to be delivered to cancer cells through highly fenestrated and leaky blood vessels surrounding the tumour. In contrast, due to their large size, NPs are unable to cross the vascular endothelial barrier of the normal blood vessels surrounding the normal tissue. This facilitates the deposition and localisation of the NPs at the tumour site. Consequently, NPs accumulate in the tumour where they deliver their cargo of cytotoxic drug. Furthermore, the lymphatic vessels are quite limited in the tumour which reduces the clearance and the filtration of the particles at the tumour site. This results in retention of the particles at the target site for longer than normal drug molecules.[57-60] Active targeting is another approach to achieve delivery of the cytotoxic drug to tumour cells. In active targeting, the surface of the NP is functionalised with an active ligand that specifically binds to certain receptor overexpressed

on the surface of the tumour cells but that are expressed at significantly lower levels on the surface of the normal cells. This enables targeted delivery of the NPs drug cargo to tumour cells.[61-64] Although the targeted delivery of the chemotherapeutic agents using nanotechnology is a widely used concept in the literature, the clinical translation of the NPs drug delivery system, regarding the therapeutic efficacy, toxicity and cost effectiveness, is still debatable and has been criticised by some researchers. A multivariate analysis of a 10-year period was conducted and the study has revealed that the percentage of the NPs dose administered to solid tumour in mouse model was very low with median delivery efficiency of 0.7 %. This is primarily attributed to various *in vivo* elimination mechanisms of the NPs. Reticuloendothelial system (RES) in the liver, spleen and lymph nodes containing macrophages that identify the NPs and subsequently engulf and degrade them. Moreover, NPs with particle diameter smaller than 5.5 nm are excreted by renal filtration.[65] Very recently, Sindhwani *et al* have reported that 97% of injected NPs in a particular study were delivered to tumour sites via trans-cellular pathways through the endothelial cells of the tumour vasculatures and not via inter-cellular pathways through endothelial gaps of leaky tumour blood vessels. This study revealed that the occurrence of inter-cellular gaps between the endothelial cells was significantly less frequent than the intra-cellular vacuoles and transcellular channels. The data also showed that the NPs extravasated and reached the tumour interstitial fluid primarily by vesicular formation (such as caveolae mediated process) in the tumour endothelial cells and subsequent transcytosis, thus suggesting a key role of active transport in delivery of NPs to tumour cells. This finding contradicts the concept of passive targeted delivery of NPs and their enhanced accumulation in the tumour extracellular space by the EPR effect in certain cases and also provides an insight about the currently inefficient clinical translation of the nanomedicines for human use.[66]

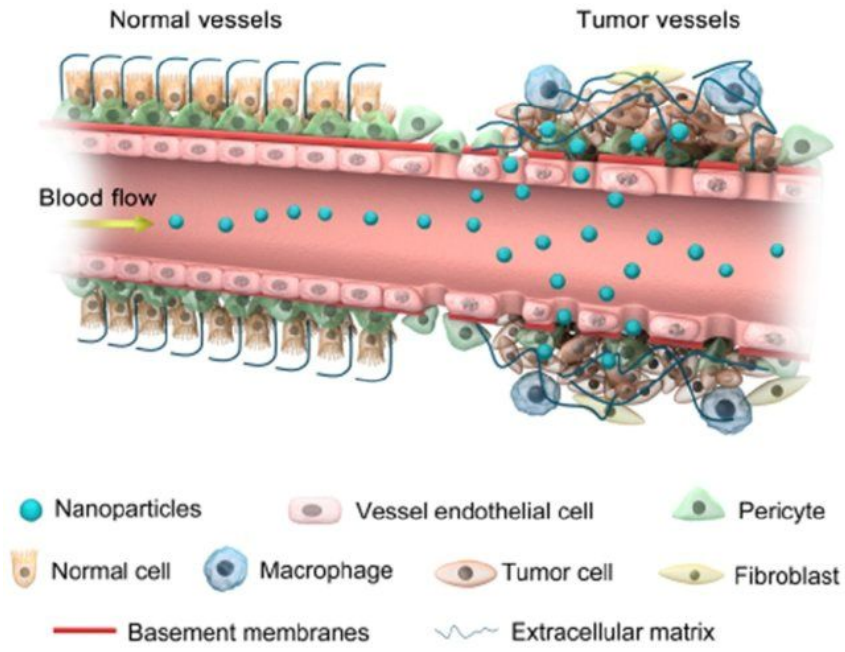


Figure 1.5 Schematics shows the accumulation of the NPs at the tumour site due to the EPR effect. NPs can only pass through porous blood vessels surrounding tumour tissues whilst they cannot cross through the endothelial barrier of the healthy vasculatures supplying the normal cells. Adapted from Abdalla et al.[67]

NPs used to deliver drug actives to the target site need to be biocompatible and/or biodegradable.[68-69] Different kinds of NPs are usually used for this purpose, including organic and inorganic NPs. Organic NPs encompass polymeric NPs, liposomes, solid-lipid NPs, nanocrystals, dendrimers and protein based NPs. Polymeric NPs have a diameter ranging from 10-1000 nm and are usually made of biocompatible polymer such as polylactide co-glycolide copolymers (PLGA), polycaprolactones (PCLs), polyacrylates and natural polymers including collagen, gelatin and alginate.[69] Polymeric NPs could also be classified into three different groups; polymeric micelles, drug-polymer conjugates (prodrugs) and hydrogels. In the polymeric micelles; the drug can be incorporated through the hydrophobic interactions such as the use of amphiphilic co-polymer for drug delivery. Drug-polymer conjugate where the drug is incorporated through covalent bond to a linear polymer, the bond is usually stimuli responsive where it breaks in order to release a dug to exert its action. Hydrogels are where the drug is loaded inside an aqueous core. Inorganic NPs consist of a group of noble metal NPs like gold and silver NPs where they have proven low toxicity due to their inertness.

Inorganic NPs also include superparamagnetic NPs, carbon based nanostructures like carbon nanotubes and ceramic NPs such as silica, alumina NPs.[70]

1.4.1 Ligand decorated nanoparticles and targeted drug delivery

The nanoparticle surface can be functionalised with a wide array of biomolecules that serve as a targeting ligands which specifically interact with certain receptors upregulated by tumour cells. The presence of the ligands on the surface of the NPs enhances a preferential cellular uptake through a process called receptor mediated endocytosis (RME), thus active targeting of cytotoxic drugs to tumour cells can be achieved.[71-72]

Several biomolecular ligands have been harnessed in order to achieve targeted drug delivery of the NPs including monoclonal antibodies (mAbs), peptide, antibody fragments (FAB), whole protein (transferrin), aptamers and vitamins (folate).[73]

Monoclonal antibodies are widely used for targeting cancer cells ,where certain antibodies can specifically bind antigens that are overexpressed on the surface of tumour cells such as the use of antibodies to target human epidermal growth factor (HER2), epidermal growth receptors (EGFR), prostate specific membrane antigen (PSMA).[74] Trastuzumab is a humanised antibody that specifically binds to HER2 expressing breast cancer cells. Trastuzumab conjugated albumin NPs had shown a preferential cell uptake by HER2 positive breast cancer cells (SK-BR-3 and BT-474 cells) compared to HER2 negatives cell lines (MCF-7 cells).[75] Cetuximab; a chimeric human-murine antibody that competitively binds to EGFRs overexpressed on the cancer cell surface was utilised to functionalise the surface of gold NPs in order to target EGFR upregulated by pancreatic cells. The resultant accumulation of gold NPs in pancreatic cells was further exploited to selectively heat the tumour cells in the thermal ablation therapy.[76] Prostate-specific membrane antigen (PSMA) is a tumour antigen that is overexpressed by prostate cancer cells. Paclitaxel loaded micelles functionalised with an antibody against PSMA were utilised for the treatment of prostate cancer xenograft mice *in vivo*. The results showed that PSMA functionalised micelles significantly prevented the

growth of the tumour compared to non-functionalised micelles.[77] Antibody fragments are also used to functionalise the surface of the NPs for active targeting. Antigen-binding fragments (Fab) and single-chain variable fragments (scFV) are the most commonly used antibody fragments for this purpose. Anti ED-B scFV that specifically binds to ED-B fibronectin which is an isoform that is solely expressed in tumour tissues, has been successfully used to functionalise the surface of the liposomes to target F9 teratocarcinoma tumours.[78] Moreover liposomes that encapsulated doxorubicin were functionalised with a mAb fragment that is specific for beta 1 integrins expressed on non-small cell lung carcinoma cells. These Fab-functionalised liposomes significantly reduced the lung tumour cells spread *in vivo*.[79]

Aptamer based targeting has also been utilised. Aptamers are small single stranded oligonucleotides; DNA or RNA sequence that folds in a specific way and are able to specifically bind to certain biomolecules and proteins. Docetaxel loaded PLGA-PEG NPs were functionalised with an aptamer that specifically binds to PSMA expressed on the surface of prostate epithelial cells (LNCaP). These aptamer conjugated NPs showed higher *in vitro* cytotoxicity compared to unmodified NPs.[80]

Transferrin; a protein carrier for iron which involves in the cellular uptake of iron through a selective binding to transferrin receptors (TfR) on the cell surface. TfR are usually overexpressed by cancer cells to fulfil the increased demand for iron by deprived rapidly proliferating cancer cells. Paclitaxel loaded PLGA NPs were conjugated with transferrin as a targeting ligand. Transferrin conjugated PLGA NPs showed enhanced antiproliferative effect against transferrin expressed breast cancer cell lines (MCF-7) compared to non-functionalised PLGA NPs due to the enhanced internalisation achieved by RME and the sustained action of paclitaxel inside the cells.[81]

Folate is a B_9 vitamin essential for DNA biosynthesis, which selectively binds to high affinity glycosylphosphatidyl-inositol-linked folate receptor (FR) that are overexpressed by many

cancer cell types. Daunorubicin loaded liposomes were conjugated with folate ligands in order to target FR upregulated on the surface of KB oral carcinoma cells, Chinese hamster ovary (CHO-FR-beta) and KG-1 human acute myelogenous leukaemia cells. The folate conjugated liposomes showed a promoted cellular uptake and cell toxicity compared to non-conjugated liposomes.[82]

1.4.2 Silica nanoparticles

Silica NPs provide preferable characteristics when compared to polymeric NPs due to the versatile chemistry of the silane groups and improved colloidal characteristics of silica NPs.[83-85] Silica NPs can be functionalised with numerous functional groups, such as amine, carboxylic acid, azide, alkyl in order to enable further attachment of different ligands, including biomolecules, to their surface.[86-88]

Silica NPs are classified into two major groups. Porous and non-porous silica NPs. Non-porous NPs are usually used as nanosensors as a specific fluorophore can be covalently conjugated within the silica matrix; for instance pH sensitive nanosensors were successfully designed and calibrated for intracellular measurements.[89]

Porous silica NPs are usually used for drug loading and subsequent delivery to the target site. However the pores could vary from as small as 1 nm to as large as 10 to 20 nm. Particles with small pores are only used for loading small drug molecules.[90-91] Whilst particles with large pores are utilised as carriers for large drug molecules such as protein and DNA for gene delivery.[92-93] Mesoporous silica NPs, which have pores diameters ranging from 2 to 50 nm, have been widely used for cytotoxic agents delivery in cancer treatment.[94]

1.5 Circulating tumour cells: Diagnosis, detection and treatment

1.5.1 Liquid biopsy `

Liquid biopsy (fluid phase biopsy) is the sampling of non-solid biological tissue, primarily blood in order to analyse certain biomarkers.[95] liquid biopsy is usually used for diagnosis and prognosis of the chronic diseases. The most common advantage of liquid biopsy over the conventional diagnostic procedures is that it is relatively less invasive, thus it is a convenient

method for diseases screening. Liquid biopsy could be also conducted more frequently relative to the conventional diagnostics. This technology also allows monitoring of the treatment and any disease relapse.[96]

Liquid biopsy has been used in different medical fields for diagnosis of the diseases. For instance, in cancer diagnosis (CTCs) and/or circulating tumor DNA (ctDNA) are collected from patients' blood samples.[97-99] When cancer cells die, they release their DNA content in the blood stream, the released DNA is called ctDNA. The ctDNA copies resemble the DNA fragment in the original tumour cells and thus they could be utilised in order to track the cancer and its progression. Polymerase chain reaction (PCR) method like digital PCR or next generation sequencing (NGS) could be used to analyse and amplify ctDNA to track the cancer progression. For instance, NGS based methods offer a general and comprehensive information about the genetic make-up of a cancer in contrast PCR based methods enable more targeted strategy for detecting a minimal residuals of the cancer and monitoring cancer treatment and disease prognosis.[100-104]

Liquid biopsy could be used to detect a small changes in tumour and its biomarkers several months or even years in advance when compared to the conventional imaging techniques. Thus, liquid biopsy could be a powerful technique for early detection and diagnosis of cancer, before it starts to spread to distant organs, monitoring of cancer progression and any treatment resistance mutations at early stages.[105-106]

Moreover, liquid biopsy could be used for heart attack diagnosis, where circulating endothelial cells (CECs) are usually sampled.[107-108] Other biomarkers could also be analysed in order to diagnose certain cardiovascular diseases by for instance isolating protoporphyrin IX from blood samples atherosclerosis could be diagnosed.[109]

In prenatal diagnosis, testing of cell-free fetal DNA in maternal plasma could be utilised for the screening of fetal abnormalities like Down syndrome and for early detection of trisomy 21 and trisomy 18.[110-111]

Furthermore, liquid biopsy could also involve biological fluids other than the blood. For instance, cerebrospinal fluid could be tested to analyse certain biomarkers in order to early detect and diagnose the occurrence of central nervous system diseases such as idiopathic normal pressure hydrocephalus and glioma.[112-113]

1.5.2 Approaches used for Inhibition of circulating tumour cells dissemination

Several attempts have been reported in order to inhibit the metastatic process by either tracking, capturing, subsequently killing circulating tumour cells in the systemic circulation or by blocking their adhesion to vascular endothelium.

For example, dendrimers were conjugated to certain antibodies that preferentially bind to specific proteins on the surface of circulating tumour cells. Dendrimers conjugated to $aSLe^x$, an antibody that binds to carbohydrate ligands overexpressed on the surface of the circulating tumour cells, or anti-EpCAM, an antibody that binds epithelial cell adhesion molecules similarly overexpressed on circulating tumour cells, were used to track and capture HT29 colon cancer cells. These dendrimers showed specific binding to HT29 suspensory cells, as confirmed by fluorescence microscopy. In addition, dendrimers conjugated with both antibodies reduced the adhesion of HT29 cells to HUVECs to a greater extent than dendrimers conjugated to a single antibody. This reflects the advantage of utilising dual antibody conjugates for the capture of circulating tumour cells to prevent their invasion.[114]

A combination of bismuth and iron oxide NPs was used for capturing and localising the tumour cells. The NPs were conjugated with folate ligands to capture Hela cells (human adenocarcinoma cells overexpressing folate receptors) suspended in phosphate buffer using a micro-magnet. The tracking capability of these NPs was confirmed by X-ray fluorescence (XRF) intensity, where Hela cells treated by folate conjugated bismuth NPs showed higher XRF intensity compared to treated MG-63 cells (human osteosarcoma cells that do not overexpress folate receptors) or Hela cells treated by folate unconjugated bismuth NPs.

Furthermore, the NPs had a cytotoxic effect on Hela cells after exposure to X-ray as confirmed by comet assay, which is a method used to measure DNA strand breaks through electrophoresis, where these DNA fragments are observed by fluorescence microscopy. The intensity of the comet tail indicates the extent of DNA damage. The higher percentage of the DNA in the tails occurred in Hela cells treated by combined NPs and X-ray irradiation relative to cells treated by X-ray or the NPs respectively. This cytotoxic effect was also confirmed by MTT assays, where higher percentages of Hela cells were killed after treatment by combined X-ray and NPs compared to those treated with X-rays alone.[115]

Biodegradable mPEG-PLA (methoxypoly (ethylene glycol)-poly (lactide)) NPs were loaded with apigenin or apigenin polyaminoesters (PAE) to inhibit the adhesion of human breast adenocarcinoma cells (MDA-MB-231 cells) to HUVECs. Both NPs reduced the adhesion of MDA-MB-231 cells labelled with Cell Tracker Orange to HUVECs stained with Calcein AM compared to blank NPs. Moreover NPs loaded with apigenin or apigenin polyaminoesters (PAE) showed a significant reduction of intercellular adhesion molecule 1 (ICAM-1) expression in HUVECs stimulated by tumour necrosis factor alpha (TNF-α), which is supposed to be elevated to facilitate tumour cell adhesion. In contrast, blank NPs failed to reduce ICAM-1 in stimulated HUVECs.[116]

Furthermore, cimetidine; a histamine H_2 receptor antagonist drug that inhibits stomach acid production has also shown to have an improved clinical outcomes in colorectal cancer patients. The mode of action of this drug in cancer treatment was elucidated by Kobayashi *et al*. It has been demonstrated that Cimetidine can block the adhesion interaction between colorectal cancer cell lines (HT-29) to the cultured endothelial cell monolayer (HUVECs). Cimitidne had also shown a significant reduction in E-selectin receptors expression on the surface of HUVECs stimulated by IL-1β as indicated by immunohistochemistry and flow cytometry. P-selectin supression by cimitide is thought to be responsible for the disruption of the adhesion interaction between circulating tumour cells and E-selectin receptors

upregulated on the cell surface of the vascular enodthelial cells. Additionally, nude mouse animal model injected with HT 29 cells was used in order to investigate the effect of cimetidine on liver metastasis *in vivo*. The results have shown that the percentage of mice that had developed liver metastatic foci (Foci that are larger than 0.1 mm in diameter) was less when mice treated with 200 mg/kg/day of cimetidine compared to untreated control groups.[117]

Nitric oxide (NO) role in metastasis inhibition was investigated by Lu *et al*. They found out that NO; a vasodilator can disrupt the adhesion between circulating tumour cells and the endothelial bed of the vasculatures through inhibition of cell adhesion molecules (CAMs) expression specifically vascular adhesion molecule 1 (VCAM-1). S-nitrosocaptopril (CAP-NO) which is a typical NO donor had reduced the cellular adhesion between metastatic cancer cells (HT-29) and vascular endothelial cells (HUVECs) in cell culture. IL-1β was used in order to activate HUVECs, consequently overexpress cells adhesion molecules (CAM). The underlying mechanism by which NO works was further investigated. NO was found to specifically downregulate VCAM-1 as confirmed by flowcytometry (immunohistochemistry) and western blot. Furthermore, haemoglobin; that is a scavenger for NO, could reverse the inhibitory effect of CAP-NO on cellular adhesion between HT29 cells and HUVECs and the expression of VCAM-1 on cell surface of IL-1β stimulated HUVECs. Thus, indicating the key role of blocking metastatic cells adhesion to vascular endothelium in cancer metastasis inhibition.[118]

Anti NF-κB reagents including Pentoxyphyllin, Aspirin and N-acetyl-L-Cysteine (NAC) were used in order to block the adhesion between metastatic cancer cells and vascular endothelium. Nuclear factor kappa B light chain (NF-κB) is a transcription factor that controls gene expression of certain cytokines and cell adhesion molecules mainly E-selectin, ICAM-1 and VCAM-1. Anti NF-κB reagents significantly inhibited the adhesion interaction between OG90 cancer cells (derived from small cell anaplastic carcinoma of the lung) and IL-1β

stimulated HUVECs. IL-1β was used in order to induce the translocation of NF-κB from the cytoplasm to the nucleus and increase the expression of the cell adhesion molecules (CAMs).[119]

1.5.3 Approaches used for detection of circulating tumour cells and early diagnosis of metastasis

A DNA encoded for the expression of carcinoembryonic antigen (CEA) was detected using a microfluidic based gold NPs sensing system. CEA is a glycoprotein that is normally present in a very low level in the blood, however during the metastasis, circulating tumour cells overexpress CEA that could serve as a ligand for L and E selectin thus helping the dissemination of cancer cells. The detection system was made of microbeads embedded in a microfluidic chip, where the beads surfaces were functionalised with an electron rich protein and a capture probe (complementary DNA sequence for the target DNA strand). Multi-functional gold NPs were also synthesised and functionalised with a Horse Reddish Peroxidase (HRP) enzyme and a different DNA sequence that matches the target DNA of the CEA antigen and. When the target DNA from the circulating tumour cells (HT29) was added to the detection system, both capture probe on the surface of the beads and the probe attached to the surface of gold NPs bound to the target DNA making a sandwich. In turn, in the presence of hydrogen peroxide, HRP on the surface of the gold NPs had converted the added Tyramine-Biotin to short lived radicals. The produced radicals of Tyramine-Biotin reacted with the tyrosine residues of the electron rich protein attached to the surface of the beads making a covalent bonds with the electron rich proteins, thus exposing multiple biotin moieties on the surface of the beads. The added fluorescent streptavidin quantum dots could react with the exposed biotin moieties and the fluorescence signal was detected indicating the presence of the target DNA. The study had claimed a detection limit of 1 tumour cell expressing a CEA antigen per 1 ml of the blood sample.[120]

A sandwich hybridization assay was also used in order to detect PCA3 RNA; which is a nucleotide sequence overexpressed in prostate cancer cells. The detection system comprises

anti-sense RNA conjugated gold NPs and metallic or silica coated nanowires embedded in a chip that are functionalised with a capture anti-sense RNA. In this device, the target PCA3 RNA of the circulating tumour cells binds to the capture anti-sense RNA attached to the nanowires. When gold NPs are added to the sample in the device, the anti-sense on the particles surface binds to the PCA3 RNA thus sandwiching the target RNA between gold NPs and the nanowires. The binding of gold NPs to the surface of nanowires induced a shift in the resonance frequency of the nanowires, which was measured by laser interferometry. The frequency shift was directly proportional to the mass of the bound antisense conjugated gold NPs, consequently the amount of the target RNA was measured, thus providing a quantitative measurement of the circulating tumour cells burden.[121]

1.6 Aim of the thesis

The aim of this work was to synthesise silica NPs with heparin as a targeting ligand in order to block P-selectin receptors on the surface of vascular endothelial cells simultaneously exploiting the advantage of long circulating NPs compared with using heparin polymer as such. The proposed P-selectin dependent adhesion of heparin conjugated NPs to the endothelial cells was hypothesised to disrupt the P-selectin mediated interaction between circulating tumour cells and vascular endothelium that subsequently leads to circulating tumour cells extravasation and invasion to distant organs. The use of systemic circulation dynamics to study the nanoparticle adhesion to cell surface receptors is an interesting approach to mimic the *in vivo* particles distribution/circulation which could accelerate the clinical translation of the nanomedicines. However only few detailed studies have been conducted using this approach and none to date has considered the use of heparin conjugated NPs for binding to P-selectin receptors expressed on vascular endothelial cells under dynamic conditions. Accordingly a thorough study of heparin conjugated particles adhesion to HUVECs as a model for vascular endothelium, using circulatory system dynamics simulator, was conducted as illustrated in chapter 2.

Furthermore, this research was intended to make chemical modifications to the heparin structure in order to produce heparin derivatives which were hypothesised to reduce the adverse effects of heparin and improve its inhibitory activity against heparanase that is implicated in the spreading of cancer cells. Subsequently attaching the modified heparin derivatives to silica NPs surfaces exploiting the EPR effect in order to enhance their accumulation in the tumour extracellular fluid to be further utilised for heparanase inhibition in the future as demonstrated in chapter 3.

Moreover, this research aimed to detect one of the key metastatic biomarkers; heparanase enzymes that are upregulated during the early stages of cancer metastasis, thus enabling an early diagnosis of cancer. Therefore, different types of heparinase responsive sensors were developed based on Förster (fluorescence) resonance energy transfer (FRET) phenomenon. In light of that, it was hypothesised that when heparinase cleaves heparin chains into smaller fragments and/or monomers, the fluorescently quenched fluorophore in the FRET pair attached to heparin is expected to restore its fluorescence upon FRET pair separation and a fluorescence signal recovery could be monitored as an indicator for heparinase action. Thus, the main intention for developing these sensors is to use them for a turn-off to turn-on system that is able to detect the presence of bacterial heparinase and supposedly the mammalian form; heparanase as discussed in chapter 4.

In summation, heparin and heparin derivatives were appended to the surfaces of silica NPs in order to be harnessed for targeting extracellular biomarkers e.g. P-selectin and heparanase implicated in cancer metastasis. This work has also encompassed development of FRET based constructs for testing their ability to detect heparinase a bacterial form of mammalian heparanase that is involved in cancer metastasis.

2 Chapter two: Synthesis of heparin conjugated nanoparticles to target cell surface P-selectin of endothelial cells to Inhibit metastasis

2.1 Introduction

2.1.1 P-selectin, heparin and metastasis

2.1.1.1 P-selectin role in metastasis

P-selectin is a cell adhesion molecule produced by platelets and endothelial cells, it is either membrane or soluble protein. The membrane form of P-selectin is a single polypeptide composed of 789 amino acid residues. P-selectin is structured into a amine terminal domain of ~120 residues similar to that of calcium dependent animal lectin, the rest of the protein consists of an FGF-like domain, complement regulatory protein-like residues, a transmembrane domain, and a cytoplasmic domain at the carboxyl-terminus.[122-124] P-selectin is usually stored in the α-granules of platelets, it is also found in Weibel-Palade bodies of endothelial cells. During inflammation, P-selectin is translocated to the surface of activated platelets and stimulated endothelial cells. Consequently, leukocytes expressing PSGL1 a ligand for P-selectin bind to endothelial cells and platelets, thus facilitating the recruitment of the leukocytes to the site of the inflammation.[125-128]

Metastasis is a complex process that involves several steps; including epithelial-mesenchymal transition, extracellular matrix degradation by heparanases to facilitate the entry of the metastatic cells into the circulatory system, the rolling adhesion of the circulating tumour cells over the vascular endothelium and the subsequent vascular extravasation of the tumour cells and invasion to distant organs.[129-130]

Circulating tumour cells should accumulate at certain region of the blood vessels where the vasculatures are narrow enough to hinder the circulation of the tumour cells. This process is called tumour cells arrest which is required for tumour cell extravasation through blood vasculature and subsequent invasion to distant organs. P-selectin plays a crucial role in cancer metastasis and tumour cells spreading and dissemination through mediating circulating tumour cells arrest in blood vessels. P-selectin acts as a cell adhesion molecule that facilitates the rolling adhesion of circulating tumour cells in systemic circulation. Metastatic tumour cells in systemic circulation express sialylated surface protein; sialyl Lewis^X

(sLe^x) which binds to the upregulated P-selectin receptors on the surface of endothelial cells lining the blood vasculature. Subsequently, metastatic cells extravasate and transmigrate across vascular endothelium to distant organs in order to create secondary tumours.[131-135]

Metastatic cancer cells arrest that occurs in large blood vessels is primarily brought by the adhesive interaction between metastatic cells glycoprotein ligand and P-selectin membrane receptors of the endothelial cells lining the blood vessels.[136]

The key role of P-selectin in mediating the process of metastasis has been described including P-selectin knock down attenuated metastasis *in vivo.* Young et al intravenously injected LS180 colon carcinoma cells that express sLe^x into P-selectin deficient and P-selectin expressing mice. Few numbers of P-selectin deficient mice developed lung metastasis compared with P-selectin positive mice. Thus reinforcing the critical role of P-selectin adhesion molecule in tumour cell invasion and metasatasis.[137]

Moreover, P-selectin is also involved in circulating tumour cells interaction with platelets. Platelets express P-selectin during the process of metastasis and bind to glycoprotein ligands expressed on the surface of metastatic tumour cells. Consequently platelets form microemboli that surround circulating tumour cells.[138] The formed complex of the platelets and circulating tumour cells assists the spread of tumour cells though various mechanisms. These include facilitating the arrest of circulating tumour cells in blood vessels by increasing the sizes of the formed microemboli and decreasing the shear stress brought by blood flow.[139] Thus enhancing the interaction between the circulating tumour cells and vascular endothelium, subsequently tumour cell extravasation and spreading. Furthermore, the formed microemboli help the tumour cells escape the immune system, thus acting as a protective shell.[50, 140]

2.1.1.2 Inhibition of metastasis by heparin through blocking of cell adhesion receptors

Heparin attenuates metastasis and circulating tumour cells dissemination by blocking P-selectin receptors where it acts as a competitive inhibitor to the endogenous heparan

sulphate. Thus disrupting the binding of metastatic cancer cells to P-selectin receptors overexpressed on vascular endothelium.[141] For example, It has been reported that porcine intestinal mucosa derived heparin had the ability to bind to P-selectin receptors in similar way to that of endogenous HS.[142]

It has also been reported that unfractionated heparin had the highest inhibitory effect against both P-selectin and L-selectin binding to human colon carcinoma cells relative to that of low molecular weight heparins or fondaparinux, which is a synthetic oligosaccharides made of pentasaccharide sequence that specifically binds to antithrombin and induces its activation, hence fondaparinux has potent anticoagulant effect. *In vivo* experiments were conducted using mice injected with green fluorescent protein (GFP) labelled colon carcinoma. Mice were then subcutaneously injected with different doses of heparins. At low dose, unfractionated heparin showed the best inhibitory effect against metastasis as confirmed by the fluorescence of lung cancer homogenate. While at high dose, both unfractionated heparin and low molecular weight heparin (Tinzaparin) were able to mitigate metastasis in mice by significantly inhibiting the spread of B16F10 melanoma cells after they were injected in mice as indicated by lung weight measurement, compared to Fondaparinux which had no effect. Indicating that there is no role of antithrombin binding domain in mediating heparin antimetastatic activity .[143]

Furthermore, heparin was able to diminish lung metastasis in wild-type mice treated with metastatic colon adenocarcinoma (MC-38) cells labelled with GFP, as indicated by GFP fluorescence measurements of mice lungs. The inhibitory effect of heparin was similar to the effect of P-selectin deficiency in mice. Administration of heparin to P-selectin deficient mice did not enhance antimetastatic effect brought by the absence of P-selectin. This reflects that heparin has antimetastatic activity through the disruption of P-selectin mediated metastatic cell invasion.[144] Heparin reduces the metastasis not only by disrupting the rolling adhesion of metastatic cancer cells but also by other antimetastatic mechanisms including the reduction

of the microemboli formation around the circulating tumour cells and heparanase inhibitory activity.[145]

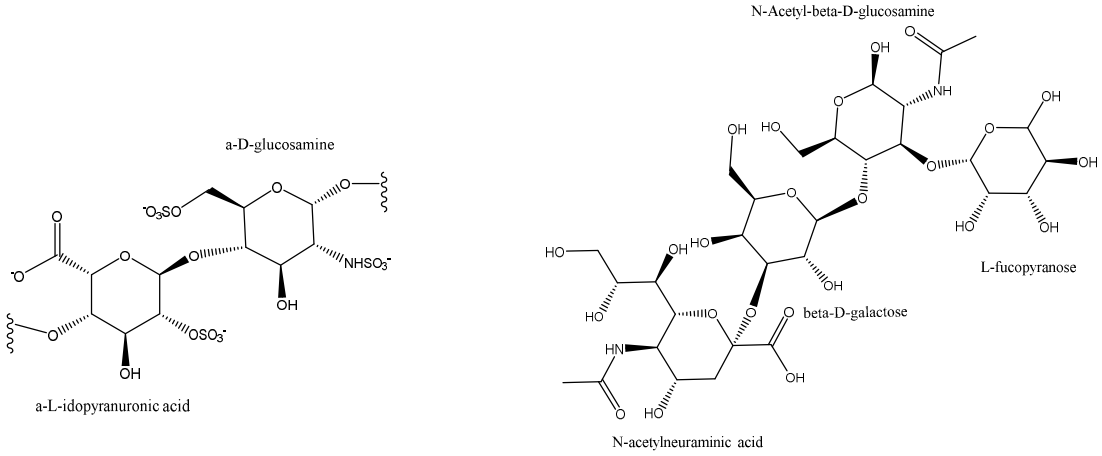
2.1.2 Flow conditions use in systemic circulation simulators

The binding of NPs to cell surface under flow conditions has not been extensively explored, however it is of significance to monitor NPs binding under flow conditions that mimic the *in vivo* dynamics in contrast to static conditions.[146] The mechanical properties and fluid dynamics of the blood vessels have been established using experiments considering flow conditions and physiological geometries in order to simulate the systemic circulation in human arteries and veins.[147] Binding of NPs used as targeted drug carriers to vascular endothelium is complex process as it is modulated by several factors including hydrodynamic force, shear stress and bond formation dynamics.[148]

Different systemic circulation simulators were developed in order to study nano- and micro-particles adhesion to cell surface. Antony *et al* used microfluidic channels for studying particles adhesion to endothelial cell surface in order to mimic the microcirculation. They functionalised the particles surface with specific antibodies In order to bind to cell adhesion molecules; ICAM-1 on the surface of endothelial cells.[149] *In vitro* model of microfluidic device was developed in order to mimic the physiological flow conditions. The adhesion of wheat germ agglutinin (WGA) functionalised microparticles to epithelial cells was studied compared to the adhesion of microparticles conjugated with BSA as non-specific protein. A paramount finding in this study was that the non-specific binding of BSA conjugated particles to cell surface was minimal compared with WGA conjugated particles under flow conditions.[150] Flow chambers were also utilised in order to simulate the systemic circulation. Where, PLGA NPs were conjugated with glycocalicin which is a glycoprotein expressed on the outer surface of intact platelets that binds to P-selectin receptors upregulated on the surface of stimulated endothelial cells.[151] The adhesion of PLGA microspheres coated with Sialyl-Lewis x (SLe^x) to flow chambers coated with selectin proteins was also investigated under flow conditions.[152]

2.2 Aim

Heparin has structural similarities to Sialyl Lewis x (sLe^x) implicated in the metastasis process. Figure 2.1 shows the structural similarities between heparin and sLe^x. However, heparin polymer is renally excreted within two hours which limits its use in cancer metastasis.



Heparin disaccharide **Sialyl Lewis X (sLe^x)**

Figure 2.1 The structure of the most commonly occurring disaccharide repeating unit in heparin chain (left) and Sialyl Lewis x (sLe^x) (right).The structural similarities between the two ligands include the presence of amino sugar residue; D-glucosamine and the presence of L-idopyranuronic acid in heparin chain that resembles N-acetylneuraminic acid in sLe^x.

In light of that, the aim of this study was to synthesise heparin conjugated NPs which are expected to have prolonged systemic circulation.[153] Whilst reducing the anticoagulant activity of heparin upon the conjugation process to NPs surfaces in order to decrease the haemorrhagic side effects associated with native heparin. Moreover, the aim also encompasses synthesis of two structurally related polymers as controls; namely chondroitin sulphate polymer as it resembles heparin and belongs to the same family of glycosaminoglycans (GAGs) and sodium alginate polymer as it has similar backbone and negative charge to GAGs polymers though it lacks the sulphate groups. Ultimately, heparin conjugated NPs were engineered in order to target and block P-selectin upregulated on surface of HUVECs. Thus, quelling the metastatic cells adhesion to vascular endothelium and cancer cells dissemination as illustrated in Figure 2.2.

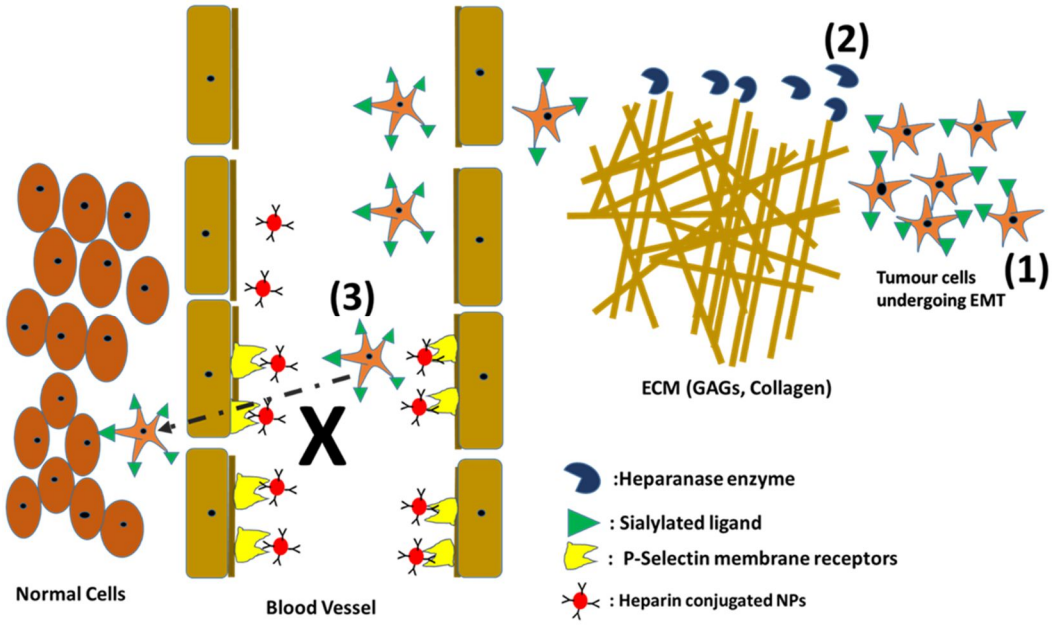


Figure 2.2 Illustrative diagram shows stages of metastatic process and the aim of this study in utilising heparin conjugated NPs to disrupt metastasis at stage number (3). Metastasis starts at EMT (epithelial mesenchymal transition) stage where cells start to change morphology and become more metastatic. Heparanase degrades ECM (extracellular matrix) to create a path for metastatic cells to enter systemic circulation, then they bind to certain receptors (P-selectin) upregulated on endothelial cells, which enhance the rolling adhesion of metastatic cells to extravasate and invade distance organs.

2.3 Experimental

2.3.1 Materials

Ammonium hydroxide (NH_4OH) (28-30%), Tetraethylorthosilicate (TEOS) (≥ 99%), (3-Aminopropyl)triethoxysilane (APTES), N-(3-Dimethylaminopropyl)-N'-ethylcarbodiimide hydrochloride (EDC), Azure A (certified by the Biological Stain Commission (dye content 70 %)), Heparin from porcine intestine (≥ 180 USP units/mg ,average MW =17 kDa), Alginic acid sodium salt from brown algae-low viscosity (Viscosity= 8-12 cP, average MW = 55 kDa), Chondroitin sulphate sodium salt from shark cartilage (average MW = 73 kDa), Ethylenediaminetetraacetic acid (EDTA), 1,9-Dimethyl Methylene Blue zinc chloride double salt (DMMB), Tris(hydroxymethyl)aminomethan (Trizma base) and Trypsin-EDTA solution were purchased from Sigma Aldrich. Ethanol absolute was purchased from Fisher chemical, 2-(N-morpholino)ethane sulfonic acid (MES) was purchased from PanReac, 5-(and-6)-Carboxytetramethylrhodamine Succinimidyl Ester (5(6)-TAMRA, SE), Alexa Fluor 633 NHS

Ester (Succinimidyl Ester), 5-(and-6)-Carboxyfluorescein Succinimidyl Ester mixed isomers (5(6)-FAM-SE) were purchased from Thermo Fisher Scientific, sodium hydroxide was purchased from VWR International Ltd. Anti-Xa heparin kit was purchased from Iduron. HUVECs, Endothelial Cell Basal Medium MV2 and Endothelial Cell Growth Medium MV2 supplement packs were obtained from PromoCell, Hoechst 33342 was purchased from Thermo Scientific, micro-Slide I Luer channel slides (µ-Slide I Luer o.88 mm), flow control pump and perfusion set were purchased form ibidi Cells in Focus , paraformaldehyde (PFA) was purchased from Electron Microscopy Sciences, CD62P (P-Selectin) Monoclonal Antibody (AK-4) and P-Selectin Monoclonal Antibody (AK-6)-FITC were purchased from ThermoFisher Scientific. Leica SPE11confocal microscope, Astrios Cell Sorter flow cytometer, Cary eclipse fluorescence spectrometer, Cary 50 bio UV-visible spectrophotometer, FEI Tecnai BioTwin-12 TEM (Transmission Electron microscope), Malvern Zetasizer Nano ZS, Buchi Rotavap R-200, Hermle Z300 Centrifuge, SP 260PZ syringe pump, GVD3 freeze dryer and Spark microplate reader (TECAN) were used.

2.3.2 Methods

2.3.2.1 Synthesis of labelled amine functionalised nanoparticles

TAMRA-SE (1 mg, 1.9 µmol), FAM-SE (1 mg, 2.1 µmol) and Alexa633-SE (1 mg, 0.87 µmol) were individually dissolved in 1 mL of pure ethanol, then the mixture was sonicated for 15 minutes. After that, APTES (18 µL, 76.9 µmol) was added to the mixture, left on an oscillator for 24 hours to allow the reaction to proceed and covered with aluminium foil to protect the dye to produce APTES-TAMRA, APTES-FAM and APTES-Alexa 633 conjugates respectively. 300 µL of each prepared conjugate was then added to a conical flask containing 50 mL ethanol and 3 mL NH_4OH and left to stir for 3 hours. After that 4 mL of TEOS was added dropwise using a syringe pump at a rate of 0.5 ml/min and left to stir for 3 hours. After synthesis the suspension was centrifuged at 7500 g for 20 minutes and washed with 40 mL ethanol in triplicate. Finally, the suspension was rotary evaporated to produce fluorescent silica NPs labelled with TAMRA, FAM and Alexa 633 respectively. 60 mg of these fluorescent

NPs were suspended in 10 mL ethanol, left under sonication then moved to a magnetic stirrer at 1500 rpm. 1 mL of NH_4OH was added to the suspended NPs and left to stir for 15 minutes. After that -0.5 mL of APTES was added to the above mixture and left for 24 hours to allow the polycondensation of the APTES on the surface of the silica nanoparticles. Finally, the suspension was centrifuged at 7500 g for 20 minutes, washed with 40 ml ethanol in triplicate and rotary evaporated to synthesise amine functionalised silica NPs labelled with TAMRA, FAM and Alexa 633 respectively.

2.3.2.2 Synthesis of heparin, chondroitin and alginate conjugated nanoparticles

Heparin (25 mg, 1.47 µmol) was dissolved in 2.5 mL MES (pH 5.6). Sodium alginate (27.5 mg, 0.5 µmol) was dissolved in 1 mL MES buffer (pH 5.6). Chondroitin sulphate (36.5 mg, 0.5 µmol) was also dissolved in 1 mL MES buffer (pH 5.6). Then, EDC (2.5 mg, 13 µmol) was added to heparin solution and left to stir for 2 hours. EDC (1 mg, 5.2 µmol) was added to either alginate solution or chondroitin sulphate solution and left to stir for 2 hours. After that, amine functionalised NPs (20 mg) produced as described in section 2.3.2.1 were added to each solution and left to stir for 12 hours. Finally the resultant suspensions were centrifuged at 3000 g for 20 minutes and washed four times with 20 mL water. The obtained NPs were freeze dried for 24 hours.

2.3.2.3 Synthesis of heparin conjugated microparticles

Micron-sized silica particles were synthesised using Stober process and seed growth. 5 mL of ammonium hydroxide (28-30%) was added to 16.75 mL ethanol and left to stir for 15 minutes. Then 60 µL of APTES-TAMRA conjugate prepared as described in section 2.3.2.1 was added to the above solution and left under stirring for 3 hours to allow hydrolysis of alkoxy groups. After that, 0.5 mL of TEOS (99%) was added using syringe pump at rate 0.5 mL/min and left under stirring for 24 hours, followed by of another 0.5 mL of TEOS for 24 hours. Finally the resultant suspensions were centrifuged at 7500 g for 20 minutes and washed four times with 20 mL ethanol. The obtained micron sized particles were rotary evaporated for drying.

2.3.2.4 Nanoparticles characterisation

Particle size and zeta potential measurements of silica NPs were recorded using a Malvern Zetasizer Nano ZS (Dynamic light scattering technique). Particle size measurements were carried out using back scatter mode at 173° angle with 633 nm laser. The equilibration time for each sample was 120 seconds before the acquisition of the next sample. The count rate was set between 100-500 kcps by automatically adjusting the laser power using an attenuator. The temperature was set at 25 °C and the viscosity of the dispersant was 1.2 cP with 1.362 refractive index. All samples were prepared in 1/10 phosphate buffer saline (15 mM PBS) for size and zetapotential measurements. Data were recorded for each sample and repeated for three times of 15 runs (size) and 12 runs (zeta) for each reading. Data analysis was carried out using Malvern Zetasizer Software.

To measure the size, 5 mg of amine functionalised, heparin, chondroitin sulphate and alginate conjugated silica NPs were suspended in 1 mL ethanol or 15 mM PBS then diluted to produce a concentration of 0.05 mg/mL. For zeta potential measurements, 5 mg of the prepared silica NPs were suspended in 5 mL deionised water 1 mg/mL

Fluorescence microscope was used to measure the size of heparin conjugated microparticles. 10 µL of heparin conjugated microparticles (0.1 mg/mL) was placed on a glass slide and left to dry for 1 hour. The slide was taken to the fluorescence microscope, then bright field and fluorescence images of the particles were acquired. The resultant images were further analysed using ImageJ (Fiji) and Prism (GraphPad) in order to calculate the size and the frequency distribution of the particles.

FEI Tecnai BioTwin-12 TEM was used for NPs imaging, where 0.1 mg/mL of each type of the NPs was prepared. 15 µl of the resultant suspension was dropped on to copper grids and left for 10 minutes to allow the NPs to settle. Finally, the solvent was removed by filter paper and the sample was loaded into TEM for imaging.

For fluorescence measurements, 1 mL of heparin conjugated NPs labelled with TAMRA, chondroitin conjugated NPs labelled with FAM and alginate conjugated NPs labelled with

Alexa 633 (5 mg/mL) were placed in cuvettes and the fluorescence emission spectra were recorded using Cary eclipse fluorimeter. Chondroitin sulphate, heparin and alginate conjugated NPs were excited at 490 nm, 540 nm and 630 nm respectively with an excitation slit width of 2.5 nm and emission slit width of 2.5 nm.

2.3.2.5 Thermogravimetric analysis (TGA)

Heparin (5 mg), heparin conjugated silica NPs (2 mg), blank silica NPs (6 mg) and amine functionalised silica NPs (6 mg) were accurately weighed and placed in the pans of the thermogravimetric (TGA-Q500). The temperature range was set from 0 to 600 °C and the heating rate was 10 °C/min under inert conditions (argon gas).

2.3.2.6 Azure A and DMMB assays

Equal volumes of (0.025mg/mL, 85.6 nmol/mL) azure A stock solution and 20 µg/mL of heparin polymer, 1 mg/mL of heparin conjugated NPs or 1 mg/mL of amine functionalised NPs were mixed. The absorption wavelength of the resultant mixture was determined using a UV-Visible spectrophotometer or plate reader. For the DMMB assay, 200 µL of 0.1 mg/mL stock solution of either chondroitin sulphate or sodium alginate were added to a 24 well microplate containing 1 mL of DMMB stock solution0.016 (mg/mL, 38.5 nmol/mL) with pH 1.5 and 800 µL water. Whereas 1 mL of 1 mg/mL of either chondroitin sulphate NPs or alginate NPs was added to 1 mL of 0.016 mg/mL DMMB stock solution with pH 1.5. 200 µL of either chondroitin sulphate or sodium alginate solution (0.1 mg/mL) was added to the 24 well microplate containing 1 ml of DMMB stock solution (0.016 mg/mL) with pH 7.2 and 800 µL water. Whereas 1 mL of 1 mg/ml of either chondroitin sulphate NPs or alginate NPs was added to 1 mL of DMMB stock solution (0.016 mg/mL) with pH 7.2. Finally UV visible scan was done for the all resultant mixtures using plate reader (TECAN).

2.3.2.7 Anticoagulant assay (Anti Xa assay)

Anticoagulant activity of the NPs was determined by anti Xa assay. Heparin binds to antithrombin-factor Xa complex, consequently it inhibits factor Xa. The inhibited factor Xa is not able to break down the chromogenic substrate and release the chromophore (pNA).

Aliquots (200 µL) of different concentrations of heparin polymer (62.5, 125, 250 and 500 ng/mL) and different concentrations of heparin , alginate and chondroitin sulphate conjugated NPs (25, 60, 75 and 100 µg/mL) were prepared in Tris-EDTA buffer with pH 8.4, placed in a 48 well plate and incubated for 2 minutes at 37 °C. Then 200 µL of the antithrombin solution was added and mixed for 2 minutes at 37 °C. Then 200 µL of the Factor Xa solution was added and mixed for 2 minutes at 37°C. 200 µL of the chromogenic substrate (Xa substrate) solution was then added and mixed for 2 minutes at 37 °C. Finally 200 µL of 20% (v/v) acetic acid was added to stop the reaction, mixed and the plate was set aside at room temperature. The absorbance of the samples was measured at 405 nm directly using plate reader.

2.3.2.8 Cell culture and maintenance

HUVECs from PromoCell were grown and maintained in Endothelial Cell Growth Medium MV2 that was exchanged every 48 hours. In order to split the cells, 1 mL of trypsin was added to HUVECs grown in a T75–flask for 4 minutes then 5 mL of the media was added to inactivate trypsin. The resultant cell suspension was centrifuged at 1200g for 5 minutes. The pellet was resuspended in 2 mL media and 0.5 mL of the suspended cells was added to 10 mL MV2 media in T75-flask to allow cells to grow at 5% CO_2 and 37 °C. Cells were used in passages between 2 and 6.

2.3.2.9 Immunofluorescence assay of P-selectin expression

100,000 of HUVEC cells were seeded in a 24 well plate for 24 hours. The cells were either treated by 1 mL of 0.1 mM of histamine containing MV2 media or left untreated for 10 minutes at 5% CO_2 and 37 °C. Cells were then washed three times with PBS to remove the media and the treatment. Then the cells were fixed by adding 1 mL of 4% PFA to each well for 20 minutes at room temperature. Then the cells were washed with PBS for three times and blocked by adding 1 mL of 1 % normal goat serum in PBS to each well for 1 hour. Then 10 µl FITC–labelled anti CD62P antibodies was diluted in 100 µl of 10 % normal goat serum and added to histamine stimulated and unstimulated HUVECs for 1 hour at room

temperature. After that, the cells were washed with PBS for three times to remove the excess antibodies. Finally, the cells were imaged using a fluorescence microscope.

2.3.2.10 Basal P-selectin expression by flow cytometry

100,000 cells were seeded in 24 well plate for 24 hours. Then cells were washed with PBS and 1 mL of PBS containing 1% normal goat serum was added to the cells for 1 hour. Cells were harvested using 200 µL trypsin for 4 minutes followed by 1 mL of MV2. The cells were centrifuged at 1200 g and resuspended in 10% normal goat serum PBS containing 10 µg/mL FITC–labelled anti CD62P antibodies in falcon tubes for 1 hour at room temperature. The cells were washed with PBS for three times to remove excess antibodies, centrifuged then resuspended in 0.5 mL PBS and taken for flow cytometry for measurement.

2.3.2.11 Competitive assay of heparin conjugated NPs P-selectin dependent adhesion under static conditions

100,000 HUVEC cells were grown in a 24 well plate for 24 hours. Then the cells were stimulated with 1 mL of MV2 media containing 0.1 mM histamine for 10 minutes. Subsequently, 1 mL of MV2 media containing 1 mg/mL of free heparin was added to histamine stimulated and unstimulated cells saturate the receptors. Then 1 mL of heparin conjugated NPs (50 µg/mL) was added to histamine stimulated and unstimulated cells and incubated for 30 minutes in 5% CO_2 and 37 °C incubator and covered with aluminium foil. After that, the cells were washed with PBS three times to remove the unbound NPs and reduce trypsin inactivation by the media. 200 µL of trypsin was then added to each well to cover the cells and left in the incubator for 4 minutes. Trypsin was quenched by adding 0.5 mL of the media to each well. Finally, the cells were placed in a 15 mL falcon tubes without fixation for direct flow cytometry measurements.

2.3.2.12 Flow assays

250,000 HUVEC cells were seeded in µ-Slide I Luer and allowed to settle and grow for 72 hours before use. The cells were covered with 250 µl of 1 in 10,000 diluted Hoechst 33342 dye and incubated for 15 minutes and covered with aluminium foil at 5% CO_2 and 37 °C. Then the cells were washed once with pre warmed PBS to remove excess Hoechst. The cells were

fixed with 4% PFA for 20 minutes at room temperature. Finally, the cells were washed by PBS once and covered with PBS and imaged using a fluorescence microscope.

For studying NPs or heparin microparticles adhesion to HUVECs under flow, 250,000 HUVEC cells were seeded in µ-Slide I Luer and allowed to grow for 72 hours. Then the micro channel slide was transferred to a fluorescence microscope stage and connected to the perfusion set of the ibidi pump system. A 50 cm long with 0.8 mm internal diameter perfusion set and 0.8 mm micro-channel slide were used. In order to achieve 1.16 dyn/cm^2, the flow rate of the pump was adjusted at 3.33 mL/min using 27 mbar pressure. 10 mL of CO_2 independent media containing mixture of 10 µg/mL of heparin, chondroitin and alginate conjugated NPs was allowed to flow through the micro channel slide using ibidi pump system at the desired flow rate and shear stress. After that, three different images were acquired from three different random regions of the slide using a fluorescence microscope. Same procedure was conducted in order to study the difference in heparin conjugated microparticles and NPs adhesion to HUVEC surface separately.

For competitive assay under flow conditions, 300 µl of CO_2 independent media containing 10% normal goat serum and 50 µg/mL of unlabelled anti P-selectin antibodies was used to cover 250,000 HUVEC cells grown in µ-Slide I Luer and left for 1 hour at room temperature under static conditions. Then 10 mL of CO_2 independent media containing mixture of 10 µg/mL of heparin, chondroitin and alginate conjugated NPs was allowed to flow through the micro channel slide using ibidi pump system at the same flow rate and shear stress previously used. Images were acquired from three different random regions of the slide using a fluorescence microscope.

2.4 Results and discussion

2.4.1 Synthesis of heparin, chondroitin and alginate conjugated silica NPs

Silica NPs were prepared by the Stöber process as previously described,[154] TEOS was hydrolysed under alcoholic solution (ethanol) by ammonium hydroxide (NH_4OH) to form silanol groups which then condensed to form siloxane bonds that constitutes the matrix of

the produced bare silica NPs (NPs). Figure 2.3 shows the hydrolysis and polycondensation mechanisms of the silica particles formation.

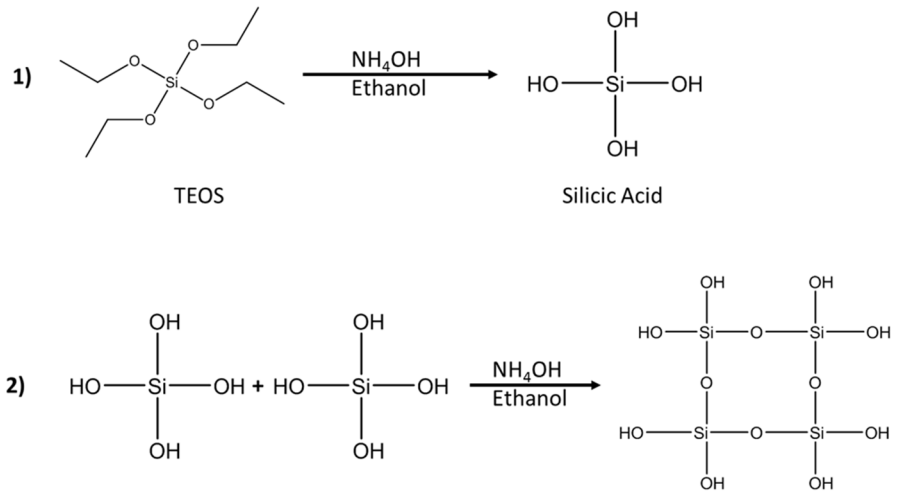


Figure 2.3 Schematics showing the synthesis of bare silica NPs. Steps of silica NPs formation, 1) Hydrolysis of TEOS in presence of NH_4OH to form silanol groups. 2) Condensation of silanol groups to form siloxane bonds (Si-O-Si).

Moreover; silica NPs were labelled with different fluorophores before appending heparin, alginate and chondroitin sulphate in order to facilitate NPs tracking in one experiment to reduce the experimental variations. Figure 2.4 shows the chemical conjugation of different fluorophores into silica matrix of the NPs.

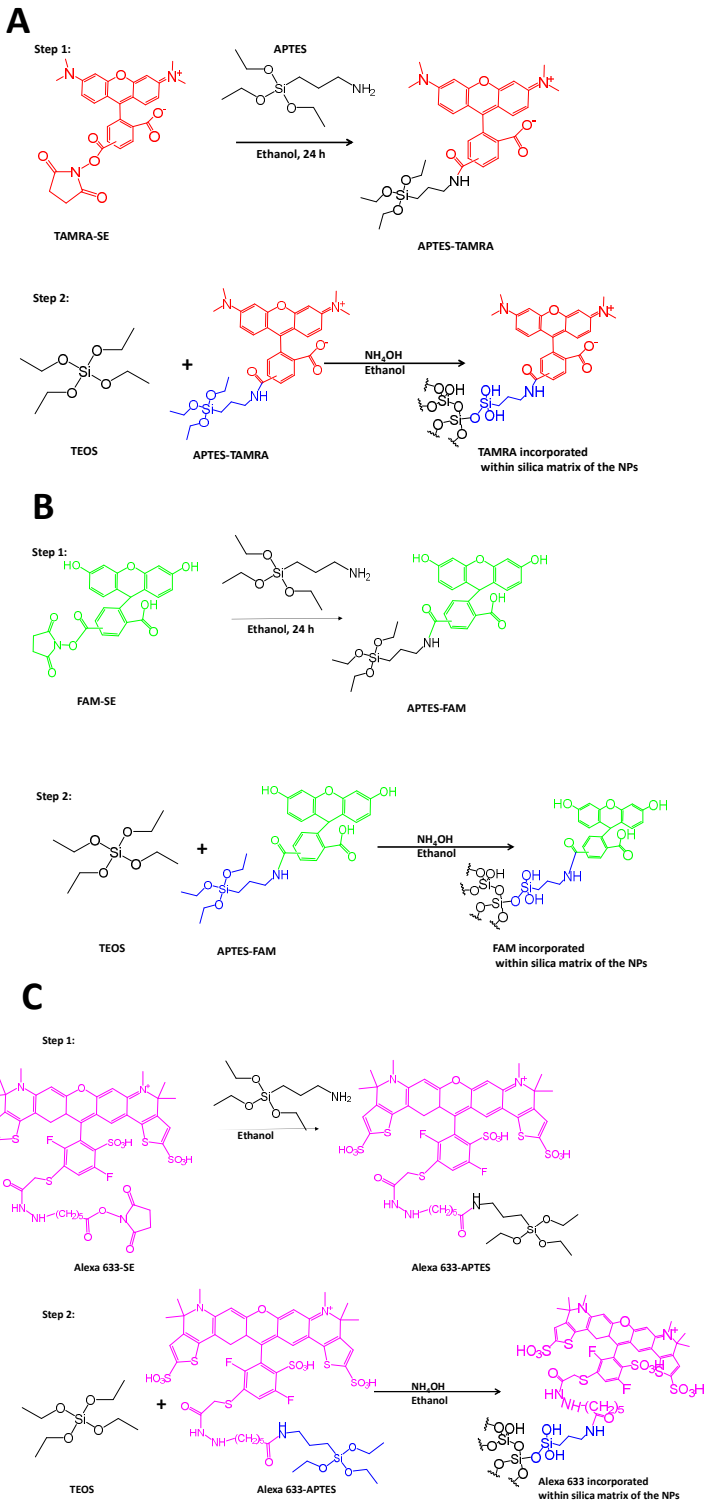


Figure 2.4 The mechanism of fluorophore incorporation within the matrix of silica NPs which comprises two steps; the first step involves the covalent conjugation of the fluorophore to APTES linker and the second step encompasses the incorporation of the APTES-fluorophore conjugate within the silica matrix of the NPs during the polycondensation reaction between APTES and TEOS during the formation of silica NPs. ***A:*** *Synthesis of TAMRA labelled silica NPs.* ***B:*** *Synthesis of FAM labelled silica NPs.* ***C:*** *Synthesis of Alexa 633 labelled silica NPs.*

The surface of bare silica NPs was further functionalised with amine groups using a solution phase silanisation process, where ethoxy groups of the organosilane (APTES) were hydrolysed in the presence of aqueous ammonia to produce free hydroxyl groups that subsequently condensed with the exposed hydroxyl groups on the surface of bare silica NPs, thus producing amine functionalised silica NPs as shown in Figure 2.5.

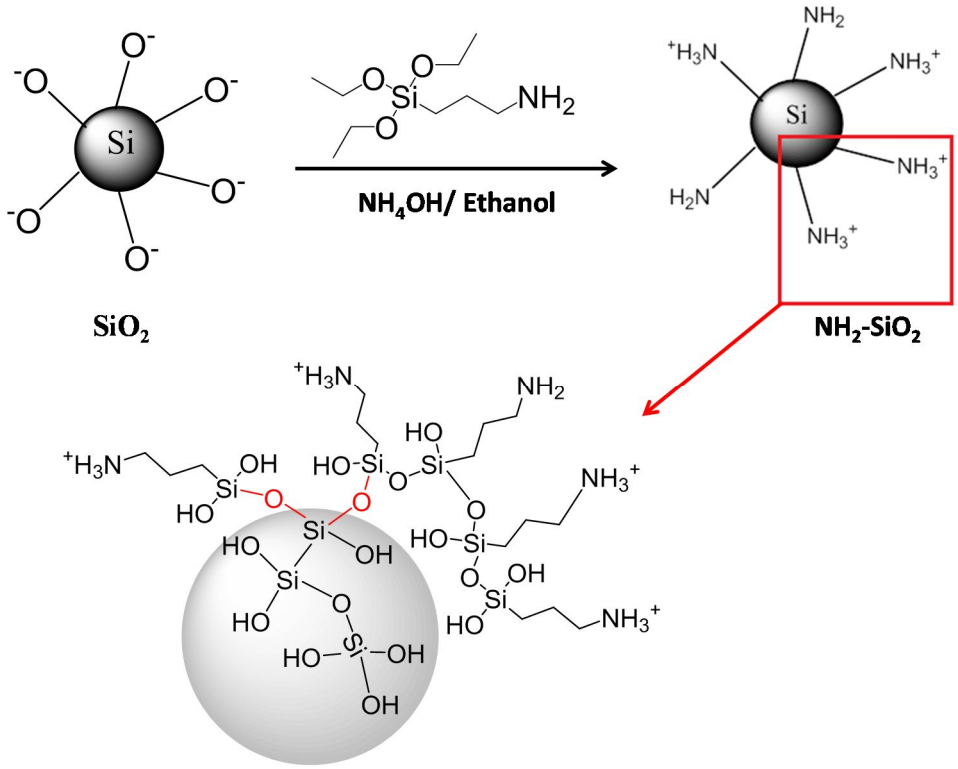


Figure 2.5 Schematic illustration of organosilane molecules (APTES) attachment to the surface of bare silica NPs (SiO_2 NPs) in order to form amine functionalised silica NPs (NH_2-SiO_2). Ethoxy groups of APTES were hydrolysed in presence of NH_4OH, subsequently reacted with free hydroxyl groups on the surface of bare silica NPs to form a covalent siloxane bonds (red).

Heparin, chondroitin sulphate and sodium alginate were then grafted onto the surface of amine functionalised silica NPs (NPs) using EDC as a coupling agent. Which was used to activate the carboxylate groups of these polymers in order to react with amine groups of silica NPs using intrachain conjugation method as illustrated in Figure 2.6. Intrachain conjugation method was used in this study as end-chain conjugation method of heparin to the surface totally preserves the anticoagulant activity of immobilised heparin.[155-156] Consequently, heparin attached to the surface by end-point conjugation is expected to have

high bleeding side effects. Figure 2.7 illustrates the difference between the end-point and intrachain conjugation of heparin to NPs surfaces.

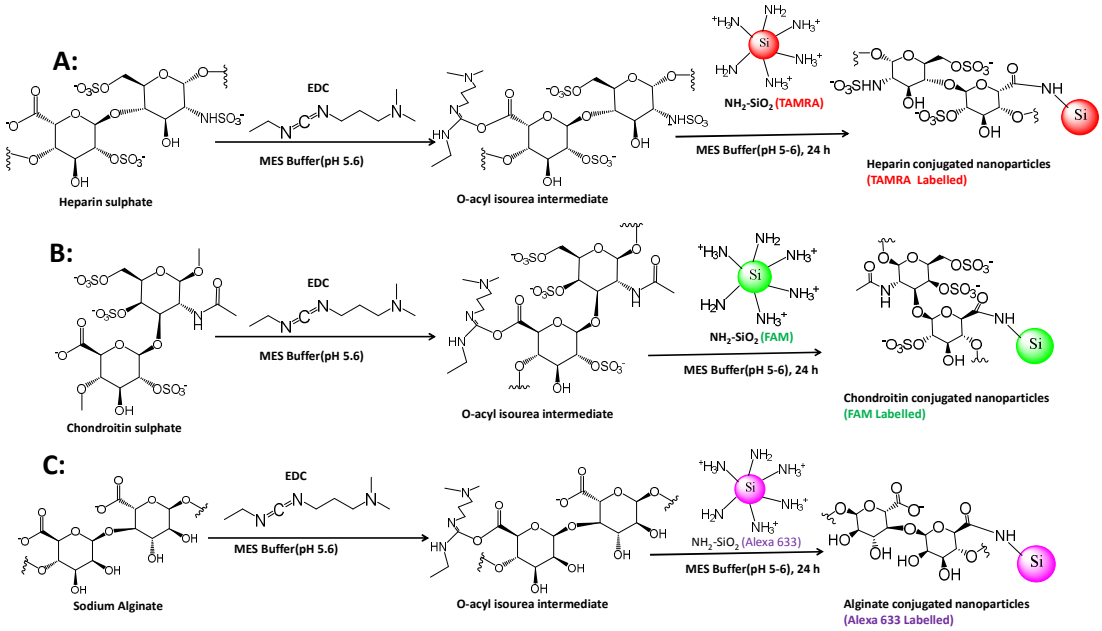


Figure 2.6 Schematic representation of synthesis of heparin, chondroitin sulphate and alginate conjugated silica NPs labelled with TAMRA, FAM and Alexa 633 respectively using EDC as a zero length linker that activates the carboxylate groups of these polymers. A: coupling of heparin to amine functionalised TAMRA labelled silica NPs (NH_2-SiO_2) to produce heparin conjugated NPs (HP-SiO_2), B: coupling of chondroitin sulphate to amine functionalised FAM labelled silica NPs (NH_2-SiO_2) to produce chondroitin conjugated NPs (CH-SiO_2), C: coupling of sodium alginate to amine functionalised Alex 633 labelled silica NPs (NH_2-SiO_2) to produce alginate conjugated NPs (ALG-SiO_2).

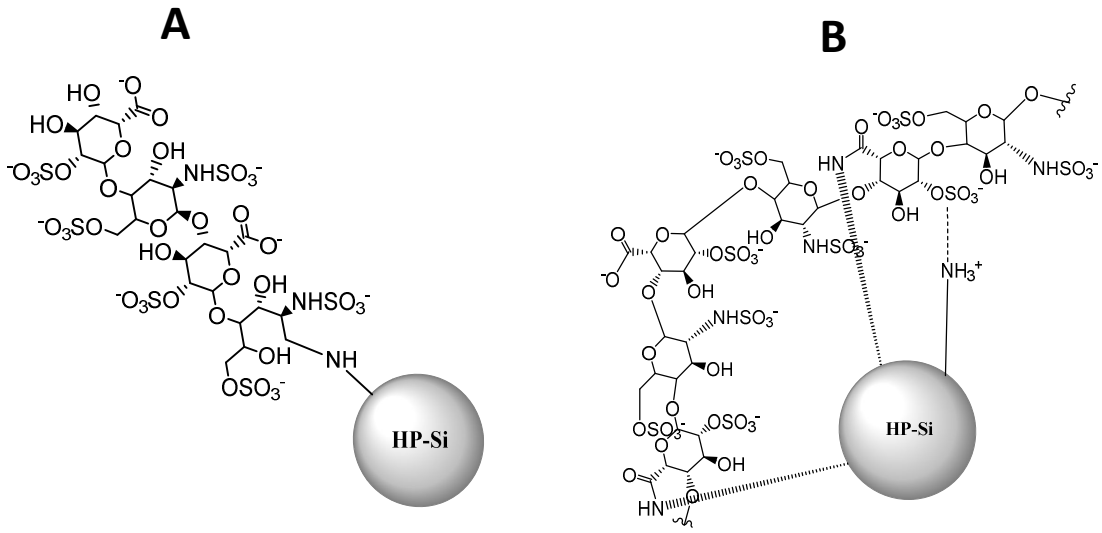


*Figure 2.7 Schematic representation of heparin conjugation to the surface of amine functionalised NPs using **A:** end-chain immobilisation method and **B:** Intrachain conjugation method.*

2.4.2 Characterisation

2.4.3 Particle Size

All prepared NPs had relatively similar mean particle size which is around 200 nm as measured by DLS. However NPs that have modified surfaces with hydrophilic polymers including heparin, alginate and chondroitin showed significantly higher diameters compared with non-grafted amine functionalised NPs as shown in Figure 2.8 A and B. This is attributed to these hydrophilic polymers forming a hydration layer around the particle surface.[157-160] Moreover, the polydispersity index of all NPs types was measured as illustrated in Figure 2.8 C and the values were below 0.2 i.e. within the commonly acceptable range in order to use NPs for drug delivery.[161-162]

Figure 2.9 shows that the TEM images and corresponding histograms are consistent with DLS data with slightly lower values as can be explained TEM measuring the diameter of the particle in the dried state negating the effect of the hydration layer.[163-164] The particles had spherical shape which is an inherent property of silica NPs.[165]

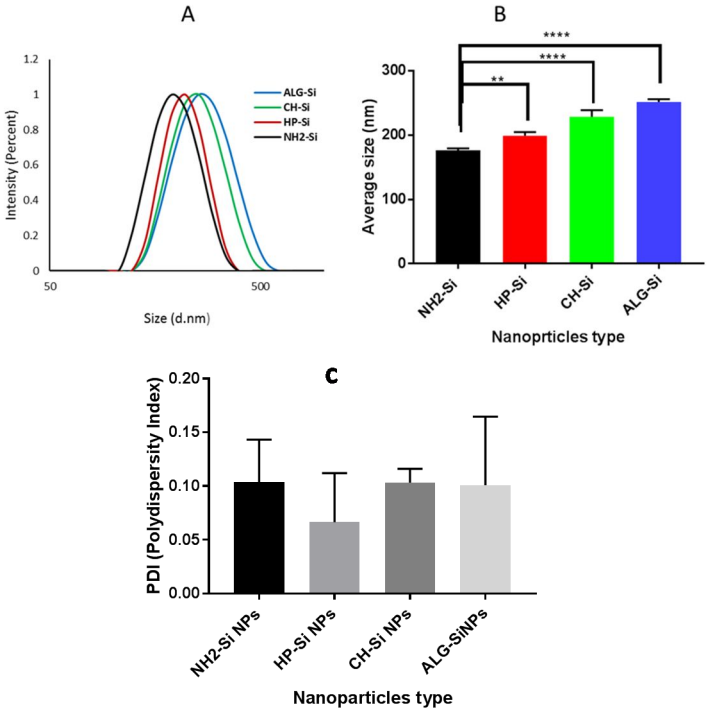


Figure 2.8 . Size of the non-grafted and polymer grafted NPs measured by dynamic light scattering (DLS). ***A:*** *Particle size distribution of heparin conjugated NPs (HP-Si), alginate conjugated NPs (ALG-Si), chondroitin conjugated NPs (CH-Si) and non-grafted amine functionalised NPs (NH2-Si).* ***B:*** *Quantitative measurement of the average particle size of the NPs shown in A.* ***C:*** *Polydispersity index values of the NPs shown in A. Data was analysed using one way ANOVA test (column analyses), multiple comparison by comparing the mean of each column to the mean of the control column (NH2-Si). Error bars indicate SD (n = 3), ** is P ≤ 0.01, *** is P ≤ 0.001**** is P ≤ 0.0001.*

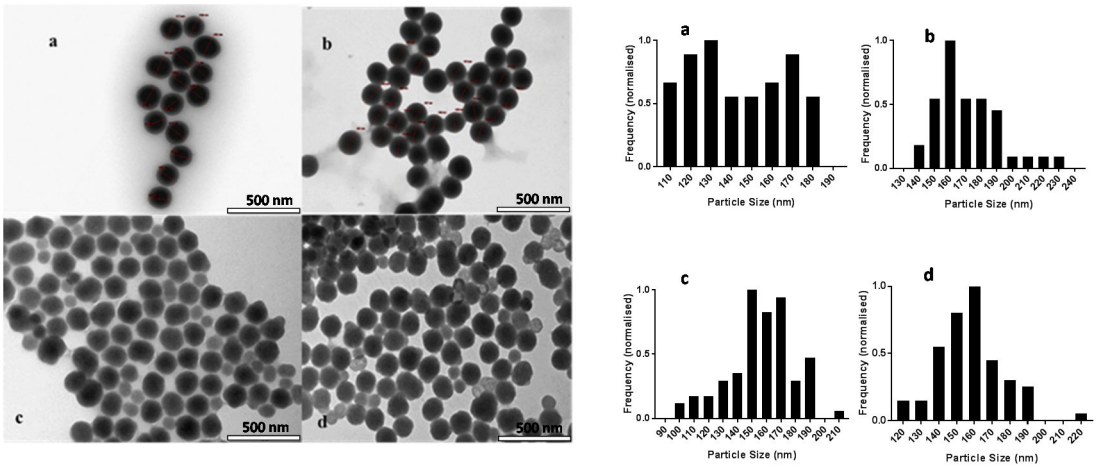


Figure 2.9 TEM images (left) and corresponding histograms (right) of amine functionalised NPs (a) heparin conjugated NPs (b), chondroitin conjugated NPs (c) and alginate conjugated NPs (d) (scale bar = 500 nm). Histograms were generated by calculating the diameter of n numbers for each type of the NPs (n = 40).

2.4.4 Zeta potential

NPs conjugated with heparin, sodium alginate and chondroitin sulphate had negative zeta potential values compared with amine functionalised NPs as shown in Figure 2.10. This indicates successful grafting of the negatively charged polymers to the surface of amine functionalised silica NPs.

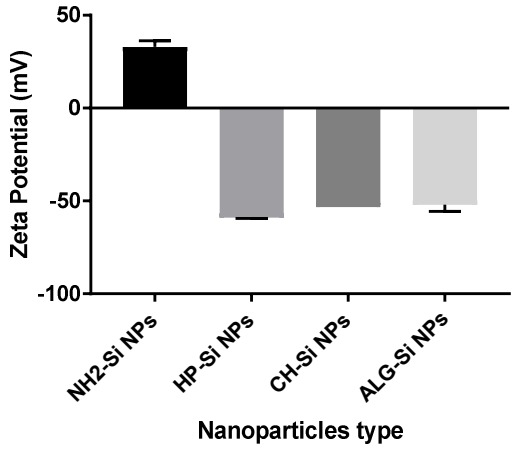


Figure 2.10 Zeta potential measurements of negatively charged heparin conjugated NPs (HP-Si), alginate conjugated NPs (ALG-Si), and chondroitin conjugated NPs (CH-Si) and positively charged amine functionalised NPs (NH2-Si). Error bars indicate SD (n = 3).

2.4.5 Fluorescence of the NPs

Fluorophores were chemically incorporated within the silica matrix by incorporation of dye-APTES conjugate with TEOS during the synthesis of the NPs. Chemical conjugation of the fluorophore was used in order to ensure NPs labelling with minimal loss and leaching of the dye over time. Figure 2.11 shows that chondroitin NPs labelled with FAM had a maximum emission wavelength at 525 nm, heparin NPs labelled with TAMRA had a maximum emission wavelength at 575 nm and alginate NPs labelled with Alexa 633 had a maximum emission

wavelength at 650 nm. This indicates that the fluorophores were successfully incorporated into the NPs and remained after washing steps.

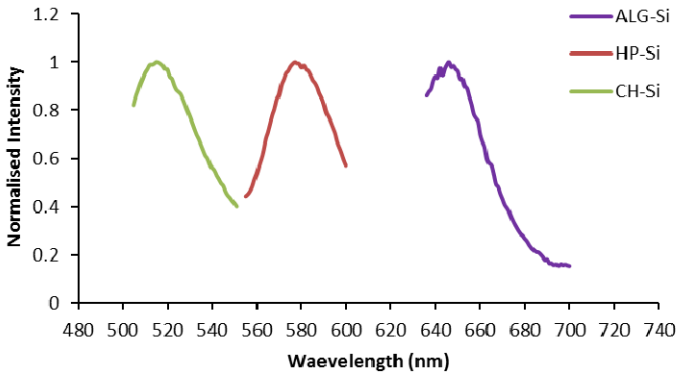


Figure 2.11 Fluorescence spectra of TAMRA labelled heparin conjugated NPs (HP-Si), Alexa 633 labelled alginate conjugated NPs (ALG-Si), FAM labelled chondroitin conjugated NPs (CH-Si), showing the maximum emission wavelengths of the fluorophore incorporated NPs. Fluorescence intensity was normalised to the maximum intensity.

2.4.6 Determination of the polymers grafted onto the NPs' surface

2.4.6.1 Confirmation of heparin grafting using TGA

Thermogravimetric analysis (TGA) was conducted in order to confirm the presence of heparin on the NPs surfaces, Figure 2.12 shows TGA curves of heparin conjugated NPs, amine functionalised NPs, bare silica NPs and heparin alone. Heparin conjugated NPs had greater weight loss than non-heparin conjugated ones (bare or amine functionalised) as a result of heparin decomposition between 200-600 °C, which indicates the presence of heparin on the nanosurface, in addition HP-Si curve had an increased gradient (0.031) compared with NH_2-Si curve (0.014) within 200-600 °C temperature range.

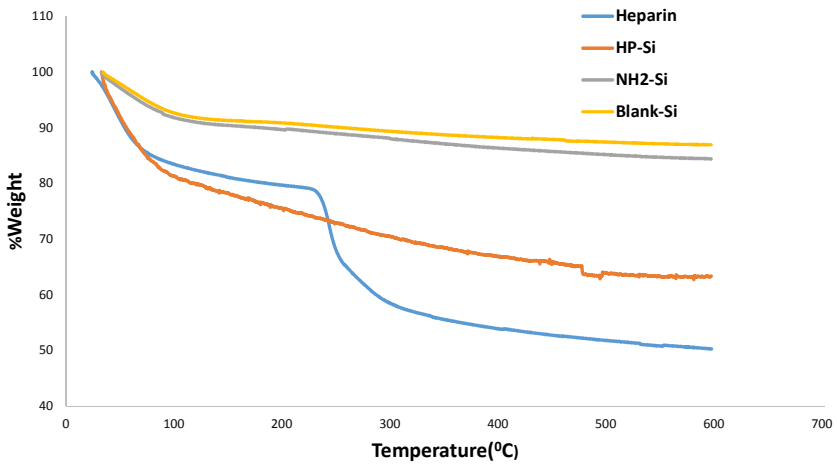


Figure 2.12 TGA curves of heparin alone, heparin conjugated NPs (HP-Si), amine functionalised NPs (NH_2-Si) and bare silica NPs (Blank-Si).

2.4.6.2 Confirmation of heparin grafting using azure A assay

The presence of heparin on the NPs surface was identified using an azure A assay as it is a highly sensitive test for quantitative measurement of heparin.[166] In principle, when azure A reagent is added to heparin solution its maximum absorption wavelength is shifted to a shorter wavelength (blue shift). This is due to the interaction between the negative sulphate groups of heparin and the positive amine groups of azure A which leads to dimerization of azure A molecules, thus reducing the delocalisation of electrons as illustrated in Figure 2.13.[167-169]

Figure 2.14 shows that heparin conjugated NPs made a significant hypsochromic shift to the maximum absorption wavelength of azure A (λ_{max}), similar to the effect of native heparin polymer. In contrast to non-grafted amine functionalised NPs, that did not affect azure A wavelength. This supports that heparin was successfully grafted onto the NPs surface.

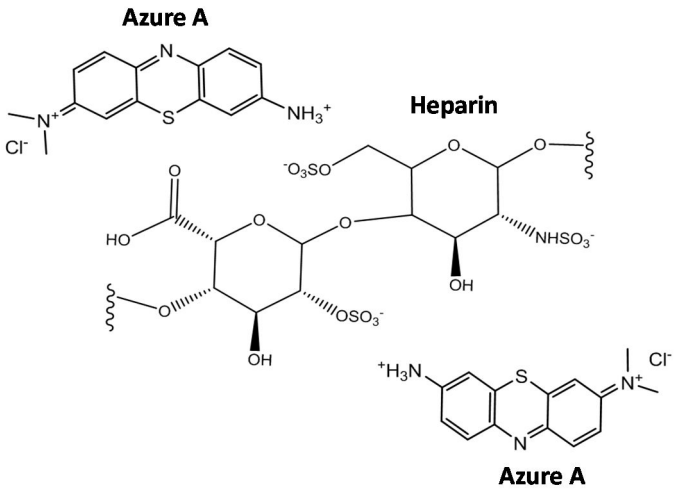


Figure 2.13 Schematic representation of possible electrostatic interaction between heparin and two molecules of azure A to form a dimer.

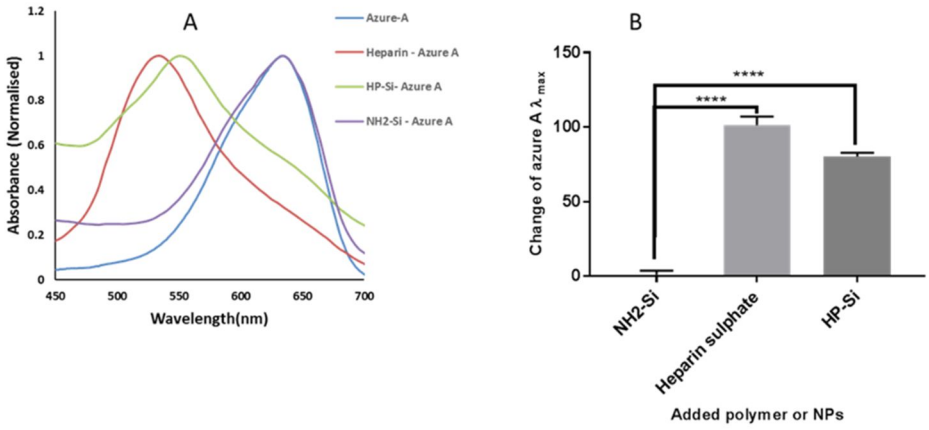


Figure 2.14 Effect of heparin polymer, heparin conjugated NPs and non-grafted amine functionalised NPs on maximum absorption wavelength of azure A dye. ***A:*** *UV-visible absorption wavelength spectra of 0.0125mg/mL azure A alone (Blue), and after addition of 20 µg/mL heparin (Red), 0.5 mg/mL heparin conjugated NPs (Green), and 0.5 mg/mL amine functionalised NPs (Purple).* ***B:*** *Quantitative measurements of azure A lambda max change upon addition of heparin polymer, heparin conjugated NPs (HP-Si), and non-grafted amine functionalised NPs (NH2-Si). Data was analysed using one way ANOVA test (column analyses), multiple comparison by comparing the mean of each column to the mean of the control column (NH_2-Si). Error bars indicate SD (n = 3). **** is P ≤ 0.0001.*

2.4.6.3 Determination of the percentage of heparin grafted to NPs surface using azure A assay and TGA analysis

The percentage of heparin covering the surfaces of silica NPs was calculated using azure A assay and TGA analysis. Figure 2.15 shows that the percentage (w/w) of heparin conjugated to the surface of amine functionalised silica NPs was around 6% using TGA method whilst around 4% as indicated by azure A assay. Although there was a statistically significant difference between the two methods, azure A method is considered more accurate as it

measures the chemical entity of heparin compared with measuring the decomposition of the organic material on the NPs surfaces used in TGA method .[170]

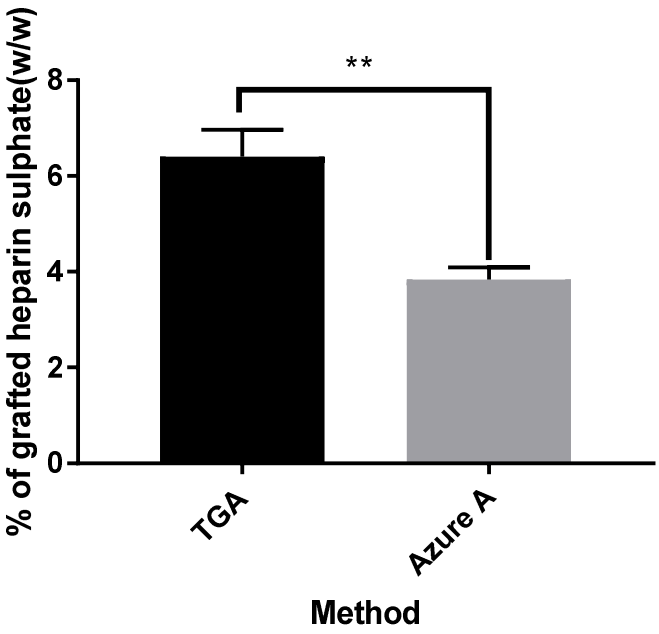


*Figure 2.15 Percentage of heparin attached to the surface of silica NPs through EDC coupling reaction. Error bars indicate SD (n=3). Data was analysed using t test. ** is P ≤ 0.01.*

2.4.6.4 Confirmation of chondroitin and alginate grafting using DMMB assay

Chondroitin and alginate conjugation to the particles' surface was confirmed using a DMMB (1,9-Dimethyl Methylene Blue) assay at different pH values. In principle, cationic DMMB binds to polyanionic substrates and this interaction causes a metachromatic blue shift of DMMB maximum wavelength.[171-173]

At pH 7.2, both alginate and chondroitin conjugated NPs induced a blue shift of DMMB maximum wavelength similar to the effect of alginate and chondroitin polymers as shown in Figure 2.16 A. However chondroitin conjugated NPs have induced a significantly higher shift relative to alginate conjugated NPs as demonstrated in Figure 2.16 B. Which is attributed to the engagement of carboxylate groups of alginate with amine groups on the particles' surface through amide bond. In contrast, chondroitin sulphate polymer and chondroitin conjugated NPs significantly induced a metachromatic shift of DMMB maximum wavelength at pH 1.5 relative to alginate polymer and alginate conjugated NPs as shown in Figure 2.16 C and D.

This supports that the difference in surface chemistries between alginate and chondroitin conjugated NPs can be further distinguished at low pH values.

Alginate polymer and alginate conjugated NPs had no effect on the DMMB wavelength at pH 1.5 as expected due to the complete protonation of the anionic carboxylate groups. Consequently the absence of the electrostatic interaction between alginate and DMMB which is required for the metachromatic shift, which can be illustrated in Figure 2.17.[174] Furthermore, DMMB colour change upon addition of chondroitin and alginate NPs was visually detected at different pH values as depicted in Figure 2.18.

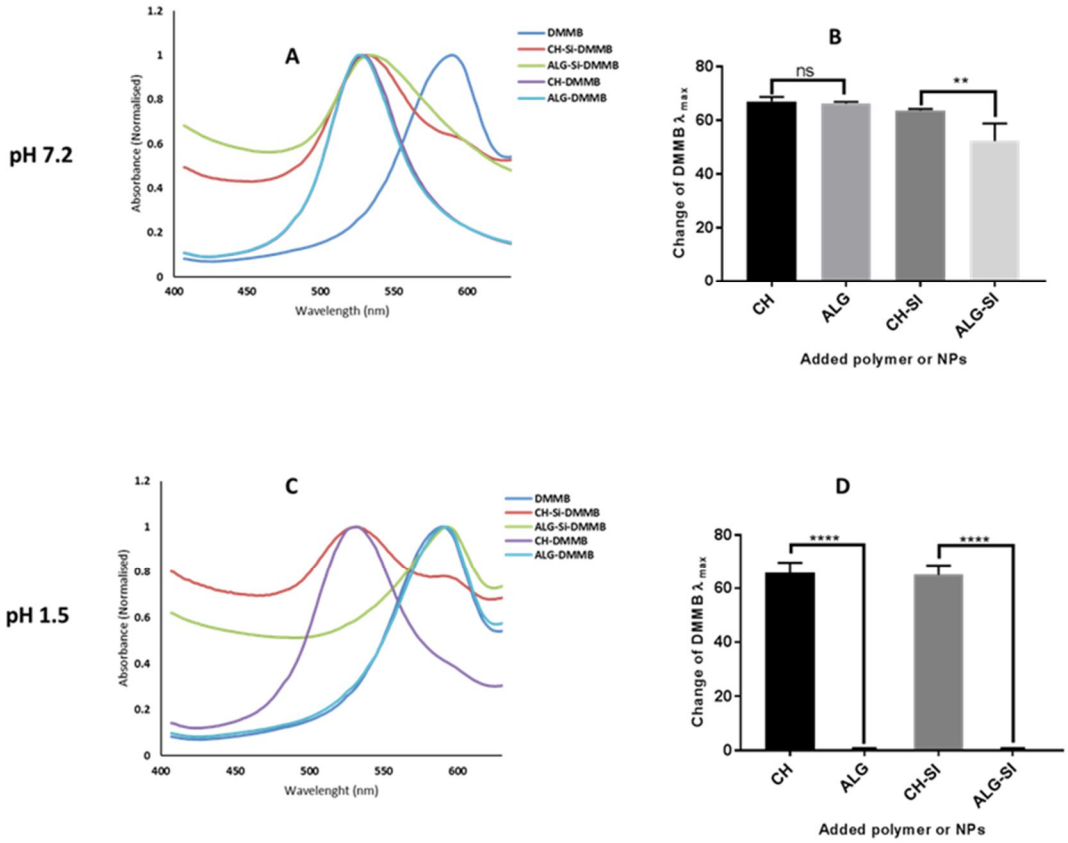


*Figure 2.16 Effect of sodium alginate, chondroitin sulphate polymers, alginate conjugated NPs and chondroitin conjugated NPs on the maximum absorption wavelength of DMMB dye at various pH values. A: UV-visible absorption wavelength of DMMB dye alone, and after addition of chondroitin sulphate polymer (CH-DMMB), sodium alginate polymer (ALG-DMMB), chondroitin conjugated NPs (CH-Si-DMMB) and alginate conjugated NPs (ALG-Si-DMMB) at pH 7.2. B: Quantitative measurements of DMMB lambda max change upon addition of the polymers and NPs shown in A at pH 7.2. C: UV-visible absorption wavelength of DMMB dye alone, and after addition of chondroitin sulphate polymer (CH-DMMB), sodium alginate polymer (ALG-DMMB), chondroitin conjugated NPs (CH-Si-DMMB), alginate conjugated NPs (ALG-Si-DMMB) at pH 1.5. D: Quantitative measurements of DMMB lambda max change upon addition of the polymers and NPs shown in A at pH 1.5. Data was analysed using t test. Error bars indicate SD (n = 3), ns is $P > 0.05$, ** is $P \leq 0.01$, **** is $P \leq 0.0001$.*

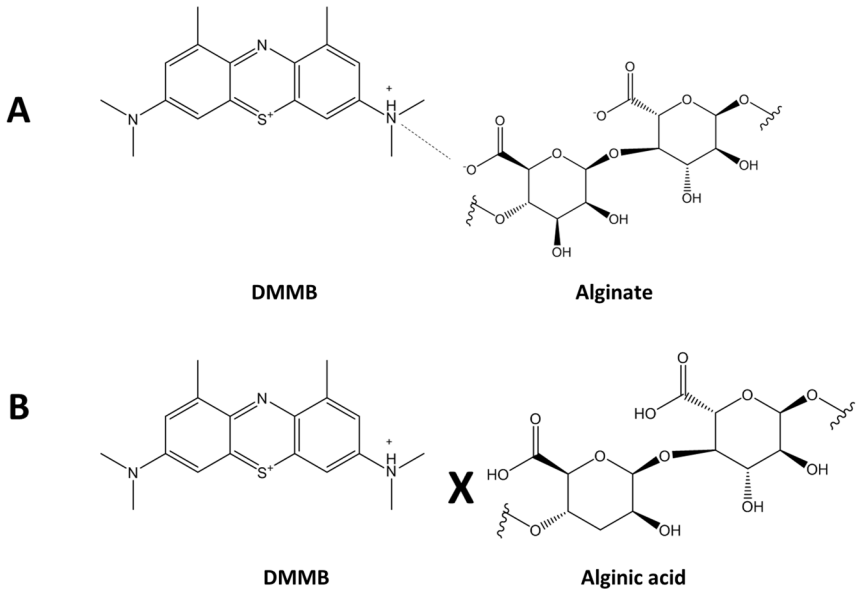


Figure 2.17 Schematic illustrates the electrostatic interaction between negatively charged sodium alginate and positively charged cationic DMMB. ***A:*** *Electrostatic Interaction between the polymer and the dye at pH = 7.2 due to complete ionisation of sodium alginate carboxylate groups.* ***B:*** *Absence of electrostatic interaction between the polymer and the cationic dye at pH 1.5 due to protonation of the alginate carboxylate groups.*

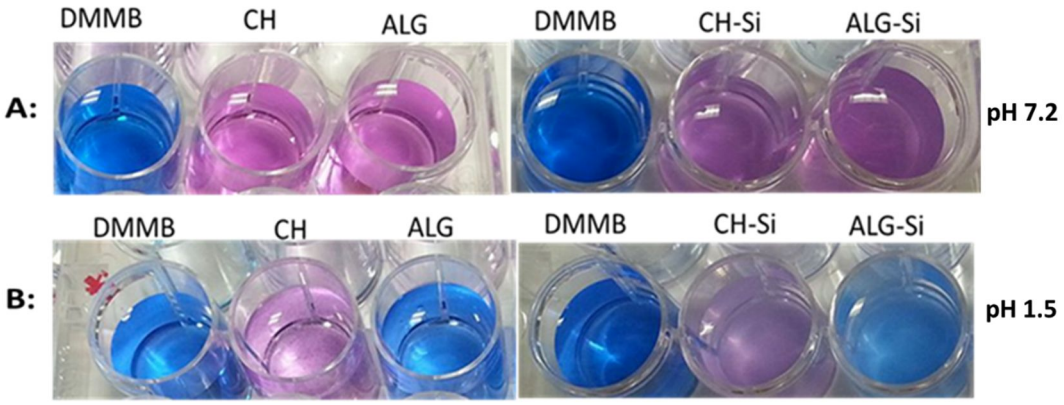


Figure 2.18 Visual monitoring of the effect of chondroitin sulphate, sodium alginate polymers and their corresponding NPs on DMMB colour. ***A:*** *Colour change of DMMB after addition of chondroitin sulphate polymer (CH), sodium alginate polymer (ALG), chondroitin conjugated NPs (CH-Si), alginate conjugated NPs (ALG-Si) at pH 7.2.* ***B:*** *Colour change of DMMB after addition of chondroitin sulphate polymer (CH), sodium alginate polymer (ALG), chondroitin conjugated NPs (CH-Si), alginate conjugated NPs (ALG-Si) at pH 1.5.*

2.4.7 Anticoagulant activity of the modified NPs

The anticoagulant activity of the NPs was measured using an anti-Xa assay. The principle of this test is that heparin increases the activity of antithrombin (ATIII) to approximately 1000 times after binding. ATIII in turn inactivates factor Xa protease. Consequently heparin prevents factor Xa from cleaving a susceptible chromogenic peptide substrate after the arginine residue and thus releasing pNA (para nitroalanin) upon the cleavage process as

demonstrated in Figure 2.19 A.[175-176] In this sense, heparin activity is inversely proportional to the released pNA optical density as shown in Figure 2.19 B.

Heparin conjugated NPs significantly reduced the released pNA optical density compared with alginate conjugated NPs and chondroitin conjugated NPs as shown in Figure 2.19 C. This can be explained by the unique structural and conformational properties of heparin that has retained biological activity and ATIII binding property in contrast to alginate and chondroitin conjugated NPs. However, higher concentration of heparin grafted to the surface of silica NPs was required to achieve similar effect of ATIII activation compared to native heparin polymer taking into account that the percentage of heparin grafted onto particles' surface was about 5% as described in section 2.4.6.3. Indicating that heparin anticoagulant activity was reduced upon conjugation to the NPs. This is ascribed to the amidation of heparin carboxylate group through the conjugation process as carboxylate group plays an important role in heparin binding to ATIII.[177-178]

Furthermore, the engagement of heparin groups through electrostatic interaction with positively charged amine groups on the surface of the NPs could make ATIII binding sequence less exposed thus reducing heparin binding to ATIII.[179]

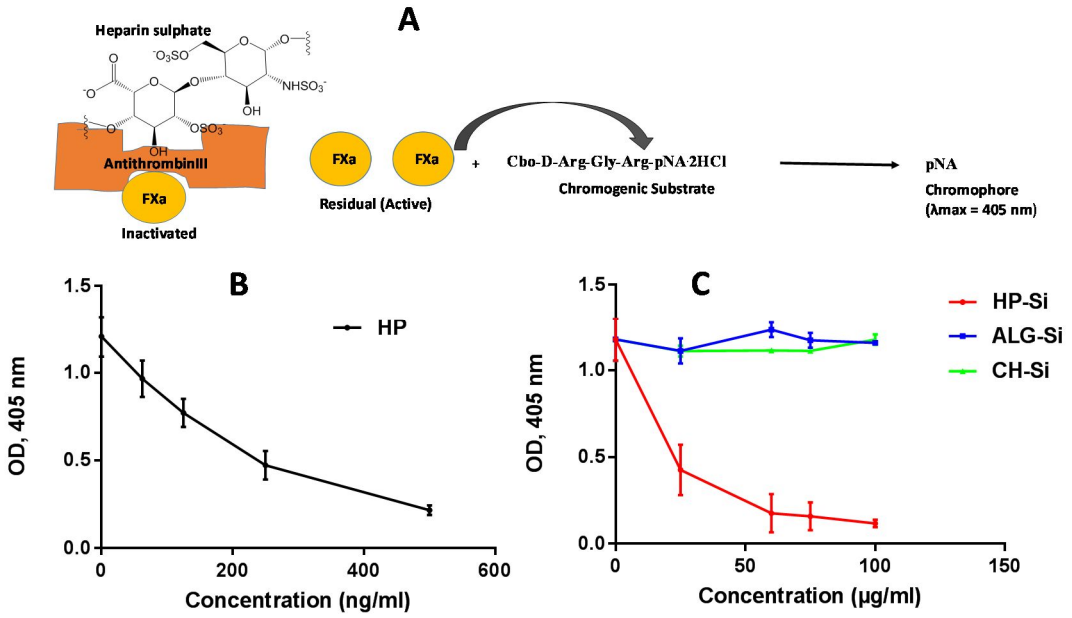


Figure 2.19 Anticoagulant activity represented by the optical density of the released pNA that is inversely proportional to anticoagulant activity of heparin and its derivatives. ***A:*** *Schematic representation of anti Xa assay mechanism showing that the measurable chromophore pNA is only released by the residual (Heparin-unbound) active factor Xa,* ***B:*** *Anticoagulant activity of native heparin polymer (HP),* ***C:*** *Anticoagulant activity of heparin conjugated NPs (HP-Si), alginate conjugated NPs (ALG-Si) and chondroitin conjugated NPs (CH-Si). Data was analysed using two way ANOVA test (grouped analyses), p-value of the multiple comparison is < 0.0001 for HP-Si vs CH-Si, HP-Si vs ALG-Si and > 0.05 for CH-Si vs ALG-Si. Error bars indicate SD (n = 3).*

2.4.8 Synthesis of heparin conjugated silica microparticles

In order to study the effect of particle size on the Particle-Cell adhesion interaction under flow conditions. Heparin conjugated microparticles were synthesised using Stober process by adjusting the amount of ammonium hydroxide and the concentration of TEOS used to synthesise heparin conjugated silica NPs.

2.4.9 Particle Size

The diameter of heparin conjugated microparticles was *circa* 1.4 µm as indicated by optical images and the representative histograms shown in Figure 2.20 A, B and C. PDI was also calculated from the histogram using the equation PDI = $SD^2/mean^2$ as demonstrated in Figure 2.20 D. The estimated PDI value was within the acceptable range as previously described in section 2.4.3.

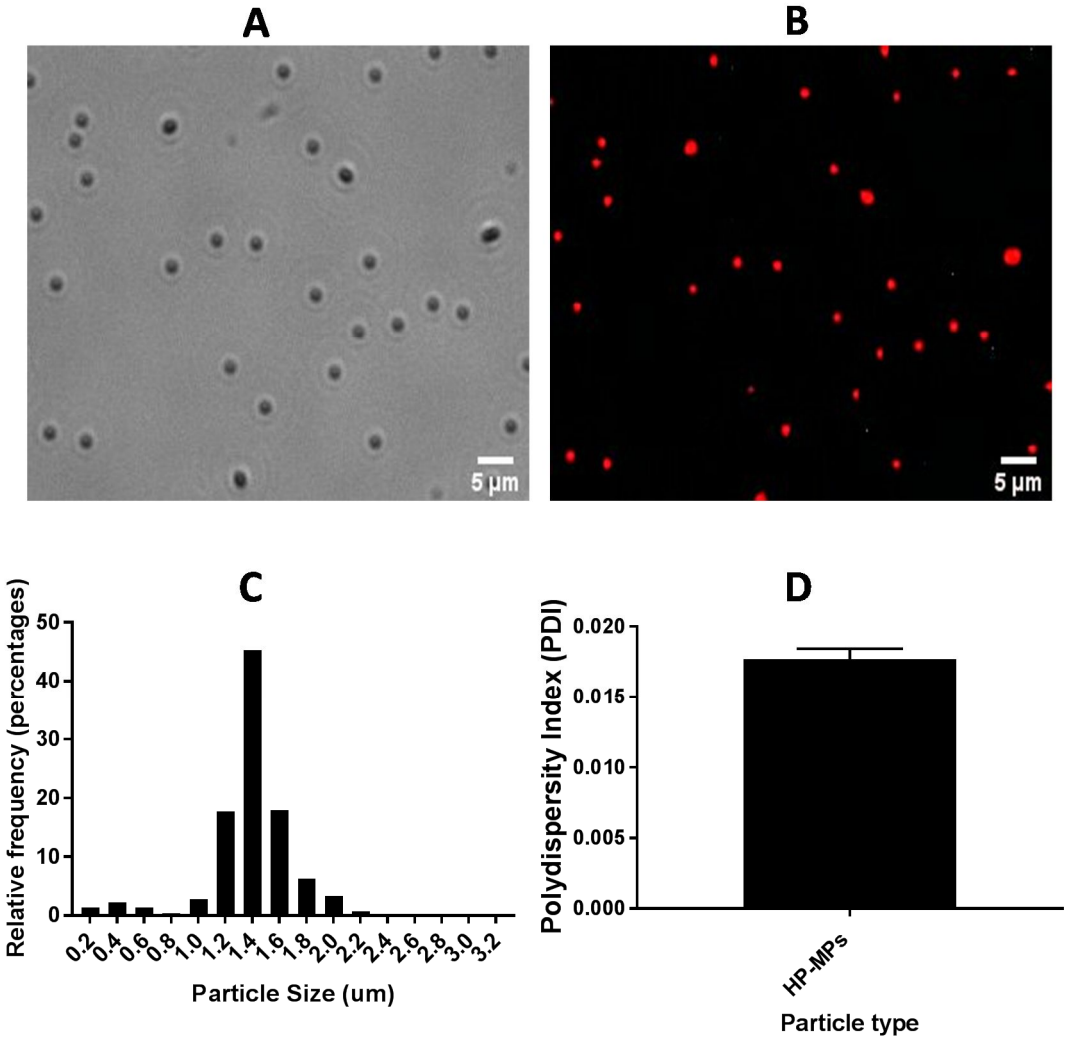


Figure 2.20 Particle characterisation. ***A:*** *Bright field image* ***B:*** *Fluorescence image of 1.4 µm size heparin conjugated particles (HP-MPs)* ***C:*** *Histogram showing particles distribution.* ***D:*** *Polydispersity index (PDI) of heparin conjugated microparticles (HP-MPs) estimated using the equation: PDI = $SD^2/mean^2$. Histogram was generated using GraphPad Prism by measuring the diameters of n numbers of particles (n=700). Scale bar= 100 µm.*

2.4.10 Cellular uptake of heparin conjugated microparticles compared to NPs

Cellular uptake is influenced by cell surface binding, where binding of solutes/particles to the surface of the cell might induce their internalisation. Particles that are intended to target certain receptors that are extracellularly overexpressed, have to accumulate at cell surface and show less tendency of cellular internalisation. Accordingly cell uptake study was performed for heparin conjugated microparticles and NPs.

Heparin conjugated microparticles (1.4 µm size) have shown less cellular uptake compared with heparin conjugated NPs as indicated by the confocal microscopy images shown in Figure 2.21 A. Heparin conjugated microparticles had significantly less cellular internalisation

than heparin conjugated NPs after normalisation of the colour intensity of the taken up particles to the number of the cells as shown in Figure 2.21 B. Which is an expected effect of the microparticle diameter on cellular uptake.[180-181] However, as the particles size influences the total measured fluorescence of the particles, the measured difference might be underestimated as the microparticles have 7 times larger diameter than the NPs. Consequently, the microparticles could have 343 (7^3) times higher fluorophore content per particle in comparison with the NPs taking into account that the volume of the sphere is $(4/3)*\pi*r^3$.

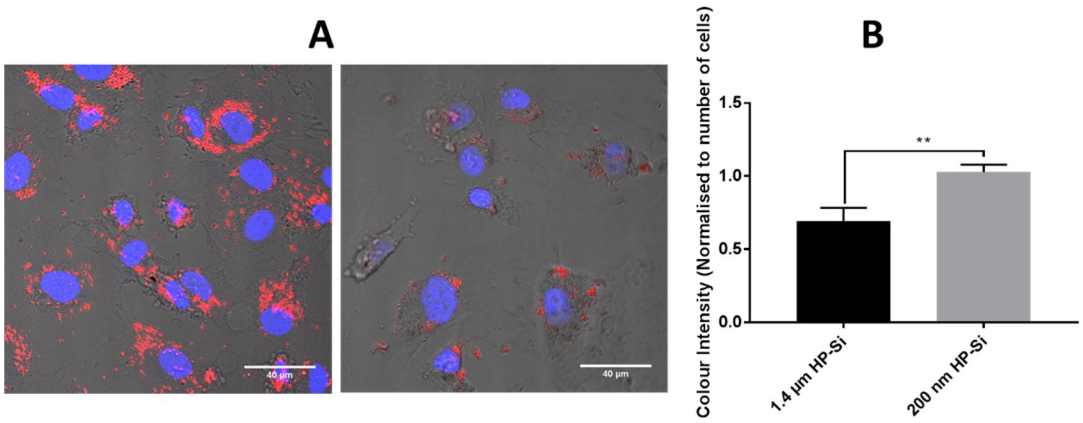


Figure 2.21 ***A:*** *Confocal microscopy images of HUVECs cellular uptake of heparin conjugated NPs with 200 nm size (left) and heparin conjugated microparticles with 1.4 µm size (right).* ***B:*** *Quantitative measurement of different sizes of heparin particles internalisation by HUVECs treated with 25 µg/mL particles. Data was analysed using unpaired t test. Error bars indicate SD (n = 3, 3 different random regions were taken). ** is P ≤ 0.01. Scale bar = 40 µm.*

2.4.11 Monitoring of heparin, chondroitin and alginate conjugated NPs-cellular binding under flow conditions

In order to study the adhesion of the NPs to cell surface under shear stress to mimic the systemic circulation, HUVECs were grown to near confluency into µ-channel slides and allowed to adhere over certain period of time. The cultivated HUVECs look in a healthy state using the optimised culture protocol as shown in Figure 2.22.

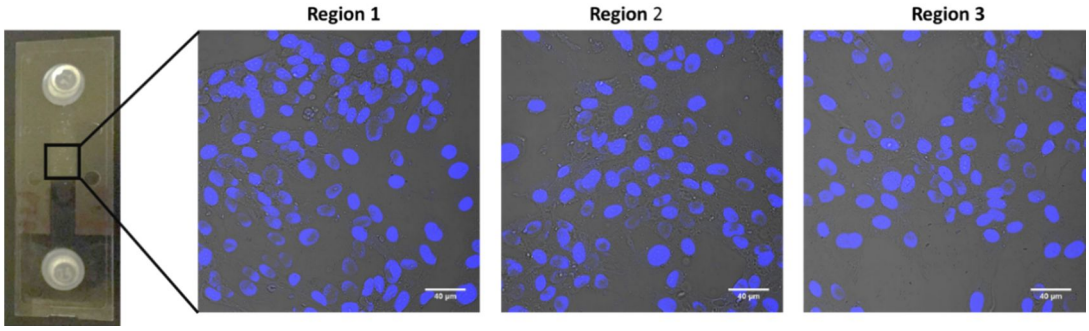


Figure 2.22 HUVECs grown in ibidi µ-channel slide (left) for 72 hours and corresponding fluorescence images of the cells having nuclei stained with Hoechst showing near confluency growing. Images were taken from three different regions of the slide. Scale bar = 40 µm.

The shear stress across the blood vessel walls caused by blood circulation varies from region to region and organ to organ in the human body. It is inversely proportional to the third power of the blood vessel radius, subsequently It can be lower than 1 dyn/cm^2 for large veins and as high as 40 dyn/cm^2 in small venules, it could be also the highest in small arterioles with shear stress value is 60-80 dyn/cm^2.[182-183] The shear stress that was applied to the cultured HUVECs was 1.16 dyn/cm^2. This value was chosen to mimic the shear stress of the large veins of the human body.

Heparin (red) and chondroitin (green) conjugated NPs were more bound to the surface of HUVEC cells compared with alginate (purple) conjugated NPs as illustrated in Figure 2.23.

Cellular adhesion of heparin, chondroitin and alginate conjugated NPs were tracked over time. The NPs appear to start adhering to the surface of HUVECs and stay bound over the time where a distinct change in NPs-HUVECs binding was observed as indicated in Figure 2.24. This indicates that the NPs are firmly and tightly adhered to the surface of HUVEC cells, which is attained by the balance between the force driven by ligand-P-selectin receptor interaction and the disruptive force of the flowing media above the cell surface.

As the surface charge of the NPs is negative, the non-specific binding of the NPs to cell surface is assumed to be minimal.[184-185] Consequently the preferential cellular adhesion of heparin and chondroitin conjugated NPs could be explained by the ability of heparin[186-187] and chondroitin sulphate [188-189] to bind to P-selectin; a membrane receptor expressed on the

surface of the stimulated endothelial cells. Although P-selectin upregulation needs endothelial cells stimulation such as inflammation, it is normally expressed on the surface of cultured HUVEC cells.[190-194] Figure 2.25 shows the basal expression of the membrane receptor; P-Selectin on the surface of HUVECs.

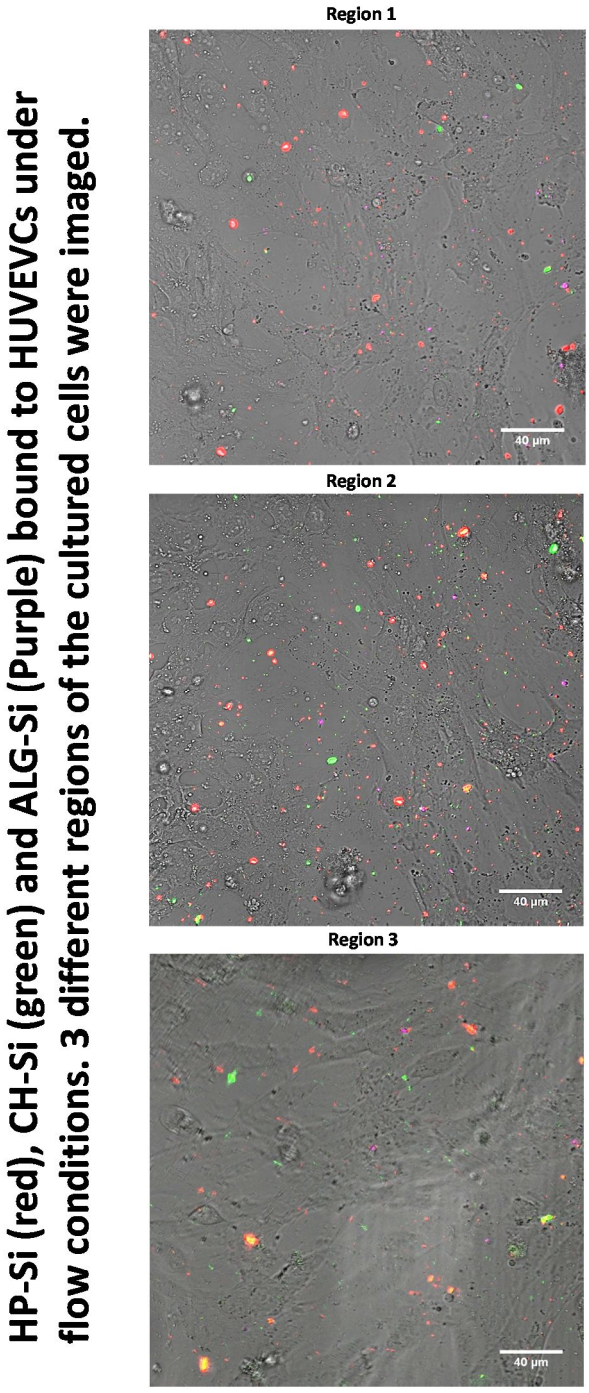


Figure 2.23 Fluorescence microscopy images of HUVECs treated with mixture of 200 nm heparin conjugated NPs labelled with TAMRA (red), chondroitin conjugated NPs labelled with FAM (green) and alginate conjugated NPs labelled with Alexa 633 (purple) under flow conditions. Images were taken from three different regions of µ-channel slide. Shear stress = 1.16 dyn/cm^2. Scale bar = 40 µm.

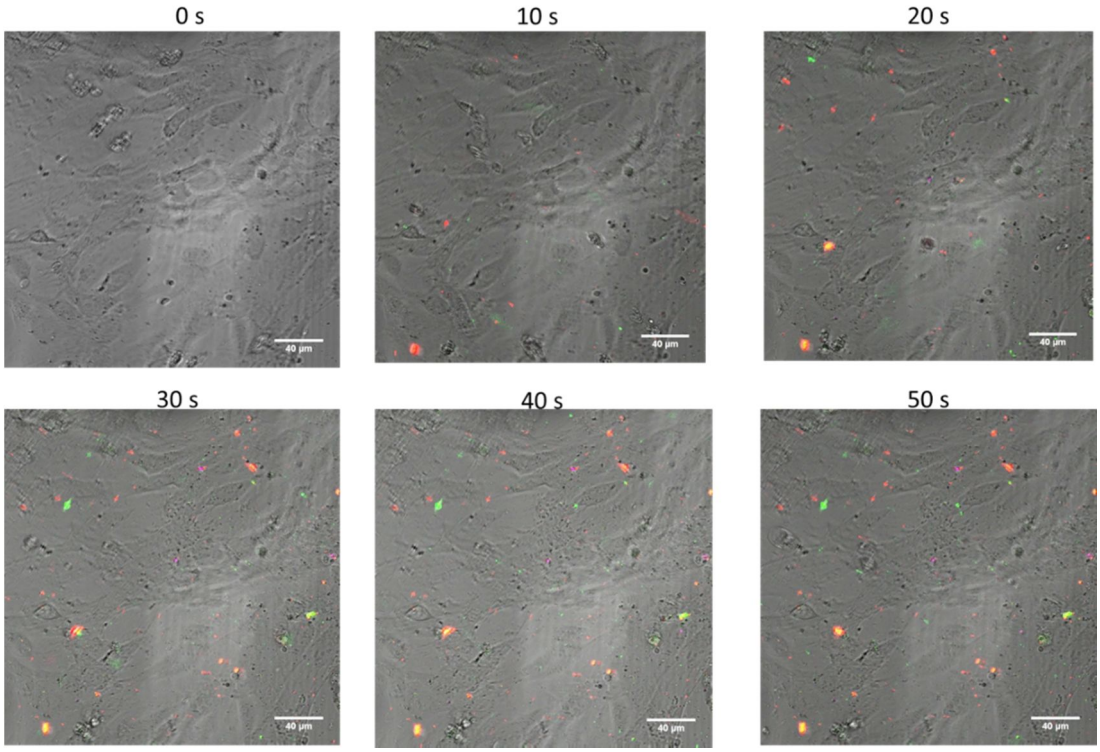


Figure 2.24 Time lapse fluorescence images of HUVECs treated with mixture of 200 nm heparin conjugated NPs labelled with TAMRA (red), chondroitin conjugated NPs labelled with FAM (green) and alginate conjugated NPs labelled with Alexa 633 (magenta) under flow conditions. Images were taken every 10 seconds. Shear stress = 1.16 dyne/cm². Scale bar = 40 µm.

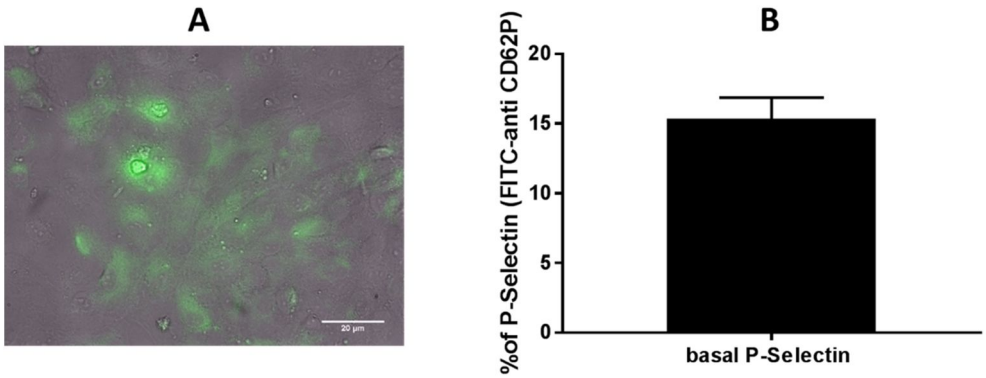


Figure 2.25 P-selectin expression on the surface of HUVEC cells. ***A:*** *Fluorescence image of HUVECs treated with FITC labelled anti CD62 antibody (immunostaining).* ***B:*** *percentage of basal P-selectin expression on HUVEC cell surface using flow cytometry. Scale bar = 20 µm. n=3, Error bars indicate SD (n = 3). % of P-selectin was represented by the percentage of labelled cells with FITC anti-P-selectin antibodies relative to the whole population of treated cells.*

To confirm that heparin and chondroitin functionalised NPs were specifically bound to cell surface expressed P-selectin, an experiment was performed using anti P-selectin antibodies

to block the basal P-selectin receptors expressed on HUVEC cell surface. The NPs were then allowed to flow above the cell surface in order to investigate the role of P-selectin in NPs adhesion to cell surface.

Figure 2.26 A displays that heparin and chondroitin conjugated NPs adhesion to HUVEC cell surface was supressed. This is ascribed to the competitive inhibition of the NPs binding to HUVECs surface by anti P-selectin antibodies that are occupying P-selectin receptors as illustrated in Figure 2.26 B. This finding supports that heparin and chondroitin conjugated NPs exploit P-selectin adhesion molecules for binding and adhesion to cell surface.

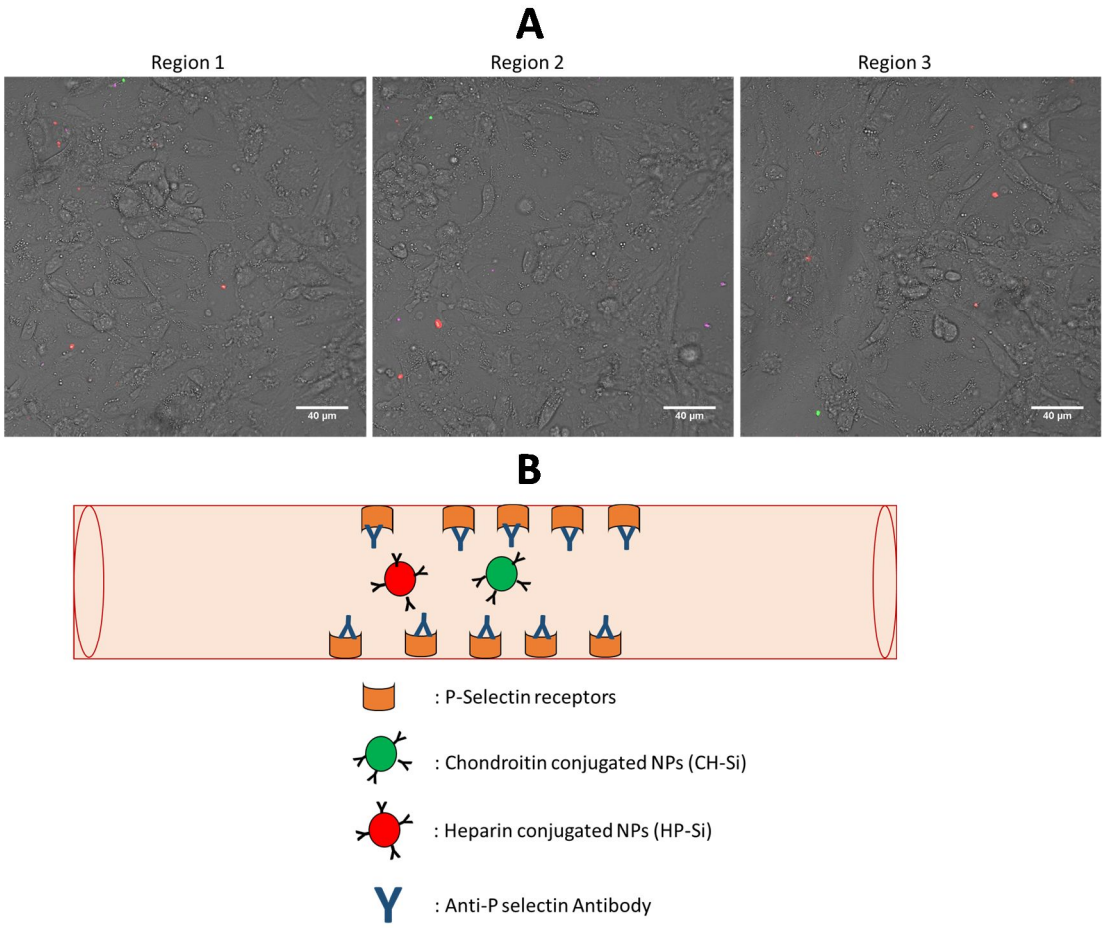


Figure 2.26 ***A:*** *Fluorescence microscopy images of HUVECs incubated with Anti P-selectin antibody for 1 hour under static conditions followed by treatment with mixture of 200 nm heparin conjugated NPs labelled with TAMRA (red), chondroitin conjugated NPs labelled with FAM (green) and alginate conjugated NPs labelled with Alexa 633 (magenta) under flow conditions. Images were taken from three different regions of the µ-channel slide. Shear stress = 1.16 dyn/cm². Scale bar = 40 µm.* ***B:*** *Schematic representation showing that P-selectin dependent binding of heparin and chondroitin conjugated NPs to HUVECs surface is disrupted by anti P-selectin antibodies.*

2.4.12 P-selectin dependent heparin conjugated NPs-HUVECs binding

Heparin has been reported to be more clinically advantageous in inhibition of cancer metastasis and dissemination of circulating tumour cells compared with chondroitin sulphate as described in section 2.1.1.2. Accordingly, the binding of heparin conjugated particles to P-selectin was further investigated.

2.4.12.1 Confirmation of P-selectin dependent heparin conjugated NPs-HUVECs binding using competitive assay

In order to ensure the specific adhesion of heparin conjugated NPs to HUVEC cell surface, free heparin ligand was used to saturate the P-selectin receptors under static conditions. Free heparin was used as a competitive inhibitor of heparin bound to NPs surface.

Histamine, an inflammatory agent, has been used to upregulate endothelial cell P-selectin expression.[195-197] Figure 2.27 A displays the expression of P-selectin on the surface of a histamine stimulated HUVECs compared to unstimulated cells using immunofluorescence assay. It is clear that histamine stimulated cells have shown more fluorescence (P-selectin expression) compared with unstimulated cells.

After P-selectin upregulation, the competitive assay was conducted. Heparin ligand significantly reduced the binding/uptake of heparin conjugated NPs to HUVEC cells in histamine stimulated and unstimulated cells. However, the reduction effect was more pronounced in histamine stimulated cells compared with unstimulated cells as shown in Figure 2.27 B. This is attributed to the effect of free heparin ligands that are already occupying P-selectin receptors expressed on the surface of HUVECs thus reducing the binding of heparin conjugated NPs to cell surface as illustrated in Figure 2.28. Moreover, the reduction effect observed in histamine unstimulated cells could be explained by basal expression of P-selectin on the cell surface of cultured HUVECs that contributes to NPs binding even in the absence of the stimulant to upregulate the receptors.

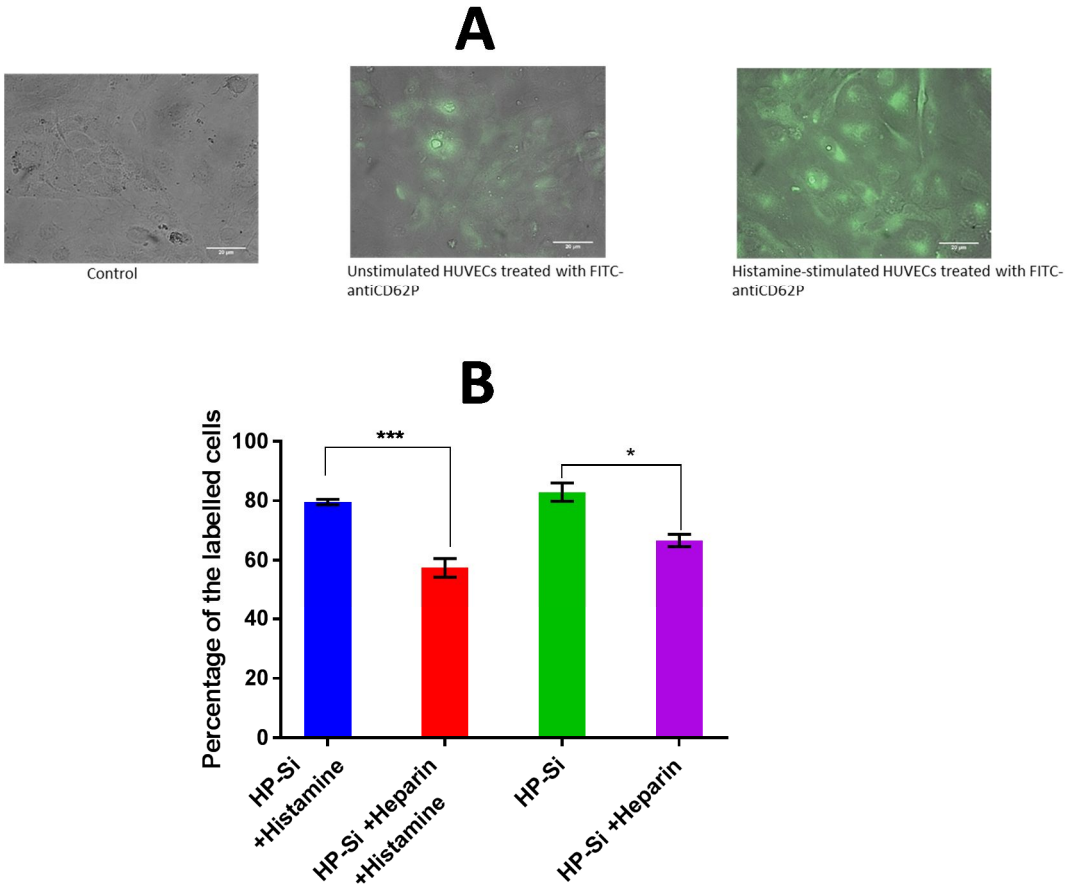


Figure 2.27 ***A:*** *Immunofluorescence assay showing fluorescence images of HUVECS treated with FITC-Anti CD62P antibody displaying P-selectin receptor expression before and after histamine stimulation.* ***B:*** *Quantitative analysis of heparin conjugated NPs (50 µg/mL) internalisation/ cell surface binding to HUVEC cells stimulated by histamine (0.1 mM) to upregulate P-selectin before and after addition of free heparin (1 mg/mL). Data was analysed using one way ANOVA test (column analyses), multiple comparison. Error bars indicate SD (n = 3). *** is P ≤ 0.001.*

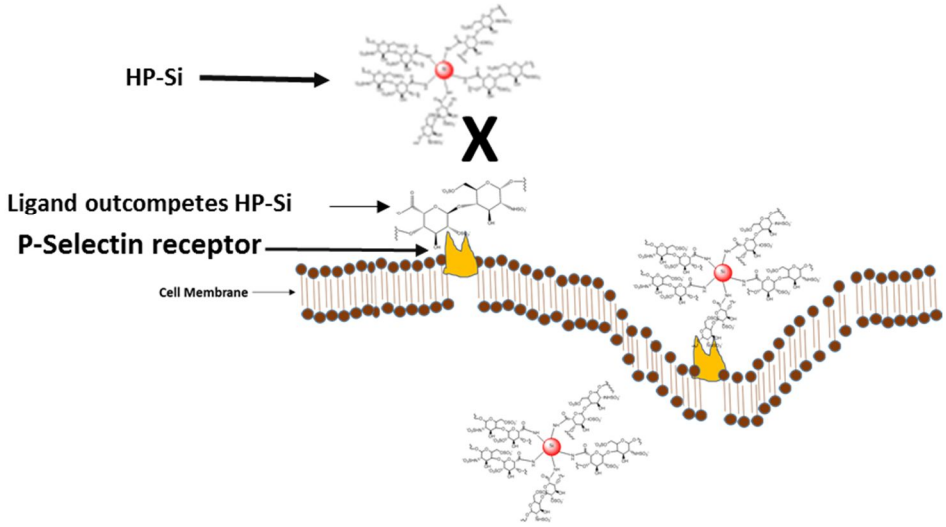


Figure 2.28 Cartoon showing that heparin conjugated NPs (HP-Si) outcompeted by heparin ligands that are already occupying P-selectin receptors expressed on the surface of endothelial cells (competitive assay).

2.4.12.2 Monitoring of heparin conjugated particles-HUVECs binding under flow conditions

A comparative study of heparin conjugated particles binding to the surface of endothelial cells (HUVECs) was conducted under flow conditions using florescence microscope.

Figure 2.29 shows that heparin conjugated microparticles and heparin conjugated NPs were bound to the surface of HUVECs, however heparin conjugated NPs appear to be more bound to the cell surface. Binding of ligand decorated particles to cell surface receptors is multifactorial and can be governed by particle size, surface area of the particles, colloidal stability, surface charge and ligand density.[198-204] Particle diameter and surface area of contact appear to be dominant in this case.

Although heparin conjugated microparticles were less internalised by cells under static conditions over the time as described in 2.4.10, the smaller heparin conjugated NPs have shown greater binding to HUVECs' surface under simulated circulatory system dynamics compared with heparin conjugated microparticles.

In addition, microparticles are more rapidly excreted than the NPs as they are more prone to immune system,[205-208] consequently 1.4 µm particles would have less circulation time than

the 200 nm-sized heparin conjugated NPs. Collectively, the 200 nm- sized heparin conjugated NPs could be superior to the heparin conjugated microparticles in cancer metastasis inhibition.

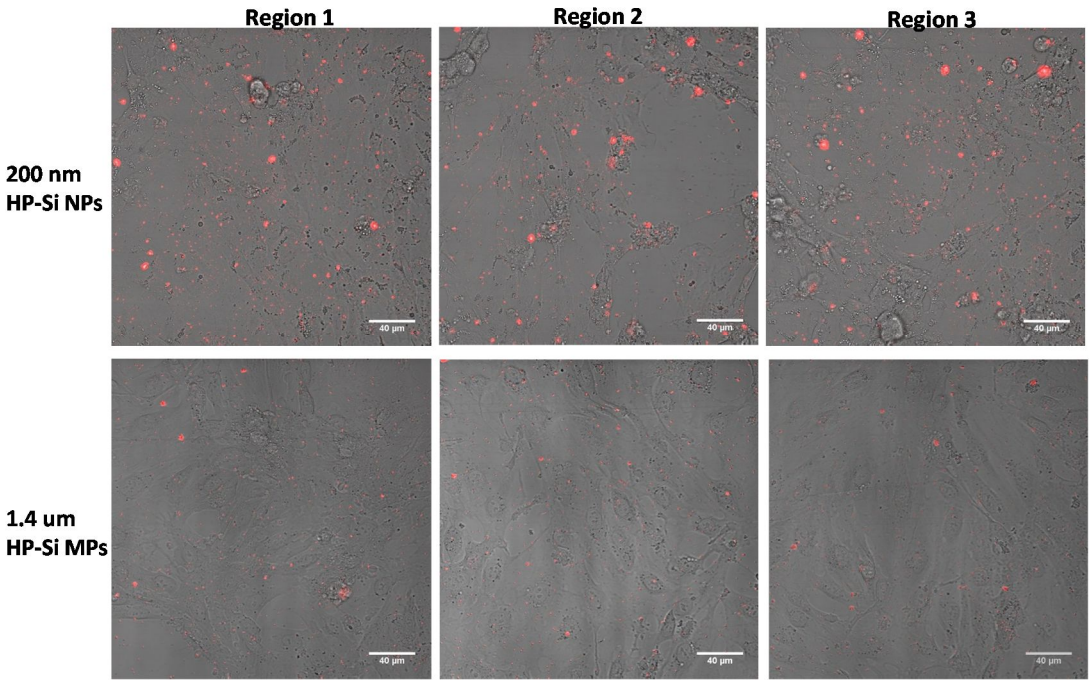


Figure 2.29 Confocal microscopy images of HUVECs treated with 200 nm-heparin conjugated NPs (HP-Si NPs) and 1.4 µm-heparin conjugated microparticles (HP-Si MPs) under flow conditions. Shear stress = 1.16 dyn/cm². n=3. Scale bar = 40 µm.

2.5 Conclusions

Heparin was successfully conjugated to the surface of silica NPs by intrachain conjugation method and characterised by TGA and colorimetric assay using azure A dye as indicator for the presence of heparin chemical entity. Furthermore chondroitin and alginate conjugated NPs were also fabricated to serve as controls and characterised by colorimetric method using DMMB as an indicator dye. In addition, a fluorescently labelled heparin conjugated microparticles were also designed and characterised by fluorescence microscopy.

Heparin has preserved some of its biological activity after surface modification, however the anticoagulant activity was decreased upon conjugation process as indicated by anti Xa assay. Thus reducing the side effects of heparin with respect to bleeding after conjugation to NPs surfaces.

Moreover, heparin and chondroitin conjugated NPs were able to preferentially bind to HUVEC cell surface while alginate conjugated NPs showed minimal under flow conditions. Heparin and chondroitin conjugated NPs have shown a P-selectin dependent adhesion to HUVEC cell surface as indicated by the competitive assay performed under flow conditions.

Additionally, heparin conjugated NPs can bind to cell surface P-selectin expressed on the surface of HUVEC cells under static conditions as indicated by the competitive assay using heparin as a substrate. Heparin conjugated NPs have shown greater HUVECs binding under a simulatory systemic circulation dynamics compared with heparin conjugated microparticles.

In summation, heparin conjugated NPs could be further inspected as a potential therapeutics for metastasis by for example testing their ability to displace the migrating cancer cells from P-selectin binding reducing the rolling adhesion of the metastatic cells and their subsequent invasion.

3 Chapter Three: Synthesis of heparin analogues conjugated NPs for heparanase inhibition

3.1 Introduction

3.1.1 Heparanase role in metastasis

Heparanase is a mammalian enzyme produced by normal human cells. It is 65 kDa protein that is synthesised in the Golgi apparatus initially in an inactive form. The inactive form is then transported to the cell surface through endosomes/lysosomes, during which processes it undergoes proteolytic activation to produce a heterodimer protein consisting of 50 kDa fragment and 8 kDa fragment attached together by a linker peptide. [209-210]

The action of heparanase, an endoglycosidase, is to cleave heparan sulphate; one of the key extracellular matrix components (ECM). Accordingly, heparanase facilitates the release of growth factors, such as FGF and VEGF, which are usually bound to heparan sulphate in the ECM. In these cases, heparan sulphate functions as a stabiliser to protect the growth factors from the extracellular environment. The release of the growth factors enables their binding to cell surface receptors in order to initiate mitogenic activity and cellular growth during mammalian embryonic development.[211-213]

Heparanase also plays a crucial role in cancer metastasis, in part by creating a path for tumour cells that have become metastatic and more motile, by degrading heparan sulphate in the basement membrane of the subendothelium and the extracellular matrix surrounding the tumour cells. Thus it facilitates the migration of metastatic cells from the primary tumour site in order to enter the systemic circulation through the endothelium of blood vessels. [214-221]

Nakajima *et al* have reported that B16 melanoma mouse cells with high metastatic potential overexpress heparanase, enabling them to colonise the lungs by degrading the extracellular matrix (ECM) and the basement membrane of the pulmonary blood vessels. In this study, increased activity of endoglycosidase overexpressed in B16 melanoma cells was reported by measuring the degradation products of the extracellular matrix of the cultured vascular endothelial cells. The degradation products of the ECM were primarily heparan sulphate fragments indicating the overactivity of heparanase in metastatic melanoma cell lines.[222]

Yang *et al* have found out that elevated levels of heparanase were responsible for the spreading of myeloma cells *in vivo* after injecting the mice with heparanase bearing myeloma cells. These data indicated the vital role of heparanase in dissemination of these cancer cells distantly from the primary tumour site, where they metastasised not only within the bones but also to other organs including lung, spleen and liver.[223]

There is also an interplay of heparanase with syndecan in cancer metastasis. Heparanase also promotes the progression of cancer metastasis by modulation and regulation the synthesis and shedding of syndecan from the cell surface. Cancer progression is strongly influenced by the action of syndecan through regulation of growth factors and angiogenesis during cancer growth and spreading. [224]

Accordingly, heparanase-inhibiting biomolecules could be utilised to treat cancer metastasis thanks to their potential inhibition of tumour invasion.

1.1.1 Heparin analogues

Modified heparin derivatives have been used to treat cancer metastasis by interrupting the ECM degrading activity of heparanases. Modified heparin derivatives have less anticoagulant activity compared to intact heparin, thus they have been additional advantage over native heparin. The most commonly studied heparin modifications are glycol splitting and heparin desulphation. In glycol split heparin, the chemical bond between C2 and C3 of glucuronic acid or non-sulphated iduronic acid is broken using periodate, thus opening the uronic acid ring within heparin chain. Whilst desulphated heparin is usually prepared by removal of sulphate groups on the oxygen or nitrogen atoms of uronic acid and glucosamine residues. Figure 3.1 shows various modifications that are performed on heparin iduronic acid or glucosamine monomers.

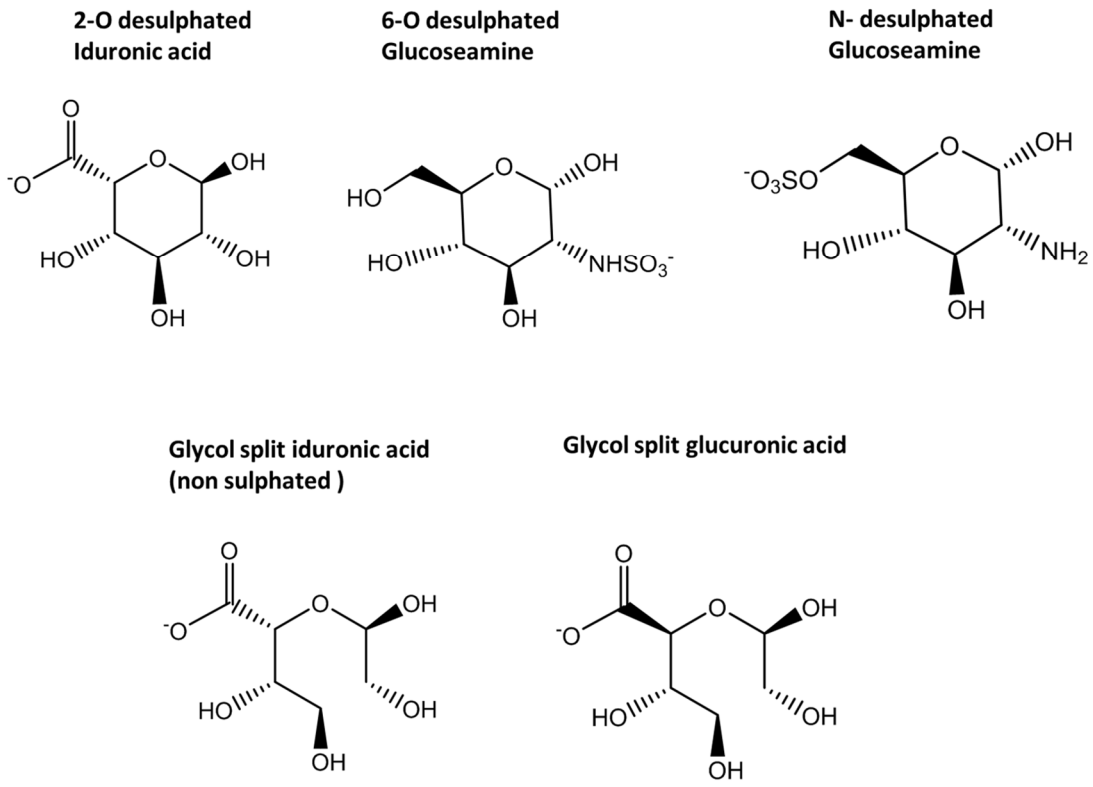


Figure 3.1 Chemical structure of heparin monomer modifications carried out to produce different modified heparin derivatives; namely 2-O, 6-O desulphation, N-desulphation, Glycol splitting of non-sulphated iduronic acid or glucuronic acid.

Irimura *et al* found out that heparin derivatives had different inhibitory effects against heparanase, where the desulphated form of heparin (complete desulphation of both N-SO_3 and O-SO_3 together) had completely lost its heparanase inhibitory activity. This indicates the importance of the sulphate group in heparanase inhibition; however, other modified heparins retained some inhibitory effect but to a lesser extent than intact heparin. For example, reduction of carboxylate groups of the iduronic acid residues gave rise to reduction of heparanase inhibitory effect of heparin, but not complete ablation of activity, indicating that this group has a role in heparanase inhibition although it is not essential for complete inhibition. In experimental metastatic lung colonisation, apart from the desulphated from, all heparin forms showed a dramatic decrease in the number of metastatic colonies after mice had been injected with metastatic B16BL6 melanoma cells. However, intact heparin had the highest effect, due to its ability to interact with other metastatic mechanisms, such as

inhibition of platelet aggregation, that usually forms protective micro emboli around the metastatic cells.[225]

It has also been reported that heparin was able to decrease heparanase activity using a series of modified heparin derivatives. Heparin needs at least 2-O sulphate group (iduronic acid residues) or 6-O sulphate group (glucosamine residues) to exert its inhibitory effect on heparanase, while heparin modified by N-desulphation and N-acetylation (50% N-acetylation) was unable to retain its inhibitory effect. Varying the configuration of iduronic acid during desulphation to glucuronic acid also reduced the heparanase inhibitory effect of heparin; additionally, glycol splitting of desulphated iduronic acid residue (at 2, 3 carbon bond), had a greater inhibitory effect against heparanase than heparin. Glycol split heparin derivatives were not degraded by the enzymatic cleavage of heparanase compared to that of heparin or N-acetyl heparin, again glycol split heparin could retain its heparanase inhibitory effect even in the presence of N-acetylation.[226]

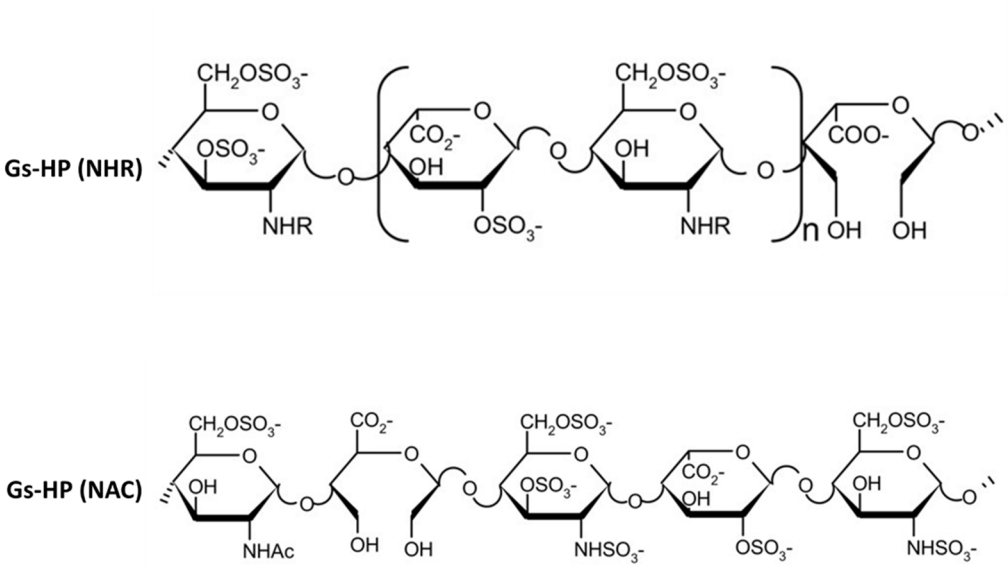


Figure 3.2 Chemical structure of glycol split heparin derivatives prepared by sodium periodate. Gs-HP (NHR): is a glycol split heparin with either N-sulphate or NH2 (R = SO_3^- or H) group in the glucose amine residue. Gs-HP (NAC): is a glycol split heparin with either N-Acetyl the glucose amine residue. Adapted from Naggi et al.[226]

Bar-Ner *et al* have made a chemical modification on heparin to produce heparin deravitives with antioagulent activity of less than 7 % relative to intact unmodified native heparin.[227] In their study, they tested the ability of chemically modified low anticoagulant heparin species to block and inhibit the activity of heparanase against extracellular matrix degradation by measuring the extent of the radiolabelled heparan sulphate cleavage by heparanase. They reported that the presence of O- or N-sulphate groups was essential for heparanase inhibitory activity. Complete removal of sulphate groups on both oxygen and nitrogen atoms of glucuronic acid and glucosamine, respectively, totally abolished the inhibitory effect of modified heparin against heparanase. Furthermore, it was found that heparan sulphate is 25 times less potent as a heparanase inhibitor than heparin, as the heparan derivative is the natural substrate for mammalian heparanase. Additionally, the inhibitory effect of modified heparin derivatives against heparanase was molecular weight dependent, and decreased as the size of the heparin chain was reduced.[227]

Lapierre *et al* have also investigated the structural features of heparin that affect the heparanase inhibitory activity of heparin. They found that N-desulphation of heparin followed by N-acetylation markedly reduced its heparanase inhibitory activity. Removal of the carboxylate group of the glucuronic acid decreased the anti-heparanase activity of heparin by 18%. Furthermore, at least one negative charge on either glucuronic acid or glucose amine residue is essential for heparanase inhibitory activity. 2,3-O-desulphated heparin has been found to be an antiangiogenic agent which was effective as native heparin after it had been tested using a chick chorioallantoic membrane (CAM) bioassay. A 2,3-O-desulphated heparin derivative dramatically reduced the tumour growth of a subcutaneous human adenocarcinoma injected in nude mice. It also enhanced the survival rate of the mice injected with B16-F10 melanoma cells.[228] Figure 3.3 demonstrates the chemical structure of 2,3-O sulphated and desulphated heparin disaccharide unit.

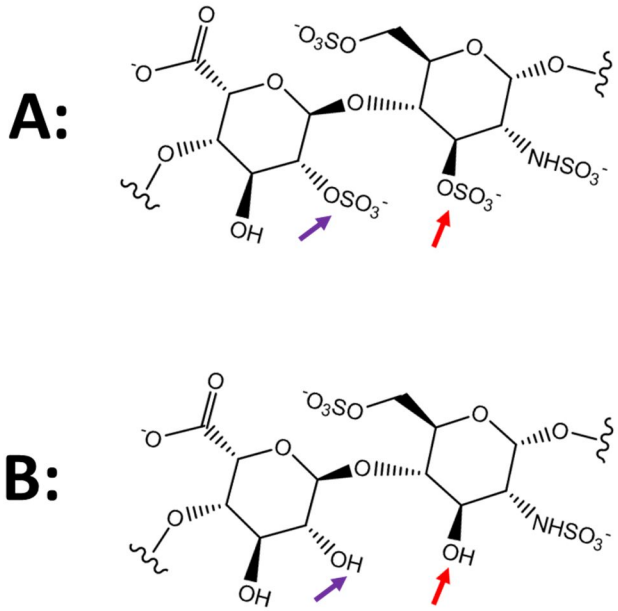


Figure 3.3 Chemical structure of 2-O (Iduronic acid), 3-O (Glucosamine) sulphated heparin repeated units (A) and 2-O (Iduronic acid), 3-O (Glucosamine) desulphated heparin repeated units (B). Purple arrows indicate the 2-O sulphation and desulphation in A and B respectively, red arrows indicate 3-O sulphation and desulphation in A and B respectively.

1.1.2 Passive targeting of cancer using NPs

NPs have been used to deliver anticancer therapeutics exploiting the enhanced permeability and retention (EPR) effect in animal models.[229-231] NPs of virus-scale sizes (50-200 nm) and with strongly hydrophilic external surfaces are not usually excreted through renal filtration which leads to build up of the NPs concentration in systemic circulation. NPs cannot normally cross the endothelial tight junctions of normal blood vessels, however they can pass through leaky and highly fenestrated blood vessels surrounding a specific solid tumour. Furthermore, the lymphatic drainage in the tumour microenvironment is relatively low. Accordingly, a high concentration of the NPs carrying anticancer therapeutics can be retained within the tumour area. In light of that, NPs with sizes ranging from 50 to 200 nm have been evaluated for delivery of anticancer therapeutics to tumours and to decrease the off target associated side effects. [55, 232-236] For instance, Lu *et al* showed that fluorescently labelled mesoporous silica

NPs were preferentially accumulated in xenografted tumour sites but not in other parts of the mice. Furthermore, camptothecin loaded mesoporous silica NPs showed significant reductions in tumour growth compared to unloaded silica NPs and an untreated controlled group. These studies demonstrated that NPs can passively deliver anticancer drug molecules to cancer site via the EPR effect.[237]

3.2 Aim

As some heparin derivatives have shown less anticoagulant potency than intact heparin, but with similar or higher heparanase inhibitory activity i.e. glycol split heparin, the aim of work described in this chapter was to synthesise two chemically modified heparins and probe their chemical and biological properties. Accordingly, glycol-spilt heparin and 2-O-desulphated heparin were prepared and then loaded onto the surface of silica NPs. The use of silica NPs as carriers for the heparin mimics was intended to provide the additional advantages of passive targeting to the tumour site compared to the conventional delivery of the polymeric derivatives as such. In this sense, the passive accumulation of the modified heparins appended to the NPs surface in the interstitial fluid of the tumour could increase the concentration of heparin mimics at tumour site. Where they can decoy and block heparanases overexpressed in the tumour microenvironment and reduce the degradation of the extracellular matrix surrounding the tumour cells before the metastatic cells start to enter the blood capillaries and invade different sites as depicted in Figure 3.4. In contrast, lower concentration of heparin derivatives would be expected if they were used as such due to the rapid renal clearance. The developed materials could be further utilised as potential therapeutics for cancer metastasis by inhibiting the progression of metastatic cancer cells.

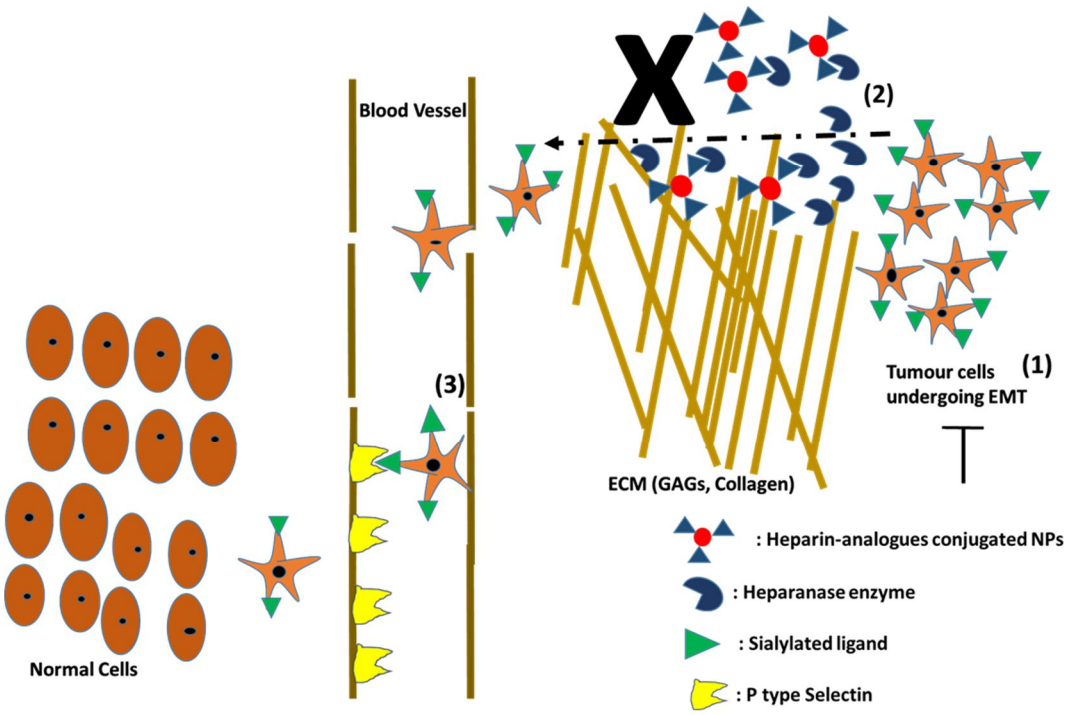


Figure 3.4 Schemtic reperesentation of metastatic stages. Heparin derivatives conjugated silica NPs are supposed to inhibit heparnase at stage 2. Conseqently reducing the degradation of the exctracellaular matrix surrounding the tumour cells and metastatic cencer progression.

3.3 Materials and methods

3.3.1 Materials and equipment

Acetic acid and sodium periodate were purchased from Fisher Scientific. Sodium acetate, Sodium borohydride and heparin, Azure A were purchased from Sigma Aldrich. Sodium hydroxide was purchased from VWR International. SnakeSkin™ Dialysis Tubing (3.5K MWCO, 22 mm) was purchased from ThermoFisher Scientific. Anti-Xa heparin kit was purchased from Iduron. Malvern Zetasizer Nano ZS, Buchi Rotavap R-200 , Hermle Z300 Centrifuge, SP 260PZ syringe pump, GVD3 freeze dryer, Spark microplate reader (TECAN) and Bruker NMR400 spectrometer were used.

3.3.2 Methods

3.3.2.1 NMR measurements of the prepared polymers

^{1}H NMR spectra were recorded using a Bruker DPX400 Ultrashield spectrometer at 400 MHz. All chemical shifts were reported in ppm. All samples were prepared in deuterium oxide (D_2O)

at concentration of 20 mg/mL. The following abbreviations have been used to report ^{1}H NMR spectra of the polymers: s= singlet, t= triplet, m: multiplet.

3.3.2.2 Particle size and zeta potential measurements

Particle size and zeta potential measurements of silica NPs were recorded using a Malvern Zetasizer Nano ZS. Particle size measurements were carried out using back scatter mode at 173° angle with 633 nm laser. The equilibration time for each sample was 120 seconds before the acquisition of the next sample. The count rate was set between 100-500 kcps by automatically adjusting the laser power using an attenuator. The temperature was set at 25 °C and the viscosity of the dispersant was 1.2 cP with 1.362 refractive index. All samples were prepared in 1/10 phosphate buffer saline (15 mM PBS) for size and zeta potential measurements. Data were recorded for each sample and repeated for three times of 15 runs (size) and 12 runs (zeta) for each reading.

Particle diameter of the NPs was measured using Dynamic light scattering technique. The suspended NPs undergo random movement (Brownian motion) with certain velocity that is related to the particle diameter. Particles scatter the incident light in different directions (Rayleigh scattering) and thus the intensity of the scattered light fluctuates according to the particle's velocity (Diffusion coefficient). The intensity and the rate at which the scattered light fluctuates are measured by Zetasizer Nano detector and the instrument software computes the hydrodynamic diameter of the suspended particle from the diffusion coefficient (D) using Stokes-Einstein's theory as shown in Equation 3.1:

$$d_H = kT/3\pi\eta D$$

Equation 3.1 Stokes-Einstein's equation

Where, d_H is the hydrodynamic diameter of the particle (m), k is Boltzmann constant (kg·m^2/s^2·K or J/s^2), T is the absolute temperature (K), η is the solvent viscosity (kg/m·s) and D is the diffusion coefficient (m^2/s).

Zeta potential of the NPs was measured by electrophoretic light scattering (ELS) technique using Mavern Zetasizer Nano ZS. When an electric field is applied on the charged NPs in suspension, they move in a defined direction and velocity (electrophoretic mobility) that is proportional to the particle's charge. While the particles are moving, the incident light is scattered at certain angle and thus the speed of the particles is measured from the frequency shift. This signal is utilised by the instrument to calculate the electrophoretic mobility (UE) and eventually compute the zeta potential value of the suspended particles using Henry's equation as shown in Equation 3.2. The Smoluchowski approximation to Henry's function ($f(ka)$ = 1.5) was applied for aqueous medium.

$$U_E = 2\varepsilon\zeta f(ka)/3\eta$$

Equation 3.2 Henry's equation

Where U_E is the electrophoretic mobility (µm·cm/V·s), ε is the dielectric constant of the medium (kg·m·s^{-2}·V^{-2}), ζ is the zeta potential (V), η is the solvent viscosity (kg/m·s) and $f(ka)$ is Henry's function.

1.1.2.1 Heparin characterisation

Heparin (from porcine intestinal mucosa) was purchased from Sigma Aldrich. However as a biological product it was necessary to confirm identity and purity by ^{1}H-NMR. Characterisation data shown below were according to those reported for heparin polysaccharide.[238-239]

^{1}H NMR (400 MHz, D2O): δ(ppm) = 1.15-1.1 (t, GlcNS6S, –CH2), 1.97 (s, GlcNAc6S, -CO-CH3, α to carbonyl), 3.22-3.2 (m, GlcNS6S H2), 3.41-3.29 (m, GlcA H2, H3), 3.63-3.58 (m, GlcNS6S H3), 3.77-3.67 (m, GlcNS6S H4), 3.89-3.87 (m, GlcNS6S H5), 3.97-3.92 (m, IdoA2S H4), 4.037 (s, IdoA2S H3), 4.21-4.13(m, GlcNS6S H6), 4.27 (s, IdoA2S H2), 4.46-4.33 (m, GlcA H1),4.94-4.86 (m, IdoA2S H5), 5.23-5.10 (m, IdoA2S H1), 5.51-5.34 (m, GlcNS6S3S H1).

1.1.2.2 Synthesis of glycol split heparin

Glycol split heparin was prepared using periodate oxidation and borohydride reduction. Heparin (100 mg, 5.88 µmol) was dissolved in 5 mL sodium acetate buffer at pH 5. Then, sodium periodate (63 mg, 294 µmol) (IO_4) was added to the above solution and stirred for 24 hours at 4 ^{0}C in the dark. 1 mL ethylene glycol was added to the above solution to quench any excess unreacted periodate. The solution was then dialysed against distilled water using 3.5 kDa molecular cut-off membrane for 24 hours with water change every 6 hours. Then the pH of the solution was adjusted to 7.0 before adding sodium borohydride to avoid the hydrolysis of sodium borohydride in the acidic medium. After that (11 mg, 294 µmol) of sodium borohydride ($NaBH_4$) were added to the solution and left under stirring in the presence of ice for 5 minutes then left under stirring for 3 hours. Aliquots of 1M HCl were added to bring the pH of the solution to 4 in order to destroy any excess borohydride, and the reaction was then stirred for 15 minutes. Aliquots of 1M NaOH were then added to neutralise the solution. Finally, the solution was dialysed against distilled water for 48 hours, and freeze dried to produce glycol split heparin (77mg, 77% yield). ^{1}H NMR (400 MHz, D2O): δ(ppm) = 1.97 (s, GlcNAc6S, -CO-CH3, α to carbonyl), 3.23-3.20 (m, GlcNS6S H2), 3.63-3.59 (m, GlcNS6S H3), 3.79-3.69 (m, GlcNS6S H4), 3.90-3.88 (m, GlcNS6S H5), 3.98-3.94 (m, IdoA2S H4), 4.04 (s, IdoA2S H3), 4.21-4.14 (m, GlcNS6S H6), 4.28 (s, IdoA2S H2), 4.45-4.33 (m, GlcA H1), 5.05-4.85 (m, IdoA2S H5), 5.25-5.12 (m, IdoA2S H1), 5.48-5.31 (m, GlcNS6S3S H1).

1.1.2.3 Synthesis of desulphated heparin

Desulphated heparin was prepared using a sodium hydroxide alkalinisation method. Sodium borohydride (50 mg, 1.32 mmol) was added to 10 mL of 0.5 N sodium hydroxide solution to prevent heparin depolymerisation in alkaline medium. Then (100 mg, 5.88 µmol) of heparin were dissolved in the above solution to produce 2% (w/v) of heparin solution. The pH of the solution was decreased from ~ 14 to 13 using 1N HCl and left to stir for 30 minutes. The solution was then lyophilized for 24 hours to produce a yellow solid. This material was then dissolved in deionised water and the pH adjusted to 8 using 1N HCl to produce a sodium salt.

The solution was dialysed against distilled water using 3.5 kDa cutoff dialysis membrane for 24 hours and lyophilised to produce desulphated heparin (63 mg, 63% yield). ^{1}H NMR (400 MHz, D_2O): δ(ppm) = 1.98 (s, GlcNAc6S, -CO-CH_3, α to carbonyl), 3.18-3.16 (m, GlcNS6S H2), 3.37-3.28 (m, GlcA H2, H3), 3.70-3.58 (m, GlcNS6S H3), 3.74-3.71 (m, GlcNS6S H4), 3.86-3.84 (m, GlcNS6S H5), 3.98-3.94 (m, IdoA2S H4), 4.06 (s, IdoA2S H3), 4.10-4.03(m, GlcNS6S H6), 4.12 (s, IdoA2S H2), 4.41-4.26 (m, GlcA H1), 4.90-4.87 (m, IdoA2S H5), 5.01-4.96 (m, IdoA2S H1), 5.53-5.26 (m, GlcNS6S3S H1).

1.1.2.4 Anticoagulant activity of glycol split heparin

Different concentrations of either heparin, glycol split heparin (62.5, 125, 250 and 500 ng/mL) or glycol split heparin conjugated NPs (12.5, 25, 60, 75 and 100 µg/mL) were dissolved in Tris-EDTA buffer with pH 8.4 in order. An aliquot (200 µL) of the prepared samples was placed in a 48 well plate and incubated for 2 minutes at 37°C. Then 200 µL of the antithrombin solution (0.5 IU/mL) was added and mixed for 2 minutes at 37°C. Subsequently, 200 µL of the Factor Xa solution (2.5 µg/mL) was added and mixed for 2 minutes at 37°C. 200 µL of the chromogenic factor Xa substrate solution (0.625 mg/mL) was then added and mixed for 2 minutes at 37°C. Finally, 200 µL of 20% (v/v) acetic acid was added to stop the reaction and the plate was set aside at room temperature. The absorbance of the samples was measured at 405 nm using TECAN plate reader.

1.1.2.5 Metachromatic assay of Desulphated heparin

Equal volumes of azure A stock solution (0.025mg/mL, 8.56 µmol/mL) and 20 µg/mL of either O-desulphated heparin or heparin polymer were mixed and place in a 24 well plate. Then, the absorption spectra of the resultant mixtures were determined using plate reader. For visual monitoring of azure A colour change, different concentrations of either O-desulphated heparin or heparin (2.5, 5, 10 and 20 µg/mL) were prepared and mixed in equal volumes of (0.025 mg/mL, 8.56 µmol/mL) azure A in 24 well plate. Images of the colour change were taken by camera.

1.1.2.6 Synthesis of glycol split conjugated and desulphated conjugated NPs

Either (23.5 mg, 1.47 µmol) of glycol split heparin or (22 mg, 1.47 µmol) desulphated heparin was dissolved in 2.5 mL MES with pH 5.6. Then EDC (2.5 mg, 13 µmol) was added to each solution and left to stir for half an hour. After that, amine functionalised NPs (20 mg) prepared as described in chapter 1 were suspended in 20 mL MES (pH 5.6) and added to the above solutions and left to stir for 24 hours. Finally the resultant suspensions were centrifuged at 3000 x g for 20 minutes and washed with 20 mL water for four times. The obtained NPs were freeze dried for 24 hours.

1.1.2.7 Characterisation of glycol split conjugated and desulphated conjugated NPs

To measure the size, 4 mg of the either desulphated heparin or glycol split heparin conjugated silica NPs were suspended in 4 mL deionised water to produce 1 mg/mL stock suspension. Which was further diluted in 15 mM PBS to produce a concentration of 0.05 mg/mL suspension.

To measure the zeta potential of the NPs, 5 mg of either desulphated heparin or glycol split heparin conjugated silica NPs were suspended in 5 mL PBS (mM) in order to obtain 1 mg/mL suspensions.

3.4 Results and discussion

3.4.1 Synthesis of glycol split heparin

Glycol split heparin was synthesised using the sequential periodate oxidation-sodium borohydride reduction method. This reaction involves two steps, the first one is periodate oxidation where periodate reacts with heparin chain at C2,C3 of the glucuronic acid or non-sulphated iduronic acid residues and forms an unstable intermediate followed by formation of two aldehyde groups at C2 and C3 of the chain. The second step involves the reduction of aldehyde groups at C2,C3 using a reducing agent; sodium borohydride in order to produce hydroxyl groups at the same positions within the heparin chain as shown in Figure 3.5. Glycol splitting of heparin increases the chain flexibility and extension due to the ring opening of the glucuronic acid residues. Subsequently, it introduces conformational flexibility to the polysaccharide chain that can alter the interactions at the heparanase active site.[240-242]

Figure 3.6 illustrates the structure of heparin tetrasaccharide unit and its interaction with the heparanase active site.

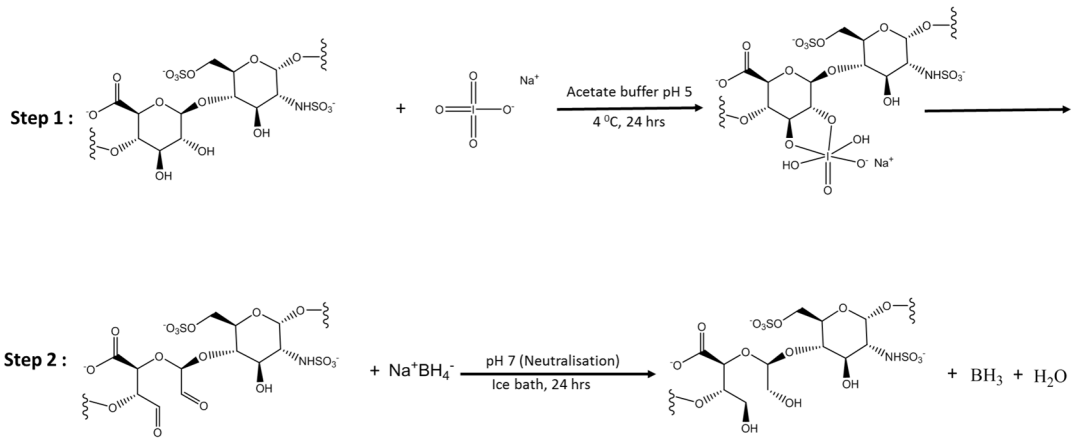


Figure 3.5 Schematic illustration of glycol split heparin synthesis. Step 1 involves periodate oxidation of 2,3 oxygen atoms to produce heparin periodate intermdiate. Step 2 involves the reduction of aldhyde groups formed at C2 and C3 of glucuronic acid residues using sodium borohydride as a reducing agent to produce hydroxyl groups at the same postions.

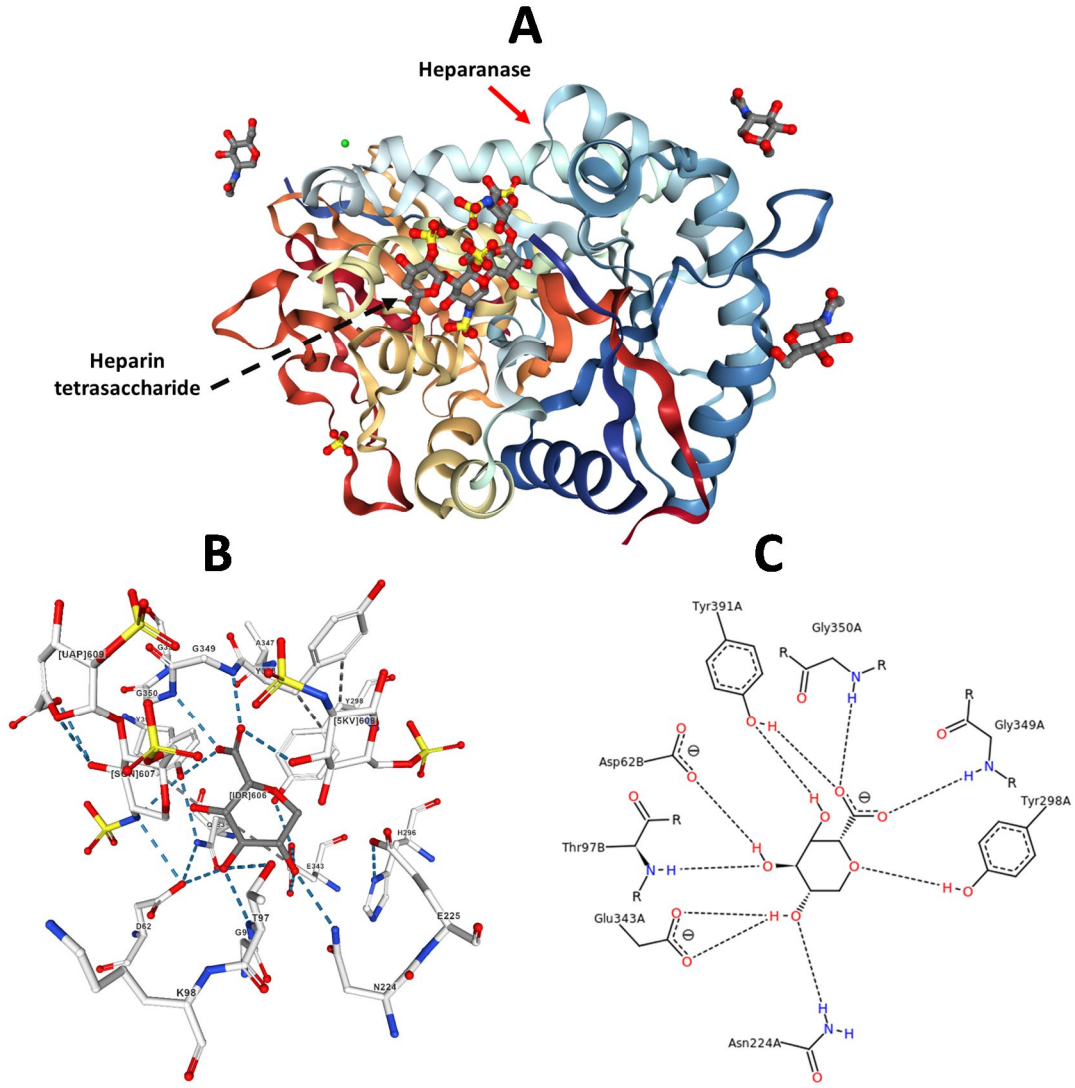


*Figure 3.6 Illustration showing **A:** 3D chemical structure of heparin tetrasaccharide ligand bound to the active site of heparanase (Sticks represent covalent bonds, balls represent atoms. grey= carbon, red= oxygen, blue= nitrogen, yellow= sulphur). **B:** 3D view of the ligand (Iduronic acid)-active site interaction (Grey dashed lines represent hydrophobic interaction, blue dashed lines represent hydrogen bonds, IDR606: Iduronic acid ligand. The following abbreviations represent the amino acids of heparanase at active site; N224: Asparagine. E225, E343: Glutamic acid. T97: Threonine. D62: Aspartic acid. A347: Alanine. K98: Lysine. G49, G350, G349, G96: Glycine. Y348, Y298, Y391: Tyrosine. **C:** Simplified 2D view of the ligand–active site interaction (Black dashed lines indicate hydrogen bonds, Asn: Asparagine, Glu: Glutamic acid, Thr: Threonine, Asp: Aspartic acid, Tyr: Tyrosine, Gly: Glycine), Experimental data was obtained by X-ray diffraction method. Figure was adapted from Wu et al.*[243]

3.4.2 Polymer characterisation using ^{1}H-NMR

Proton NMR was conducted in order to confirm the structure of the produced glycol split heparin. Periodate cleavage occurs specifically at vicinal diols within the heparin backbone. Consequently the 2, 3 carbon bond of non-sulphated iduronic or glucuronic acid residue is the only susceptible bond for cleavage. Figure 3.7 indicates that some characteristic peaks of

glucuronic acid protons at C2, C3 (GlcA H2, H3) have disappeared compared to unmodified native heparin though it is not a complete disappearance of these peaks. This is attributed to C2-C3 bond breakage that has changed the surrounding environment and neighbouring functional groups of C2, C3 protons.

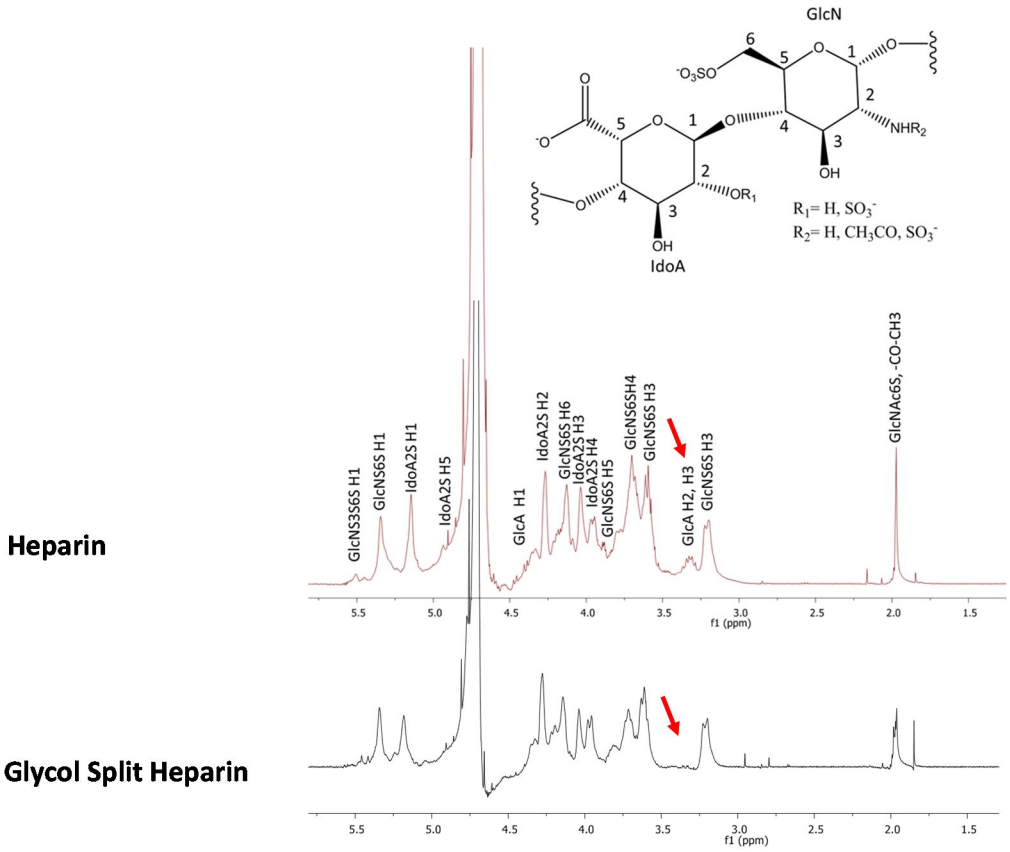


Figure 3.7 H^1 NMR spectra of native heparin and glycol split heparin. Red arows show the major peak of glucuronic acid protons at C2 and C3 of the ring, where some have disapeared in glycol split heparin. Heparin chemical shift (400 MHz, D2O); δ(ppm) = 1.15-1.1 (t, GlcNS6S, –CH2), 1.97 (s, GlcNAc6S, -CO-CH3, α to carbonyl), 3.22-3.2 (m, GlcNS6S H2), 3.41-3.29 (m, GlcA H2, H3), 3.63-3.58 (m, GlcNS6S H3), 3.77-3.67 (m, GlcNS6S H4), 3.89-3.87 (m, GlcNS6S H5), 3.97-3.92 (m, IdoA2S H4), 4.037 (s, IdoA2S H3), 4.21-4.13(m, GlcNS6S H6), 4.27 (s, IdoA2S H2), 4.46-4.33 (m, GlcA H1),4.94-4.86 (m, IdoA2S H5), 5.23-5.10 (m, IdoA2S H1), 5.51-5.34 (m, GlcNS6S3S H1). Glycol split heparin chemical shift; δ(ppm) = 1.97 (s, GlcNAc6S, -CO-CH3, α to carbonyl), 3.23-3.20 (m, GlcNS6S H2), 3.63-3.59 (m, GlcNS6S H3), 3.79-3.69 (m, GlcNS6S H4), 3.90-3.88 (m, GlcNS6S H5), 3.98-3.94 (m, IdoA2S H4), 4.04 (s, IdoA2S H3), 4.21-4.14 (m, GlcNS6S H6), 4.28 (s, IdoA2S H2), 4.45-4.33 (m, GlcA H1), 5.05-4.85 (m, IdoA2S H5), 5.25-5.12 (m, IdoA2S H1), 5.48-5.31 (m, GlcNS6S3S H1).

3.4.3 Anticoagulant assay

In order to monitor the anticoagulant properties of glycol split heparin, an anticoagulant assay based on anti Xa and antithrombin interaction with glycol split heparin was performed as described in chapter 2. Figure 3.8 shows unmodified native heparin (HP) caused more

pronounced reduction in the optical density of the produced pNA compared to glycol split heparin (GS-HP) (P value <0.0001). This means that glycol split heparin had less anticoagulant properties compared to native heparin, thus the bleeding side effects associated with heparin anticoagulant properties will be reduced in glycol split heparin.

Furthermore, the low anticoagulant effect of glycol split heparin is attributed to the conformational changes in heparin backbone after bond breakage. Thus, disruption of pentasaccharide sequence of heparin that specifically binds to antithrombin (ATIII) active site as depicted in Figure 3.9.[239]

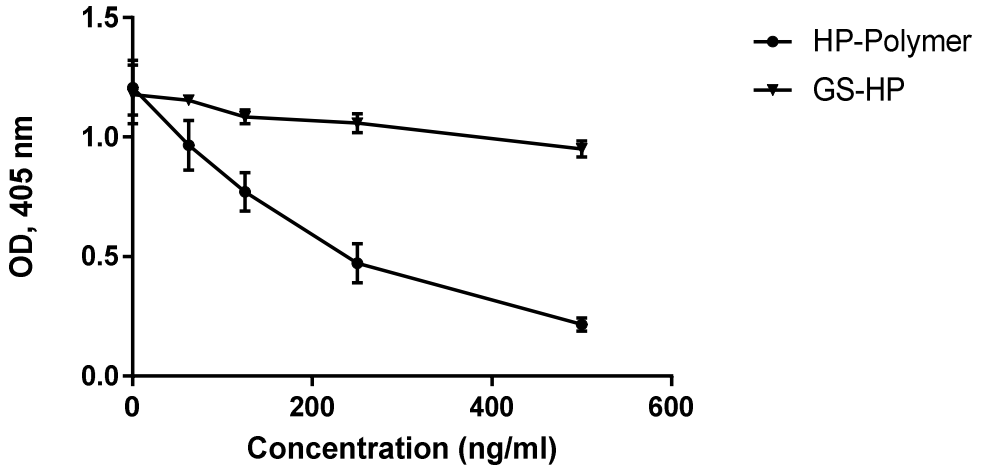


Figure 3.8 Anticoagulant activity of intact heparin polymer (HP) and glycol split heparin (GS-HP) represented by the optical density of the released pNA that is inversely proportional to anticoagulant activity of heparin and its derivatives. Data was analysed using two way ANOVA test (grouped analyses), Error bars indicate SD (n = 3). P value < 0.0001.

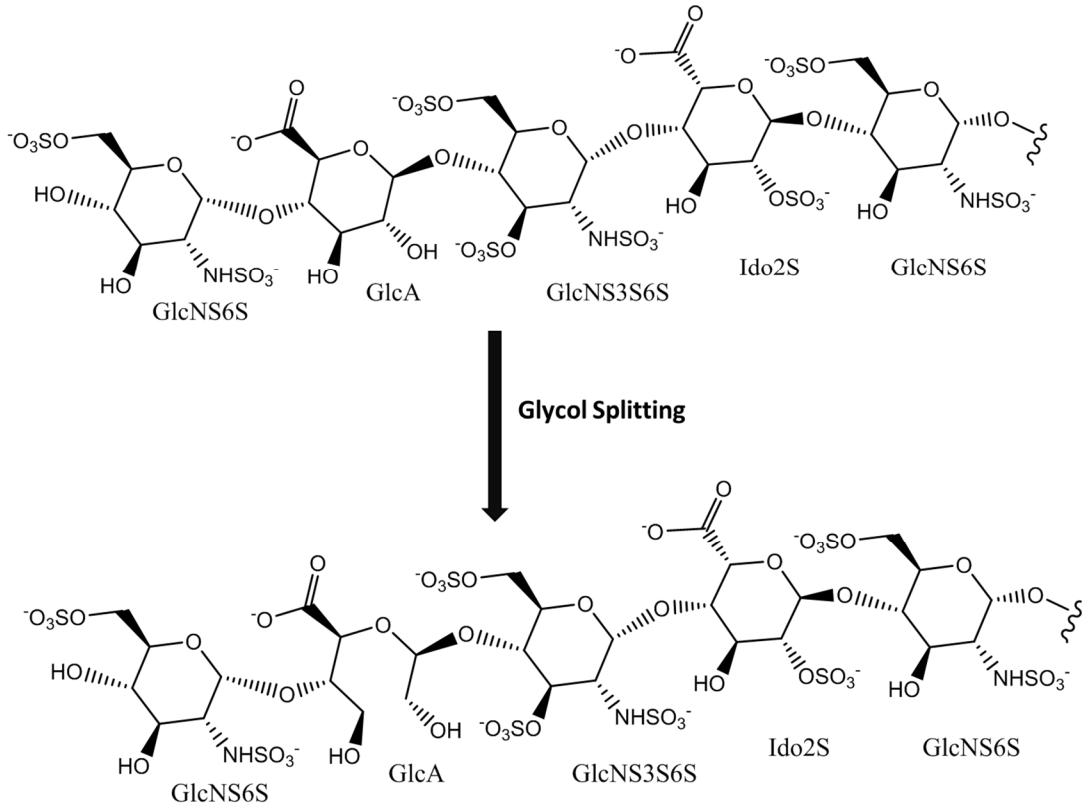


Figure 3.9 Schematic reperesentation of glycol splitting of heparin pentasahraide sequence; consisiting of the antithrombin binding residues showing that splitting of glucuronic acid residue might be responsile for the disruption of the binding ability of this sequence with its antithrombin binding site.

3.4.4 Synthesis of glycol split heparin conjugated NPs

Glycol split heparin was grafted onto the surface of previously prepared amine functionalised NPs in chapter 1. N-(3-Dimethylaminopropyl)-N'-ethylcarbodiimide hydrochloride (EDC) was used to activate glycol split heparin carboxylate groups followed by coupling of these groups to amine groups on the surface of amine functionalised NPs to form amide bonds as illustrated in Figure 3.10.

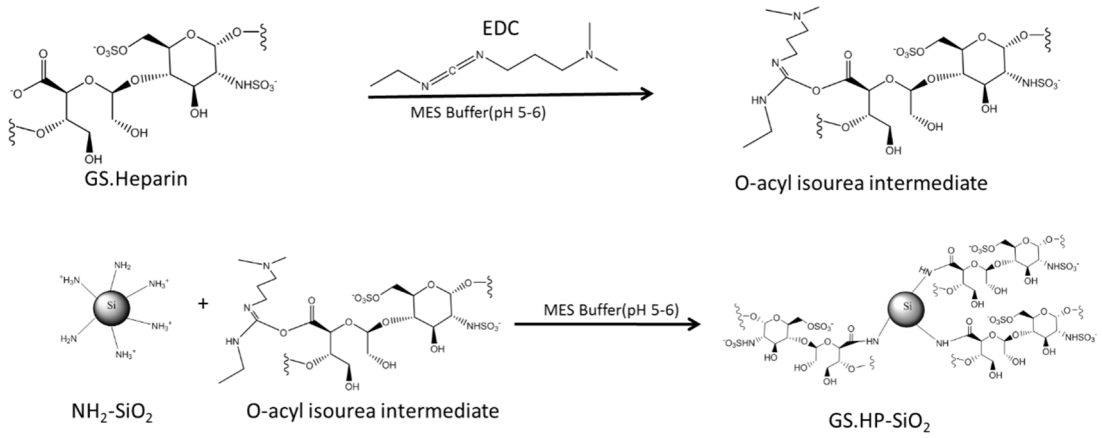


Figure 3.10 Schematic representation of synthesis of glycol heparin conjugated silica NPs by coupling of amine functionalised silica NPs (NH_2-SiO_2) to glycol split heparin using EDC to produce heparin conjugated NPs (GS.HP-SiO_2).

3.4.5 Characterisation of glycol split heparin conjugated NPs

The prepared glycol split heparin conjugated NPs were characterised using Dynamic Light Scattering (DLS). Figure 3.11 A shows that the average particles size was around 200 nm which is slightly higher than the average size of the precursor amine functionalised NPs (around 160 nm) which could be ascribed to the formation of hydrophilic shell around the particles' surface. The polydispersity index of the NPs was measured as demonstrated in Figure 3.11 B and the values were below the acceptable range (less than 0.2) for the NPs commonly used to deliver therapeutics to tumour as described in section 2.4.3.

Furthermore, the zeta potential of the NPs was also measured as demonstrated in Figure 3.11 C. The zeta potential value of amine functionalised changed from positive to negative after grafting of glycol split heparin onto the surface of amine functionalised NPs, which is similar to the surface charge of heparin conjugated NPs. This indicates successful and complete conjugation of glycol split heparin to the particles' surface.

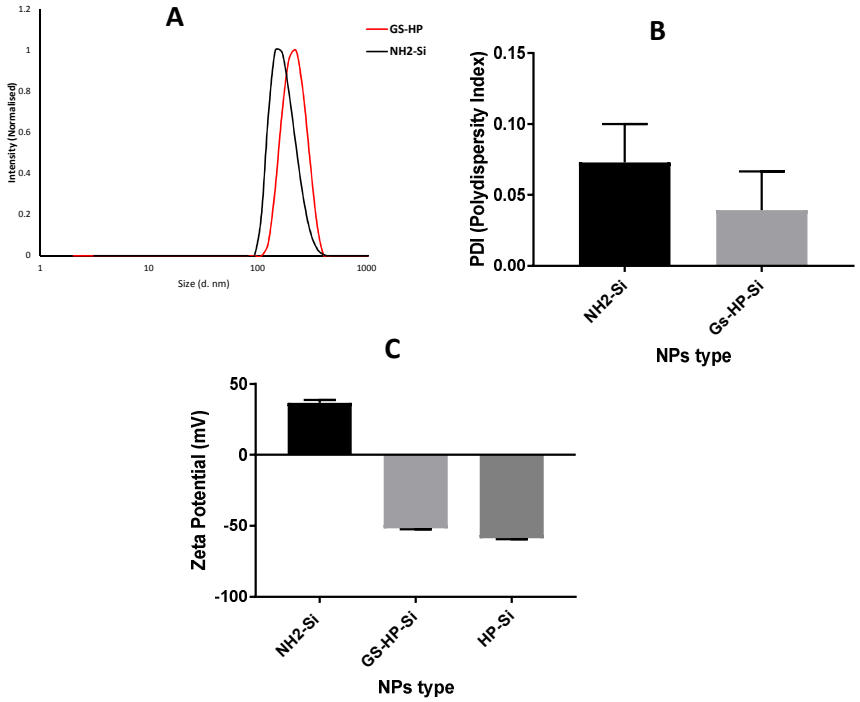


Figure 3.11 Characterisation of glycol split heparin conjugated NPs. ***A:*** *Particle diemeter of glycol split heparin conjugated NPs (GS-HP) compared to amine functionalised NPs (NH_2-Si).* ***B:*** *Polydispersity index (PDI) of the NPs shown in A.* ***C:*** *Zeta potential values of glycol split heparin conjugated NPs (GS-HP) and heparin conjugated NPs (HP-Si) compared to amine functionalised NPs (NH_2-Si) showing surface charge conversion.*

3.4.6 Anticoagulant properties of glycol split heparin conjugated NPs

In order to further identify the presence of glycol split heparin on the surface of the NPs, an anticoagulant assay of glycol split conjugated NPs was conducted as described in chapter 2. Figure 3.12 shows that heparin conjugated NPs significantly reduced the optical density of the released pNA compared to glycol split heparin conjugated NPs. This indicates successful conjugation of glycol split heparin to the particles surfaces with markedly lower anticoagulant properties than unmodified heparin attached to NPs surfaces.

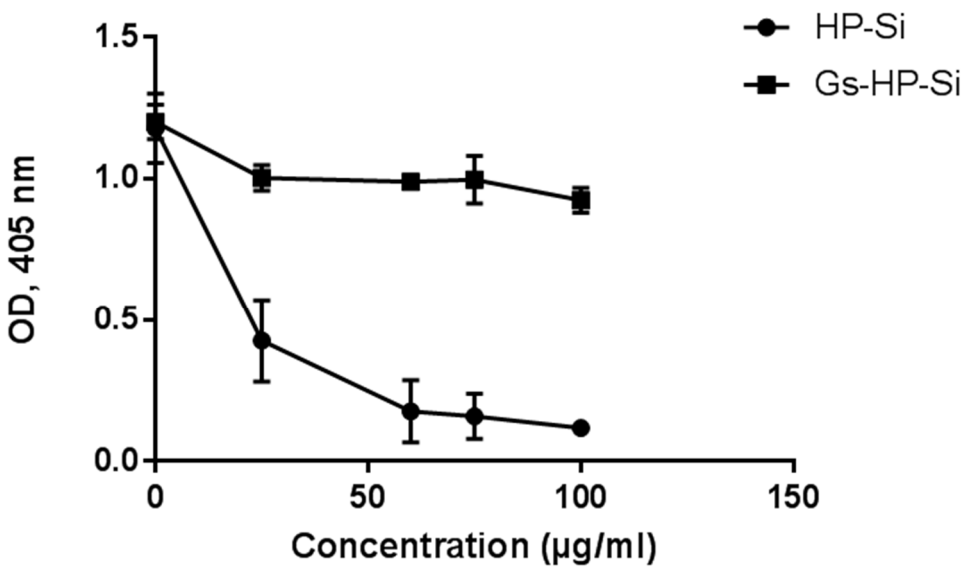


Figure 3.12 Optical density of the released pNA measured at 405 nm representing the anticoagulant activity of heparin conjugated NPs (HP-Si) and glycol split NPs (GS.HP-Si). Data was analysed using two way ANOVA test (grouped analyses), Error bars indicate SD (n = 3). P value <0.0001.

3.4.7 Synthesis of desulphated heparin polymer

Desulphated heparin was prepared using alkalinisation with sodium hydroxide ions followed by lyophilisation of heparin. Selective desulphation of heparin occurs at C2 at certain pH value (pH 13) to produce 2-O-desulphated heparin.[244-246] The hydroxide ions form an epoxide intermediate at C2-C3 of the iduronic acid residue which is the first step of the reaction. In the second step the epoxy intermediate is hydrolysed during the lyophilisation process that speeds up the hydrolysis reaction. After hydrolysis of the epoxide, hydroxyl groups are formed at C2 and C3 resulting in removal of the sulphate group at C2 as illustrated in Figure 3.13.

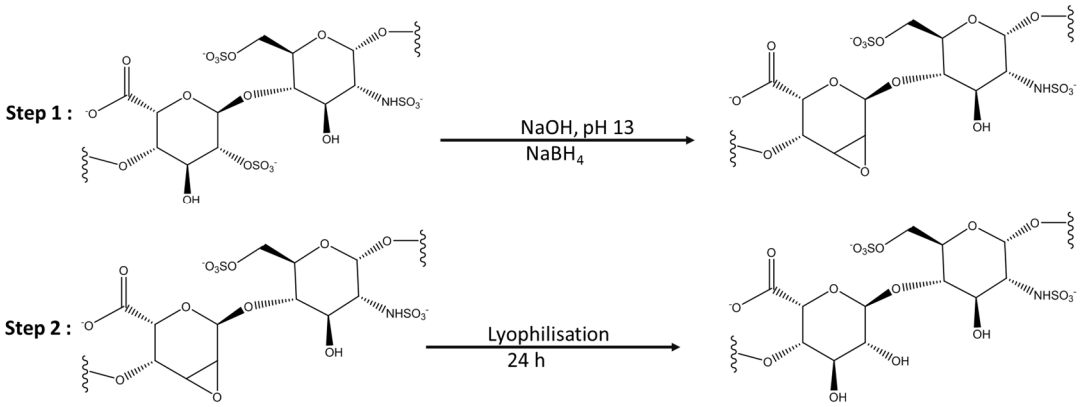


Figure 3.13 Schematic of O-desulphated heparin synthesis. Step 1 reperesents alkalinasation of heparin in order to form C2-C3 epoxy intermediate. Step 2 reperesents the lyophylisation of the prodeced epoxy intermediate resulting in hydrolysis of epoxy group and formation of hydroxyl groups at the same positions to produce 2-O desulphated heparin.

3.4.8 H^1 NMR spectrum of desulphated heparin

H^1NMR was performed to confirm the structure of desulphated heparin after removal of sulphate groups at C2. Figure 3.14 demonstrates that there was a decrease in the chemical shift of the iduronic acid anomeric carbon proton (IdoA2S H1). This can be explained by the desulphation of iduronic acid at carbon 2 that led to nucleus shielding of the anomeric carbon proton, by the adjacent electrons after the removal of the electron withdrawing sulphate group process, resulting in the observed upfield chemical shift.

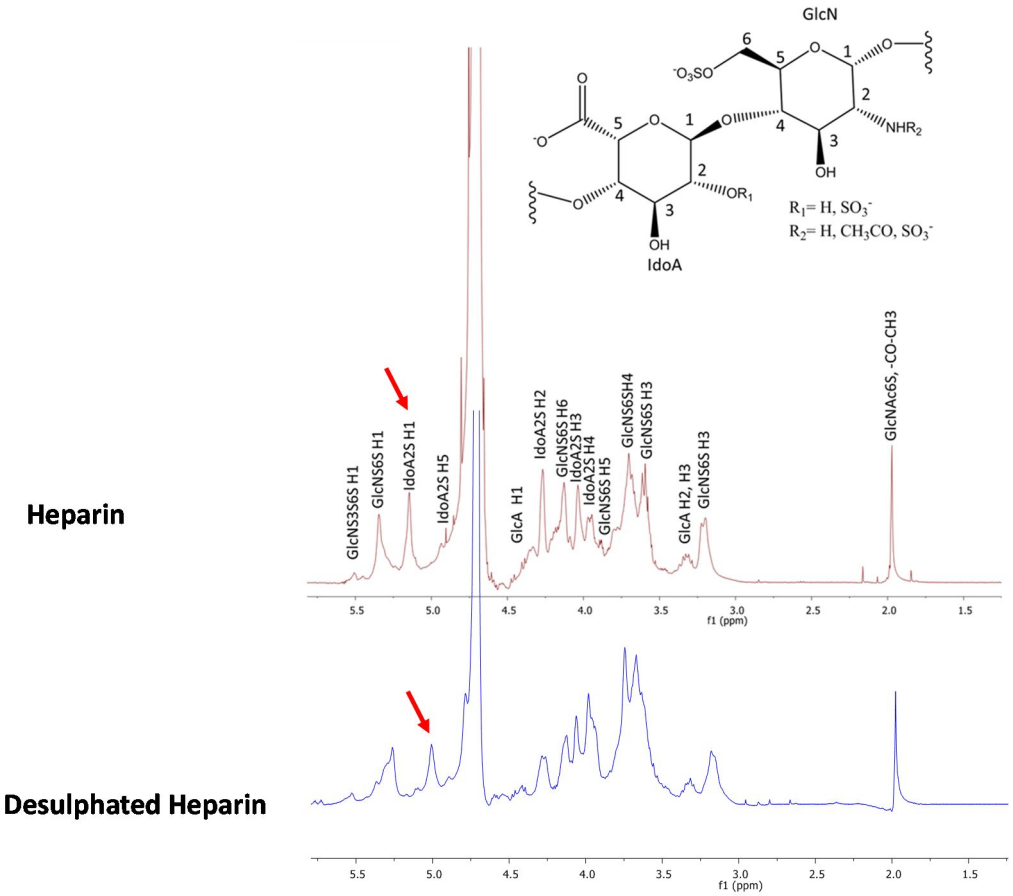


Figure 3.14 H[1] NMR spectra of native heparin and desulphated heparin Red arrows show the peak of iduronic acid proton at C1 of the ring where a dramatic shift occurred in desulphated heparin compared to the same peak in intact heparin. Heparin chemical shift (400 MHz, D2O); δ(ppm) = 1.15-1.1 (t, GlcNS6S, –CH2), 1.97 (s, GlcNAc6S, -CO-CH3, α to carbonyl), 3.22-3.2 (m, GlcNS6S H2), 3.41-3.29 (m, GlcA H2, H3), 3.63-3.58 (m, GlcNS6S H3), 3.77-3.67 (m, GlcNS6S H4), 3.89-3.87 (m, GlcNS6S H5), 3.97-3.92 (m, IdoA2S H4), 4.037 (s, IdoA2S H3), 4.21-4.13(m, GlcNS6S H6), 4.27 (s, IdoA2S H2), 4.46-4.33 (m, GlcA H1),4.94-4.86 (m, IdoA2S H5), 5.23-5.10 (m, IdoA2S H1), 5.51-5.34 (m, GlcNS6S3S H1). δ(ppm) = 1.98 (s, GlcNAc6S, -CO-CH3, α to carbonyl), 3.18-3.16 (m, GlcNS6S H2), 3.37-3.28 (m, GlcA H2, H3), 3.70-3.58 (m, GlcNS6S H3), 3.74-3.71 (m, GlcNS6S H4), 3.86-3.84 (m, GlcNS6S H5), 3.98-3.94 (m, IdoA2S H4), 4.06 (s, IdoA2S H3), 4.10-4.03(m, GlcNS6S H6), 4.12 (s, IdoA2S H2), 4.41-4.26 (m, GlcA H1), 4.90-4.87 (m, IdoA2S H5), 5.01-4.96 (m, IdoA2S H1), 5.53-5.26 (m, GlcNS6S3S H1).

3.4.9 Determination of heparin desulphation using Azure A assay

In order to confirm the successful desulphation of heparin, the azure A assay was used. This assay, is based on colour changes arising from the electrostatic interaction between the negatively charged heparin and the positively charged cationic dye; azure A.

Desulphated heparin showed less hypsochromic (blue) shift of azure maximum wavelength compared to unmodified native heparin as shown in Figure 3.15A. Additionally, a quantitative measurement of the extent of azure A λ_{max} blue shift occurring from the differential binding of desulphated heparin and unmodified heparin was conducted by measuring the change in

azure A λ_{max} made before and after addition of each polymer to azure A. The data showed that desulphated heparin had a significantly lower effect on azure A absorption λ_{max} compared to the effect of heparin as demonstrated in Figure 3.15 B. This is explained by the weak electrostatic interaction between the cationic azure A and the anionic desulphated heparin that have fewer sulphate groups and less negative charge than unmodified heparin. Moreover, these results were reinforced by the visual monitoring of azure A colour change upon addition of desulphated and unmodified heparin. It was obvious that there was a more pronounced colour change of azure A from blue to purple with increasing concentration of the added unmodified heparin compared to the colour change after addition of different concentrations of desulphated heparin as depicted in Figure 3.16.

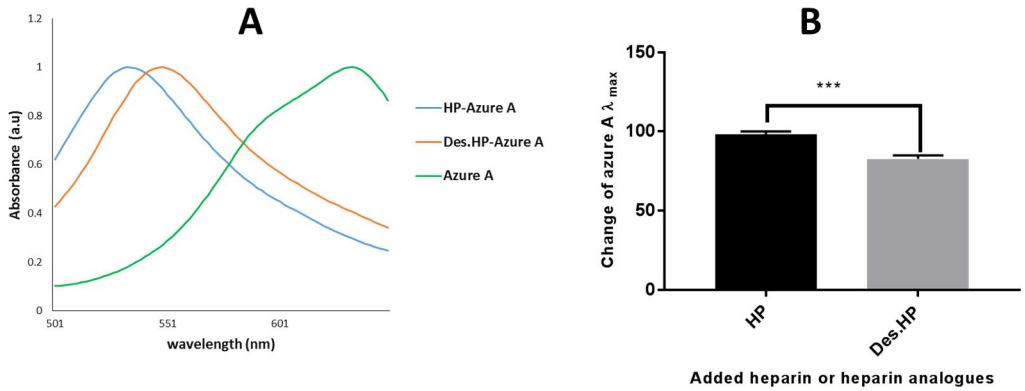


Figure 3.15 Effect of O-desulpated heparin polymer on maximum absorption wavelength of azure A dye. ***A:*** *UV-visible absorption wavelength spectra oF azure A alone (green), after addition of O-desulpated heparin polymer (red), and after addition of intact heparin sulpate (green),.* ***B:*** *Quantitative measurements of azure A lambda max change upon addition O-desulpated heparin polymer compared to that upon addition of intact heparin polymer. Data was analysed using unpaired t test. Error bars indicate SD (n = 3). *** is P ≤ 0.001.*

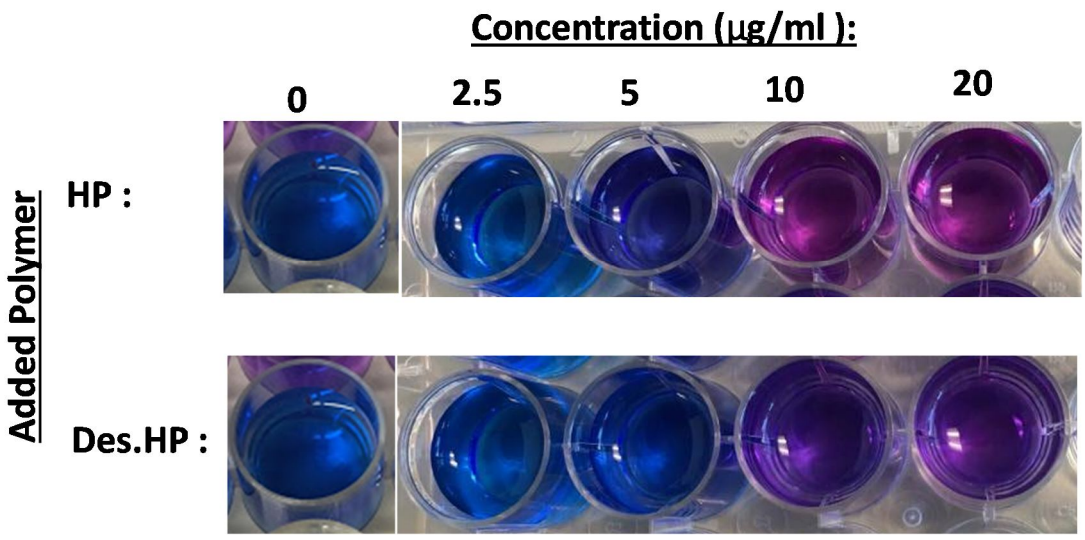


Figure 3.16 Visual monitoring of the effect of O-desulphated heparin (Des.HP) and intact heparin (HP) polymers on Azure A dye colour using diferent concentrations ranging from 0 to 20 µg/mL.

3.4.10 Characterisation of desulphated heparin conjugated NPs

Particle size and zeta potential of desulphated heparin conjugated NPs were measured using Dynamic Light Scattering (DLS). Desulphated heparin conjugated NPs (Des.HP-Si) showed a particle diameter around 190 nm which is a slightly higher than particle size of the precursors amine functionalised NPs (NH_2-Si) that was around 160 nm as demonstrated in Figure 3.17 A. Furthermore, the measured PDI values for the NPs were less than 0.2 indicating particles uniformity that is acceptable for nanotherapeutics delivery as described in section 2.4.3.

Zeta potential data showed that there was a total conversion of the surface charge of amine functionalised NPs (NH_2-Si) from positive to negative after appending the desulphated heparin to the surface of the particles. This indicated successful synthesis of desulphated heparin conjugated NPs (Des.HP-Si) as shown in Figure 3.17 C. However, the zeta potentials of desulphated heparin conjugated NPs were lower than that to heparin conjugated NPs. This also suggests that the negative charge of heparin was reduced after desulphation, as a result of removal of sulphate groups at C2.

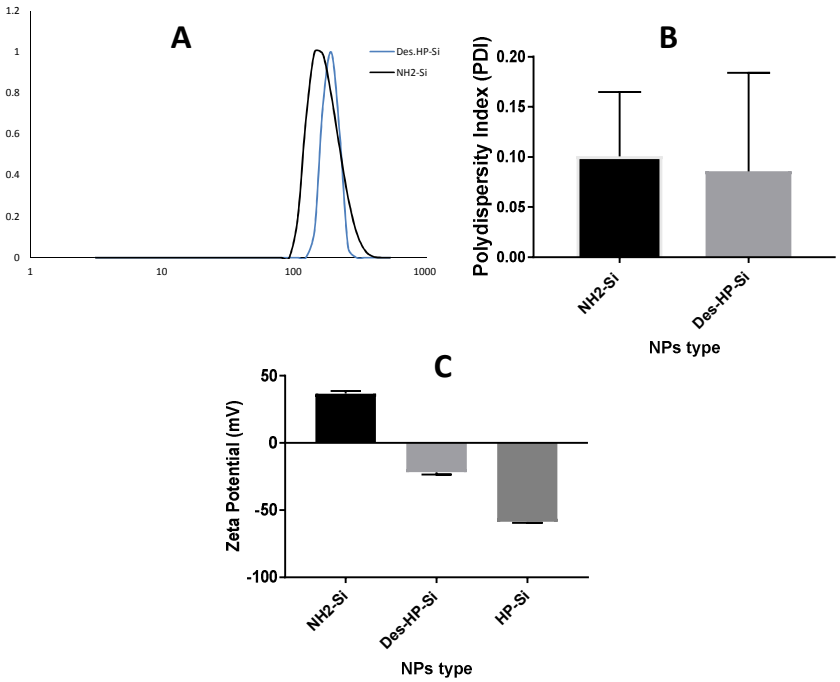


Figure 3.17 Characterisation of desulphated heparin conjugated NPs. ***A:*** *Particle diemeter of desuphated heparin conjugated NPs (Des-HP) compared to amine functionalised NPs (NH_2-Si).* ***B:*** *Polydispersity index (PDI) of the NPs shown in A.* ***C:*** *Zeta potential values of desulphated heparin conjugated NPs (Des-HP) and heparin conjugated NPs (HP-Si) compared to amine functionalised NPs (NH_2-Si) showing surface charge conversion.*

3.4.11 Synthesis of desulphated heparin conjugated NPs

Desulphated heparin was grafted onto the surface of the NPs using the EDC coupling reaction. Desulphated heparin carboxylate groups were activated by EDC to from the unstable O-acylisourea intermediate. This was followed by nucleophilic attack at the carbonyl carbon by amine groups on the surface of amine functionalised NPs as depicted by Figure 3.18.

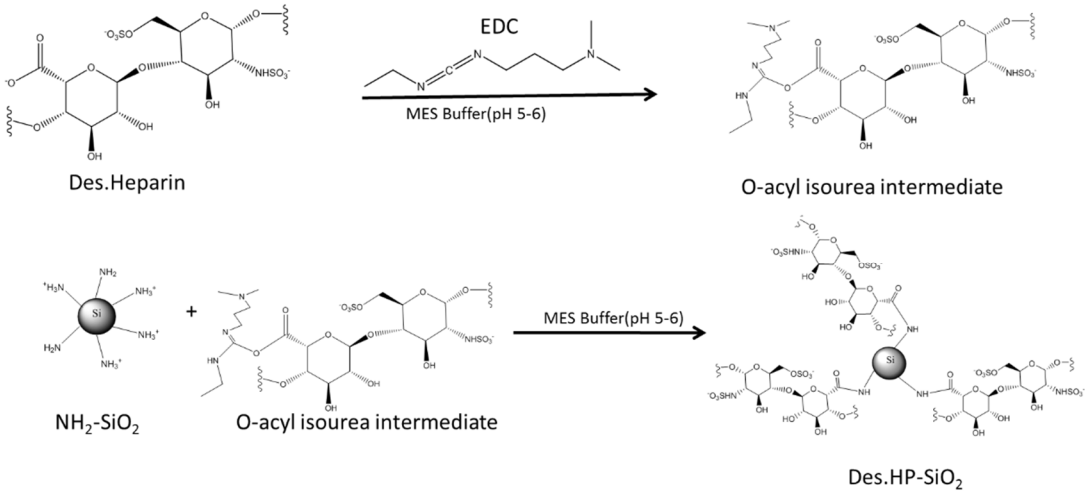


Figure 3.18 Schematic representation of synthesis of desulphated heparin conjugated silica NPs by coupling of amine functionalised silica NPs (NH_2-SiO_2) to desulphated heparin (Des.Heparin) using EDC to produce heparin conjugated NPs (Des.HP-SiO_2).

3.4.12 Identification of desulphated heparin grafted onto NPs surfaces

Desulphated heparin conjugation to the particles' surface was identified using an azure A assay. A significantly greater azure A absorption maximum blue shift was made by heparin conjugated NPs compared to desulphated heparin conjugated NPs as shown in Figure 3.19. This indicates that the interaction between the interaction between desulphated heparin on surface of the particles and azure A was markedly weaker than that between azure A and the fully sulphated heparin conjugated to the nanoparticle surfaces. This weak interaction can be attributed to the loss of heparin groups that mediate the electrostatic interaction between the cationic dye and the anionic heparin and subsequent azure A lambda max blue shift.

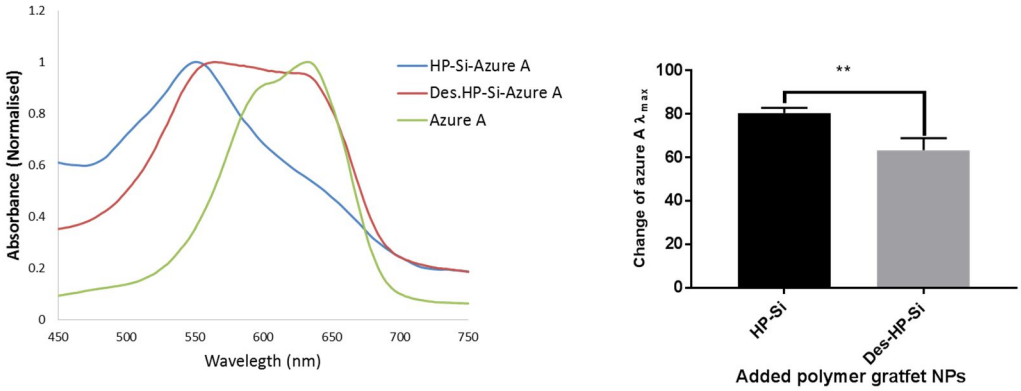


Figure 3.19 Effect of O-desulphated heparin conjugated NPs maximum absorption wavelength of azure A dye. ***A:*** *UV-visible absorption wavelength spectra of azure A alone (green), after addition of O-desulphated heparin conjugated NPs (red), and after addition of unmodified heparin conjugated NPs (blue),* ***B:*** *Quantitative measurements of azure A lambda max change upon addition O-desulphated heparin conjugated NPs (Des.HP-Si) and heparin conjugated NPs (HP-Si),. Data was analysed using unpaired t test. Error bars indicate SD (n = 3). ** is P ≤ 0.01.*

3.5 Conclusions and future work

Glycol split heparin with low anticoagulant properties was successfully synthesised using periodate oxidation followed by sodium borohydride reduction. Glycol split heparin was well characterised by H^1NMR. Anticoagulant assays showed that glycol split heparin had reduced anticoagulant properties compared to unmodified heparin. Consequently, many adverse reactions associated with heparin including bleeding side effects are expected to be avoided. Furthermore, glycol split heparin was successfully appended to the surface of silica NPs as indicated by the zeta potential conversion and its reduced anticoagulant activity after coupling to NPs surface. The diameter of the particles was measuring using DLS and was found to be ~200 nm, which is within the therapeutic range used to passively target tumour cells.

Desulphated heparin was also synthesised using an alkalinisation method that selectively removes the sulphate groups at carbon 2 of the iduronic acid residue. ^{1}H NMR data showed that successful desulphation occurred at C2 as the chemical shift of the proton at the anomeric carbon decreased due to the shielding effect of the adjacent electrons after the desulphation process. Desulphation of heparin was also confirmed using a colorimetric assay. Azure A; a cationic dye was used and the data showed that unmodified heparin caused a significantly higher blue shift of azure λ_{max} compared to desulphated heparin. Indicating a

successful removal of desulphated heparin groups that take part in the ionic interaction between the cationic dye and the anionic heparin polymer. Furthermore, desulphated heparin conjugated NPs were prepared. The particles had average sizes around 190 nm. Zeta potential data showed that the positive charge of the amine functionalised NPs was converted to an overall negative charge after coupling of the desulphated heparin to the particles' surface. Moreover, the measured zeta potential value of the desulphated heparin conjugated NPs was lower than that for heparin conjugated NPs. This reinforces the evidence of decreased heparin charge after the removal of sulphate groups at C2. The presence of desulphated heparin on the particles' surface was also identified using the azure A assay, where the data showed a weaker interaction between azure A and desulphated heparin conjugated NPs compared to that with unmodified heparin conjugated NPs.

The developed heparin analogues conjugated silica NPs could be further employed as heparanase inhibitors, for example by using a radiolabelled heparan sulphate as a substrate for the heparanase upregulated by cancer cells. These NPs could be added to tumour cells containing radiolabelled heparan sulphate in order to test the cleavage products of the radiolabelled heparan sulphate. Heparin mimics appended NPs are expected to decrease the degradation products of the radiolabelled heparan sulphate, thus they could be utilised as potential therapeutics for inhibition of metastatic cell invasion and cancer metastasis.

4 Chapter Four: Development of FRET based heparinase nanosensors

4.1 Introduction

4.1.1 Heparanase use in cancer detection

Heparanase plays a crucial role in cancer spreading and metastasis. Heparan sulphate, which is a substrate for heparanase, is considered as a key player for cell adhesion and growth. Consequently heparan sulphate mediates the activity of tumour cells by either promoting or inhibiting the spread of the cells.[41] Heparanase is upregulated in most types of metastatic cancer cells as it facilitates their spread by degrading the basement membrane extracellular matrix by cleaving heparan sulphate. This creates a path for metastatic tumour cells to extravasate and enter the systemic circulation.[210, 216, 247-248] This has made heparanase an attractive biomarker for metastatic cancer detection and early diagnosis of metastasis. For instance, heparanase overexpression was detected in cancer cells using fluorescein-labelled heparin grafted onto the surface of gold NPs. These NPs showed an enhanced fluorescence signal (FRET) when incubated with metastatic cancer cells (Hela) compared to non-metastatic cancer cells (MCF-7) or normal cells (NIH-3T3). This was a result of heparanase overexpression that led to degradation of heparin attached to the surface of the Au-NPs thus releasing the fluorophore from the quencher to produce fluorescence signal restoration.[249] Furthermore, heparanase overexpression was also detected using non-FRET based methods, for example radiolabelled N-acetylated heparin was utilised to detect the upregulation of heparanase in metastatic cells compared to non-metastatic ones by monitoring the released fragments produced after cleavage of the radiolabelled heparin substrate by heparanase enzymes. However this method is not valid for *in vivo* detection of heparanase as measuring the degradation products of the radiolabelled substrate can only be conducted *in vitro* using gel filtration analysis.[250]

4.1.2 Fluorescence quenching

Fluorescence quenching is defined as a decrease in the fluorescence intensity of the fluorophore due to an interaction with a specific quencher which absorbs the emitted energy of the fluorophore and dissipates it as heat. This process can occur by different mechanisms;

for example static quenching and dynamic quenching encompassing collisional like Dexter process and FRET (Forster Resonance energy transfer).[251]

Collisional energy transfer occurs due to spin coupling and intersystem crossing,[252] as demonstrated in Figure 4.1.

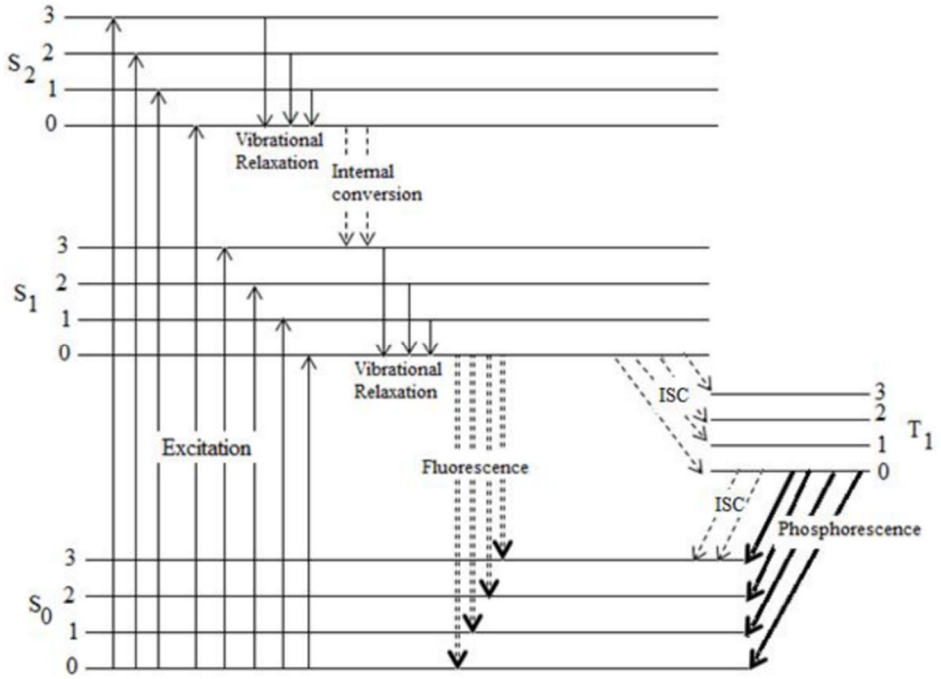


Figure 4.1 Modified form of Jablonski diagram showing intersystem crossing (ISC) between singlet excited state of the donor and triplet excited state of the acceptor.[252]

In collisional quenching the decrease in fluorescence intensity can be described by Stern-Volmer in Equation 4.1 In this expression, K is the Stern-Volmer quenching constant, kq is the bimolecular quenching constant, τ_0 is the unquenched lifetime, and $[Q]$is the molar concentration of quencher. The Stern-Volmer quenching constant kq indicates the sensitivity of the fluorophore to a quencher.

$$\frac{F_0}{F} = 1 + K\,[Q] = 1 + kq\,\tau_0[Q]$$

Equation 4.1 Stern Volmer Equation

Quenching efficiency can be calculated according to Equation 4.2 adapted from Arppe *et al*.[253] In this equation, F_Q: Florescence intensity of the reporter dye (donor) after addition of the quencher, F: Florescence intensity of the reporter dye (donor) before addition of the quencher.

$$\%\ \text{Quenching efficiency} = \left(1 - \frac{F_Q}{F}\right) \times 100$$

Equation 4.2 Quenching efficiency

4.1.3 Forester (fluorescence) resonance energy transfer (FRET) quenching

Forester (fluorescence) resonance energy transfer was initially introduced by Theodore Förster, where the energy of the donor (fluorescent substance) is transferred to the acceptor (quencher). The latter absorbs and dissipates most of the energy through non-radiative means, e.g., heat.[254] FRET quenching processes involve the interaction between donor and acceptor through space and direct donor-acceptor contact is not required for energy transfer. Figure 4.2 describes FRET mechanism and energy transfer between the donor and acceptor during electron transition.[255]

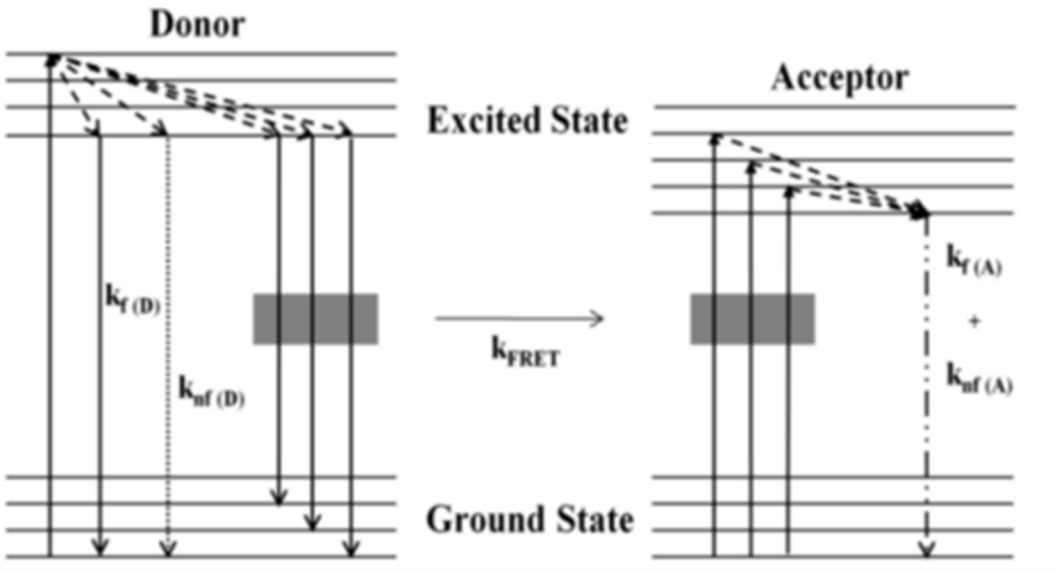


Figure 4.2 The Jablonski diagram showing the mechanism of Förster Resonance Energy Transfer (FRET). Electrons transition from the ground state to an excited state in both donor and acceptor when they are excited, and they lose energy by both fluorescence with rate constant $k_{f(D)}$ for donor or $k_{f(A)}$ for acceptor non-fluorescence mechanisms with rate constant $k_{nf(D)}$ for donor or $k_{nf(A)}$ for acceptor. Throughout FRET, excited energy of the donor is also transferred to an acceptor with rate constant k_{FRET}. [255]

The efficiency of energy transfer between the donor and the acceptor is inversely proportional to the sixth power of the donor-acceptor distance and can be calculated according to Equation 4.3. Where r is the distance between the two fluorophores or fluorophore / quencher, and R_0 is a constant called the Förster distance, at which the quenching efficiency is 50%.

$$E_{FRET} = \frac{1}{1 + (r/R_0)^6}$$

Equation 4.3 Efficiency of energy transfer

The FRET process is highly dependent on the donor-acceptor distance and it exerts its effect when the FRET pair are in close proximity to each other, i.e. where the donor-acceptor distance is typically less than 10 nm.[256-259] The energy transfer exponentially decays with the distance, this is clearly shown in Figure 4.3.

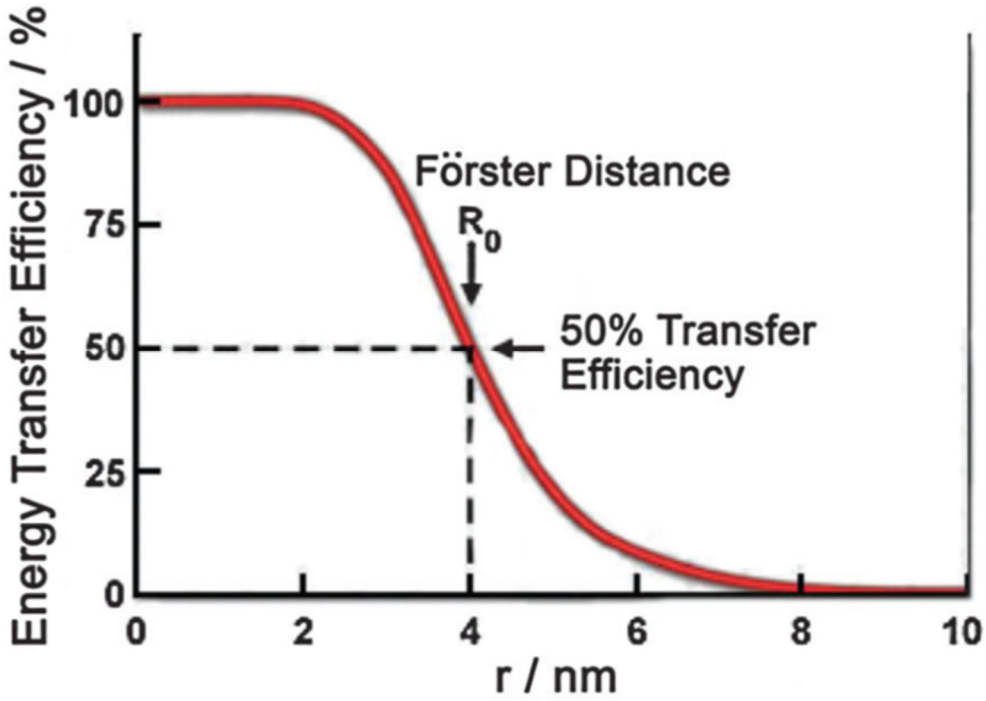


Figure 4.3 Effect of distance which separates the donor–acceptor pair on the efficiency of energy transfer attained by FRET process.[258]

Alongside the distance, the FRET process is controlled by other factors such as spectral overlap between the donor fluorescence emission spectrum and the acceptor absorption spectrum.

Furthermore, the molecular orientation of the FRET pair, the donor and acceptor plays a crucial role in efficient energy transfer, and subsequently in fluorescence quenching.[260-265]

The orientation of the FRET pair governs the dipole-dipole interaction between the donor and acceptor, hence the orientation factor was presented in mathematical equation as given in Equation 4.4

$$\kappa^2 = (\cos\theta_T - 3\cos\theta_D \cos\theta_A)^2$$

Equation 4.4 Orientation of FRET pair

Where θ_T is the angle between the donor emission and acceptor absorption transition dipoles, θ_D and θ_A are the angles between those dipoles and the connecting line between them respectively as demonstrated in Figure 4.4.

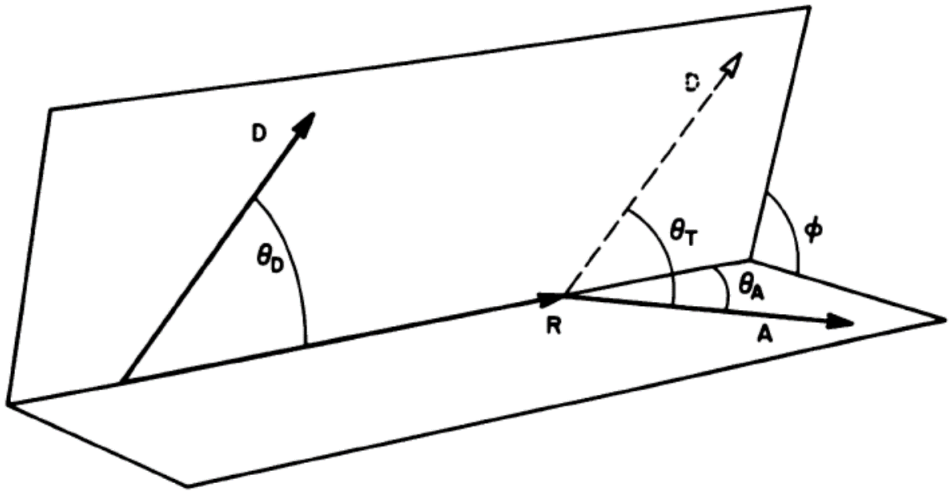


Figure 4.4 Schematic diagram visualizes the angles that are used to determine the relative orientation of the donor and acceptor transition moment.[260]

According to the above mentioned factors that affect the fluorescence quenching efficiency and donor-acceptor energy transfer, the FRET pair should be carefully chosen to achieve the required fluorescence quenching. Table 1 shows some examples of commercially available FRET donors with their most suitable acceptors of the dark quenchers, these dark quenchers are called black hole quenchers (BHQs) as they absorb the emission of the fluorescent donor.

Table 1 Commonly used fluorophores and their corresponding black hole quenchers (BHQs) which make up the donor-acceptor FRET pair system. Some of the fluorophores listed below such as CAL Fluor and Quasar dyes produced by Biosearch are used for multiplex real-time quantitative PCR. Where they have a wide range of emission maximum wavelengths (540 nm to 705 nm), these dyes are considered as a low cost alternative for fluorophores commonly used on real-time thermocyclers (TET, JOE, VIC, HEX, Texas Red, Cy3, Cy5, and Cy5.5).Where they can be coupled with the corresponding black hole quencher and used for qPCR.[266]

FLUOROPHORE	ALTERNATE DYES	DYE-5'-T_{10} EX	EM	RECOMMENDED QUENCHER	BHQ Dye QUENCHING RANGE
Biosearch Blue™		352	447	BHQ-1	BHQ-0 430-520 nm
FAM		495	520	BHQ-1	
TET		521	536	BHQ-1	
CAL Fluor® Gold 540	VIC/TET/JOE	522	544	BHQ-1	
JOE		529	555	BHQ-1	
VIC		538	554		
HEX		535	556	BHQ-1	BHQ-1 480-580 nm
CAL Fluor Orange 560	VIC/HEX/JOE	538	559	BHQ-1	
Quasar® 570	CY3	548	566	BHQ-2	
Cy™ 3		549	566		
NED		546	575		
TAMRA		557	583	BHQ-2	
CAL Fluor Red 590	TAMRA	569	591	BHQ-2	BHQ-2* 559-670 nm
Cy 3.5		581	596		
ROX		586	610	BHQ-2	
CAL Fluor Red 610	TEXAS RED/ROX/ ALEXA FLUOR® 594	590	610	BHQ-2	
Texas Red®		597	616		
CAL Fluor Red 635	LC RED® 640	618	637	BHQ-2	
Pulsar® 650		460	650	BHQ-2	
Cy 5		646	669		
Quasar 670	CY5	647	670	BHQ-2*, BHQ-3	
Cy 5.5		675	694		
Quasar 705	CY5.5	690	705	BHQ-2*, BHQ-3	BHQ-3 620-730 nm

FRET based sensing is widely used for DNA sequence detection. For instance, FRET based assays have been utilised to detect oligonucleotide sequences of DNA depending on the interaction between dye-tagged DNA strand and gold NPs.[267] It also has been reported that FRET pair labelled DNA was used to study the conformation of DNA-enzyme complexes and determine different DNA loop conformations.[268] Further FRET based probes have been used to detect Hepatitis C virus DNA facilitating the early diagnosis of Hepatitis C disease.[269] Near-infrared (NIR) sensitive DNA probes consisting of stained single stranded DNA attached to the surface of lanthanide-doped upconversion NPs have been prepared to detect DNA hybridisation.[270] A FRET pair based system composed of a fluorophore-quantum dot attached

to a molecular beacon DNA strand has been utilised to identify the complementary DNA strand by detecting the fluorescence changes upon target DNA sequence binding, thus opening the hairpin structure of the molecular beacon and separating the FRET pair.[271] In addition, a dual-nanoparticle FRET based system has been utilised to sense bleomycin, this system was made of silica NPs functionalised with fluorescent quantum dots and gold NPs modified with DNA, where they produced a quenched composite when combined. In the presence of bleomycin that induces the separation of DNA double strand, the FRET pair were parted from each other resulting in restoration of the fluorescence signal.[272] Carbon dots have been used as FRET based sensors, where the interaction between DNA attached carbon dots and ethidium bromide was utilised to monitor DNA damage due to ultraviolet light and free radicals.[273]

Furthermore the FRET phenomenon has been exploited to study protein folding and conformational changes. For example, staphylococcal nuclease and DNA labelled with FRET pair have been used to study real time fluctuations of nuclease conformational changes throughout enzymatic cleavage of the DNA strand.[274] Furthermore, genetically modified protein kinases were developed to monitor the conformational changes of the tyrosine kinase receptor in living cells. An intramolecular complex of the phosphotyrosine binding domain and the phosphotyrosine side chain is formed upon phosphorylation by a tyrosine kinase induced by growth factors, therefore these changes reflect a fluorescence intensities changes of the utilised FRET pair.[275] Additionally, FRET pairing was used to determine and map the metal ion-binding motif in the polypeptide by chasing the fluorescence changes of FRET pair labelled polypeptide containing fluorescent dye and metal binding domain; histidine. The fluorescence of this system changes due to high affinity metal ion binding to the polypeptide motif causing a fluorescence quenching of the nearby covalently attached fluorescent dye, allowing the monitoring of binding event.[276]

4.1.4 Dexter energy transfer mechanism

Dexter energy transfer (also called Exchange Energy Transfer and Dexter electron exchange) is another dynamic energy transfer mechanism. This phenomenon depends on electron exchange between the donor and acceptor, which requires a strong overlap of the donor-acceptor orbitals. Thus the energy transfer is *via* radiationless pathways, [277-279] as illustrated in Figure 4.5. Unlike the FRET process, it only occurs at very short-range distances between the donor and the acceptor; normally less than 10 Å.[280]

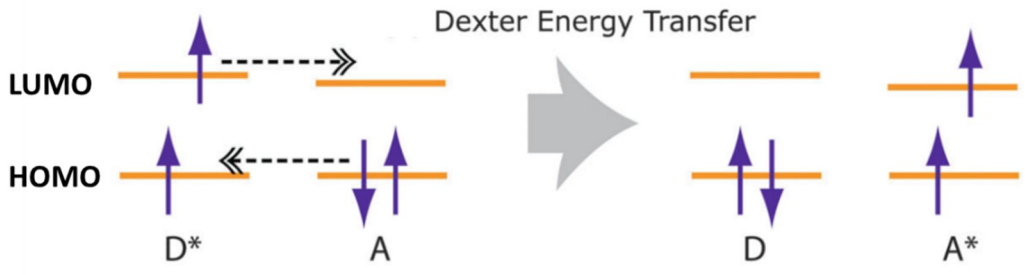


Figure 4.5 Dexter energy transfer enables diffusion of triplet excitons. Donor (D) and acceptor (A) molecules; the asterisk denotes excited state. The dashed arrows demonstrate simultaneous electronic configuration rearrangement of the electron transfer from the excited state of the donor molecule (D) to a neutral acceptor (A).[278]*

4.1.5 Static Quenching (contact quenching)

In the static quenching, the reporter dye and the quencher must be in contact with each other and this usually occurs by dipole-dipole hydrophobic interactions between the two dyes. The energy transfer occurs through complex formation of the ground states rather than the excited states producing a non-fluorescent complex.[281-284]

4.1.6 Heparinase and Heparanase differences

4.1.6.1 Heparinases

Heparinase (also called heparin lyase or heparin eliminase) is a bacterial enzyme usually produced by flavobacterium species. Heparinases cleave heparin or heparan sulphate at β 1-4 glycosidic linkage between glucosamine and uronic acid residues into small fragments with different specificities.

Accordingly they are grouped into three different types. Heparinase I which is specific for heparin and highly sulphated domains of heparan sulphate containing 2-O-sulphate iduronic acid, N-Sulphate and 6-O-sulphate glucosamine. Heparinase II is a non-specific enzyme that breaks down both heparin and heparan sulphate, where it binds to heparin and either highly sulphated domains or low sulphated domains of heparan sulphate as only the N-sulphate group is essential for activity. Heparinase III is specific for heparan sulphate, where it binds to the under-sulphated domain of heparan sulphate which contains non-sulphated uronic acid linked to either sulphated or non-sulphated glucosamine residues.[285-286] Heparinase specificities are demonstrated in Figure 4.6.

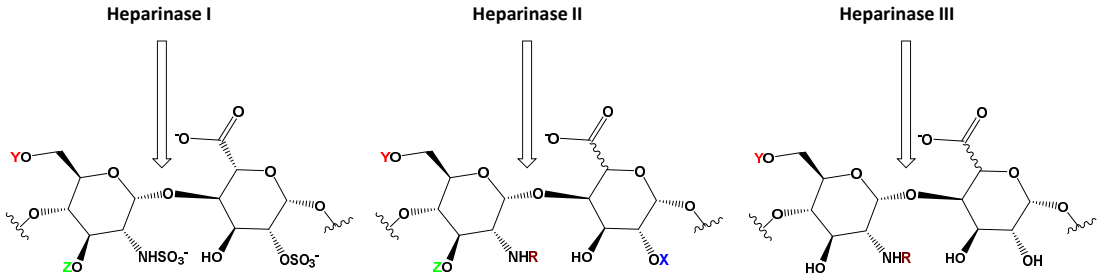


Figure 4.6 Diagram shows heparinase I, II and III specificities toward heparin and heparan sulphate. ***A:*** *Heparinase I specificity, Y= SO_3^- or H, Z= SO_3^- or H.* ***B:*** *Heparinase II specificity, X= SO_3^- or H (Iduronic or glucuronic acid), R= SO_3^- or CH_3CO, Y= SO_3^- or H.* ***C:*** *Heparinase III: Y= SO_3^- or H, R= SO_3^- or CH_3CO. ∿∿ = Covalent bond is either above or below the ring plane. Figure was adapted from Desai et al.[285]*

All heparinases cleave heparin and heparan sulphate *via* a β-elimination processes rather than hydrolysis. Thus disaccharides or oligosaccharides containing unsaturated uronic acid at C4-C5 (ΔUA) are produced at the non-reducing end of heparin or heparan sulphate chains upon cleavage of a sessile glycosidic bond between glucosamine and uronic acid. The enzymatic activity can be monitored by measuring the absorbance of the formed double bond at 232 nm wavelength.[287-289]

Heparinases degrade heparin or heparan sulphate in presence of calcium to produce unsaturated uronic acid, a low concentration of calcium ions is required for the enzymatic

activity, however the degree of degradation increases with increasing calcium ion concentration.[290] The β-elimination mechanism of heparin or heparan sulphate degradation has been elucidated by Sasisekharan et al,[291] as illustrated in Figure 4.7.

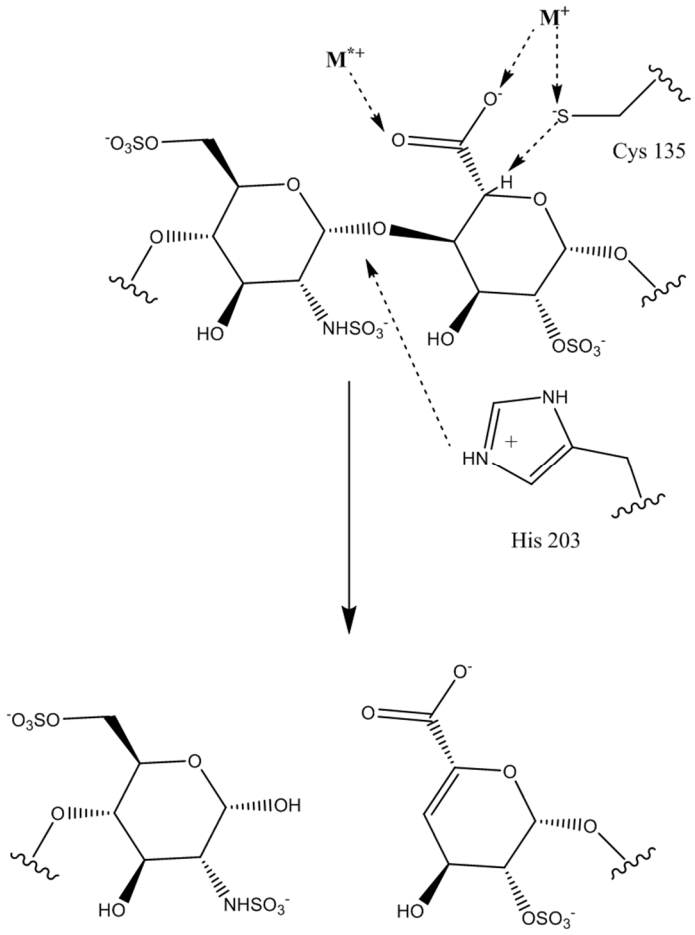


Figure 4.7 β-elimination mechanism of heparin degraded by heparinase II. The degradation mechanism involves C5 proton abstraction by deprotonated basic amino acid; Cysteine (Cys135) and subsequent proton donation by protonated acidic amino acid Histidine; (His 203) to stabilise the negative oxygen leaving group producing OH. Divalent ions (Ca^{+2}) work as a Lewis acid attracting the electrons of C5-Carboxyl groups consequently facilitating the abstraction of C5-proton by cysteine. M^{*+}= Lysine or Ca^{+2}, M^{+}= Ca^{+2}. Figure was adapted from Sasisekharan et al.[291]

In this context, glycosidic bond cleavage involves abstraction of the C5-proton of iduronic acid by basic amino acid groups of the enzyme, mainly deprotonated tyrosine or cysteine. On

the other hand, acidic groups such as protonated histidine give a proton to the negatively charged oxygen stabilising the leaving group thus forming a stable hydroxyl group.

Calcium, acting as a Lewis acid, is thought to bind to carboxylate groups at C5, consequently stabilising the enzyme-substrate complex and decreasing the pKa of C5-hydrogen adjacent to the carboxylate group. This enhances the ability of the enzyme basic amino acid moieties to abstract the proton.[292-293]

4.1.6.2 Heparanases

Heparanase is a mammalian, endo-β-D-glucuronidase enzyme that breaks down the extracellular matrix surrounding the cells. Thus heparanases produce highly sulphated regions of heparan sulphate fragments after heparan sulphate degradation, which are crucial for cell signalling and growth by controlling the release of cellular growth factors. In contrast to the heparinase mechanism, heparan sulphate cleavage by heparanase is a hydrolytic rather than elimination process,[294] as demonstrated in Figure 4.8. The primary function of heparanase is to facilitate the extravasation of the immune cells throughout the inflammation process by degrading the glycosaminoglycan heparan sulphate at the sites of injury and inflammation.[295-296] Human heparanase exerts its maximum activity at a local pH of 5.5.[297-298]

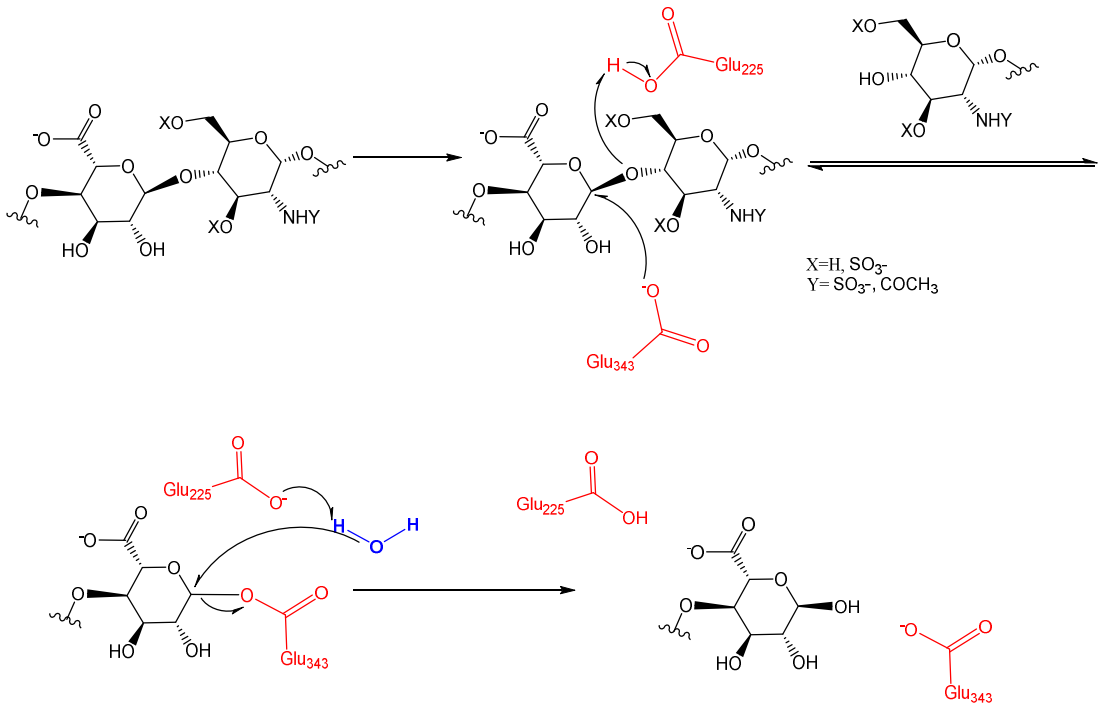


Figure 4.8 Hydrolysis mechanism of heparan glyosidic linkage cleavage by heparanase involving glutamic acid amino acid residue deprotonation in aqueous environment to provide water molecules necessary for hydrolysis, figure was adapted from Rivara et al.[294]

Human heparanase is thought to break down both heparan and heparin to small oligo saccharides of ~ 5 kDa molar mass.[299-300] It has been reported that macromolecular heparin that is bound to serglycin-type peptides can be processed and catalysed by heparanase into commercial heparin polysaccharides.[301] It was found that heparanase cleaves heparin at multiple, yet restricted cleavage sites to produce small heparin fragments, which were correlated with the reduced anticoagulant activity of heparin and low molecular weight heparin.[302]

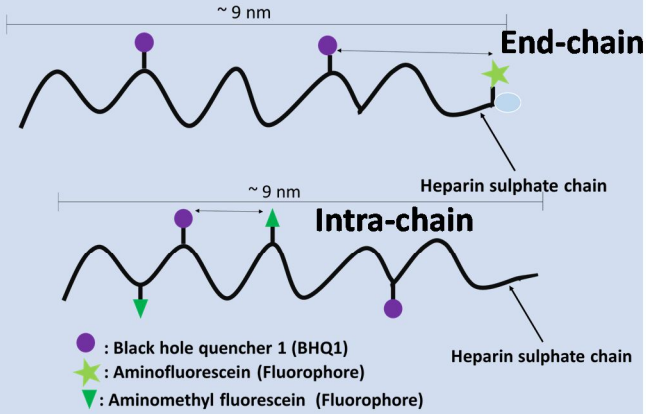
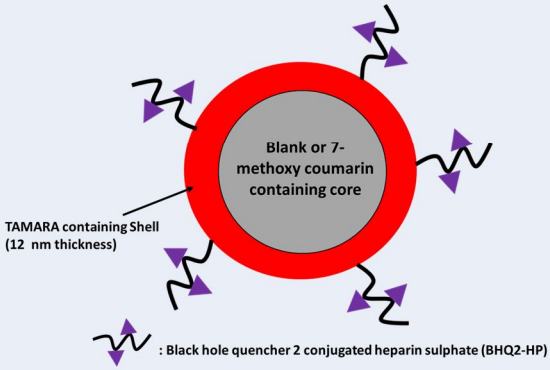
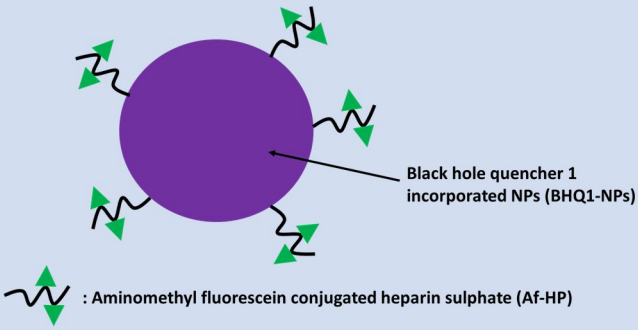
4.2 Aim

The aim of this chapter is to synthesise a FRET based donor-acceptor system that is capable of detecting heparinase which is the bacterial form of the mammalian heparanase overexpressed during the early stage of metastasis and thus it could be utilised for the diagnosis of cancer metastasis. The study is adopting a heparinase responsive model based on FRET mechanism that enables the monitoring of the changes in the fluorescence after

heparin cleavage by heparinase. It was hypothesised that the fluorescence signal of the fluorophore quenched (switch off) by a black hole quencher in the FRET pair linked to heparin is recovered (switch on) primarily due to heparin chain breakage by heparinase thus bringing the FRET pair apart from each other changing the distance between the donor and the acceptor. The intended result is a switch off to switch on system that is able to sense heparinase.

In order to achieve this aim, FRET based heparin-sensors were prepared in order to test their ability to detect the presence of heparinase through cleavage of heparin, using three different models. Model I involves the preparation of a dual labelled probe composed of BHQ1 and fluorescein that are chemically attached to heparin in order to enhance the interaction between the donor; fluorescein and the acceptor; BHQ1. In model II, BHQ 2 conjugated heparin was attached to the surface of core-shell NPs containing TAMRA in the shell and either unmodified blank core or 7-Methoxycoumarin incorporated core. Model III adopted the attachment of fluorescein labelled heparin to the surface of black hole quencher-1 incorporated NPs. Table 2 summarises the three different models and their properties.

Table 2 Illustrative diagrams of the FRET based models designed for studying of heparinase sensing and detection.

Model	details	Illustration (Cartoon)
Model I (Polymer based FRET system)	Both FRET pairs were attached to the same chain of heparin molecule by either attaching the fluorophore to the end of or within the chain	
Model II (Nanoparticles based FRET system)	The fluorophore TAMRA is incorporated within the shell of core-shell NPs whilst black hole quencher 2 conjugated heparin sulphate (BHQ2-HP) is attached to the NPs shell	
Model III (Nanoparticles based FRET system)	The black hole quencher 1 is incorporated into the NPs matrix, whereas aminomethyl fluorescein conjugated heparin sulphate (Af-HP) is linked to the surface of the NPs	

4.3 Materials and methods

4.3.1 Materials and equipment

Fluoresceinamine (5-Aminofluorescein), Sodium cyanoborohydride, Ammonium hydroxide (NH_4OH) (28-30%), Tetraethylorthosilicate (TEOS) (≥ 99%), (3-Aminopropyl)triethoxysilane

(APTES), N-(3-Dimethylaminopropyl)-N'-ethylcarbodiimide hydrochloride(EDC), Sulphuric acid, Azure A (certified by the Biological Stain Commission (dye content 70 %), Heparin (≥ 180 USP units/mg) from porcine intestine (average MW =17 kDa and heparinase I (HEPI), heparinase II (HEPII) from Flavobacterium heparinum were purchased from Sigma Aldrich, Ethanol absolute was purchased from Fisher Chemical, 2-(N-morpholino)ethane sulfonic acid (MES) was purchased from PanReac, 5-(Aminomethyl)Fluorescein, 5-(and-6)-Carboxytetramethylrhodamine Succinimidyl Ester (5(6)-TAMRA, SE), 7-methoxycoumarin succinimidyl ester (Coumarin, SE) and Sulfo-NHS (N-hydroxysulfosuccinimide), 5(6)-Carboxyfluorescein (FAM) and SnakeSkin™ Dialysis Tubing (3.5K MWCO, 22 mm) were purchased from ThermoFisher Scientific, Sodium hydroxide was purchased from VWR International Ltd, Sodium nitrite was kindly provided by University of Nottingham, BHQ1-Carboxylate, BHQ1-Amine, BHQ2-Amine and BHQ1-succinimidyl ester (BHQ1, SE) were purchased LGC Biosearch Technologies. Cary eclipse fluorescence spectrometer, Malvern Zetasizer Nano ZS, Buchi Rotavap R-200, Hermle Z300 Centrifuge, SP 260PZ syringe pump, GVD3 freeze dryer and Spark microplate reader (TECAN) were used.

4.3.2 Synthesis and characterisation of model I sensing probe

4.3.2.1 Synthesis of the dual-labelled heparin probe by intrachain conjugation of the FRET pair

To synthesise fluorescein labelled heparin, (40 mg, 2.35 µmol) of heparin was dissolved in 1 mL MES buffer pH 5.6. Then 1 mL of MES buffer containing EDC (9 mg, 46.9 µmol) was added, subsequently Sulfo-NHS (10.2 mg, 46.9 µmol) dissolved in 1 mL MES buffer was also added and the solution left under stirring for 20 minutes. Finally, aminomethyl fluorescein (0.92 mg, 2.55 µmol) was added to the above solution and the pH was adjusted to 7.4 using 10 mL of 0.2 M phosphate buffer and left under magnetic stirring for 24 hours to allow hydrolysis of the excess unreacted succinimidyl ester groups. The produced fluorescein conjugated heparin was dialysed using 3.5 kDa dialysis membrane against water for 2 days. After dialysis the product was freeze-dried for 24 hours, collected and stored in the fridge. After synthesis

of fluorescein labelled heparin probe, dual labelled heparin was prepared as follows; 20 mg of the prepared fluorescein labelled heparin was dissolved in 1 mL MES buffer pH 5.6. Then EDC (4.5 mg, 23.47 µmol) and Sulfo-NHS (5.1 mg, 23.48 µmol) were added and the solution left to stir for 20 minutes. After activation, BHQ1-Amine (0.55 mg, 1.16 µmol) was added to the above solution and the pH was raised to 7.4 using 10 mLof 0.2 M of phosphate buffer and left under stirring for 24 hours. The resultant dual-labelled heparin probe was dialysed against water using 3.5 kDa dialysis membrane for 2 days. The product (32 mg, 80% yield) was freeze-dried and stored in the fridge.

4.3.2.2 Preparation of the physical mixtures of the FRET pair and heparin

To prepare a physical mixture of oppositely charged FRET pair and heparin. 20 mg of heparin was dissolved in 1 mL of 0.2 M phosphate buffer. Then, BHQ1-Amine (0.55 mg, 1.16 µmol) and aminomethyl fluorescein (0.46 mg, 1.27 µmol) were added to heparin solution and the total volume was made up to 10 mL using phosphate buffer pH 7.4 and left to stir for 24 hours.

For physical mixture of similarly charged FRET pair and heparin; BHQ1-carboxylate-SE (0.583 mg, 1.16 µmole) and carboxyfluorescein-SE (0.48 mg, 1.27 µmole) of were added to 1 mL phosphate buffer pH 7.4 containing 20 mg heparin, the volume of the solution was adjusted to 10 mL using phosphate buffer and left to stir for 24 hours.

4.3.2.3 Synthesis of dual-labelled heparin by end-chain conjugation of the fluorophore

In order to attach the fluorophore to the end of the heparin chains, fluoresceinamine was used as amine source to carry out the direct reductive alkylation (amination) reaction. 40 mg of heparin was dissolved in 4 mL ammonium acetate pH 5 and left under magnetic stirring. Fuoresceinamine (8 mg, 2.3 µmol) was dissolved in 10 mL ammonium acetate and 5 mL ethanol to enhance the solubility of fluoresceinamine in aqueous solvent and added to heparin containing solution. Subsequently sodium cyanoborohydride (10 mg, 159.1 µmol)

was added to the above solution to reduce the formed iminium intermediate. The temperature of the reaction was adjusted to 40 °C and left to stir for 4 days. The reaction is slow due to the equilibrium between the open and closed form of the aldehyde groups at the reducing end of heparin chain therefore a reaction time longer than 48 hours is expected. The produced fluoresceinamine-labelled heparin was dialysed against water using a 3.5 kDa dialysis membrane for 3 days. The product (26 mg, 65 % yield) was freeze-dried for 24 hours and stored in the fridge. Further, 7 mg of fluoresceinamine-labelled heparin was dissolved in 1 mL MES buffer pH 5.6. Then EDC (1.58mg, 8.24 µmol) and Sulfo-NHS (1.78 mg, 8.24 µmol) were added to the solution and left to stir for 20 minutes to activate heparin carboxylate groups. After activation, BHQ1-Amine (0.206 mg, 4.34 µmol) was added to the above solution and left to stir for 24 hours. The product was dialysed against water for 2 days, subsequently freeze-dried and stored in the fridge.

4.3.2.4 Fluorescence quenching measurement

To measure the quenching efficiencies of the prepared probes, fluorophore-labelled heparin was used as a control.

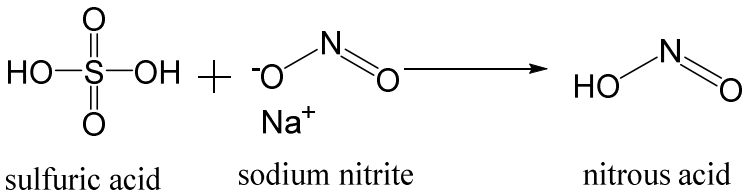
For dual labelled heparin prepared by intrachain conjugation of the FRET pair; 1 mL of aminomethyl fluorescein labelled heparin and 1 mL of dual labelled heparin having exactly the same concentration of aminomethyl fluorescein labelled heparin precursor were individually placed in a cuvette and the fluorescence emission spectra were recorded from 495 to 595 nm at 488 nm excitation wavelength using Cary eclipse fluorimeter.

For the dual labelled prepared by end-chain conjugation of the fluorophore and intrachain conjugation of the BHQ1, 1 mL of fluoresceinamine labelled heparin and 1 mL of dual labelled heparin having exactly the same concentration of fluoresceinamine labelled heparin precursor were individually placed in a cuvette and the fluorescence spectra were reported from 495 to 595 nm at 488 nm excitation wavelength using Cary eclipse fluorimeter.

For the physical mixtures, 1 mL of the prepared physical mixtures in section 4.3.2.2 and 1 mL of the mixture of heparin and either aminomethyl fluorescein or carbxyfluorescein without adding BHQ1; prepared under the same condition and concentrations of the fluorophores, were individually placed in a cuvette and the fluorescence emission spectra were recorded at 488 nm as described above.

4.3.2.5 Chemical depolymerisation using nitrous acid and fluorescence signal recovery

Nitrous acid was freshly prepared by adding 5 mL of 0.5 M sulphuric acid to 5mL of 1 M sodium nitrite to produce nitrous acid solution with pH of 1.5 as shown in Equation 4.5. Then 1 mL of the dual-labelled heparin (5 mg/mL) was mixed with 4 mL of the prepared nitrous acid and left to stir for 2 hours. 1.3 mL of 1 M sodium hydroxide was added to the above solution to bring the pH to 7.4, then 1 mL of 0.2 M phosphate buffer pH 7.4 was added. Similarly, 1 mL of 5 mg /mL of dual labelled heparin was dissolved in 6.3 mL phosphate buffer pH 7.4 to produce non-degraded dual labelled heparin and used as a control with exactly the same pH of the degraded dual labelled heparin. 1 mL of each solution was placed in the fluorimeter and the fluorescence scan was recorded using excitation wavelength of 488 nm and emission wavelengths ranging from 500 to 600 nm.



Equation 4.5 Chemical equation of nitrous acid production with pH 1.5 by reacting sulphuric acid with sodium nitrite.

4.3.2.6 Azure A assay for heparin degradation monitoring

Depolymerised heparin (5mg/mL) was prepared using the same method in section 4.3.2.5. 1 mL of 400 µg/mL of either depolymerised heparin or intact heparin was added to 1 mL of azure A solution (0.0125 mg/mL, 4.25 µmol/mL) at pH 7.4. Then the absorbance scan was recorded for each sample using TECAN plate reader.

4.3.2.7 Heparinase assay

500 µL of the dual labelled heparin (2 mg /mL) dissolved in 0.1 M sodium acetate buffer with pH 7 and contains 5 mM of calcium was placed into 2 wells of a 24-well plate. Then, 10 µL of heparinase I (HEPI) with concentration of 20 milliunits/mL and 10 ul of heparinase II (HEPII) with concentration of 8 milliunits/mL were added to one well. Mixture of HEPI &HEPII was used in order to ensure near complete degradation of heparin into disaccharides units as previously reported.[303] The plate was placed in the water bath at 30 ^{0}C in order to maintain the enzyme activity over time and left for 24 hours. The other well was used as a control and 20 µL of 0.1 M sodium acetate buffer pH 7 was added to maintain the same volume for both wells. After that, 200 µL from each well was placed in a cuvette containing 1 mL sodium acetate buffer with pH 7 and the fluorescence of each sample was recorded from 500 to 600 nm using 488 nm excitation wavelength.

4.3.3 Preparation of nanosensors using model II

4.3.3.1 Synthesis of core-shell NPs

The procedure was optimised to produce NPs with the smallest shell thickness possible. This was achieved by adjusting the reagent concentrations used to prepare amine functionalised silica NPs (TEOS, TAMRA-APTES conjugate, free APTES and ammonium hydroxide) and the reaction time.

NPs with different shell thicknesses were synthesised by two different approaches; the first approach was by a two-step method which involved the addition of the fluorophore source (TAMRA-APTES conjugate) to the plain silica NPs in order to attach the fluorophore to the NPs surface first followed by amine functionalisation using APTES as an amine source. The second approach, was the co-addition method, where both TAMRA-APTES conjugate and APTES were added together to functionalise simultaneously the NPs surface with amine groups and the fluorophore.

TAMRA-APTES conjugate was prepared by dissolving TAMRA-SE (1 mg, 1.9 nmol) in 1ml of pure ethanol, then the mixture was sonicated for 15 minutes. After that APTES (18 µl, 76.9

nmol) was added to the mixture, left on an oscillator for 24 hours to allow the reaction to proceed and covered with aluminium foil to protect the dye.

In order to prepare 70 nm, 45 nm and 25 nm shell thickness NPs; the two-step method was used. 70 nm shell thickness NPs were prepared as follows; a sample (100 mg) of the unmodified silica NPs previously prepared in chapter 1 was suspended in 10 mL ethanol. Then 0.3 mL of ammonium hydroxide was added to the suspension and left to stir for 15 minutes. 30 µL of TAMRA-APTES conjugate solution was added and left to stir for 3 hours, subsequently 150 µL of TEOS was added and the suspension was left to stir for 24 hours.

To prepare 45 nm shell thickness NPs; a sample (100 mg) of the unmodified silica NPs was suspended in 10 mL ethanol. Then 0.5 mL ammonium hydroxide was added to the suspension and left under stirring for 15 minutes. After that, 20 µL of TAMRA-APTES conjugates was added to the suspension and left to react for 3 hours. The suspension was then washed by adding 20 mL ethanol, centrifuged 3 times and resuspended in 10 mL ethanol. Further, 1 mL of ammonium hydroxide was added to the washed suspension and left under stirring for 15 minutes. Finally, 500 µL of free APTES was added to the above suspension and left under stirring for 24 hours.

To prepare 25 nm shell thickness; 100 mg of the unmodified silica NPs was suspended in 10 mL ethanol. 0.3 mL ammonium hydroxide was then added to the suspension and left under stirring for 15 minutes. Then, 20 µL of TAMRA-APTES conjugate was added to the suspension and left to react for 1 hour. The suspension was finally washed with 20 mL ethanol and centrifugation for 3 times and resuspended in 10 mL ethanol. The washed NPs were further modified with free amine groups, by adding 1 mL of ammonium hydroxide to the suspension which then left to stir for 15 minutes. Finally, 500 µL of free APTES was added to the above suspension and left to stir for 24 hours.

12 nm shell thickness-NPs were synthesised by the co-addition method, where both free APTES and TAMRA-APTES conjugate were added to plain unmodified silica NPs at the same

time in one pot reaction process. 100 mg of the unmodified silica NPs was suspended in 10 mL ethanol, then 1 mL of ammonium hydroxide was added and left under stirring for 15 minutes. Then a mixture of 250 µL of free APTES and 250 µL of TAMRA-APTES were added to the suspension and left under stirring for 24 hours.

All prepared NPs were washed with 20 mL ethanol for three times, centrifuged at 3300 g and dried using rotary evaporation, the collected products were stored in the fridge for further use.

4.3.3.2 Preparation of BHQ2-Heparin conjugated 12 nm-shell NPs

NPs with 12 nm shells were chosen to functionalise the surface of the NPs with black hole quencher 2 (BHQ2) as it achieved the best quench fluorescence efficiency compared to larger shell thickness-NPs.

The BHQ2-Heparin conjugate was firstly prepared using EDC/NHS coupling method as follows; 20 mg of heparin was dissolved in 1 ml mL MES buffer pH 5.6. Then EDC (4.5 mg, 23.47 µmol) and Sulfo-NHS (5.1 mg, 23.48 µmol) were added and the solution left to stir for 20 minutes. After activation, BHQ2-Amine (0.554 mg, 1.16 µmol) was added to the above solution and the pH was raised to 7.4 using 10 ml mL of 0.2 M of phosphate buffer and left under stirring for 24 hours. The resultant BHQ2-Heparin was dialysed against water using 3.5 kDa dialysis membrane for 2 days. The product was freeze-dried and stored in the fridge

In order to attach BHQ2-Heparin to the surface of amine functionalised 12 nm-shell NPs carbodiimide reaction was used. 10 mg of the prepared BHQ2-Heparin conjugate was dissolved in 10 mL of MES buffer pH 5.6. Subsequently, EDC (1 mg, 5.21 µmol) and Sulfo-NHS (1.13 mg, 5.21 µmol) were added to the solution and left under stirring for 20 minutes. Then, 20 mg of 12 nm-shell NPs was suspended in 10 mL of 0.2 M phosphate buffer pH 7.4 and added to the above solution and left to stir for 24 hours. The resultant NPs were washed with water for 4 times and centrifuged at 3300 g and freeze-dried to produce BHQ2-Heparin conjugated 12 nm-shell NPs.

4.3.3.3 Synthesis of coumarin based core-shell system

In order to prepare core-shell NPs with 7-methoxycoumarin within the core, unmodified coumarin labelled NPs were prepared as follows: 7-methoxycoumarin succinimidyl ester (Coumarin, SE) dye (1 mg, 5.67 µmol) was dissolved in 1mL of pure ethanol, then the mixture was sonicated for 15 minutes. After that 18 µL of APTES was added to the mixture and left on an oscillator for 24 hours to allow the reaction to proceed and covered with aluminium foil to protect the dye. 200 µL of the resultant solution was then added to a round bottom flask containing 50 mL of ethanol and 3 mL of ammonium hydroxide (NH_4OH) and left to stir for 12 hours. After that 4 mL of tetraethylorthosilicate (TEOS) was added dropwise using a syringe pump at a rate of 0.5 mL /min and left under stirring (1750 rpm) for 3 hours. The suspension was centrifuged at 3300 g for 20 min and washed with 40 mL ethanol for three times. Finally, the suspension was rotary evaporated to produce 7-methoxycoumarin containing silica NPs.

12 nm shell thickness-NPs with 7-methoxy coumarin incorporated within the core were then synthesised the using co-addition process detailed in 4.3.3.1. 100 mg of the unmodified 7-methoxy coumarin labelled silica NPs was suspended in 10 mL ethanol, then 1 mL of ammonium hydroxide was added and left to stir for 15 minutes. Then a mixture of 250 µL of free APTES and 250 µL of TAMRA-APTES were added to the suspension and left to stir for 24 hours. The produced coumarin based core-shell NPs (12 nm shell thickness) were dried by rotary evaporation and stored in the fridge.

Furthermore, BHQ2 conjugated heparin (BHQ2-HP) probe was grafted onto the surface of coumarin based core-shell NPs. 10 mg of BHQ2-Heparin conjugate prepared in 4.3.3.2 was dissolved in 10 mL of MES buffer pH 5.6. Subsequently, EDC (1 mg, 5.21 µmol) and Sulfo-NHS (1.132 mg, 5.21 µmol) were added to the solution and left to stir for 20 minutes. Then, 20 mg of 12 nm-shell NPs (coumarin based NPs) was suspended in 10 mL of 0.2 M phosphate buffer pH 7.4, added to the above solution and left to stir for 24 hours. The resultant NPs were washed with water for 4 times, centrifuged at 3300 g and freeze-dried to produce BHQ2-

Heparin conjugated NPs containing 12 nm TAMRA shell and 7-methoxy coumarin incorporated into the core.

4.3.3.4 Fluorescence measurements of core-shell NPs

1 mg /mL of 12 nm, 25 nm 45 nm and 70 nm shell thickness NPs were suspended in deionised water and placed in a cuvette, and the emission spectra were recorded at 540 nm excitation wavelength and emission collected between 550 nm and 600 nm.

4.3.3.5 Monitoring of spectral overlap of the donor-acceptor system in the core-shell NPs

1 mL of black hole quencher 2 (BHQ2, 100 µg/mL), black hole quencher conjugated heparin probe (BHQ2-HP, 1 mg/mL) and of BHQ2-HP grafted core-shell silica NPs (BHQ2-HP-Si; 12 nm shell thickness, 5 mg /mL) were individually placed in the UV-visible spectrophotometer and the absorption spectra were recorded at 400 to 700 nm. 1 mL of TAMRA-labelled core-shell NPs (12 nm shell thickness, 5 mg /mL) was placed in a cuvette and the fluorescence emission spectrum was recorded from 550 to 600 nm using 540 nm excitation wavelength.

4.3.4 Development of FRET based nanosensors using model III

4.3.4.1 Synthesis of the nanosensors

The developed nanosensors using this model were synthesised by attaching a fluorescein conjugated heparin to the surface of the black hole quencher incorporated silica NPs functionalised with amine groups using APTES linker.

In order to prepare amine functionalised silica NPs consisting of BHQ1 incorporated within the silica matrix , a BHQ1-APTES conjugate was firstly prepared as follows; BHQ1-succinimidyl ester (BHQ1, SE) (1 mg, 1.66 µmol) was dissolved in a mixture of 0.5 mL of pure ethanol and 0.5 mL DMF to maintain the solubility of BHQ1 and sonicated for 15 minutes. After that 18 µL of APTES was added to the mixture and left on an oscillator for 24 hours to allow the reaction to proceed and covered with aluminium foil.

After that, 450 µL of the resultant BHQ1-APTES conjugate was added to a round bottom flask containing 50 mL ethanol and 3 mL ammonium hydroxide (NH_4OH) and left to stir for 12 hours. After that 4 mL of tetraethylorthosilicate (TEOS) was added dropwise using a syringe pump at a rate of 0.5 mL /min and left to stir (1750 rpm) for 3 hours. The produced BHQ1

incorporated NPs were washed 3 times using 20 mL ethanol, rotary evaporated to dryness and stored in the fridge.

Further, 60 mg of BHQ1 Incorporated NPs were suspended in 10 mL ethanol containing 1 mL ammonium hydroxide and left to stir for 15 minutes. Then, 135 µL of APTES was added to the suspension and left to stir for 24 hours. After that the NPs were washed 3 times with ethanol and dried using a rotary evaporator to produce BHQ1 incorporated NPs functionalised with amine groups.

Fluorescent heparin probes were prepared by attaching aminomethyl fluorescein to carboxylate groups of the heparin chains. 40 mg of heparin was dissolved in 1 mL MES buffer pH 5.6. Then 1 mL of MES buffer containing EDC (9 mg, 46.9 µmol) and Sulfo-NHS (10.2 mg, 46.9 µmol) were also added to above solution and left under stirring for 20 minutes. Finally, aminomethyl fluorescein (0.92 mg, 2.55 µmol) was added to the above solution and the pH was adjusted to 7.4 using 10 mL of 0.2 M Phosphate buffer and left under magnetic stirring for 24 hours to ensure hydrolysis of the excess and unreacted succinimidyl ester groups. The produced aminomethyl fluorescein labelled heparin (Fluorescein-Heparin) probe was dialysed against water for 2 days, subsequently freeze-dried and stored in the fridge. The prepared probe was further grafted onto the surface of either unmodified blank silica NPs (BHQ1 free) or BHQ1 containing NPs as follows: 20 mg of the prepared fluorescein labelled heparin probe was dissolved in 1 mL MES buffer pH 5.6. Then 1 mL of MES buffer containing EDC (4.5 mg, 23.47 µmol) and Sulfo-NHS (5.1 mg, 23.48 µmol) dissolved in 1 mL MES buffer were added to above solution and left under stirring for 20 minutes. 20 mg of either blank silica NPs or BHQ1 containing NPs, having amine functionality grafted onto the surface and suspended in 10 mL of phosphate buffer pH 7.4, was added to fluorescein labelled heparin containing buffer and left to stir for 24 hours. Then, the NPs were washed 4 times with deionised water and centrifuged at 3300 g. The produced Fluorescein-Heparin conjugated

silica NPs containing a BHQ1 incorporated within the silica matrix (Flu-HP-Si-BHQ1) were freeze-dried for 24 hours and stored in the fridge.

4.3.4.2 Characterisation of the nanosensors

4.3.4.2.1 Absorbance

1 mL of BHQ1 incorporated NPs (5 mg/mL) and 1 mL of BHQ1-APTES conjugate (100 µg/mL) were individually suspended in deionised water and placed in 24-well plate. The absorption spectra of the samples were recorded from 400 to 700 nm.

4.3.4.2.2 Fluorescence

1 mL of aminomethyl fluorescein labelled heparin probe (1mg/mL) and free aminomethyl fluorescein dye (1 mL of 100 µg/mL) were placed in the cuvette and the fluorescence spectra were recorded from 500 to 600 nm using 488 nm excitation wavelength

4.3.4.2.3 Particle Size

Particle size measurements were carried out using a Malvern Zetasizer Nano in back scatter mode at 173° angle with 633 nm laser. The equilibration time for each sample was 120 seconds before the acquisition of the next sample. The count rate was set between 100-500 kcps by automatically adjusting the laser power using an attenuator. The temperature was set at 25 °C and the viscosity of the dispersant was 1.2 cP with 1.362 refractive index. All samples were prepared in 1/10 phosphate buffer saline (15 mM PBS). Data were recorded for each sample and repeated for three times of 15 runs for each reading. Particle diameter was measured by Dynamic Light Scattering (DLS) technique. In principle, the suspended NPs undergo random movement (Brownian motion) with certain velocity that is related to the particle diameter. Particles scatter the incident light in different directions (Rayleigh scattering) and thus the intensity of the scattered light fluctuates according to the particle's velocity (Diffusion coefficient). The intensity and the rate at which the scattered light fluctuates are measured by Zetasizer detector and the instrument software computes the

hydrodynamic diameter of the suspended particle from the diffusion coefficient (D) using Stokes-Einstein's theory as shown in Equation 4.6:

$$d_H = kT/3\pi\eta D$$

Equation 4.6 Stokes-Einstein's equation

Where, d_H is the hydrodynamic diameter of the particle (m), k is Boltzmann constant (kg·m^2/s^2·K or J/s^2), T is the absolute temperature (K), η is solvent viscosity (kg/m·s) and D is the diffusion coefficient (m^2/s).To measure the diameter of model III nanosensors, either 1 mL of 0.01 mg/mL of Flu-HP-Si (blank) silica NPs functionalised with fluorescent heparin or 1 mL of 0.01 mg/mL of Flu-HP-Si-BHQ1NPs was suspended in 15 mM PBS, placed in a cuvette and particle size distribution was measured using Malvern Zetasizer.

.

4.3.4.3 Quenching efficiency

1 mL of 1mg/mL of blank silica NPs functionalised with fluorescent heparin (Flu-HP-Si-blank NPs) and 1 mL of 1mg/mL of Flu-HP-Si-BHQ1 NPs were suspended in phosphate buffer pH 7.4, placed in a cuvette and the fluorescence spectra of the samples were recorded from 500 to 560 nm wavelengths after excitation at 488 nm wavelength.

4.3.4.4 Fluorescence signal recovery after heparinase treatment

1 mL of Flu-HP-BHQ1-Si NPs (1mg/mL) suspended in acetate buffer pH 7 containing 5 mM calcium acetate were placed into 2 scintillation vials. Then, 10 µL of heparinase I (HEPI) with concentration of 20 milliunits/mL and 10 µL of heparinase II (HEPII) with concentration of 8 milliunits/mL were added to one vial and left in the water bath at 30 ^{0}C for 24 hours, whilst 20 µL of the buffer was added to the second vial. After enzyme treatment, the pH elevation experiment was conducted as follows; the same set of the vials were used and the pH was raised to 11 by adding 1 mL of 0.2 M sodium phosphate/sodium hydroxide buffer.

The fluorescence spectra of NPs suspended in these vials were measured by placing 1 mL of the suspended NPs in a cuvette and the emission was recorded from 500 to 600 nm wavelength using 488 nm excitation wavelength.

4.4 Results and discussion

4.4.1 Synthesis of heparinase sensing probe using model I

Dual labelled heparin probes were prepared using this model by attaching the fluorophore (aminomethyl fluorescein) and the dark quencher (BHQ1-Amine) to heparin using two different methods.

The first method was intrachain chemical conjugation of the FRET pair to heparin chain by two step reaction process. In the first step; aminomethyl fluorescein amine groups were covalently attached to heparin carboxylate groups *via* amide bonds using carbodiimide chemistry utilising EDC and NHS to produce fluorescein labelled heparin. While in the second step; BHQ1 amine groups were also covalently attached to the fluorescein labelled heparin utilising same carbodiimide chemistry reaction in order to produce dual labelled heparin probe.

The second method adopted the synthesis of the dual labelled heparin by end-chain conjugation of the fluorophore; fluoresceinamine through a direct reductive amination reaction of the available aldehyde groups at the reducing termini of heparin utilising sodium cyanoborohydride to reduce the formed iminium intermediate (Schiff base) to produce fluorescein labelled heparin. Although the aldehyde group at the reducing end in equilibrium with the closed ring form; i.e. the hemiacetal group, the use of the aniline-like fluorophore; fluoresceinamine is reported to boost the efficiency of the reaction.[243] Subsequently, the dark quencher; BHQ1-Amine was conjugated to the produced fluorescent heparin through carbodiimide chemistry using EDC/NHS reaction. Figure 4.9 shows a schematic illustration of the intrachain and end-chain conjugation of the fluorophore.

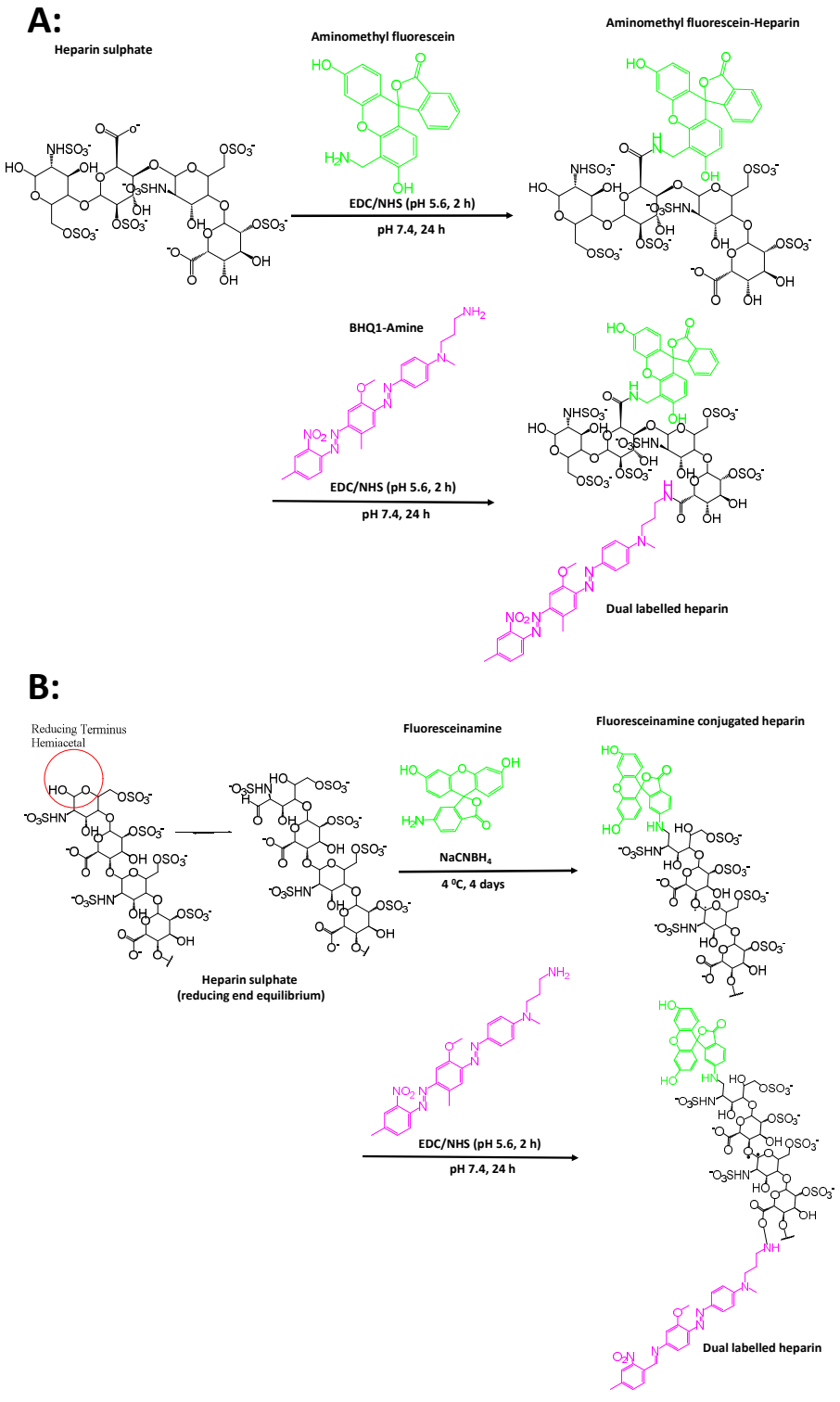


Figure 4.9 Schematic representation of Dual labelled heparin sensing probe synthesised by (A) intrachain conjugation of aminomethyl fluorescein and black hole quencher 1 (BHQ1) to heparin using EDC/NHS coupling agents, and dual labelled heparin sensing probe synthesised by end-chain conjugation of fluoresceinamine using reductive amination method and intrachain conjugation of black hole quencher 1 (BHQ-Amine) to heparin using EDC/NHS coupling agents.

4.4.1.1 *Fluorescence quenching efficiency of the dual labelled heparin prepared by intrachain conjugation method*

The fluorescence quenching of fluorescein that is bound to dual labelled heparin probe was observed by measuring the fluorescence of fluorescein labelled heparin probe obtained by the first step of the reaction compared to dual labelled heparin prepared by intrachain conjugation of the FRET pairs. The fluorescence of dual labelled heparin probe dramatically decreased compared to fluorescein labelled heparin probe as demonstrated in Figure 4.10. This indicates that the interaction between the donor; aminomethyl fluorescein and the acceptor; BHQ1-Amine is strong, where heparin acts as a bridge to bring the FRET pair close together for efficient energy transfer. Furthermore, the calculated quenching efficiency of this system using equation 2 was 55% and no additional quenching was seen after increasing the molar ratio of the black hole quencher (BHQ1) to heparin molecules as illustrated in Figure 4.11.

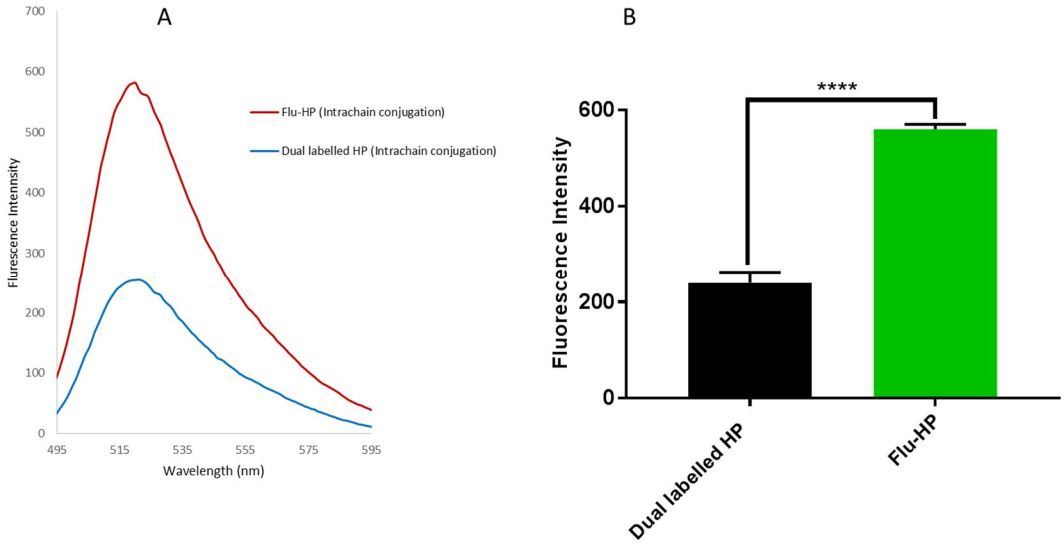


*Figure 4.10 Florescence quenching of the dual labelled heparin probe. A: Fluorescence spectrum, B: Fluorescence Intensity of dual labelled heparin prepared by intrachain conjugation of fluorescein and BHQ1 to heparin carboxylate groups (Dual labelled HP) compared to fluorescein labelled heparin(Flu-HP)prepared by intrachain conjugation of fluorescein. Data was analysed using unpaired t test. Error bars indicate SD (n = 3), ** is P ≤ 0.01, *** is P ≤ 0.001**** is P ≤ 0.0001.*

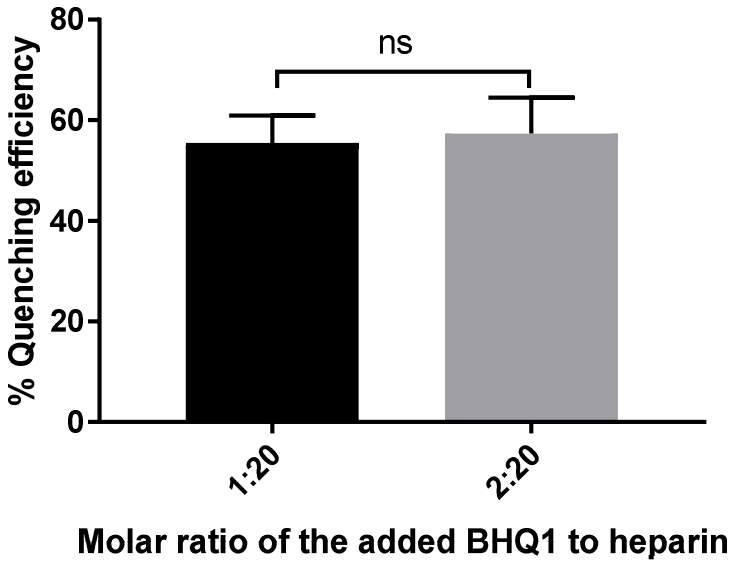


Figure 4.11 Quenching efficiency of the dual labelled heparin prepared using intrachain conjugation of the FRET pair at different molar ratio of BHQ1 to heparin showing that the maximum quenching efficiency has been achieved at 1:20 molar ratio. Data was analysed using unpaired t test. Error bars indicate SD (n = 3), ns is non-significant difference (P-value ≥ 0.05).

4.4.1.2 Fluorescence quenching efficiency of the dual labelled heparin prepared by end-chain conjugation method

The fluorescence quenching of the prepared dual labelled heparin probe was studied by measuring the fluorescence of the fluoresceinamine labelled heparin compared to the fluorescence of the dual labelled probe. The fluorescence of the dual labelled probe decreased relative to fluoresceinamine labelled heparin as demonstrated in Figure 4.12. However the calculated quenching efficiency by equation 2 was 14 % which is significantly lower than that obtained from the dual labelled heparin system prepared by intrachain conjugation of the FRET pair.

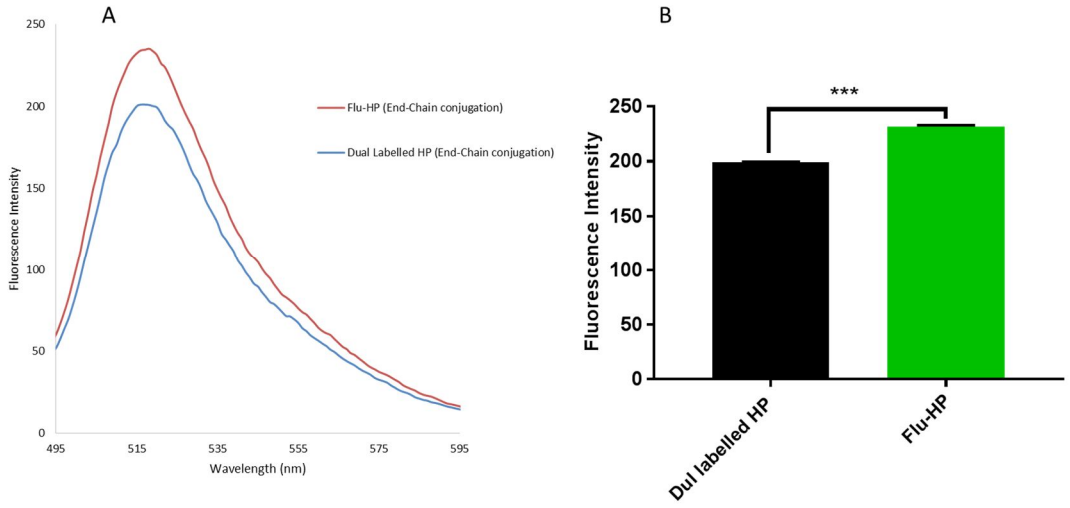


*Figure 4.12 Fluorescence quenching of the dual labelled heparin probe. A: Fluorescence spectrum, B: Fluorescence intensity of dual labelled heparin prepared by end-chain conjugation of fluorescein to heparin carboxylate groups (Dual labelled HP) compared to fluorescein labelled heparin (Flu-HP) prepared by end-chain conjugation of fluorescein. Data was analysed using unpaired t test. Error bars indicate SD (n = 3), ** is P ≤ 0.01, *** is P ≤ 0.001, **** is P ≤ 0.0001.*

4.4.1.3 Comparison study between end-chain and intrachain conjugation of the fluorophore

Although the FRET quenching process works effectively at donor-acceptor distances less than 10 nm, other factors like spectral overlap and molecular orientation also affect the fluorescence quenching and energy transfer. Molecular orientation of the FRET pair affects the geometry of dipole-dipole interaction of the donor and acceptor, consequently it governs the effective donor-acceptor distance.[304]

The quenching efficiency of the prepared dual labelled heparin probe by the previously described methods drastically differed by changing the chemical conjugation method of the donor. Intrachain conjugation of the donor and the acceptor that was used in the first method may have provided a strong van der Waals interaction between the FRET pair and enhanced the pi stacking between them so they are well aligned. Consequently the distance between the fluorophore, fluorescein and the dark quencher; BHQ1 was relatively smaller than the effective donor-acceptor distance of the dual labelled heparin probe prepared by end-chain conjugation of the donor as depicted in Figure 4.13. Hence the quenching

efficiency is higher as the FRET energy transfer is highly dependent on the Forster distance, where it is inversely proportional to the donor-acceptor distance (R) falling off at rate $1/R^6$ as demonstrated in Equation 4.3. In contrast, the dual labelled heparin probe prepared using the second method by end-chain conjugation of the fluorophore; fluoresceinamine while keeping BHQ1 attached within heparin chain, did not show as high quenching efficiency values. This could be attributed to the molecular orientations of the fluorescent donor and the acceptor. In general, atoms within specific molecules can rearrange in specific geometries in accordance to their electrostatic and van der Waals interactions in order to attain the lowest energy and most stable conformation of the molecule.[305-308] The predicted theoretical distance between end- chain conjugated fluoresceinamine and BHQ1 is larger than the donor-acceptor distance in dual labelled heparin probe prepared by intrachain conjugation method as demonstrated in the Chem3D drawing in Figure 4.13. This explains the higher quenching efficiency of dual labelled heparin prepared by intrachain conjugation method compared to that prepared by end-chain conjugation method.

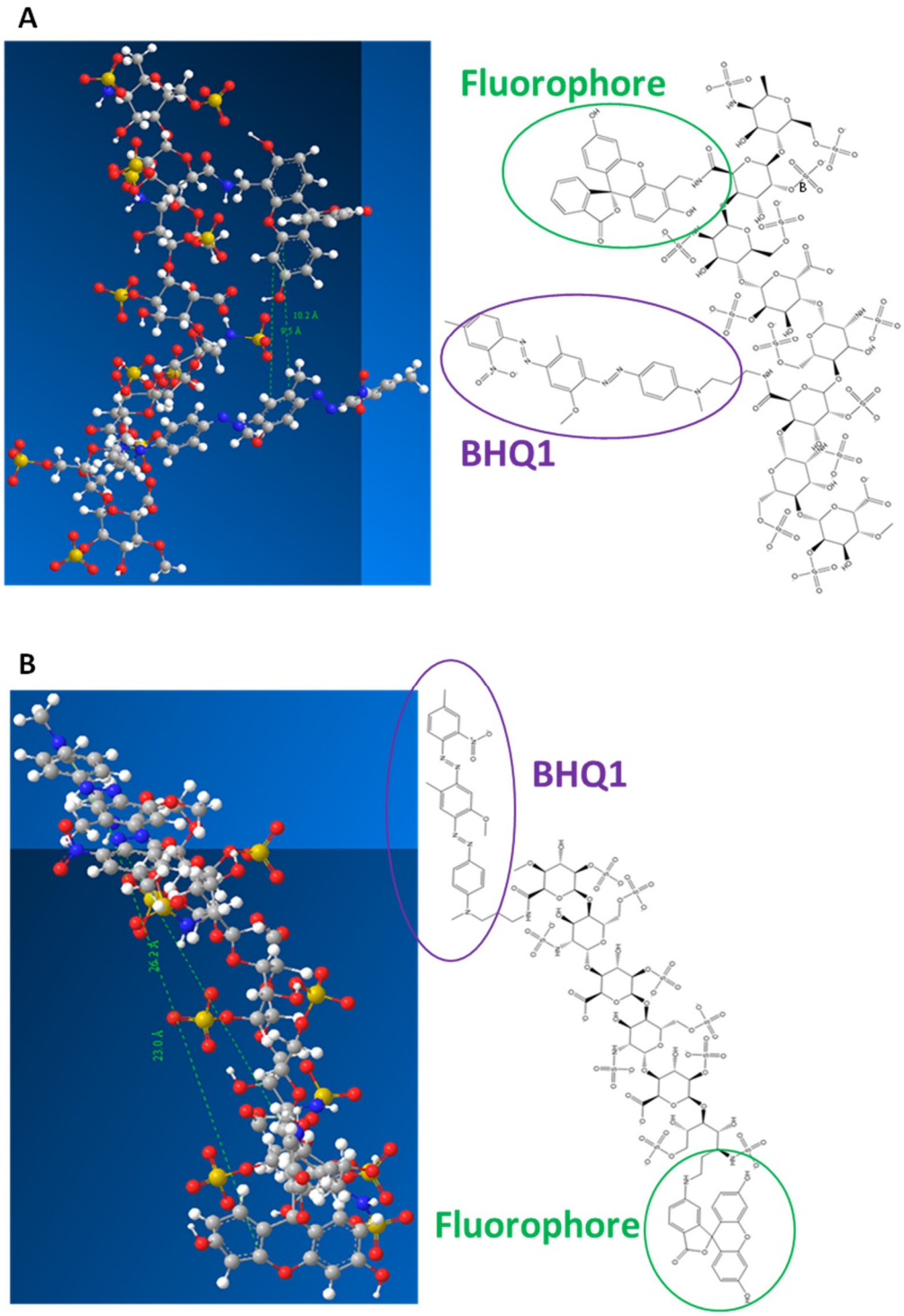


Figure 4.13 3D chemical structure of dual labelled heparin probe. A: 3D structure of dual labelled heparin prepared by intrachain conjugation of fluorescein and BHQ1. B: 3D structure of dual labelled heparin prepared by end-chain conjugation of fluorescein while attaching the BHQ1 within heparin chain. Data was analysed by MM2 energy minimization calculations using ChemBio3D software.

4.4.1.4 Study the role of covalent binding and inter/intra-molecular interaction between the FRET pair

An investigation was conducted to study the role of inter/intra-molecular dimerization in FRET pair fluorescence quenching. The results illustrated in Figure 4.14 A reveal that the measured fluorescence signal of the ternary physical mixture of positively charged BHQ1-Amine, positively charged aminomethyl fluorescein and negatively charged heparin was less than that of the physical mixture of aminomethyl fluorescein and heparin. This can be explained by the ionic interaction between the FRET pair and oppositely charged heparin chain, however the quenching efficiency was lower than that observed in the covalently bound FRET pair to heparin in dual labelled heparin probe using intrachain conjugation method. The lower quenching efficiency of the physical mixture of the FRET pairs and heparin compared to the intrachain conjugated FRET pairs in the dual labelled heparin might be attributed to non-directional ionic bonds compared to a covalent bond which brings the FRET pair in close proximity to each other in an aligned manner and maximises the quenching efficiency.[309-311] On the other hand, there was no difference in the fluorescence signal between the ternary physical mixture of negatively charged BHQ1-Carboxylate, negatively charged carboxyfluorescein and negatively charged heparin and the physical mixture of negatively charged carboxyfluorescein and negatively charged heparin as shown Figure 4.14 B.

This is considered evidence that the intra-molecular rather than inter-molecular dimerisation of the donor and acceptor in the FRET pair is required for efficient quenching as the inter-molecular interaction between a similarly charged pair, the fluorophore and the dark quencher, in the physical mixture (non-ionically bound to heparin) did not show any effect on the fluorescence intensity. This is in agreement with previously reported findings.[312]

The fluorescence quenching that was observed in the dual labelled heparin probe prepared by the intrachain conjugation was due to the covalent linking of the FRET pair to heparin chains and subsequent intra-molecular dimerisation of the donor; aminomethyl fluorescein

and the acceptor; BHQ1. Thus, these findings confirm that fluorescence quenching attained by dual labelled heparin is FRET based, and not via a collisional mechanism as the the donor-acceptor interaction is thought to happen through space but not through contact collision.

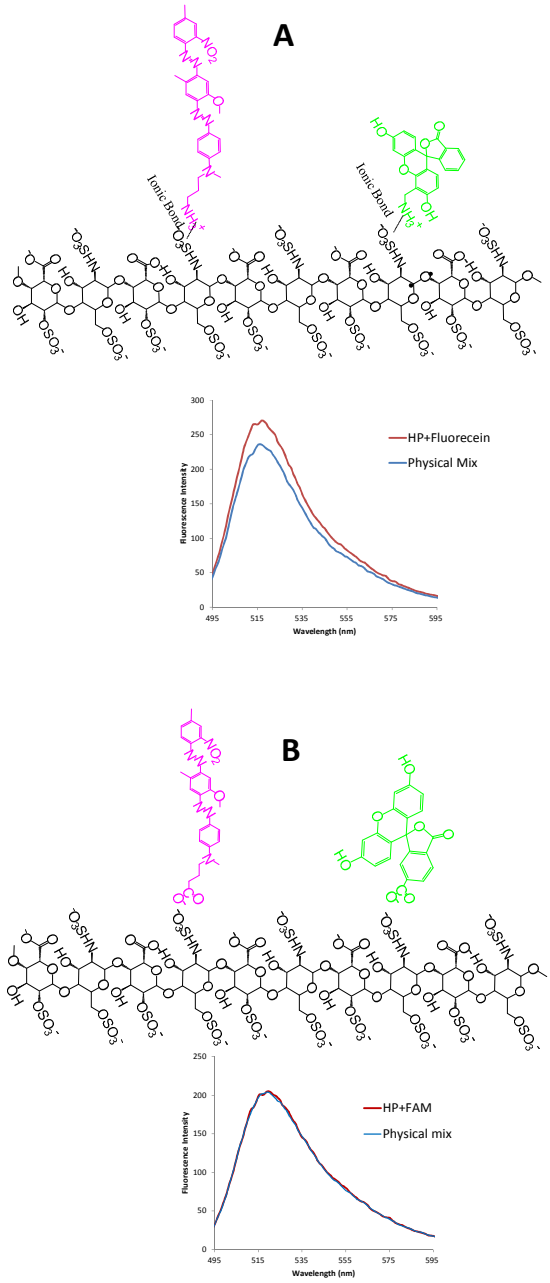


Figure 4.14 Effect of inter/intra-molecular dimerization of the FRET pairs. A: The fluorescence of fluoresceinamine in combination with positively charged BHQ1-Amine and negatively charged heparin (Physical mix) compared to physical mix of heparin and aminomethyl-fluorescein and the corresponding chemical structures of the physical mixture. B: The fluorescence of negatively charged carboxyfluorescein in combination with negatively charged BHQ1 and negatively charged heparin (Physical mix) compared to physical mixture of heparin and fluorescein (HP+FAM) and the corresponding chemical structures of the physical mixture.

4.4.1.5 *Fluorescence signal recovery of dual labelled heparin probe using chemical degradation*

In order to restore the fluorescence signal of the quenched fluorescein in dual-labelled probes prepared by intrachain conjugation, nitrous acid was used at low pH. Heparin is usually depolymerised by nitrous acid at pH 1.5 through deaminative cleavage of N-sulphate groups to produce anhydromannose derivatives of heparin which are mainly disaccharides.[313-315] Figure 4.15 illustrates the degradation of the dual-labelled heparin probe to produce heparin disaccharides, subsequently separating the fret pair. Thus the intra- molecular dimerisation is no longer available after the degradation reaction and fluorescence signal recovery is expected to occur as the energy transfer between the donor and the acceptor vanishes in the physical mixture of the FRET pair.

In order to confirm the complete degradation of heparin chain by nitrous acid at pH 1.5, the azure A test was used. Heparin depolymerised by nitrous acid described in 4.3.2.5 did not show a λ_{max} shift after mixing with azure A dye compared to intact heparin as shown in Figure 4.16. This reinforces that complete degradation of heparin with disaccharide formation was induced by nitrous acid as heparin disaccharides are not able to blue shift azure A λ_{max}, hence they lose the metachromatic activity compared to oligosaccharide and full chain non-depolymerised heparin.[168]

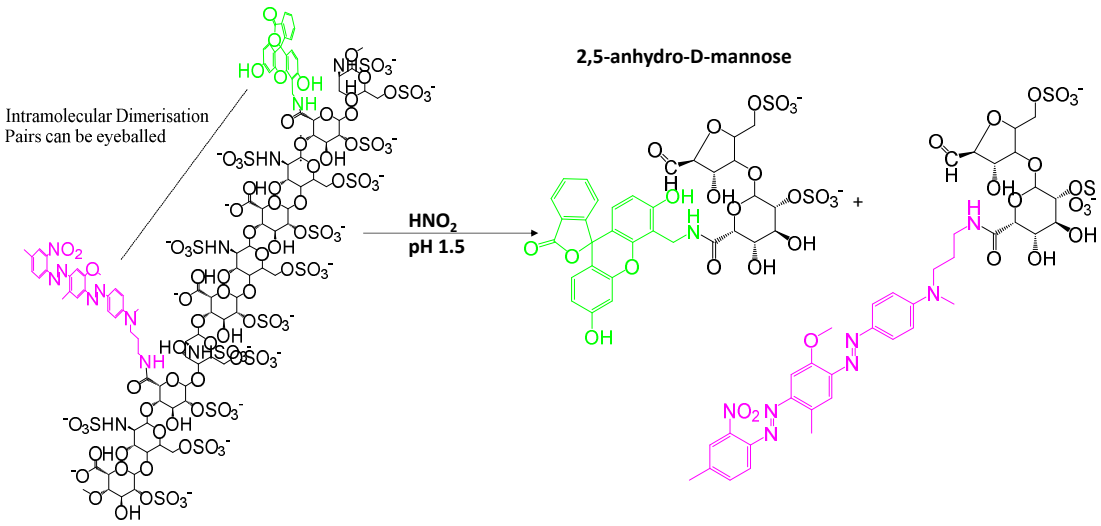


Figure 4.15 Schematic representation of dual labelled heparin probe depolymerisation by nitrous acid. Deaminative cleavage of dual labelled heparin probe to produce 2, 5-anhydromannose derivatives releasing the quenched fluorescein into the solution to recover the fluorescence signal.

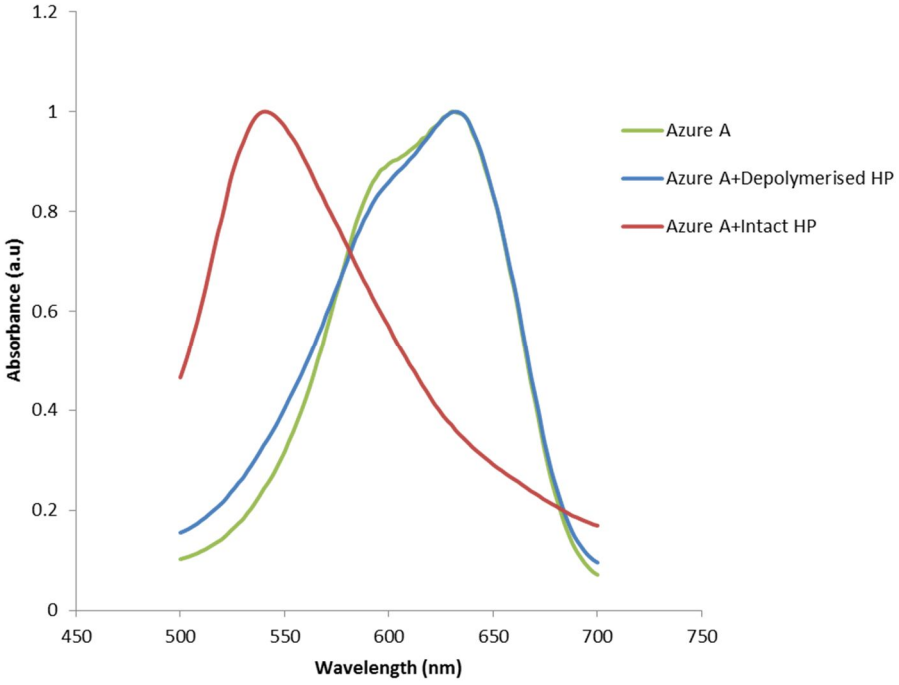


Figure 4.16 Complete degradation of heparin by Nitrous acid at pH 1.5. Azure A absorption spectrum after addition of depolymerised heparin by nitrous acid (Azure A + Depolymerised HP) and intact heparin (Azure A + Intact HP).

The fluorescence signal recovery was evaluated by measuring the fluorescence of the dual-labelled heparin before and after nitrous acid depolymerisation. The results demonstrated in Figure 4.17 show that the fluorescence intensity of dual labelled heparin markedly increased after nitrous acid degradation. This indicates a near complete restoration of fluorescein

fluorescence signal after the bond cleavage between fluorescein and BHQ1. Furthermore, ~90 % of the original aminomethyl fluorescein fluorescence intensity in the dual labelled probe was restored after chemical degradation.

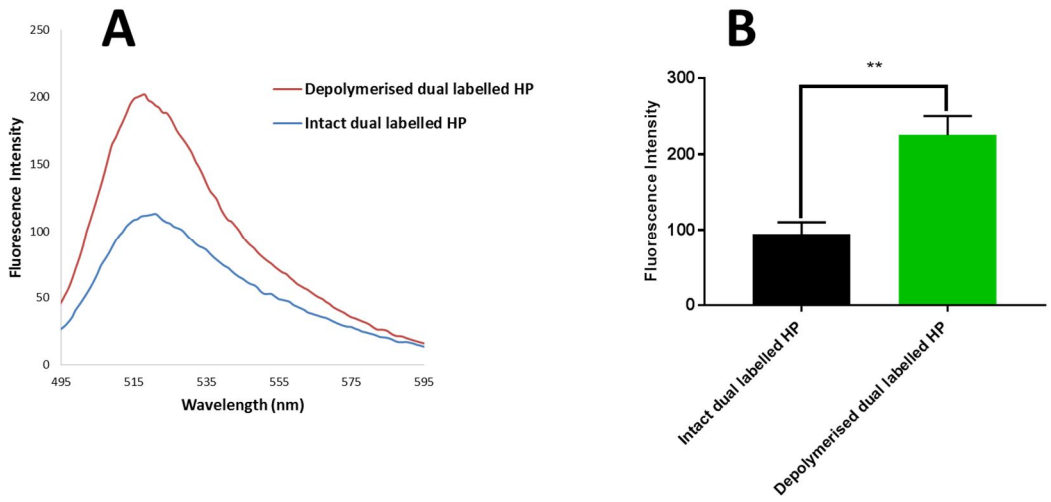


*Figure 4.17 Fluorescence signal recovery of dual labelled heparin depolymerisation using nitrous acid at pH 1.5. Emission spectra (A) and emission intensity (B) of dual labelled heparin after depolymerisation by nitrous acid. Data was analysed using unpaired t test. Error bars indicate SD (n = 3), ** is P ≤ 0.01.*

4.4.1.6 Fluorescence signal recovery of dual labelled heparin probe after heparinase treatment

The responsiveness of the prepared dual-labelled heparin probe to heparinase was evaluated by incubating the dual labelled heparin with heparinase I&II for 24 hours at 25 °C and measuring the fluorescence intensity compared to untreated dual labelled heparin as a control. The fluorescence intensity of the dual labelled heparin slightly increased after heparinase treatment compared to untreated control as depicted in Figure 4.18 This is thought to be due to incomplete digestion of the dual labelled heparin by the enzymes; heparinase I&II. Moreover, the presence of the FRET pair attached to the carboxylate groups might hinder enzyme-heparin binding, consequently reducing the activity of heparinases against heparin. It is important to note that the free carboxylate moiety of uronic acid residue

is essential for enzymatic activity of all heparinases. For instance, when heparin was treated with EDC (1-ethyl-3-[3-dimethylaminopropyl] carbodiimide), its susceptibility to heparinases was reduced. Heparinase degrading activity against heparin was decreased with the increase of the molar concentration of the reacted EDC.[316]

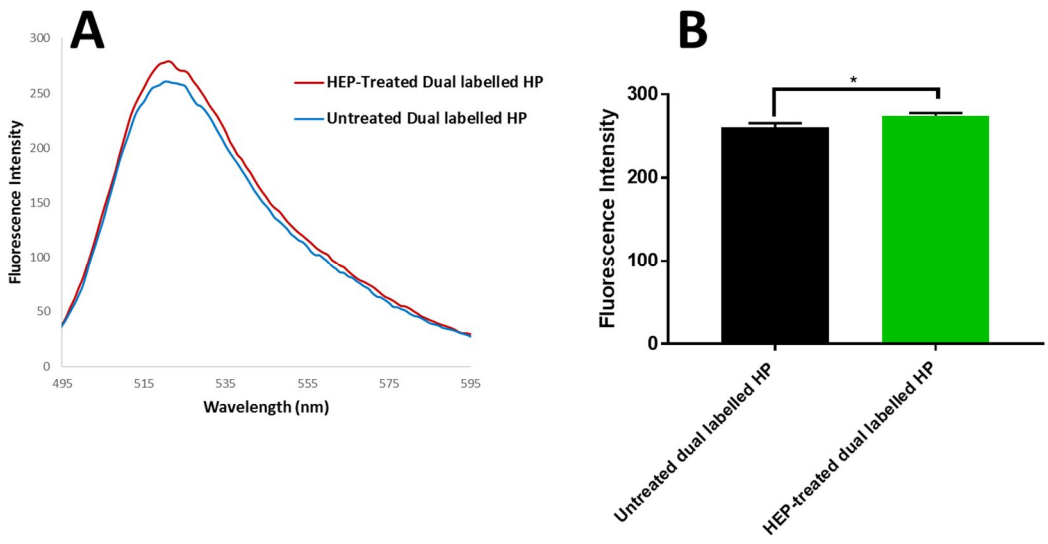


*Figure 4.18 Fluorescence signal recovery of dual labelled heparin probe after incubation with heparinase I and II for 24 hours. Fluorescence spectra (A) and Fluorescence intensity (B) of heparinase treated dual labelled heparin probe (HEP-treated dual labelled HP) compared to untreated dual labelled heparin probe (Untreated dual labelled HP). Data was analysed using unpaired t test. Error bars indicate SD (n = 3), * is P ≤ 0.05.*

4.4.2 Development of heparinase nanosensors using model II

4.4.2.1 Synthesis of core-shell NPs containing unmodified core

4.4.2.1.1 Optimisation and characterisation of the core-shell NPs

A core-shell nanoparticle system was adopted in order to enhance the fluorescence quenching between the acceptor and the donor in the FRET pair as the dual labelled heparin probe failed to achieve a prober fluorescence signal restoration after heparinases treatment as shown in section 4.4.1.6.

The diameter of silica NPs was optimised to produce different core-shell NPs with various shell thicknesses containing a covalently linked TAMRA dye. NPs with shell thicknesses; 12, 25, 45 and 75 nm were produced by optimising the amount of APTES, APTES-TAMRA conjugate attached to the surface, the concentration of the ammonium hydroxide and by controlling the time of the reaction. The shell thickness of the produced NPs was estimated by measuring the particle size of a blank unlabelled core silica NPs before and after surface modification with TAMRA. The results depicted in Figure 4.19.

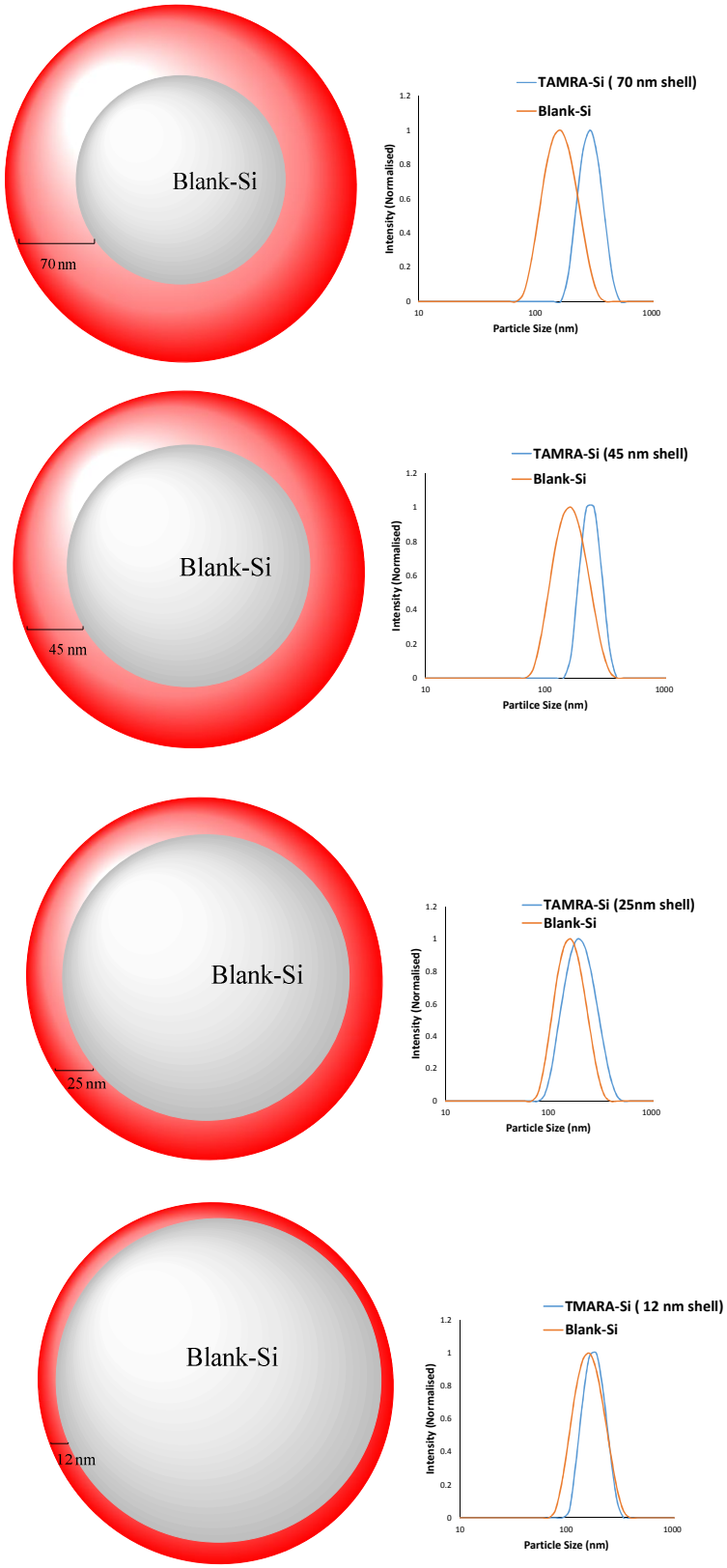


Figure 4.19 Illustrative diagram of core-shell NPs with different shell thicknesses ranging from 12 nm to 70 nm and their corresponding particles size distribuations relative to blank silica core size distribution measured by dynamic light scattering (DLS).

4.4.2.1.2 Fluorescence spectra of the optimised core-shell NPs

In order to assess the incorporation of TAMRA within the shell of the produced core-shell NPs, the fluorescence spectra was obtained by spectrofluorometer. The fluorescence of the core-shell NPs rises with increasing the shell thickness as illustrated in Figure 4.20. This indicates that high amount of TAMRA was incorporated within the shell as the thickness increases, reflecting the high fluorescence of the large thickness NPs.

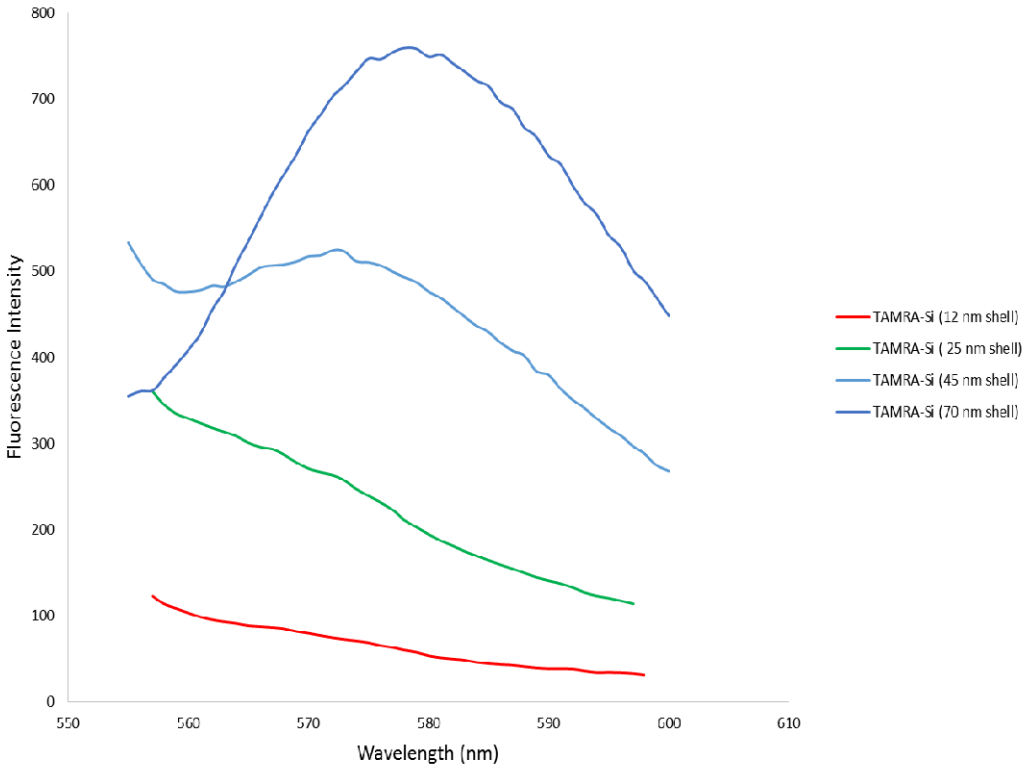


Figure 4.20 Fluorescence spectra of TAMRA incorprated within the outer layer of different core-shell silica NPs containing blank core silica matrix having diffeent thicknesses of their shells ranging from 12 nm to 70 nm.

4.4.2.1.3 Preparation of core-shell FRET based NPs

FRET based core-shell nanosensors were prepared by grafting BHQ2 conjugated heparin probe onto the surface of amine functionalised core-shell NPs containing TAMRA in the shell. The BHQ2-heparin probe was firstly synthesised using EDC/NHS coupling of the amine groups of BHQ2-Amine to heparin carboxylate groups. Then BHQ2-heparin probe was attached to

the surface of amine functionalised core-shell NPs with 12 nm shell thickness using carbodiimide chemistry as depicted in Figure 4.21.

FRET quenching works effectively when the fluorophore-quencher distance is less than 10 nm, however the fluorescence quenching by FRET mechanism is not fully understood yet and other factors can affect the efficiency of quenching.[317] Although the fluorescence signal of the core-shell NPs increased with increasing the shell thickness as demonstrated in section 4.3.3.4, 12 nm core-shell system was chosen to achieve effective fluorescence quenching of the FRET pair.

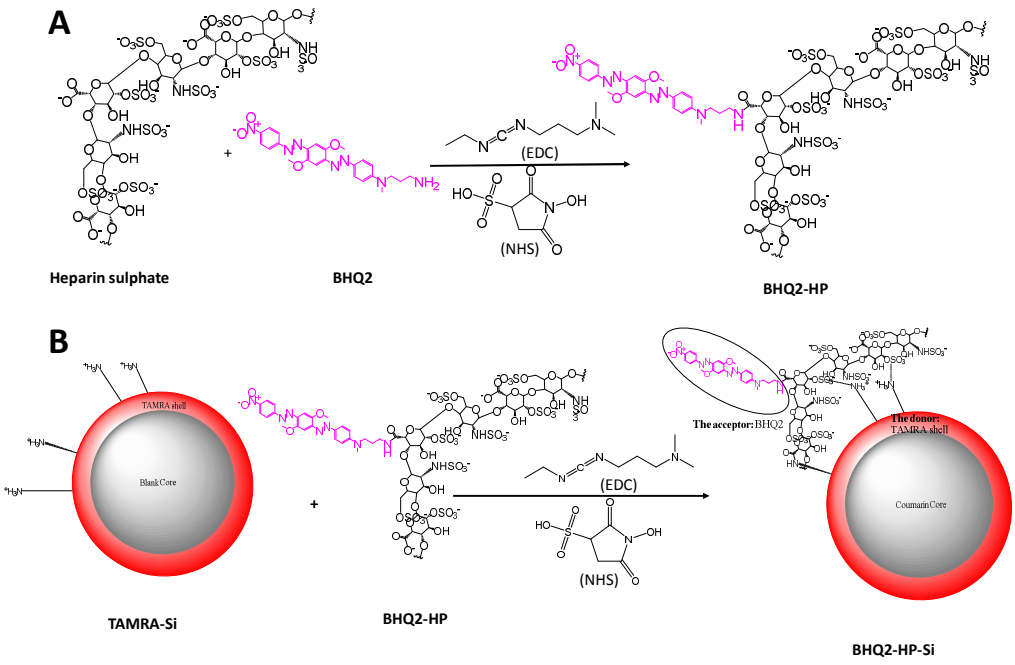


Figure 4.21 Schematics of A: BHQ2 conjugated heparin probe synthesis using EDC/NHS coupling reaction , B: BHQ2 conjugated heparin (BHQ2-HP) probe grafting onto the surface of TAMRA containing 12 nm shell NPs (TAMRA-Si) to produce FRET based TAMRA-BHQ2, donor-acceptor system (BHQ2-HP-Si) using EDC/NHS reaction.

4.4.2.1.4 Spectral overlap and fluorescence quenching of the donor-acceptor pair in the prepared nanosensors

Black hole quencher-2 (BHQ-2) is considered the most suitable dark quencher for TAMRA dye as a FRET pair as demonstrated in Table 1, since the absorption spectrum of the BHQ-2 overlaps with the emission spectrum of TAMRA.

Results illustrated in Figure 4.22 show that BHQ2-Heparin conjugate has absorption spectrum similar to free BHQ2 before conjugation indicating successful conjugation of the BHQ2 to heparin. Furthermore, the absorption spectrum of the acceptor; BHQ2-heparin conjugated to the surface of core-shell NPs overlaps well with the emission spectrum of the donor; TAMRA incorporated within the shell of the prepared NPs. This spectral overlap of the FRET pair makes the core-shell system suitable for FRET based quenching mechanism.

Fluorescence quenching of the 12 nm shell system was evaluated by measuring the fluorescence intensity of the TAMRA containing core-shell NPs with 12 nm shell thickness before and after grafting the BHQ2-Heparin conjugate to the surface of the 12 nm TAMRA containing NPs.

A significant reduction in the fluorescence of TAMRA labelled core-shell NPs was observed after conjugation BHQ2-Heparin probe to the NPs surface of the NPs as demonstrated in Figure 4.22 B and C. Indicating that FRET based quenching occurred between the donor; TAMRA dye in the shell of the NPs and the acceptor; BHQ2 that is conjugated to heparin which is attached to the surface of the NPs. In addition, the estimated quenching efficiency of the prepared system calculated using was ~ 40%.

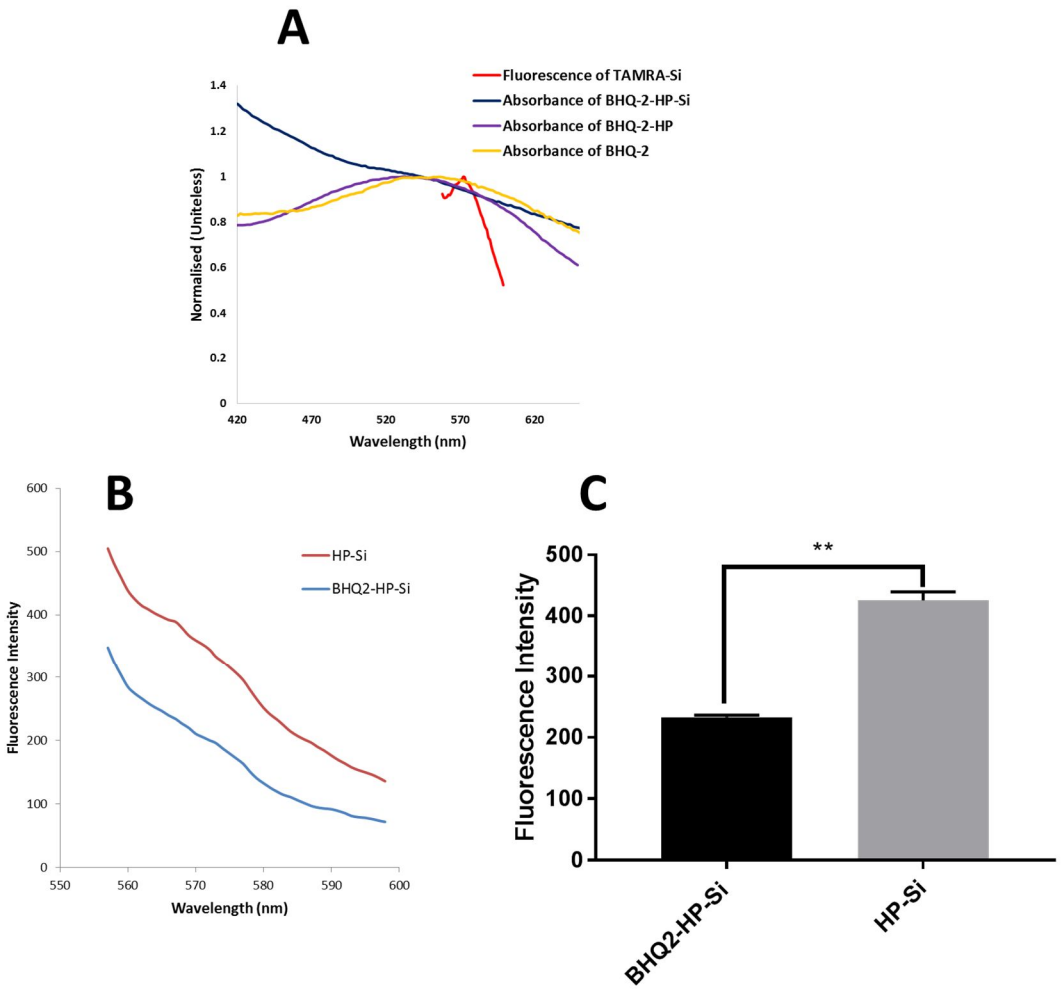


*Figure 4.22 A: Spectral overlap of the absorption spectra of black hole quencher (BHQ2), black hole quencher conjugated heparin probe (BHQ2-HP) and black hole quencher conjugated heparin grafted onto the surface of core-shell silica NPs (BHQ2-HP-Si) and the fluorescence spectrum of TAMRA-labelled core-shell NPs. Fluorescence spectra (B), and fluorescence intensity (C) heparin conjugated core-shell NPs containing TAMRA incorporated within the shell (HP-Si) compared to black hole quencher–heparin conjugated core-shell NPs containing TAMRA incorporated within the shell (BHQ2-HP-Si). Data was analysed using unpaired t test. Error bars indicate SD (n = 3), ** is P ≤ 0.01, *** is P ≤ 0.001**** is P ≤ 0.0001.*

4.4.2.2 Design of coumarin based core-shell system

Although the quenching efficiency of 12 nm-shell FRET based nanosensors was high (~40%), the prepared system is not highly controlled. The distance between the donor and the acceptor in the designed core-shell system was more than the ideal distance for effective FRET energy transfer (10 nm). This means that the obtained quenching efficiency had to be calculated using more accurate system to confirm that the attained data was reliable and realistic. Consequently the need for a better designed, well controlled system has arisen. In order to solve this problem, 7-methoxy coumarin; a BHQ2 non-responsive dye was incorporated within the core of core-shell NPs to serve as internal standard for the system which is thought to eliminate fluorescence fluctuations caused by temperature change, uneven distribution of the fluorophore concentration and particle size differences as demonstrated in Figure 4.23 A.

To confirm that 7-methoxy coumarin is a BHQ2-insensitive dye, spectral overlap between the fluorescence of 7-methoxy coumarin or 7-methoxy coumarin containing NPs and the absorbance of BHQ2-Heparin probe or BHQ2-Heparin conjugated NPs was investigated. Figure 4.23 B shows that the absorption spectra of BHQ2-Heparin probe and BHQ2-Heparin conjugated NPs are not overlapping with absorption spectra of 7-methoxy coumarin or 7-methoxy coumarin containing NPs. This makes 7-Methoxy coumarin a useful reference fluorophore as FRET quenching is highly dependent on donor-acceptor spectral overlap, also because its excitation and emission spectra are significantly different to the spectrum of the BHQ2-sensitive fluorophore; TAMRA.

The quenching efficiency of TAMRA fluorescence by BHQ2-heparin probe was studied by measuring the fluorescence intensity of coumarin based core-shell NPs at two different emission wavelengths (i.e. 7-methoxy coumarin and TAMRA emission spectra). Both, the emission spectra of the 12 nm-TAMRA incorporated shell NPs containing 7-methoxy coumarin within the core after surface modification with unmodified heparin (control NPs) and the emission spectra of 12 nm-TAMRA incorporated shell NPs containing 7-methoxy

coumarin within the core after surface modification with BHQ2 conjugated heparin were recorded after excitation at 360 nm and at 540 nm respectively.

7-mthoxy coumarin emission spectra displayed no distinct changes, remaining nearly the same before and after conjugation of BHQ2-heparin probe to core-shell NPs surface as demonstrated in Figure 4.23 C. This is expected as 7-methoxy coumarin is not responsive to BHQ2. In contrast an expected significant reduction in TAMRA emission was observed after BHQ2-heparin probe attachment to core-shell NPs as shown in Figure 4.23 D, indicating a responsiveness of TAMRA to BHQ2. Moreover, a TAMRA:Coumarin fluorescence ratio plot was generated by calculating a ratio of the emission intensities of the BHQ2 responsive; TAMRA and BHQ2 non-responsive; 7-methoxy coumarin at 380 nm and 575 nm emission wavelengths respectively as depicted in Figure 4.23 E. However, the actual quenching efficiency calculated using equation 2 was ~ 10%, which is lower than the previously estimated quenching efficiency (~40%) of 12 nm-TAMRA incorporated shell NPs containing a blank core. This is thought to be due to blank silica particle weight increase after conjugation of BHQ2-heparin probe to NPs surface compared to native heparin conjugated NPs. Assuming the same number of the precursor blank NPs before the process of conjugation, the particle-weight increase of the BHQ-HP conjugated NPs might eventually lead to a reduction in the fluorescence of BHQ2-heparin conjugated NPs correlated with the lower number of particles (lower amount of fluorophore) compared to the same amount (concentration) of native heparin conjugated NPs as demonstrated in Figure 4.24.

The quenching efficiency was measured by using TAMRA:Coumarin fluorescence ratio rather than by measuring a TAMRA fluorescence intensity before and after attaching the BHQ2. Accordingly, the reduction in the TAMRA fluorescence intensity due to particle-weight increase would not influence the measured quenching efficiency as the TAMRA:Coumarin fluorescence ratio would remain unchanged. In light of that the quenching efficiency

measured by coumarin based core-shell NPs represents the actual quenching efficiency of the core-shell system.

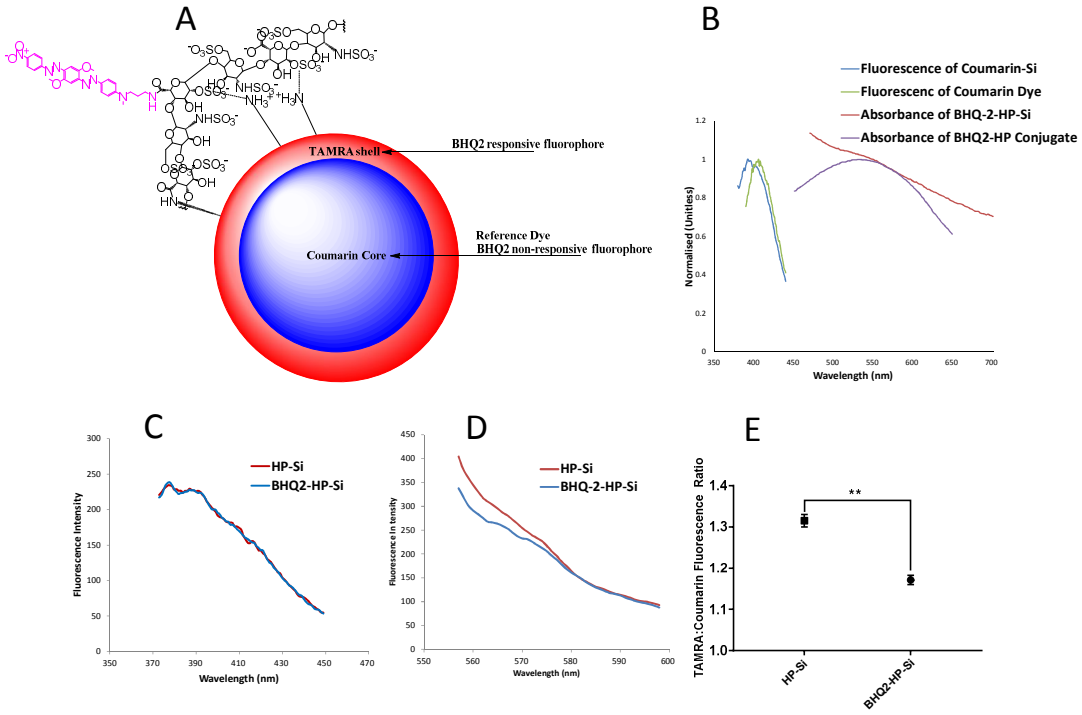


*Figure 4.23 A: Illustrative diagram of a ratiometric core-shell NPs composed of an inert nanoparticle core, encapsulating BHQ2-insensitive fluorophore; 7-Methoxycoumarin as a reference dye and shell containing BHQ2-sensitive fluorophore; TAMRA. B: Fluorescence spectra of coumarin dye and coumarin incorporated NPs (Coumarin-Si) alongside the absorption spectra of black hole quencher 2- heparin conjugate (BHQ2-HP conjugate) and black hole quencher 2-heparin conjugated core-shell silica NPs (BHQ2-HP-Si). Fluorescence spectra and fluorescent ratio of core-shell NPs containing shell modified with either heparin (HP-Si) or black hole quencher – heparin conjugate (BHQ2-HP-Si) and core consisting of coumarin as a reference fluorophore incorporated within the silica matrix. C: emission spectra of the BHQ2-insensitive fluorophore (7 methoxy coumarin), recorded on a spectrofluorometer after excitation at 360 nm. D: Emission spectra of the BHQ2-responsive dye incorporated in the nanoparticle shell (TAMRA) recodred on spectrophotometer after excitation at 540 nm, E: Fluorescent ratio of TAMRA to coumarin measured at emission wavelngths; 575 nm and 385 nm respectively. Data was analysed using unpaired t test. Error bars indicate SD (n = 3), ** is P ≤ 0.01.*

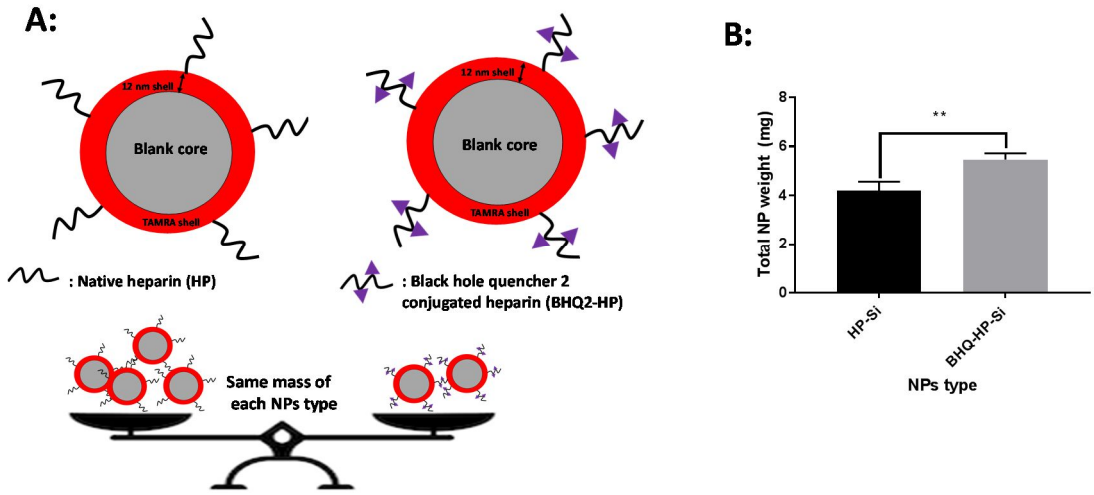


Figure 4.24 ***A:*** *Schematics showing a 12 nm core-shell NPs after appending of either native heparin (HP) or black hole quencher 2 linked heparin (BHQ2-HP). After weighing the same mass of each NPs type the number of BHQ2-HP conjugated NPs is speculated to be lower than the number of heparin conjugated NPs owing to the higher estimated particle-weight of BHQ2-HP conjugated NPs.* ***B:*** *Total Particles weight difference between BHQ2-HP conjugated NPs and heparin conjugated NPs having the same amount of the precursor blank NPs before the conjugation process and treated under exactly the same washing conditions. Data was analysed using unpaired t test. Error bars indicate SD (n = 3), ** is P ≤ 0.01.*

4.4.3 Development of heparinase nanosensors using model III

The actual quenching efficiency achieved by model II was relatively low ~10% (Coumarin based system) as the smallest shell that could have been attained was 12 nm, which is slightly larger than the optimum donor-acceptor distance for effective FRET quenching (10 nm), making the system less sensitive to heparinase and other biological applications. Consequently, model III was constructed by conjugating fluorescently labelled heparin to the surface of black hole quencher incorporated NPs.

4.4.3.1 Preparation of fluorescein labelled heparin

Aminomethyl fluorescein amine group was conjugated to heparin carboxylate group using EDC/NHS coupling reaction to obtain fluorescein labelled heparin probe as illustrated Figure 4.25 A.

The fluorescence spectrum of the produced fluorescently labelled heparin probe was measured and it was similar to that of free aminomethyl fluorescein fluorophore as shown in Figure 4.25 B. Indicating successful covalent linking of the fluorophore; aminomethyl fluorescein to heparin.

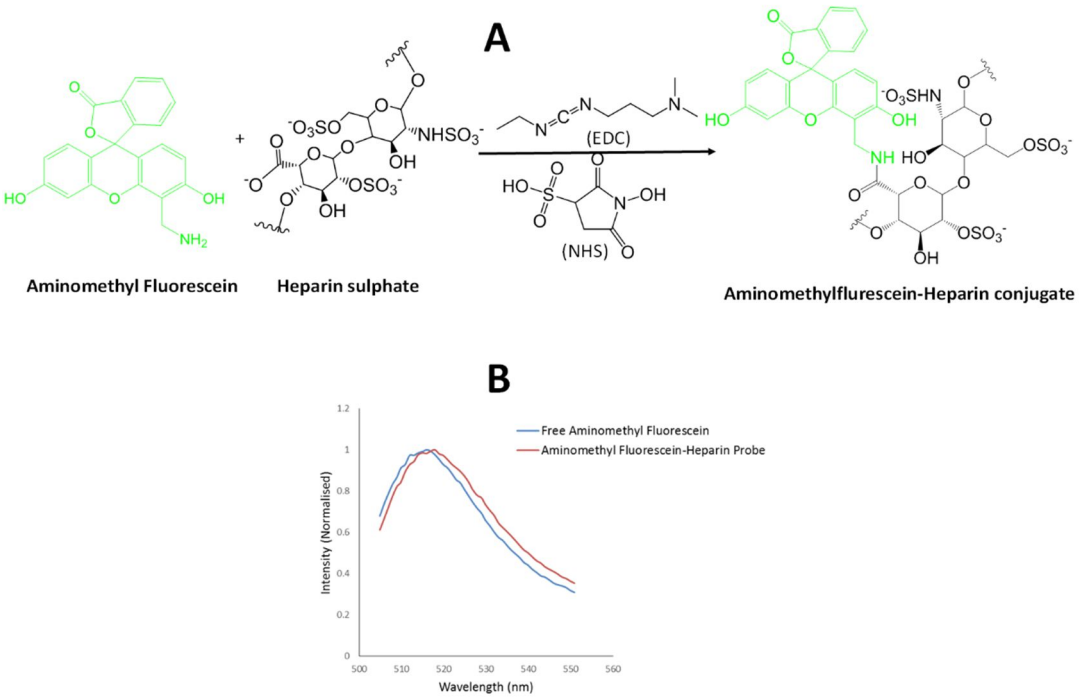


Figure 4.25 A: Schematic diagram of heparin conjugation with aminomethyl fluorescein through EDC/NHS coupling reaction to produce fluorescent heparin conjugate. B: Fluorescence spectrum of fluorescent heparin; aminomethyl fluorescein-heparin probe compared to free aminomethyl fluorescein dye.

4.4.3.2 Binding of fluorescein labelled heparin probe to the surface of BHQ1 incorporated NPs

In order to design fluorescein-BHQ1 based nanosensors, BHQ1-SE was covalently bound to APTES cross linker to produce BHQ1-APTEA conjugate. Subsequently, the conjugate was then incorporated within the silica NPs matrix through the siloxane bonds between APTES and TEOS during NPs formation as illustrated in Figure 4.26.

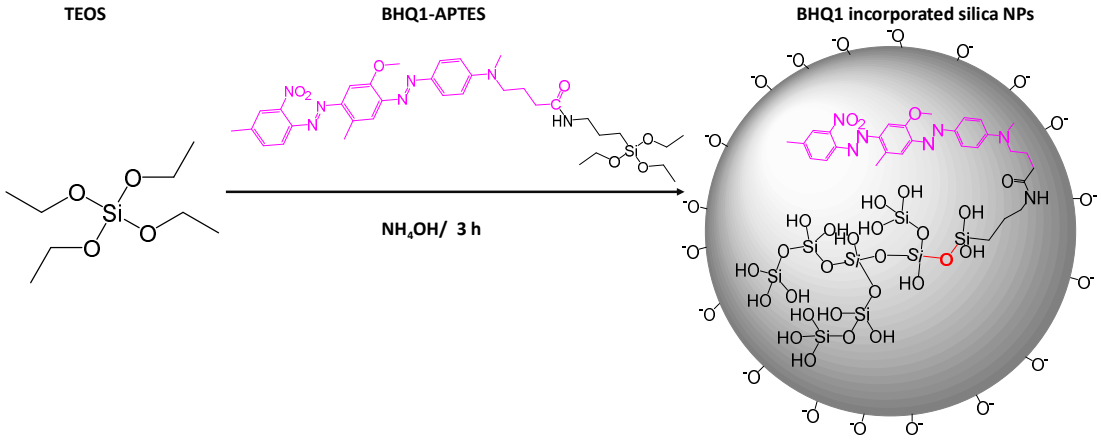


Figure 4.26 Schematic diagram of BHQ1 incorporation within the silica matrix of the NPs by attaching BHQ1-SE to APTES linker and subsequent BHQ1-APTES conjugate incorporation through formation of siloxane bonds (red) between APTES AND TEOS during the formation of silica NPs to produce BHQ1 incorporated silica NPs (BHQ1-Si).

BHQ1 incorporated silica NPs were further functionalised with amine groups on the surface of the NPs using APTES. The synthesised fluorescein labelled heparin was grafted onto the surface of amine functionalised BHQ1 incorporated silica NPs using carbodiimide chemistry to produce fluorescein-BHQ1; donor-acceptor FRET based nanosensors as depicted by Figure 4.27.

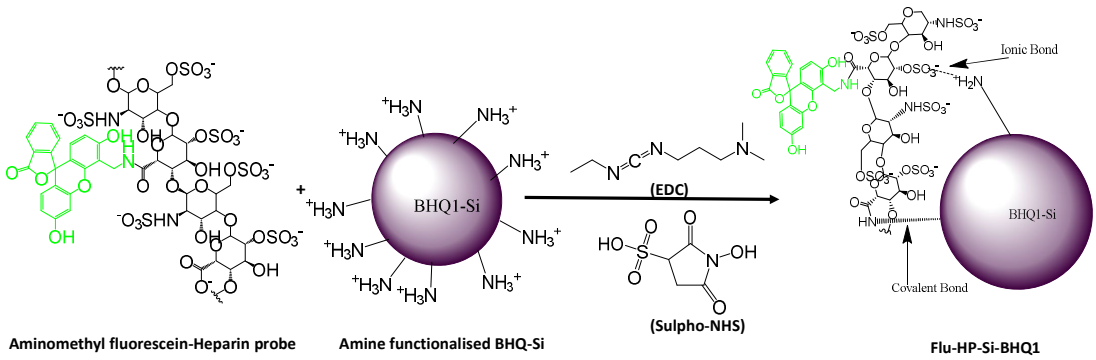


Figure 4.27 Schematic representing fluorescent heparin; aminomethyl fluorescein-heparin grafting onto the surface of black hole quenher1 (BHQ1) incorporated silica NPs using EDC/NHS coupling reaction to produce heparinase nanosensors (Flu-HP-Si-BHQ1).

4.4.3.3 Characterisation of BHQ1/Fluorescein FRET pair based nanosensors

4.4.3.3.1 Particle size

The diameter of the prepared nanosensors composed of fluorescently labelled heparin conjugated silica NPs containing a BHQ1 incorporated within the silica matrix (Flu-HP-Si-BHQ1 NPs) was measured by dynamic light scattering (DLS) and it was ~ 150 nm. In order to calculate the quenching efficiency of Flu-HP-Si-BHQ1 NPs, control NPs composed of fluorescently labelled heparin conjugated to the surface of silica NPs containing a blank silica matrix were prepared. The diameter of the control NPs was very similar to the diameter of the prepared model III nanosensors (Flu-HP-Si-BHQ1 NPs) as illustrated in Figure 4.28, thus minimizing any variation in the fluorescence measurement of the nanosensors and the control NPs due to particles size difference.

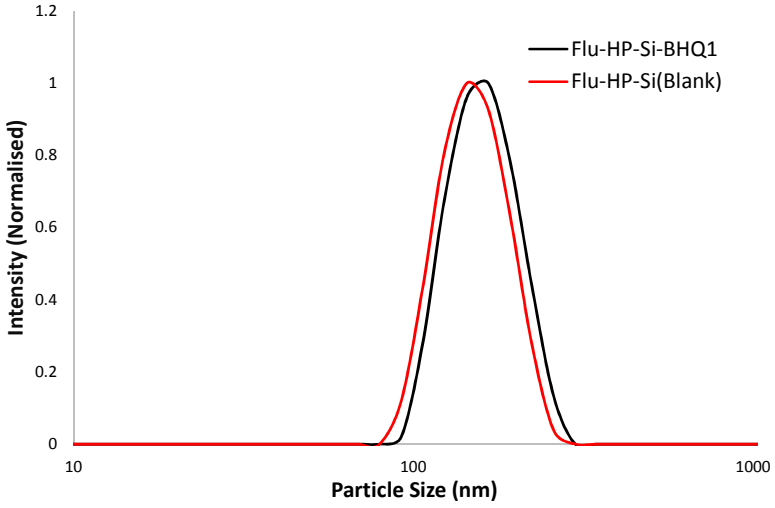


Figure 4.28 Particle size distribution of BHQ1 incorpotaed silica NPs (red) compared to blank silica marix NPs (black) meaured by DLS.

4.4.3.3.2 Absorption spectra of the nanosensors

In order to confirm the successful BHQ1 incorporation through the silica matrix during the NPs formation, the absorption spectrum of the covalently linked BHQ1 silica NPs was measured compared to that of free BHQ1 attached to APTES crosslinker. The results

demonstrated in Figure 4.29 reveal that the absorption spectrum of the BHQ1 incorporated nanosensors is quite similar to the absorption spectrum of BHQ1-APTES conjugate indicating successful incorporation of the BHQ1 quencher within the NPs matrix.

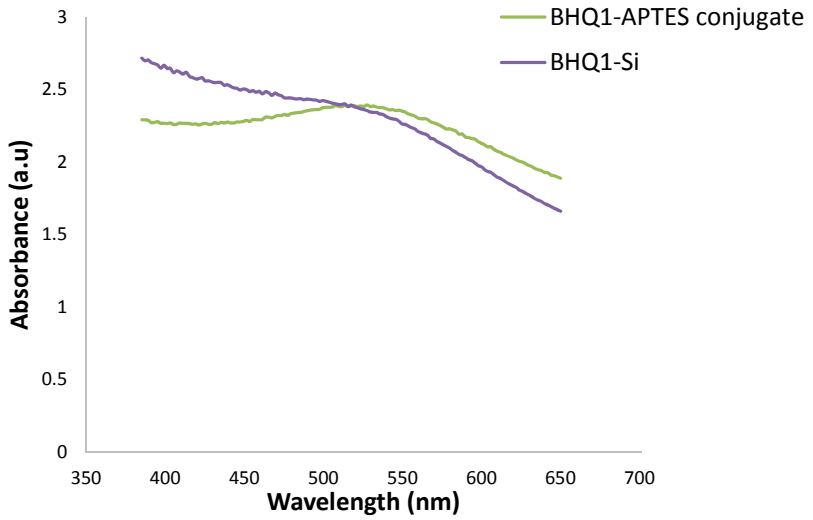


Figure 4.29 Absorption spectra of black hole quencher-1 (BHQ1) incorporated silica NPs (BHQ1-Si) compared to black hole quencher-1 (BHQ1) covalently attached to aminopropyltriethoxysilane; APTES (BHQ1-APTES conjugate).

4.4.3.4 Fluorescence quenching of the nanosensors

In order to assess the FRET pair interaction and the efficiency of energy transfer between fluorescein and BHQ1 in the nanosensors, the fluorescence intensity of either BHQ1 incorporated or blank NPs (BHQ1 free) was measured after covalent linking of the fluorescein labelled heparin probe (Flu-HP). BHQ1 containing nanosensors displayed a marked fluorescence reduction compared to NPs that have blank silica matrix after the conjugation process of fluorescein labelled heparin probe as illustrated in Figure 4.30. However the estimated quenching efficiency attained by this system was ~ 30%. Although fluorescein labelled heparin was directly attached to the surface of the nanosensors through the crosslinker APTES having very small chain length ~ 5 Å,[318] the thickness of polymerised APTES

after surface functionalisation is ~ 7 nm.[319] This makes a distance between fluorescein attached to the surface of the nanosensors and BHQ1 incorporated through the silica matrix, separating the FRET pair and minimising the donor-acceptor energy transfer.

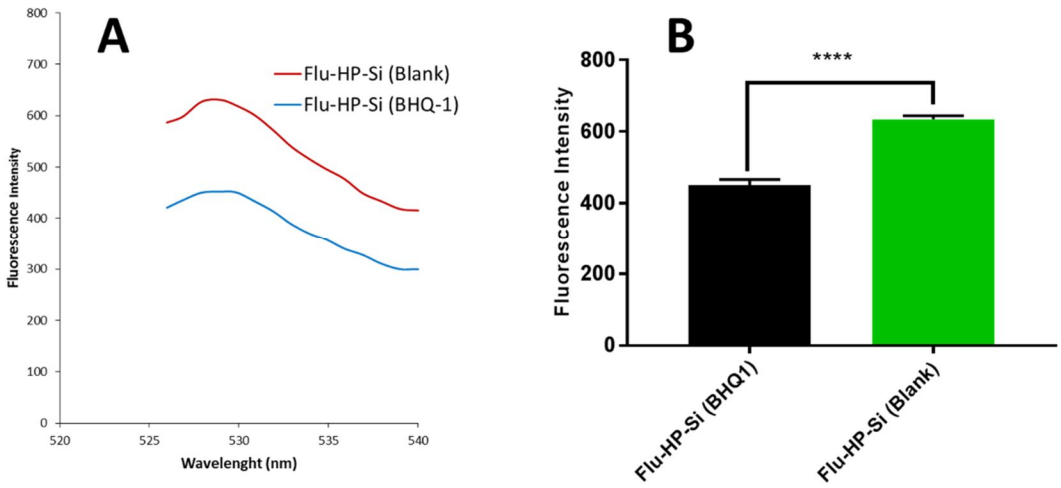


Figure 4.30 Fluorescence spectra (A) and fluorescence intensity (B) of fluorescent heparin (Flu-HP) conjugated to the surface of blank silica NPs (red) compared to fluorescent heparin labelled with aminomethyl fluorescein (Flu-HP) conjugated to the surface of black hole quencher-1 incorporated NPs (blue).

4.4.3.5 Fluorescence signal recovery after heparinase treatment

To determine the responsiveness of heparinase nanosensors to heparinase, the fluorescence intensities of the prepared nanosensors were measured in the presence and absence of heparinase I&II. Figure 4.31 A shows that there was no significant difference between the fluorescence intensities of heparinase treated and untreated nanosensors at pH 7. However, after enzyme treatment the pH of the buffer containing the nanosensors was raised from 7 to 11, accordingly a partial yet statistically significant increase was observed in the fluorescence intensity of the heparinase treated nanosensors compared to untreated nanosensors as shown in Figure 4.31 B. The pH of the untreated nanosensors was also raised to 11 using the same amount of sodium phosphate/sodium hydroxide buffer in order to exclude effect of pH on fluorescence of the aminomethyl fluorescein. A partial signal recovery of the heparinase treated nanosensors after pH raising could be explained by the presence

of ionic interaction between the negatively charged fluorescein labelled heparin probe and positively charged amine groups of BHQ1 incorporated nanosensors. Consequently, fluorescently labelled heparin fragments resulting from heparinase treatment remained close to the surface of the nanosensors, preventing fluorescence dequenching and signal recovery as demonstrated in Figure 4.32 A. In contrast, electrostatic interactions between fluorescently labelled heparin fragments and amine groups of BHQ-1 -incorporated NPs are no longer available after raising the pH of the nanosensors containing buffer as the amine groups become deprotonated at pH 11 which is above the reported pKa of immobilised APTES (pKa~ 7.6-9.6).[320-323] Subsequently the fragments are released into the bulk solution away from BHQ1 incorporated NPs surfaces as described in Figure 4.32 B.

The pH elevation was required after heparinase treatment in order to incompletely restore the fluorescence signal of the quenched fluorophore. Accordingly, this model represents a prototype that could be used to detect the presence of heparanase in blood sample taken from cancer patients; a widely used technique called liquid biopsy, where the pH of the blood sample containing appreciable amount of heparanase can be adjusted to high value (11) after adding the nanosensors. In contrast these nanosensors cannot be used for *in vivo* detection of heparanase as the physiological pH is 7.4.

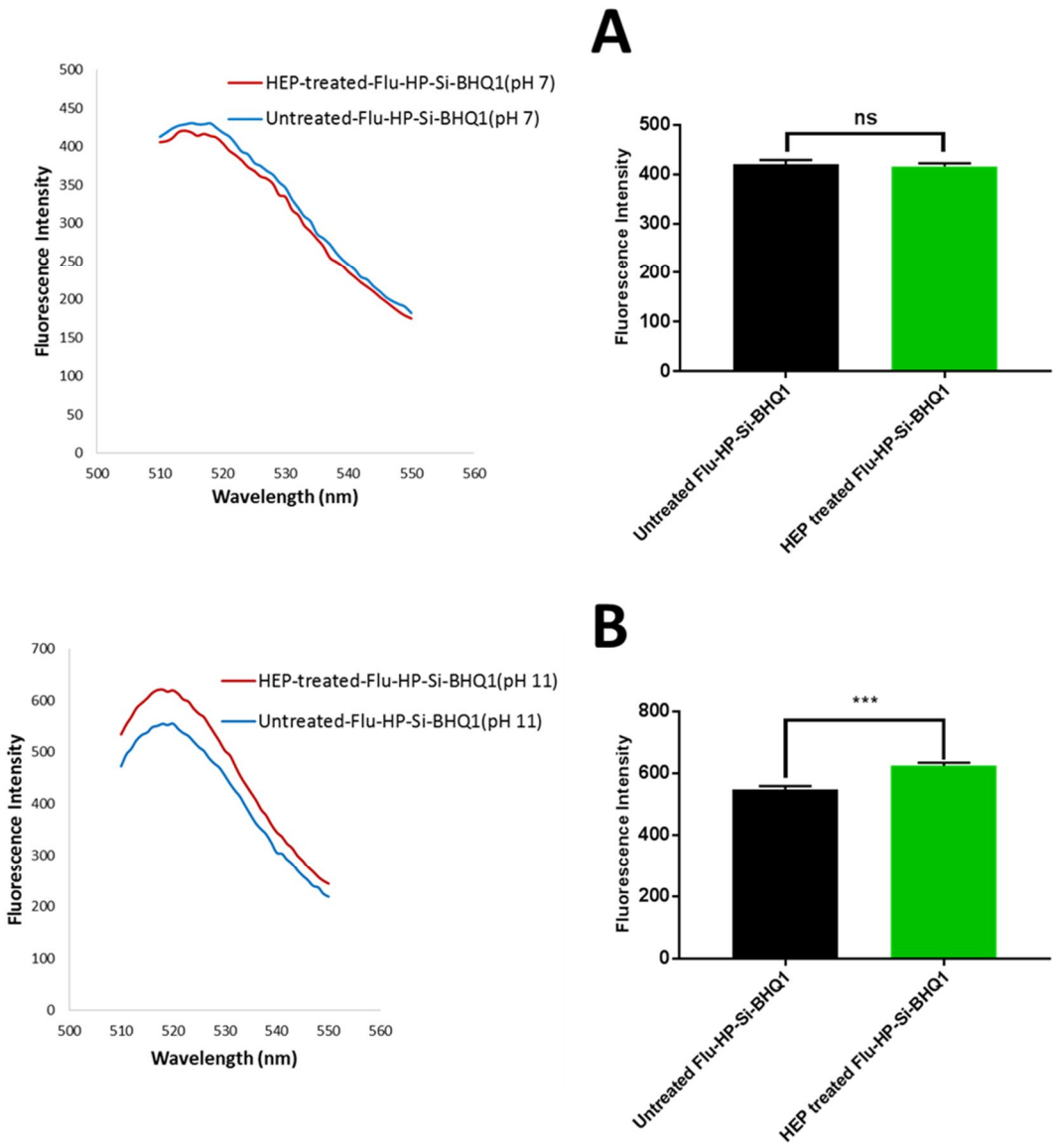


*Figure 4.31 Fluorescence signal recovery of model III nanosensors. A: Fluorescence spectra(left) and intensity (right) of fluorescein labelled heparin probe (Flu-HP) grafted onto the surface of BHQ1 incorporatde NPs with heparinase treatment (red) and without heparinase treatment (blue) at pH 7. B: Fluorescence spectra (left) and intensity (right) of fluorescein labelled heparin probe grafted onto the surface of BHQ1 incorporatde NPs with heparinase (red) and without heparinase (blue) after adjustment the pH of the buffer solution from 7 to 11 after enzyme treatment. Data was analysed using unpaired t test. Error bars indicate SD (n = 3), ns (nonsignificant) is P > 0.05, *** is P ≤ 0.001.*

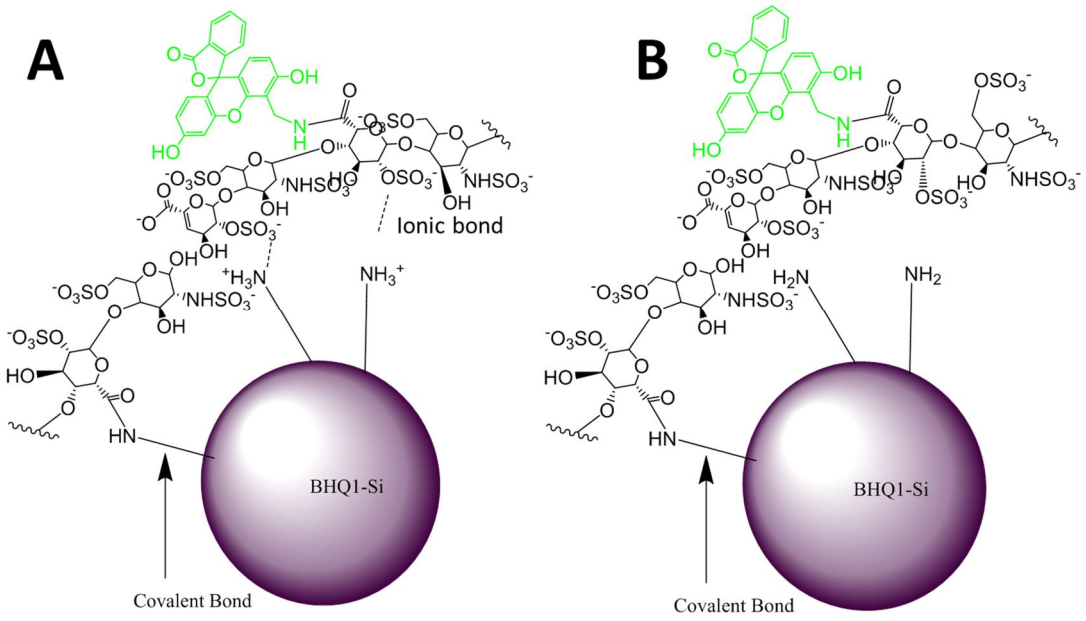


Figure 4.32 Schematic representation the role of pH adjustment in releasing of heparin fragments after treating heparinase nanosensors with heparinase I & II. A: Ionically bound heparin fragments remaining close to the surface of black hole quencher incorporated NPs at pH 7. B: Unbound heparin fragments released away from the surface of the black hole quencher incorporated NPs after adjusting the pH of the suspension from 7 to 11.

4.5 Conclusions

A series of FRET based constructs were fabricated in order to test their quenching efficiency and their ability to detect heparinase. Dual labelled heparin probe consisting of donor; fluorescein and acceptor; BHQ1 (Black hole quencher 1) was developed using model I. The maximum achieved quenching efficiency was ~55 % attained by intrachain conjugation of the FRET pair to heparin. It was concluded that intrachain conjugation of the FRET pair showed significantly greater quenching compared to a dual labelled probe having the fluorophore appended to the end of heparin chain while attaching the quencher within heparin chain. Which was attributed to the difference between the molecular orientation of the fluorophore attached to the end and within the chain of heparin, thus making the estimated distance between the donor-acceptor pair greater in the end-chain conjugation method compared with intrachain conjugation method. Moreover, the covalent binding of the FRET pair to heparin chain was required to achieve the fluorescence quenching. A high percentage (~90%) of the fluorescence signal of the FRET based system was restored by chemical

degradation of the dual labelled heparin probe by nitrous acid at pH 1.5. However, only slight signal recovery was observed when heparinase enzymes were used to cleave the dual labelled probe. This was attributed to incomplete dual labelled heparin degradation by the enzymes thus leaving the FRET pair on the same segment of the degraded heparin probe. A possible reason for incomplete degradation was postulated to be a steric hindrance brought by the FRET pairs attached to heparin carboxylate groups.

The nanosensors developed using model II have shown appreciable quenching efficiency. However; the calculated quenching efficiency was higher than expected as the distance between the FRET pair was greater than the ideal distance (10 nm) for effective FRET quenching reported previously. Hence, an internal standard (7-methoxy coumarin) was introduced to this system in order to further investigate the overestimated quenching efficiency. The quenching efficiency attained by coumarin based system did not correlate (dramatically lower) with the quenching efficiency attained by using the same system without coumarin. This discrepancy was thought to be due to an increase in particle-weight of the NPs after BHQ2-HP conjugate attachment to core-shell silica NPs surface compared to control core-shell particles functionalised with native heparin (HP). The actual quenching efficiency attained by coumarin based system was ~ 10% which is much lower than the quenching efficiency obtained by a blank core system (~ 40%). This low quenching was attributed to the distance between the FRET pair made by the thickness of the shell, where the smallest thickness that would be synthesised was ~12 nm which is slightly greater than the optimum donor-acceptor distance which ideally should be less than 10 nm.

In model III, the maximum quenching efficiency that could be achieved was ~30 %. Although the donor; fluorescein labelled heparin was directly appended to the surface of the BHQ1 containing NPs, the presence of the APTES as a crosslinker on the surface of the NPs separate the donor; fluorescein labelled heparin from the acceptor BHQ1.

Fluorescence signal recovery of model III nanosensors could not be achieved after heparinase treatment. This was attributed to ionic bonds between the negatively charged fluorescent heparin and the positively charged amine groups on the surface of BHQ1 incorporated NPs. However at elevated pH value; the fluorescence signal was partially restored after heparinase treatment. This reinforces that the cleaved fluorescent heparin fragments were released into the solution away from the surface of BHQ1 incorporated NPs after the disruption of ionic bonds at high pH value. Although model III was the most suitable model for heparinase detection, partial fluorescence signal was observed after pH elevation. Thus, the sensitivity of the developed system could be further improved in order to achieve a complete signal recovery.

Model III nanosensors would be valid for liquid biopsy applications as the responsiveness to heparinase was only observed after raising the pH of the suspension and such high pH value is not normally seen *in vivo* where the physiological pH is 7.4. Thus, Model III system could be utilised as a less invasive technique than other *in vivo* diagnostic procedures used for cancer detection. For instance, this system could be inspected to be utilised for liquid biopsy or tissue biopsy (high heparanase concentration), where blood or tissue samples can be taken from cancer patients and further processed *in vitro*.

To conclude, the results revealed that the design of FRET based system for heparinase detection is crucial to maximise the quenching efficiency and signal recovery. Sensors designed based on heparin polymer containing the FRET pair showed poor detection sensitivity. NPs based sensors showed greater detection robustness, however the dark quencher had to be incorporated within the matrix and not attached to the surface of the NPs. The amount of the quencher, molecular orientation of the fluorophore and number of covalent/ionic bonds formed between the fluorescent heparin probe and the surface of the NPs seem to play a key role in achieving the quenching efficiency and sensing capability.

5 Chapter five: Conclusion and future work

5.1 Conclusions

Heparin has previously shown compelling results for treatment of cancer metastasis and dissemination of tumour cells. The clinical importance of heparin is based on its ability to bind to cell adhesion molecules e.g. P-selectin implicated in the spread of tumour cells. Heparin has other clinical benefits in metastasis treatment including its inhibitory activity against heparanase; an enzyme highly expressed during the process of metastasis to facilitate tumour cell invasion. Heparin can also reduce the platelets binding to circulating tumour cells and prevent the formation of microemboli involved in immune system evasion by metastatic cells. Heparin resembles heparan sulphate that belongs to GAGs family and a component of extracellular matrix that is susceptible to degradation by the overexpressed heparanase during the early stage of cancer cells spreading. Therefore heparin was harnessed for detection of heparinase; a bacterial form of mammalian heparanase.

In chapter 2, heparin was attached to the surface of silica NPs through EDC coupling reaction in order to investigate their ability to block P-selectin receptors. The rationale behind appending heparin polymer to the NPs surface was to prolong the circulation time of heparin as it is rapidly excreted from human body by renal clearance. Azure A assay and thermogravimetric analysis (TGA) confirmed the successful attachment of heparin to NPs surface. The anticoagulant activity of heparin linked to NPs surface was evaluated using anti-Xa assay which showed that heparin anticoagulant effect was reduced after the conjugation process. This finding of clinical importance as heparin conjugated NPs would have less haemorrhagic side effect compared with native heparin. Moreover, chondroitin sulphate and sodium alginate having structural similarities to heparin were also conjugated to the surface of silica NPs. As circulating tumour cells bind to P-selectin overexpressed on the vascular endothelial cells during the metastasis process, cells face shear stress brought by systemic circulation during their rolling adhesion. Hence a circulatory system dynamics simulator was

developed to mimic the *in vivo* blood circulation. Heparin, chondroitin sulphate and alginate conjugated NPs were labelled with different fluorophores and their adhesion to HUVECs was monitored under a simulated circulatory system using confocal fluorescence microscopy technique. The data showed that heparin and chondroitin sulphate conjugated silica NPs were more bound to HUVECs surface in comparison with alginate conjugated NPs indicating that heparin and chondroitin sulphate appended to NPs surface preferentially bind to cell surface receptors expressed by HUVECs. Due to the reported clinical importance of heparin in cancer metastasis, heparin conjugated NPs and microparticles binding to HUVECs surface was further inspected. The results showed that heparin conjugated NPs exhibited greater P-selectin dependent binding to HUVECs' surface under flow conditions in comparison with heparin conjugated microparticles, though the latter showed less cellular internalisation under static conditions. Taken together, the binding of heparin conjugated NPs to P-selectin receptors expressed on HUVECs' surface was successfully blocked using anti-P-selectin antibodies. Thus, the data suggest that these NPs could be further investigated in order to test their ability to competitively reduce the binding of metastatic cancer cells to endothelial cell surface P-selectin receptors exploited through the rolling adhesion of circulating tumour cells during cancer metastasis.

In chapter 3, materials were developed for heparanase inhibition by modifying heparin to produce two different heparin analogues namely glycol split heparin and desulphated heparin since they provide an additional clinical advantages in comparison with native heparin such as the reduction of the bleeding side effects and the antiangiogenic activity as reported in the literature. The characterisation data of ^{1}H-NMR showed successful synthesis of glycol split heparin through the cleavage of the hexapyranose ring of the uronic acid residue and synthesis of desulphated heparin by removal of sulphate group at C2 of the iduronic acid. Glycol split heparin demonstrated lower blood thinning effect and anticoagulant activity in comparison with unmodified heparin as indicated by anti Xa assay.

This provided an evidence that the glycol splitting occurred at the glucuronic acid residue constituting the heparin pentasaccharide sequence that binds to antithrombin enzyme during the coagulation cascade. Thus reducing a haemorrhagic effect; the main adverse reaction associated with heparin. It was found that the desulphation process influences the electrostatic interaction between heparin and azure A molecules during the dimerization that induces a blue shift in the λ_{max} of azure A, where a weaker blue shift induced by desulphated heparin was observed reinforcing the removal of sulphate groups. Modified heparins were attached to silica NPs surfaces exploiting the EPR effect of the NPs in order to enhance the circulating time of these polymers and promote their accumulation at the interstitial fluid of the tumour cells where heparanase is overexpressed during the metastatic stage. The characterisation data of azure A and anti Xa assay showed successful functionalisation of silica NPs surface with heparin derivatives. To conclude, modified heparin derivatives were successfully conjugated to silica NPs and thus the capability of these NPs to inhibit heparanase could be further tested in the future.

In chapter 4, heparin was employed in order to detect heparinase which is the bacterial form of the mammalian heparanase that is overexpressed in the early stage of tumour cells spreading. Different models consisting of FRET pairs attached to heparin were developed in order to detect heparinase. Thus providing a proof of principle for the detection of the mammalian form; heparanase. In model I, heparinase sensing polymer composed of heparin and the two FRET pair; aminomethyl fluorescein and BHQ1 was designed. Although this system has shown a relatively high quenching efficiency (~55%), the signal recovery achieved after heparinase treatment was significantly lower than that achieved by chemical degradation. In the next stage, NPs based sensors consisting of blank core, a 12 nm-thick shell containing TAMRA and BHQ2-Heparin probe attached to the surface of the NPs were developed. This system showed around 40% quenching efficiency, however the actual

quenching efficiency measured by 7-methoxy coumarin containing core based system showed a dramatically lower value (*circa* 10%). One reason for this discrepancy in quenching efficacy measurements was the postulated increase in the particle-weight after BHQ2-Heparin conjugation to core-shell NPs surface in comparison with the control NPs produced by native heparin conjugation to the surface of core-shell NPs. As the ideal distance between the FRET pair is 10 nm for energy transfer, a 12 nm thick shell could be responsible for the low quenching efficiency value obtained by this model alongside other factors including molecular orientation of the fluorophore distributed within the shell with relative to BHQ2 molecules attached to the NPs surface. As the quenching efficiency achieved by this model was low, it was not tested further using heparinase or chemical degradation to recover the signal. Hence, a more improved NPs based system was developed comprising a BHQ1 incorporated silica NPs and aminomethyl fluorescein labelled heparin probe attached to the surface of the NPs through a crosslinker; APTES. Although the quenching efficiency achieved by this system was about 30%, the fluorescence signal was not restored after heparinase treatment. However, the signal recovery of the heparinase treated nanosensors was only observed after raising the pH from 7 to 11. This was thought to be due to the release of the electrostatically bound fluorescent heparin fragments away from the BHQ1 incorporated NPs. It was concluded that model III showed the best heparinase-sensing results amongst the developed models and thus it could be further adapted for the detection of heparanase sampled from the blood of cancer patients to diagnose metastasis at early stage.

Overall, heparin conjugated NPs have shown potential results in preferential binding to P-selectin as indicated by the competitive assays under static and flow conditions. Accordingly, the ability of these NPs to interfere with the fundamental mechanisms, which are underpinning the adhesion and spreading of circulating tumour cells, could be further investigated and scrutinised. Also, this thesis has provided preliminary studies and a proof of concept for detecting heparinase (a bacterial form of heparanase) by testing the efficiency

of different heparinase-sensing constructs. The developed models of this study could be further improved and investigated for detecting metastatic biomarkers i.e. mammalian heparanase, and subsequently early detection of tumour cells dissemination. Although the cellular internalisation of the NPs represents a limitation for the developed system as it is intended to target extracellular receptors (P-selectin) and enzymes (Heparanase), other advantages including the prolonged circulation of the NPs and the EPR effect could outweigh the existing limitation. Thus heparin conjugated NPs could be further utilised in the future as novel potential tools for cancer metastasis therapy and diagnosis.

5.2 Future work

This work has provided an insight and promising preliminary data that could be improved and further investigated for cancer metastasis treatment and diagnosis in the future.

In light of the current results, the future work on this area could focus on enhancing heparinase detection sensitivity of model III nanosensors. Utilising a short length crosslinker e.g. 3-Aminopropyldimethylethoxysilane (APDMES) for attaching the fluorophore to the BHQ1 incorporated NPs surfaces seems a promising approach for this purpose. In contrary to APTES, APDMES is a mono-ethoxy organosilane and cannot polymerise to form oligomer and thus it is expected to bring the FRET pair close to each other i.e. with distance less than 7 nm (the length of the formed APTES oligomer on the particles surfaces). Consequently, the quenching efficiency is expected to increase when the distance between the FRET pair decreases as the quenching efficiency exponentially decays with FRET pair distance. Eventually the sensitivity of this system is expected to be improved.

Further, the electrostatic interaction between the fluorescently labelled heparin and amine groups on the surface of black hole quencher incorporated NPs was problematic in terms of the release of the cleavable heparin away from the NPs surfaces. Therefore, a different spacer could be adopted in order to attach the fluorescent heparin to the NPs surfaces

instead of APTES. For example, a negatively charged nucleophilic groups on the surface of BHQ1 incorporated NPs using a thiol linker could be exploited to avoid the formation of the electrostatic interaction between the fluorescently labelled heparin fragments and amine groups on the NPs surfaces after heparanase treatment. However, the stability of the thioester bond that would form between heparin carboxylate and the thiol linker could be a limitation.

Additionally, as glycol split heparin and desulphated heparin are known to have anti-heparanase activity and taking together the advantage of the EPR effect and the long half-life of NPs, the developed materials could be further investigated. An assay adopting for example a radiolabelled heparan sulphate could be used in order to test the ability of the developed heparin derivatives conjugated silica NPs to reduce/abolish the activity of heparanase through monitoring of heparan sulphate degradation products. Where the heparins conjugated NPs are expected to reduce the degradation products of heparan sulphate after enzymatic digestion using heparanase. In this assay, samples of radiolabelled heparan sulphate treated with both heparanase and developed NPs could be analysed by gel filtration compared with untreated control samples. Thus, if the NPs treated samples show fewer multiple peaks, which are representing heparan sulphate fragments; compared with untreated control, it may indicate a reduction in heparan sulphate degradation and heparanase activity.

Moreover, heparin conjugated NPs have shown a preferential binding to P-selectin receptors which are expressed on HUVECs and utilised by metastatic cells for adhesion to vascular endothelium in comparison with alginate conjugated NPs and heparin conjugated microparticles as indicated by the competitive assays. Where in these assays, heparin conjugated NPs were blocked by anti-P-selectin antibodies. Accordingly, the interaction between highly metastatic cells e.g. melanoma cells and HUVECs could be further investigated in the presence of heparin conjugated NPs by using the developed circulatory

system simulator. Thus, the capability of the NPs to outcompete the circulating tumour cells from P-selectin dependent rolling adhesion to vascular endothelial cells could be further studied.

6 References

1. Freitas, R. A., *Nanomedicine, volume I: basic capabilities*. Landes Bioscience Georgetown, TX: 1999; Vol. 1.
2. Kreuter, J., Nanoparticles—a historical perspective. *International journal of pharmaceutics* **2007,** *331* (1), 1-10.
3. Pisano, C.; Cecere, S. C.; Di Napoli, M.; Cavaliere, C.; Tambaro, R.; Facchini, G.; Scaffa, C.; Losito, S.; Pizzolorusso, A.; Pignata, S., Clinical trials with pegylated liposomal Doxorubicin in the treatment of ovarian cancer. *Journal of drug delivery* **2013,** *2013*.
4. Miele, E.; Spinelli, G. P.; Miele, E.; Tomao, F.; Tomao, S., Albumin-bound formulation of paclitaxel (Abraxane® ABI-007) in the treatment of breast cancer. *International journal of nanomedicine* **2009,** *4*, 99.
5. Fadaka, A.; Ajiboye, B.; Ojo, O.; Adewale, O.; Olayide, I.; Emuowhochere, R., Biology of glucose metabolization in cancer cells. *Journal of Oncological Sciences* **2017,** *3* (2), 45-51.
6. Elstrom, R. L.; Bauer, D. E.; Buzzai, M.; Karnauskas, R.; Harris, M. H.; Plas, D. R.; Zhuang, H.; Cinalli, R. M.; Alavi, A.; Rudin, C. M., Akt stimulates aerobic glycolysis in cancer cells. *Cancer research* **2004,** *64* (11), 3892-3899.
7. Hanahan, D.; Weinberg, R. A., The hallmarks of cancer. *cell* **2000,** *100* (1), 57-70.
8. Tomasetti, C.; Li, L.; Vogelstein, B., Stem cell divisions, somatic mutations, cancer etiology, and cancer prevention. *Science* **2017,** *355* (6331), 1330-1334.
9. Soto, A. M.; Sonnenschein, C., Environmental causes of cancer: endocrine disruptors as carcinogens. *Nature Reviews Endocrinology* **2010,** *6* (7), 363.
10. Mehlen, P.; Puisieux, A., Metastasis: a question of life or death. *Nature reviews cancer* **2006,** *6* (6), 449-458.
11. Winnard Jr, P. T.; Pathak, A. P.; Dhara, S.; Cho, S. Y.; Raman, V.; Pomper, M. G., Molecular imaging of metastatic potential. *Journal of nuclear medicine: official publication, Society of Nuclear Medicine* **2008,** *49* (Suppl 2), 96S.
12. Weigelt, B.; Peterse, J. L.; Van't Veer, L. J., Breast cancer metastasis: markers and models. *Nature reviews cancer* **2005,** *5* (8), 591-602.
13. Chaffer, C. L.; Weinberg, R. A., A perspective on cancer cell metastasis. *science* **2011,** *331* (6024), 1559-1564.
14. Mehlen, P.; Puisieux, A., Metastasis: a question of life or death. *Nature reviews cancer* **2006,** *6* (6), 449.
15. Lee, W.-C.; Kopetz, S.; Wistuba, I. I.; Zhang, J., Metastasis of cancer: when and how? Oxford University Press: 2017.
16. Kalluri, R.; Weinberg, R. A., The basics of epithelial-mesenchymal transition. *The Journal of clinical investigation* **2009,** *119* (6), 1420-1428.
17. Behrens, J., The role of cell adhesion molecules in cancer invasion and metastasis. *Breast cancer research and treatment* **1993,** *24* (3), 175-184.
18. Strell, C.; Entschladen, F., Extravasation of leukocytes in comparison to tumor cells. *Cell Communication and Signaling* **2008,** *6* (1), 10.
19. Giavazzi, R.; Foppolo, M.; Dossi, R.; Remuzzi, A., Rolling and adhesion of human tumor cells on vascular endothelium under physiological flow conditions. *The Journal of clinical investigation* **1993,** *92* (6), 3038-3044.
20. Chitty, J. L.; Filipe, E. C.; Lucas, M. C.; Herrmann, D.; Cox, T. R.; Timpson, P., Recent advances in understanding the complexities of metastasis. *F1000Research* **2018,** *7*.

21. Krause, T.; Turner, G., Are selectins involved in metastasis? *Clinical & experimental metastasis* **1999,** *17* (3), 183-192.
22. Seyfried, T. N.; Huysentruyt, L. C., On the origin of cancer metastasis. *Critical reviews in oncogenesis* **2013,** *18* (1-2), 43.
23. Khatib, A.-M.; Kontogiannea, M.; Fallavollita, L.; Jamison, B.; Meterissian, S.; Brodt, P., Rapid induction of cytokine and E-selectin expression in the liver in response to metastatic tumor cells. *Cancer research* **1999,** *59* (6), 1356-1361.
24. Guan, X., Cancer metastases: challenges and opportunities. *Acta pharmaceutica sinica B* **2015,** *5* (5), 402-418.
25. Sasisekharan, R.; Raman, R.; Prabhakar, V., Glycomics approach to structure-function relationships of glycosaminoglycans. *Annu. Rev. Biomed. Eng.* **2006,** *8*, 181-231.
26. Habuchi, H.; Habuchi, O.; Kimata, K., Sulfation pattern in glycosaminoglycan: does it have a code? *Glycoconjugate journal* **2004,** *21* (1-2), 47-52.
27. Jackson, R. L.; Busch, S. J.; Cardin, A. D., Glycosaminoglycans: molecular properties, protein interactions, and role in physiological processes. *Physiological reviews* **1991,** *71* (2), 481-539.
28. Mattson, J. M.; Turcotte, R.; Zhang, Y., Glycosaminoglycans contribute to extracellular matrix fiber recruitment and arterial wall mechanics. *Biomechanics and modeling in mechanobiology* **2017,** *16* (1), 213-225.
29. Matsuo, I.; Kimura-Yoshida, C., Extracellular distribution of diffusible growth factors controlled by heparan sulfate proteoglycans during mammalian embryogenesis. *Philosophical Transactions of the Royal Society B: Biological Sciences* **2014,** *369* (1657), 20130545.
30. Nakano, T.; Dodd, C. M.; Scott, P. G., Glycosaminoglycans and proteoglycans from different zones of the porcine knee meniscus. *Journal of orthopaedic research* **1997,** *15* (2), 213-220.
31. Jerzyńska, J.; Stelmach, I.; Kuna, P., The role of heparin in allergic inflammation. *Polski merkuriusz lekarski: organ Polskiego Towarzystwa Lekarskiego* **2000,** *8* (47), 341-346.
32. Neve, A.; Cantatore, F. P.; Maruotti, N.; Corrado, A.; Ribatti, D., Extracellular matrix modulates angiogenesis in physiological and pathological conditions. *BioMed research international* **2014,** *2014*.
33. Borza, D.-B., Glomerular basement membrane heparan sulfate in health and disease: a regulator of local complement activation. *Matrix Biology* **2017,** *57*, 299-310.
34. Rabenstein, D. L., Heparin and heparan sulfate: structure and function. *Natural product reports* **2002,** *19* (3), 312-331.
35. Afratis, N.; Gialeli, C.; Nikitovic, D.; Tsegenidis, T.; Karousou, E.; Theocharis, A. D.; Pavão, M. S.; Tzanakakis, G. N.; Karamanos, N. K., Glycosaminoglycans: key players in cancer cell biology and treatment. *The FEBS journal* **2012,** *279* (7), 1177-1197.
36. Nelson, S. M.; Greer, I. A., The potential role of heparin in assisted conception. *Human Reproduction Update* **2008,** *14* (6), 623-645.
37. Shriver, Z.; Capila, I.; Venkataraman, G.; Sasisekharan, R., Heparin and heparan sulfate: analyzing structure and microheterogeneity. In *Heparin-A Century of Progress*, Springer: 2012; pp 159-176.
38. Raman, S.; Hsu, T.-H.; Ashley, S. L.; Spindler, K. R., Usage of integrin and heparan sulfate as receptors for mouse adenovirus type 1. *Journal of virology* **2009,** *83* (7), 2831-2838.
39. Wu, Z. L.; Zhang, L.; Yabe, T.; Kuberan, B.; Beeler, D. L.; Love, A.; Rosenberg, R. D., The involvement of heparan sulfate (HS) in FGF1/HS/FGFR1 signaling complex. *Journal of Biological Chemistry* **2003,** *278* (19), 17121-17129.
40. Barrowcliffe, T.; Mulloy, B.; Johnson, E.; Thomas, D., The anticoagulant activity of heparin: measurement and relationship to chemical structure. *Journal of pharmaceutical and biomedical analysis* **1989,** *7* (2), 217-226.

41. Sanderson, R. D. In *Heparan sulfate proteoglycans in invasion and metastasis*, Seminars in cell & developmental biology, Elsevier: 2001; pp 89-98.
42. Couchman, J. R.; Multhaupt, H.; Sanderson, R. D., Recent insights into cell surface heparan sulphate proteoglycans and cancer. *F1000Research* **2016,** *5*.
43. Sarrazin, S.; Lamanna, W. C.; Esko, J. D., Heparan sulfate proteoglycans. *Cold Spring Harbor perspectives in biology* **2011,** *3* (7), a004952.
44. Gallagher, J. T.; Turnbull, J. E., Heparan sulphate in the binding and activation of basic fibroblast growth factor. *Glycobiology* **1992,** *2* (6), 523-528.
45. Schlessinger, J.; Plotnikov, A. N.; Ibrahimi, O. A.; Eliseenkova, A. V.; Yeh, B. K.; Yayon, A.; Linhardt, R. J.; Mohammadi, M., Crystal structure of a ternary FGF-FGFR-heparin complex reveals a dual role for heparin in FGFR binding and dimerization. *Molecular cell* **2000,** *6* (3), 743-750.
46. Flaumenhaft, R.; Rifkin, D. B., The extracellular regulation of growth factor action. *Molecular biology of the cell* **1992,** *3* (10), 1057-1065.
47. Sasisekharan, R.; Shriver, Z.; Venkataraman, G.; Narayanasami, U., Roles of heparan-sulphate glycosaminoglycans in cancer. *Nature Reviews Cancer* **2002,** *2* (7), 521.
48. Vlodavsky, I.; Ilan, N.; Nadir, Y.; Brenner, B.; Katz, B.-Z.; Naggi, A.; Torri, G.; Casu, B.; Sasisekharan, R., Heparanase, heparin and the coagulation system in cancer progression. *Thrombosis research* **2007,** *120*, S112-S120.
49. Bendas, G.; Borsig, L., Cancer cell adhesion and metastasis: selectins, integrins, and the inhibitory potential of heparins. *International journal of cell biology* **2012,** *2012*.
50. Honn, K. V.; Tang, D. G.; Crissman, J. D., Platelets and cancer metastasis: a causal relationship? *Cancer and Metastasis Reviews* **1992,** *11* (3-4), 325-351.
51. Christianson, H. C.; Svensson, K. J.; van Kuppevelt, T. H.; Li, J.-P.; Belting, M., Cancer cell exosomes depend on cell-surface heparan sulfate proteoglycans for their internalization and functional activity. *Proceedings of the National Academy of Sciences* **2013,** *110* (43), 17380-17385.
52. Patra, J. K.; Das, G.; Fraceto, L. F.; Campos, E. V. R.; del Pilar Rodriguez-Torres, M.; Acosta-Torres, L. S.; Diaz-Torres, L. A.; Grillo, R.; Swamy, M. K.; Sharma, S., Nano based drug delivery systems: recent developments and future prospects. *Journal of nanobiotechnology* **2018,** *16* (1), 71.
53. Singh, S.; Pandey, V. K.; Tewari, R. P.; Agarwal, V., Nanoparticle based drug delivery system: advantages and applications. *Indian Journal of Science and Technology* **2011,** *4* (3), 177-180.
54. Rizvi, S. A.; Saleh, A. M., Applications of nanoparticle systems in drug delivery technology. *Saudi Pharmaceutical Journal* **2018,** *26* (1), 64-70.
55. Bazak, R.; Houri, M.; El Achy, S.; Hussein, W.; Refaat, T., Passive targeting of nanoparticles to cancer: A comprehensive review of the literature. *Molecular and clinical oncology* **2014,** *2* (6), 904-908.
56. Talekar, M.; Kendall, J.; Denny, W.; Garg, S., Targeting of nanoparticles in cancer: drug delivery and diagnostics. *Anti-Cancer Drugs* **2011,** *22* (10), 949-962.
57. Maeda, H., Macromolecular therapeutics in cancer treatment: the EPR effect and beyond. *Journal of Controlled Release* **2012,** *164* (2), 138-144.
58. Maeda, H.; Greish, K.; Fang, J., The EPR effect and polymeric drugs: a paradigm shift for cancer chemotherapy in the 21st century. In *Polymer therapeutics II*, Springer: 2006; pp 103-121.
59. Maeda, H.; Nakamura, H.; Fang, J., The EPR effect for macromolecular drug delivery to solid tumors: Improvement of tumor uptake, lowering of systemic toxicity, and distinct tumor imaging in vivo. *Advanced drug delivery reviews* **2013,** *65* (1), 71-79.
60. Maeda, H.; Wu, J.; Sawa, T.; Matsumura, Y.; Hori, K., Tumor vascular permeability and the EPR effect in macromolecular therapeutics: a review. *Journal of controlled release* **2000,** *65* (1-2), 271-284.

61. Singh, R.; Lillard Jr, J. W., Nanoparticle-based targeted drug delivery. *Experimental and molecular pathology* **2009,** *86* (3), 215-223.
62. Sudimack, J.; Lee, R. J., Targeted drug delivery via the folate receptor. *Advanced drug delivery reviews* **2000,** *41* (2), 147-162.
63. Bareford, L. M.; Swaan, P. W., Endocytic mechanisms for targeted drug delivery. *Advanced drug delivery reviews* **2007,** *59* (8), 748-758.
64. Bae, Y. H.; Park, K., Targeted drug delivery to tumors: myths, reality and possibility. *Journal of controlled release* **2011,** *153* (3), 198.
65. Wilhelm, S.; Tavares, A. J.; Dai, Q.; Ohta, S.; Audet, J.; Dvorak, H. F.; Chan, W. C., Analysis of nanoparticle delivery to tumours. *Nature reviews materials* **2016,** *1* (5), 1-12.
66. Sindhwani, S.; Syed, A. M.; Ngai, J.; Kingston, B. R.; Maiorino, L.; Rothschild, J.; MacMillan, P.; Zhang, Y.; Rajesh, N. U.; Hoang, T., The entry of nanoparticles into solid tumours. *Nature Materials* **2020**, 1-10.
67. Abdalla, A. M.; Xiao, L.; Ullah, M. W.; Yu, M.; Ouyang, C.; Yang, G., Current challenges of cancer anti-angiogenic therapy and the promise of nanotherapeutics. *Theranostics* **2018,** *8* (2), 533.
68. Mahapatro, A.; Singh, D. K., Biodegradable nanoparticles are excellent vehicle for site directed in-vivo delivery of drugs and vaccines. *Journal of nanobiotechnology* **2011,** *9* (1), 55.
69. Calzoni, E.; Cesaretti, A.; Polchi, A.; Di Michele, A.; Tancini, B.; Emiliani, C., Biocompatible polymer nanoparticles for drug delivery applications in cancer and neurodegenerative disorder therapies. *Journal of functional biomaterials* **2019,** *10* (1), 4.
70. Bamrungsap, S.; Zhao, Z.; Chen, T.; Wang, L.; Li, C.; Fu, T.; Tan, W., Nanotechnology in therapeutics: a focus on nanoparticles as a drug delivery system. *Nanomedicine* **2012,** *7* (8), 1253-1271.
71. Gao, H.; Yang, Z.; Zhang, S.; Cao, S.; Shen, S.; Pang, Z.; Jiang, X., Ligand modified nanoparticles increases cell uptake, alters endocytosis and elevates glioma distribution and internalization. *Scientific reports* **2013,** *3*, 2534.
72. Yameen, B.; Choi, W. I.; Vilos, C.; Swami, A.; Shi, J.; Farokhzad, O. C., Insight into nanoparticle cellular uptake and intracellular targeting. *Journal of controlled release* **2014,** *190*, 485-499.
73. Bazak, R.; Houri, M.; El Achy, S.; Kamel, S.; Refaat, T., Cancer active targeting by nanoparticles: a comprehensive review of literature. *Journal of cancer research and clinical oncology* **2015,** *141* (5), 769-784.
74. Goodall, S.; Jones, M. L.; Mahler, S., Monoclonal antibody-targeted polymeric nanoparticles for cancer therapy–future prospects. *Journal of Chemical Technology & Biotechnology* **2015,** *90* (7), 1169-1176.
75. Steinhauser, I.; Spänkuch, B.; Strebhardt, K.; Langer, K., Trastuzumab-modified nanoparticles: optimisation of preparation and uptake in cancer cells. *Biomaterials* **2006,** *27* (28), 4975-4983.
76. Glazer, E. S.; Massey, K. L.; Zhu, C.; Curley, S. A., Pancreatic carcinoma cells are susceptible to noninvasive radio frequency fields after treatment with targeted gold nanoparticles. *Surgery* **2010,** *148* (2), 319-324.
77. Taylor, R. M.; Sillerud, L. O., Paclitaxel-loaded iron platinum stealth immunomicelles are potent MRI imaging agents that prevent prostate cancer growth in a PSMA-dependent manner. *International journal of nanomedicine* **2012,** *7*, 4341.
78. Marty, C.; Odermatt, B.; Schott, H.; Neri, D.; Ballmer-Hofer, K.; Klemenz, R.; Schwendener, R., Cytotoxic targeting of F9 teratocarcinoma tumours with anti-ED-B fibronectin scFv antibody modified liposomes. *British journal of cancer* **2002,** *87* (1), 106.
79. Sugano, M.; Egilmez, N. K.; Yokota, S. J.; Chen, F.-A.; Harding, J.; Huang, S. K.; Bankert, R. B., Antibody targeting of doxorubicin-loaded liposomes suppresses the growth and metastatic spread of established human lung tumor xenografts in severe combined immunodeficient mice. *Cancer research* **2000,** *60* (24), 6942-6949.

80. Farokhzad, O. C.; Cheng, J.; Teply, B. A.; Sherifi, I.; Jon, S.; Kantoff, P. W.; Richie, J. P.; Langer, R., Targeted nanoparticle-aptamer bioconjugates for cancer chemotherapy in vivo. *Proceedings of the National Academy of Sciences* **2006,** *103* (16), 6315-6320.
81. Sahoo, S. K.; Labhasetwar, V., Enhanced antiproliferative activity of transferrin-conjugated paclitaxel-loaded nanoparticles is mediated via sustained intracellular drug retention. *Molecular pharmaceutics* **2005,** *2* (5), 373-383.
82. Ni, S.; Stephenson, S. M.; Lee, R. J., Folate receptor targeted delivery of liposomal daunorubicin into tumor cells. *Anticancer research* **2002,** *22* (4), 2131-2135.
83. Wang, F.; Tan, W. B.; Zhang, Y.; Fan, X.; Wang, M., Luminescent nanomaterials for biological labelling. *Nanotechnology* **2005,** *17* (1), R1.
84. Bagwe, R. P.; Hilliard, L. R.; Tan, W., Surface modification of silica nanoparticles to reduce aggregation and nonspecific binding. *Langmuir* **2006,** *22* (9), 4357-4362.
85. Wang, L.; Tan, W., Multicolor FRET silica nanoparticles by single wavelength excitation. *Nano letters* **2006,** *6* (1), 84-88.
86. Zhang, Y.; Hsu, B. Y. W.; Ren, C.; Li, X.; Wang, J., Silica-based nanocapsules: synthesis, structure control and biomedical applications. *Chemical Society Reviews* **2015,** *44* (1), 315-335.
87. Tamba, B.; Dondas, A.; Leon, M.; Neagu, A.; Dodi, G.; Stefanescu, C.; Tijani, A., Silica nanoparticles: preparation, characterization and in vitro/in vivo biodistribution studies. *European Journal of Pharmaceutical Sciences* **2015,** *71*, 46-55.
88. Lin, Y.-S.; Abadeer, N.; Haynes, C. L., Stability of small mesoporous silica nanoparticles in biological media. *Chemical Communications* **2011,** *47* (1), 532-534.
89. Desai, A. S.; Chauhan, V. M.; Johnston, A. P.; Esler, T.; Aylott, J. W., Fluorescent nanosensors for intracellular measurements: synthesis, characterization, calibration, and measurement. *Frontiers in physiology* **2014,** *4*, 401.
90. Yano, K.; Fukushima, Y., Synthesis of mono-dispersed mesoporous silica spheres with highly ordered hexagonal regularity using conventional alkyltrimethylammonium halide as a surfactant. *Journal of Materials Chemistry* **2004,** *14* (10), 1579-1584.
91. Lodha, A.; Lodha, M.; Patel, A.; Chaudhuri, J.; Dalal, J.; Edwards, M.; Douroumis, D., Synthesis of mesoporous silica nanoparticles and drug loading of poorly water soluble drug cyclosporin A. *Journal of pharmacy & bioallied sciences* **2012,** *4* (Suppl 1), S92.
92. Gao, Z.; Zharov, I., Large pore mesoporous silica nanoparticles by templating with a nonsurfactant molecule, tannic acid. *Chemistry of Materials* **2014,** *26* (6), 2030-2037.
93. Wu, M.; Meng, Q.; Chen, Y.; Zhang, L.; Li, M.; Cai, X.; Li, Y.; Yu, P.; Zhang, L.; Shi, J., Large pore-sized hollow mesoporous organosilica for redox-responsive gene delivery and synergistic cancer chemotherapy. *Advanced materials* **2016,** *28* (10), 1963-1969.
94. Watermann, A.; Brieger, J., Mesoporous silica nanoparticles as drug delivery vehicles in cancer. *Nanomaterials* **2017,** *7* (7), 189.
95. Crowley, E.; Di Nicolantonio, F.; Loupakis, F.; Bardelli, A., Liquid biopsy: monitoring cancer-genetics in the blood. *Nature reviews Clinical oncology* **2013,** *10* (8), 472.
96. De Rubis, G.; Krishnan, S. R.; Bebawy, M., Liquid biopsies in cancer diagnosis, monitoring, and prognosis. *Trends in pharmacological sciences* **2019**.
97. Heitzer, E.; Ulz, P.; Geigl, J. B., Circulating tumor DNA as a liquid biopsy for cancer. *Clinical chemistry* **2015,** *61* (1), 112-123.
98. Wan, J. C.; Massie, C.; Garcia-Corbacho, J.; Mouliere, F.; Brenton, J. D.; Caldas, C.; Pacey, S.; Baird, R.; Rosenfeld, N., Liquid biopsies come of age: towards implementation of circulating tumour DNA. *Nature Reviews Cancer* **2017,** *17* (4), 223.
99. Alix-Panabieres, C.; Pantel, K., Circulating tumor cells: liquid biopsy of cancer. *Clinical chemistry* **2013,** *59* (1), 110-118.
100. Catarino, R.; Ferreira, M. M.; Rodrigues, H.; Coelho, A.; Nogal, A.; Sousa, A.; Medeiros, R., Quantification of free circulating tumor DNA as a diagnostic marker for breast cancer. *DNA and cell biology* **2008,** *27* (8), 415-421.

101. Dawson, S.-J.; Tsui, D. W.; Murtaza, M.; Biggs, H.; Rueda, O. M.; Chin, S.-F.; Dunning, M. J.; Gale, D.; Forshew, T.; Mahler-Araujo, B., Analysis of circulating tumor DNA to monitor metastatic breast cancer. *New England Journal of Medicine* **2013,** *368* (13), 1199-1209.
102. Tang, J.-C.; Feng, Y.-L.; Guo, T.; Xie, A.-Y.; Cai, X.-J., Circulating tumor DNA in hepatocellular carcinoma: trends and challenges. *Cell & bioscience* **2016,** *6* (1), 32.
103. Diaz Jr, L. A.; Bardelli, A., Liquid biopsies: genotyping circulating tumor DNA. *Journal of clinical oncology* **2014,** *32* (6), 579.
104. Pécuchet, N.; Rozenholc, Y.; Zonta, E.; Pietrasz, D.; Didelot, A.; Combe, P.; Gibault, L.; Bachet, J.-B.; Taly, V.; Fabre, E., Analysis of base-position error rate of next-generation sequencing to detect tumor mutations in circulating DNA. *Clinical chemistry* **2016,** *62* (11), 1492-1503.
105. Schiffman, J. D.; Fisher, P. G.; Gibbs, P., Early detection of cancer: past, present, and future. *Am Soc Clin Oncol Educ Book* **2015,** *35* (1), 57-65.
106. Olsson, E.; Winter, C.; George, A.; Chen, Y.; Howlin, J.; Tang, M. H. E.; Dahlgren, M.; Schulz, R.; Grabau, D.; van Westen, D., Serial monitoring of circulating tumor DNA in patients with primary breast cancer for detection of occult metastatic disease. *EMBO molecular medicine* **2015,** *7* (8), 1034-1047.
107. Chiva-Blanch, G.; Padró, T.; Alonso, R.; Crespo, J.; Perez de Isla, L.; Mata, P.; Badimon, L., Liquid Biopsy of Extracellular Microvesicles Maps Coronary Calcification and Atherosclerotic Plaque in Asymptomatic Patients With Familial Hypercholesterolemia: A Computed Tomographic Angiography Imaging Study. *Arteriosclerosis, thrombosis, and vascular biology* **2019,** *39* (5), 945-955.
108. Strain, J. E.; Grose, R. M.; Factor, S.; Fisher, J. D., Results of endomyocardial biopsy in patients with spontaneous ventricular tachycardia but without apparent structural heart disease. *Circulation* **1983,** *68* (6), 1171-1181.
109. da Silva, M. N.; Sicchieri, L. B.; de Oliveira Silva, F. R.; Andrade, M. F.; Courrol, L. C., Liquid biopsy of atherosclerosis using protoporphyrin IX as a biomarker. *Analyst* **2014,** *139* (6), 1383-1388.
110. Langlois, S.; Brock, J.-A.; Wilson, R. D.; Audibert, F.; Carroll, J.; Cartier, L.; Gagnon, A.; Johnson, J.-A.; MacDonald, W.; Murphy-Kaulbeck, L., Current status in non-invasive prenatal detection of Down syndrome, trisomy 18, and trisomy 13 using cell-free DNA in maternal plasma. *Journal of Obstetrics and Gynaecology Canada* **2013,** *35* (2), 177-181.
111. Sparks, A. B.; Struble, C. A.; Wang, E. T.; Song, K.; Oliphant, A., Noninvasive prenatal detection and selective analysis of cell-free DNA obtained from maternal blood: evaluation for trisomy 21 and trisomy 18. *American journal of obstetrics and gynecology* **2012,** *206* (4), 319. e1-319. e9.
112. Pyykkö, O. T.; Lumela, M.; Rummukainen, J.; Nerg, O.; Seppälä, T. T.; Herukka, S.-K.; Koivisto, A. M.; Alafuzoff, I.; Puli, L.; Savolainen, S., Cerebrospinal fluid biomarker and brain biopsy findings in idiopathic normal pressure hydrocephalus. *PloS one* **2014,** *9* (3), e91974.
113. Mouliere, F.; Mair, R.; Chandrananda, D.; Marass, F.; Smith, C. G.; Su, J.; Morris, J.; Watts, C.; Brindle, K. M.; Rosenfeld, N., Detection of cell-free DNA fragmentation and copy number alterations in cerebrospinal fluid from glioma patients. *EMBO molecular medicine* **2018,** *10* (12).
114. Xie, J.; Zhao, R.; Gu, S.; Dong, H.; Wang, J.; Lu, Y.; Sinko, P. J.; Yu, T.; Xie, F.; Wang, L., The architecture and biological function of dual antibody-coated dendrimers: enhanced control of circulating tumor cells and their hetero-adhesion to endothelial cells for metastasis prevention. *Theranostics* **2014,** *4* (12), 1250.
115. Hossain, M.; Luo, Y.; Sun, Z.; Wang, C.; Zhang, M.; Fu, H.; Qiao, Y.; Su, M., X-ray enabled detection and eradication of circulating tumor cells with nanoparticles. *Biosensors and Bioelectronics* **2012,** *38* (1), 348-354.

116. Cochran, D. B.; Gray, L. N.; Anderson, K. W.; Dziubla, T. D., Degradable poly (apigenin) polymer inhibits tumor cell adhesion to vascular endothelial cells. *Journal of Biomedical Materials Research Part B: Applied Biomaterials* **2015**.
117. Kobayashi, K.-i.; Matsumoto, S.; Morishima, T.; Kawabe, T.; Okamoto, T., Cimetidine inhibits cancer cell adhesion to endothelial cells and prevents metastasis by blocking E-selectin expression. *Cancer research* **2000,** *60* (14), 3978-3984.
118. Lu, Y.; Yu, T.; Liang, H.; Wang, J.; Xie, J.; Shao, J.; Gao, Y.; Yu, S.; Chen, S.; Wang, L., Nitric oxide inhibits hetero-adhesion of cancer cells to endothelial cells: restraining circulating tumor cells from initiating metastatic cascade. *Scientific reports* **2014,** *4*, 4344.
119. Tozawa, K.; Sakurada, S.; Kohri, K.; Okamoto, T., Effects of anti-nuclear factor κ B reagents in blocking adhesion of human cancer cells to vascular endothelial cells. *Cancer research* **1995,** *55* (18), 4162-4167.
120. Zhang, H.; Fu, X.; Hu, J.; Zhu, Z., Microfluidic bead-based multienzyme-nanoparticle amplification for detection of circulating tumor cells in the blood using quantum dots labels. *Analytica chimica acta* **2013,** *779*, 64-71.
121. Sioss, J. A.; Bhiladvala, R. B.; Pan, W.; Li, M.; Patrick, S.; Xin, P.; Dean, S. L.; Keating, C. D.; Mayer, T. S.; Clawson, G. A., Nanoresonator chip-based RNA sensor strategy for detection of circulating tumor cells: response using PCA3 as a prostate cancer marker. *Nanomedicine: Nanotechnology, Biology and Medicine* **2012,** *8* (6), 1017-1025.
122. Chou, K.-C., The convergence-divergence duality in lectin domains of selectin family and its implications. *FEBS letters* **1995,** *363* (1-2), 123-126.
123. Chou, K.-C., Knowledge-based model building of the tertiary structures for lectin domains of the selectin family. *Journal of protein chemistry* **1996,** *15* (2), 161-168.
124. Chou, K.-C.; Heinrikson, R. L., Prediction of the tertiary structure of the complement control protein module. *Journal of protein chemistry* **1997,** *16* (8), 765-773.
125. Geng, J.-G., Platelet and endothelial cell P-selectin and its leukocyte sialoglycoprotein ligand. *Trends in Glycoscience and Glycotechnology* **1995,** *7* (36), 333-342.
126. Geng, J.-G., Interaction of vascular endothelial cells with leukocytes, platelets and cancer cells in inflammation, thrombosis and cancer growth and metastasis. *Acta Pharmacologica Sinica* **2003,** *24* (12), 1297-1300.
127. Geng, J. G., Directional migration of leukocytes: their pathological roles in inflammation and strategies for development of anti-inflammatory therapies. *Cell research* **2001,** *11* (2), 85.
128. Butcher, E. C., Leukocyte-endothelial cell recognition-three (or more) steps to specificity and diversity. *Cell* **1991,** *67*, 1033-1036.
129. Yokota, J., Tumor progression and metastasis. *Carcinogenesis* **2000,** *21* (3), 497-503.
130. Valastyan, S.; Weinberg, R. A., Tumor metastasis: molecular insights and evolving paradigms. *Cell* **2011,** *147* (2), 275-292.
131. Chen, M.; Geng, J.-G., P-selectin mediates adhesion of leukocytes, platelets, and cancer cells in inflammation, thrombosis, and cancer growth and metastasis. *Archivum immunologiae et therapiae experimentalis* **2006,** *54* (2), 75-84.
132. Läubli, H.; Borsig, L. In *Selectins promote tumor metastasis*, Seminars in cancer biology, Elsevier: 2010; pp 169-177.
133. Ugorski, M.; Laskowska, A., Sialyl Lewis^ a: a tumor-associated carbohydrate antigen involved in adhesion and metastatic potential of cancer cells. *ACTA BIOCHIMICA POLONICA-ENGLISH EDITION-* **2002,** *49* (2), 303-312.
134. Kannagi, R.; Izawa, M.; Koike, T.; Miyazaki, K.; Kimura, N., Carbohydrate-mediated cell adhesion in cancer metastasis and angiogenesis. *Cancer science* **2004,** *95* (5), 377-384.
135. Kappelmayer, J.; Nagy, B., The Interaction of Selectins and PSGL-1 as a Key Component in Thrombus Formation and Cancer Progression. *BioMed research international* **2017,** *2017*.

136. Chambers, A.; Groom, A.; MacDonald, I., ā€ Dissemination and Growth of Cancer Cells in Metastatic Sites, ā€ Nat. *Rev. Cancer* **2002,** *2*, 563ā.
137. Kim, Y. J.; Borsig, L.; Varki, N. M.; Varki, A., P-selectin deficiency attenuates tumor growth and metastasis. *Proceedings of the National Academy of Sciences* **1998,** *95* (16), 9325-9330.
138. Schlesinger, M., Role of platelets and platelet receptors in cancer metastasis. *Journal of hematology & oncology* **2018,** *11* (1), 125.
139. Azevedo, A. S.; Follain, G.; Patthabhiraman, S.; Harlepp, S.; Goetz, J. G., Metastasis of circulating tumor cells: favorable soil or suitable biomechanics, or both? *Cell adhesion & migration* **2015,** *9* (5), 345-356.
140. Gupta, G. P.; Massagué, J., Cancer metastasis: building a framework. *Cell* **2006,** *127* (4), 679-695.
141. Borsig, L.; Wong, R.; Feramisco, J.; Nadeau, D. R.; Varki, N. M.; Varki, A., Heparin and cancer revisited: mechanistic connections involving platelets, P-selectin, carcinoma mucins, and tumor metastasis. *Proceedings of the National Academy of Sciences* **2001,** *98* (6), 3352-3357.
142. Koenig, A.; Norgard-Sumnicht, K.; Linhardt, R.; Varki, A., Differential interactions of heparin and heparan sulfate glycosaminoglycans with the selectins. Implications for the use of unfractionated and low molecular weight heparins as therapeutic agents. *Journal of Clinical Investigation* **1998,** *101* (4), 877.
143. Stevenson, J. L.; Choi, S. H.; Varki, A., Differential metastasis inhibition by clinically relevant levels of heparins—correlation with selectin inhibition, not antithrombotic activity. *Clinical Cancer Research* **2005,** *11* (19), 7003-7011.
144. Borsig, L.; Wong, R.; Hynes, R. O.; Varki, N. M.; Varki, A., Synergistic effects of L-and P-selectin in facilitating tumor metastasis can involve non-mucin ligands and implicate leukocytes as enhancers of metastasis. *Proceedings of the National Academy of Sciences* **2002,** *99* (4), 2193-2198.
145. Varki, A.; Varki, N., P-selectin, carcinoma metastasis and heparin: novel mechanistic connections with therapeutic implications. *Brazilian Journal of Medical and Biological Research* **2001,** *34* (6), 711-717.
146. Godoy-Gallardo, M.; Ek, P. K.; Jansman, M.; Wohl, B.; Hosta-Rigau, L., Interaction between drug delivery vehicles and cells under the effect of shear stress. *Biomicrofluidics* **2015,** *9* (5), 052605.
147. Giddens, D.; Zarins, C.; Glagov, S., The role of fluid mechanics in the localization and detection of atherosclerosis. *Journal of biomechanical engineering* **1993,** *115* (4B), 588-594.
148. Haun, J. B.; Hammer, D. A., Quantifying nanoparticle adhesion mediated by specific molecular interactions. *Langmuir* **2008,** *24* (16), 8821-8832.
149. Thomas, A.; Tan, J.; Liu, Y., Characterization of nanoparticle delivery in microcirculation using a microfluidic device. *Microvascular research* **2014,** *94*, 17-27.
150. Fillafer, C.; Ratzinger, G.; Neumann, J.; Guttenberg, Z.; Dissauer, S.; Lichtscheidl, I. K.; Wirth, M.; Gabor, F.; Schneider, M. F., An acoustically-driven biochip–impact of flow on the cell-association of targeted drug carriers. *Lab on a Chip* **2009,** *9* (19), 2782-2788.
151. Kona, S.; Dong, J.-F.; Liu, Y.; Tan, J.; Nguyen, K. T., Biodegradable nanoparticles mimicking platelet binding as a targeted and controlled drug delivery system. *International journal of pharmaceutics* **2012,** *423* (2), 516-524.
152. Eniola, A. O.; Rodgers, S. D.; Hammer, D. A., Characterization of biodegradable drug delivery vehicles with the adhesive properties of leukocytes. *Biomaterials* **2002,** *23* (10), 2167-2177.
153. Kang, H.; Mintri, S.; Menon, A. V.; Lee, H. Y.; Choi, H. S.; Kim, J., Pharmacokinetics, pharmacodynamics and toxicology of theranostic nanoparticles. *Nanoscale* **2015,** *7* (45), 18848-18862.

154. Stöber, W.; Fink, A.; Bohn, E., Controlled growth of monodisperse silica spheres in the micron size range. *Journal of colloid and interface science* **1968,** *26* (1), 62-69.
155. Biran, R.; Pond, D., Heparin coatings for improving blood compatibility of medical devices. *Advanced drug delivery reviews* **2017,** *112*, 12-23.
156. Larm, O.; Larsson, R.; Olsson, P., A new non-thrombogenic surface prepared by selective covalent binding of heparin via a modified reducing terminal residue. *Biomaterials, medical devices, and artificial organs* **1983,** *11* (2-3), 161-173.
157. Pelaz, B.; del Pino, P.; Maffre, P.; Hartmann, R.; Gallego, M.; Rivera-Fernandez, S.; de la Fuente, J. M.; Nienhaus, G. U.; Parak, W. J., Surface functionalization of nanoparticles with polyethylene glycol: effects on protein adsorption and cellular uptake. *ACS nano* **2015,** *9* (7), 6996-7008.
158. Michalet, X.; Pinaud, F.; Bentolila, L.; Tsay, J.; Doose, S.; Li, J.; Sundaresan, G.; Wu, A.; Gambhir, S.; Weiss, S., Quantum dots for live cells, in vivo imaging, and diagnostics. *science* **2005,** *307* (5709), 538-544.
159. Sperling, R.; Liedl, T.; Duhr, S.; Kudera, S.; Zanella, M.; Lin, C.-A.; Chang, W.; Braun, D.; Parak, W., Size determination of (bio) conjugated water-soluble colloidal nanoparticles: a comparison of different techniques. *The Journal of Physical Chemistry C* **2007,** *111* (31), 11552-11559.
160. Pellegrino, T.; Kudera, S.; Liedl, T.; Muñoz Javier, A.; Manna, L.; Parak, W. J., On the development of colloidal nanoparticles towards multifunctional structures and their possible use for biological applications. *small* **2005,** *1* (1), 48-63.
161. Clarke, S. Development of hierarchical magnetic nanocomposite materials for biomedical applications. Dublin City University, 2013.
162. Danaei, M.; Dehghankhold, M.; Ataei, S.; Hasanzadeh Davarani, F.; Javanmard, R.; Dokhani, A.; Khorasani, S.; Mozafari, M., Impact of particle size and polydispersity index on the clinical applications of lipidic nanocarrier systems. *Pharmaceutics* **2018,** *10* (2), 57.
163. Hu, S.; Sun, L.; Liu, M.; Zhu, H.; Guo, H.; Sun, H.; Sun, H., A highly dispersible silica pH nanosensor with expanded measurement ranges. *New Journal of Chemistry* **2015,** *39* (6), 4568-4574.
164. Zhu, Y.; Fang, Y.; Borchardt, L.; Kaskel, S., PEGylated hollow mesoporous silica nanoparticles as potential drug delivery vehicles. *Microporous and Mesoporous Materials* **2011,** *141* (1), 199-206.
165. Wang, X.-D.; Shen, Z.-X.; Sang, T.; Cheng, X.-B.; Li, M.-F.; Chen, L.-Y.; Wang, Z.-S., Preparation of spherical silica particles by Stöber process with high concentration of tetra-ethyl-orthosilicate. *Journal of colloid and interface science* **2010,** *341* (1), 23-29.
166. Volpi, N., Electrophoresis separation of glycosaminoglycans on nitrocellulose membranes. *Analytical biochemistry* **1996,** *240* (1), 114-118.
167. Jaques, L., Heparin: an old drug with a new paradigm. *Science* **1979,** *206* (4418), 528-533.
168. Grant, A. C.; Linhardt, R. J.; Fitzgerald, G. L.; Park, J. J.; Langer, R., Metachromatic activity of heparin and heparin fragments. *Analytical biochemistry* **1984,** *137* (1), 25-32.
169. Bai, S.; Thomas, C.; Ahsan, F., Dendrimers as a carrier for pulmonary delivery of enoxaparin, a low-molecular weight heparin. *Journal of pharmaceutical sciences* **2007,** *96* (8), 2090-2106.
170. Klein, M. D.; Drongowski, R. A.; Linhardt, R. J.; Langer, R. S., A colorimetric assay for chemical heparin in plasma. *Analytical biochemistry* **1982,** *124* (1), 59-64.
171. Zheng, C.; Levenston, M., Fact versus artifact: avoiding erroneous estimates of sulfated glycosaminoglycan content using the dimethylmethylene blue colorimetric assay for tissue-engineered constructs. *European cells & materials* **2015,** *29*, 224.
172. Enobakhare, B. O.; Bader, D. L.; Lee, D. A., Quantification of sulfated glycosaminoglycans in chondrocyte/alginate cultures, by use of 1, 9-dimethylmethylene blue. *Analytical biochemistry* **1996,** *243* (1), 189-191.

173. Richardson, J.; Dettmar, P.; Hampson, F.; Melia, C., A simple, high throughput method for the quantification of sodium alginates on oesophageal mucosa. *European journal of pharmaceutics and biopharmaceutics* **2004,** *57* (2), 299-305.
174. Farndale, R. W.; Buttle, D. J.; Barrett, A. J., Improved quantitation and discrimination of sulphated glycosaminoglycans by use of dimethylmethylene blue. *Biochimica et Biophysica Acta (BBA)-General Subjects* **1986,** *883* (2), 173-177.
175. Teien, A. N.; Lie, M.; Abildgaard, U., Assay of heparin in plasma using a chromogenic substrate for activated factor X. *Thrombosis research* **1976,** *8* (3), 413-416.
176. Hasegawa, H.; OGUMA, Y.; TAKEI, H.; SEYA, T.; YAMAUCHI, M.; MURAKOSHI, T.; NAGATA, H.; MURAO, M., Assay of heparin in plasma using a chromogenic substrate and its clinical applications. *Japanese heart journal* **1980,** *21* (3), 367-380.
177. Park, K.; Lee, G. Y.; Kim, Y.-S.; Yu, M.; Park, R.-W.; Kim, I.-S.; Kim, S. Y.; Byun, Y., Heparin–deoxycholic acid chemical conjugate as an anticancer drug carrier and its antitumor activity. *Journal of controlled release* **2006,** *114* (3), 300-306.
178. Agarwal, A.; Danishefsky, I., Requirement of free carboxyl groups for the anticoagulant activity of heparin. *Thrombosis research* **1986,** *42* (5), 673-680.
179. Olsson, P.; Sanchez, J.; Mollnes, T. E.; Riesenfeld, J., On the blood compatibility of end-point immobilized heparin. *Journal of Biomaterials Science, Polymer Edition* **2000,** *11* (11), 1261-1273.
180. Hu, Y.; Xie, J.; Tong, Y. W.; Wang, C.-H., Effect of PEG conformation and particle size on the cellular uptake efficiency of nanoparticles with the HepG2 cells. *Journal of Controlled Release* **2007,** *118* (1), 7-17.
181. Zauner, W.; Farrow, N. A.; Haines, A. M., In vitro uptake of polystyrene microspheres: effect of particle size, cell line and cell density. *Journal of Controlled Release* **2001,** *71* (1), 39-51.
182. Ballermann, B. J.; Dardik, A.; Eng, E.; Liu, A., Shear stress and the endothelium. *Kidney International* **1998,** *54*, S100-S108.
183. Paszkowiak, J. J.; Dardik, A., Arterial wall shear stress: observations from the bench to the bedside. *Vascular and endovascular surgery* **2003,** *37* (1), 47-57.
184. Crayton, S. H.; Elias, D. R.; Al Zaki, A.; Cheng, Z.; Tsourkas, A., ICP-MS analysis of lanthanide-doped nanoparticles as a non-radiative, multiplex approach to quantify biodistribution and blood clearance. *Biomaterials* **2012,** *33* (5), 1509-1519.
185. Thorek, D. L.; Tsourkas, A., Size, charge and concentration dependent uptake of iron oxide particles by non-phagocytic cells. *Biomaterials* **2008,** *29* (26), 3583-3590.
186. Wang, J.-G.; Geng, J.-G., Affinity and kinetics of P-selectin binding to heparin. *Thrombosis and haemostasis* **2003,** *90* (02), 309-316.
187. Simonis, D.; Fritzsche, J.; Alban, S.; Bendas, G., Kinetic analysis of heparin and glucan sulfates binding to P-selectin and its impact on the general understanding of selectin inhibition. *Biochemistry* **2007,** *46* (20), 6156-6164.
188. Monzavi-Karbassi, B.; Stanley, J. S.; Hennings, L.; Jousheghany, F.; Artaud, C.; Shaaf, S.; Kieber-Emmons, T., Chondroitin sulfate glycosaminoglycans as major P-selectin ligands on metastatic breast cancer cell lines. *International journal of cancer* **2007,** *120* (6), 1179-1191.
189. Garcia, J.; Callewaert, N.; Borsig, L., P-selectin mediates metastatic progression through binding to sulfatides on tumor cells. *Glycobiology* **2006,** *17* (2), 185-196.
190. Khew-Goodall, Y.; Butcher, C.; Litwin, M.; Newlands, S.; Korpelainen, E.; Noack, L.; Berndt, M.; Lopez, A.; Gamble, J.; Vadas, M., Chronic expression of P-selectin on endothelial cells stimulated by the T-cell cytokine, interleukin-3. *Blood* **1996,** *87* (4), 1432-1438.
191. Khew-Goodall, Y.; Wadham, C.; Stein, B. N.; Gamble, J. R.; Vadas, M. A., Stat6 activation is essential for interleukin-4 induction of P-selectin transcription in human umbilical vein endothelial cells. *Arteriosclerosis, Thrombosis, and Vascular Biology* **1999,** *19* (6), 1421-1429.

192. Cleator, J. H.; Zhu, W. Q.; Vaughan, D. E.; Hamm, H. E., Differential regulation of endothelial exocytosis of P-selectin and von Willebrand factor by protease-activated receptors and cAMP. *Blood* **2006,** *107* (7), 2736-2744.
193. Stocker, C. J.; Sugars, K. L.; Harari, O. A.; Landis, R. C.; Morley, B. J.; Haskard, D. O., TNF-α, IL-4, and IFN-γ regulate differential expression of P-and E-selectin expression by porcine aortic endothelial cells. *The Journal of Immunology* **2000,** *164* (6), 3309-3315.
194. Kameda, H.; Morita, I.; Handa, M.; Kaburaki, J.; Yoshida, T.; Mimori, T.; Murota, S. I.; Ikeda, Y., Re-expression of functional P-selectin molecules on the endothelial cell surface by repeated stimulation with thrombin. *British journal of haematology* **1997,** *97* (2), 348-355.
195. Jones, D.; Abbassi, O.; McIntire, L.; McEver, R.; Smith, C. W., P-selectin mediates neutrophil rolling on histamine-stimulated endothelial cells. *Biophysical Journal* **1993,** *65* (4), 1560.
196. Asako, H.; Kurose, I.; Wolf, R.; Defrees, S.; Zheng, Z.; Phillips, M. L.; Paulson, J. C.; Granger, D. N., Role of H1 receptors and P-selectin in histamine-induced leukocyte rolling and adhesion in postcapillary venules. *The Journal of clinical investigation* **1994,** *93* (4), 1508-1515.
197. Easton, A. S.; Dorovini-Zis, K., The kinetics, function, and regulation of P-selectin expressed by human brain microvessel endothelial cells in primary culture. *Microvascular research* **2001,** *62* (3), 335-345.
198. Elias, D. R.; Poloukhtine, A.; Popik, V.; Tsourkas, A., Effect of ligand density, receptor density, and nanoparticle size on cell targeting. *Nanomedicine: nanotechnology, biology and medicine* **2013,** *9* (2), 194-201.
199. Yuan, H.; Zhang, S., Effects of particle size and ligand density on the kinetics of receptor-mediated endocytosis of nanoparticles. *Applied Physics Letters* **2010,** *96* (3), 033704.
200. McKenzie, M.; Ha, S. M.; Rammohan, A.; Radhakrishnan, R.; Ramakrishnan, N., Multivalent Binding of a Ligand-Coated Particle: Role of Shape, Size, and Ligand Heterogeneity. *Biophysical journal* **2018,** *114* (8), 1830-1846.
201. Jiang, W.; Kim, B. Y.; Rutka, J. T.; Chan, W. C., Nanoparticle-mediated cellular response is size-dependent. *Nature nanotechnology* **2008,** *3* (3), 145.
202. Patil, V. R. S.; Campbell, C. J.; Yun, Y. H.; Slack, S. M.; Goetz, D. J., Particle diameter influences adhesion under flow. *Biophysical Journal* **2001,** *80* (4), 1733-1743.
203. Sabri, S.; Pierres, A.; Benoliel, A.-M.; Bongrand, P., Influence of surface charges on cell adhesion: difference between static and dynamic conditions. *Biochemistry and cell biology* **1995,** *73* (7-8), 411-420.
204. Wattenbarger, M.; Graves, D.; Lauffenburger, D., Specific adhesion of glycophorin liposomes to a lectin surface in shear flow. *Biophysical journal* **1990,** *57* (4), 765-777.
205. Gutierro, I.; Hernandez, R.; Igartua, M.; Gascon, A.; Pedraz, J., Size dependent immune response after subcutaneous, oral and intranasal administration of BSA loaded nanospheres. *Vaccine* **2002,** *21* (1-2), 67-77.
206. Toy, R.; Roy, K., Engineering nanoparticles to overcome barriers to immunotherapy. *Bioengineering & translational medicine* **2016,** *1* (1), 47-62.
207. Owens III, D. E.; Peppas, N. A., Opsonization, biodistribution, and pharmacokinetics of polymeric nanoparticles. *International journal of pharmaceutics* **2006,** *307* (1), 93-102.
208. Petros, R. A.; DeSimone, J. M., Strategies in the design of nanoparticles for therapeutic applications. *Nature reviews Drug discovery* **2010,** *9* (8), 615.
209. Vlodavsky, I.; Friedmann, Y., Molecular properties and involvement of heparanase in cancer metastasis and angiogenesis. *The Journal of clinical investigation* **2001,** *108* (3), 341-347.
210. Vlodavsky, I.; Friedmann, Y.; Elkin, M.; Aingorn, H.; Atzmon, R.; Ishai-Michaeli, R.; Bitan, M.; Pappo, O.; Peretz, T.; Michal, I., Mammalian heparanase: gene cloning, expression and function in tumor progression and metastasis. *Nature medicine* **1999,** *5* (7), 793.

211. Patel, V. N.; Knox, S. M.; Likar, K. M.; Lathrop, C. A.; Hossain, R.; Eftekhari, S.; Whitelock, J. M.; Elkin, M.; Vlodavsky, I.; Hoffman, M. P., Heparanase cleavage of perlecan heparan sulfate modulates FGF10 activity during ex vivo submandibular gland branching morphogenesis. *Development* **2007,** *134* (23), 4177-4186.
212. Matsuo, I.; Kimura-Yoshida, C., Extracellular modulation of Fibroblast Growth Factor signaling through heparan sulfate proteoglycans in mammalian development. *Current opinion in genetics & development* **2013,** *23* (4), 399-407.
213. Elkin, M.; Ilan, N.; Ishai-Michaeli, R.; Friedmann, Y.; Papo, O.; Pecker, I.; Vlodavsky, I., Heparanase as mediator of angiogenesis: mode of action. *The FASEB Journal* **2001,** *15* (9), 1661-1663.
214. Vlodavsky, I.; Goldshmidt, O.; Zcharia, E.; Atzmon, R.; Rangini-Guatta, Z.; Elkin, M.; Peretz, T.; Friedmann, Y. In *Mammalian heparanase: involvement in cancer metastasis, angiogenesis and normal development*, Seminars in cancer biology, Elsevier: 2002; pp 121-129.
215. Gohji, K.; Katsuoka, Y.; Okamoto, M.; Kamidono, S.; Kitazawa, S.; Toyoshima, M.; Dong, J.; Nakajima, M., Human heparanase: roles in invasion and metastasis of cancer. *Hinyokika kiyo. Acta urologica Japonica* **2000,** *46* (10), 757.
216. Nakajima, M.; Irimura, T.; Nicolson, G. L., Heparanases and tumor metastasis. *Journal of cellular biochemistry* **1988,** *36* (2), 157-167.
217. Vlodavsky, I.; Eldor, A.; Haimovitz-Friedman, A.; Matzner, Y.; Ishai-Michaeli, R.; Lider, O.; Naparstek, Y.; Cohen, I.; Fuks, Z., Expression of heparanase by platelets and circulating cells of the immune system: possible involvement in diapedesis and extravasation. *Invasion & metastasis* **1992,** *12* (2), 112-127.
218. Vlodavsky, I.; Elkin, M.; Ilan, N., Impact of heparanase and the tumor microenvironment on cancer metastasis and angiogenesis: basic aspects and clinical applications. *Rambam Maimonides medical journal* **2011,** *2* (1).
219. Vlodavsky, I.; Elkin, M.; Abboud-Jarrous, G.; Levi-Adam, F.; Fuks, L.; Shafat, I.; Ilan, N., Heparanase: one molecule with multiple functions in cancer progression. *Connective tissue research* **2008,** *49* (3-4), 207-210.
220. McKenzie, E. A., Heparanase: a target for drug discovery in cancer and inflammation. *British journal of pharmacology* **2007,** *151* (1), 1-14.
221. Boyd, D. D.; Nakajima, M., Involvement of heparanase in tumor metastases: a new target in cancer therapy? Oxford University Press: 2004.
222. Nakajima, M.; Irimura, T.; Di Ferrante, D.; Di Ferrante, N.; Nicolson, G. L., Heparan sulfate degradation: relation to tumor invasive and metastatic properties of mouse B16 melanoma sublines. *Science* **1983,** *220* (4597), 611-613.
223. Yang, Y.; MacLeod, V.; Bendre, M.; Huang, Y.; Theus, A. M.; Miao, H.-Q.; Kussie, P.; Yaccoby, S.; Epstein, J.; Suva, L. J., Heparanase promotes the spontaneous metastasis of myeloma cells to bone. *Blood* **2005,** *105* (3), 1303-1309.
224. Yang, Y.; MacLeod, V.; Miao, H.-Q.; Theus, A.; Zhan, F.; Shaughnessy, J. D.; Sawyer, J.; Li, J.-P.; Zcharia, E.; Vlodavsky, I., Heparanase enhances syndecan-1 shedding: a novel mechanism for stimulation of tumor growth and metastasis. *Journal of Biological Chemistry* **2007**.
225. Irimura, T.; Nakajima, M.; Nicolson, G. L., Chemically modified heparins as inhibitors of heparan sulfate specific endo-. beta.-glucuronidase (heparanase) of metastatic melanoma cells. *Biochemistry* **1986,** *25* (18), 5322-5328.
226. Naggi, A.; Casu, B.; Perez, M.; Torri, G.; Cassinelli, G.; Penco, S.; Pisano, C.; Giannini, G.; Ishai-Michaeli, R.; Vlodavsky, I., Modulation of the heparanase-inhibiting activity of heparin through selective desulfation, graded N-acetylation, and glycol splitting. *Journal of Biological Chemistry* **2005,** *280* (13), 12103-12113.

227. Bar-Ner, M.; Eldor, A.; Wasserman, L.; Matzner, Y.; Cohen, I. R.; Fuks, Z.; Vlodavsky, I., Inhibition of heparanase-mediated degradation of extracellular matrix heparan sulfate by non-anticoagulant heparin species. *Blood* **1987,** *70* (2), 551-557.
228. Lapierre, F.; Holme, K.; Lam, L.; Tressler, R. J.; Storm, N.; Wee, J.; Stack, R. J.; Castellot, J.; Tyrrell, D. J., Chemical modifications of heparin that diminish its anticoagulant but preserve its heparanase-inhibitory, angiostatic, anti-tumor and anti-metastatic properties. *Glycobiology* **1996,** *6* (3), 355-366.
229. Meng, H.; Xue, M.; Xia, T.; Ji, Z.; Tarn, D. Y.; Zink, J. I.; Nel, A. E., Use of size and a copolymer design feature to improve the biodistribution and the enhanced permeability and retention effect of doxorubicin-loaded mesoporous silica nanoparticles in a murine xenograft tumor model. *ACS nano* **2011,** *5* (5), 4131-4144.
230. Hansen, A. E.; Petersen, A. L.; Henriksen, J. R.; Boerresen, B.; Rasmussen, P.; Elema, D. R.; Rosenschöld, P. M. a.; Kristensen, A. T.; Kjær, A.; Andresen, T. L., Positron emission tomography based elucidation of the enhanced permeability and retention effect in dogs with cancer using copper-64 liposomes. *ACS nano* **2015,** *9* (7), 6985-6995.
231. Wang, L.; Huang, J.; Chen, H.; Wu, H.; Xu, Y.; Li, Y.; Yi, H.; Wang, Y. A.; Yang, L.; Mao, H., Exerting enhanced permeability and retention effect driven delivery by ultrafine iron oxide nanoparticles with T 1–T 2 switchable magnetic resonance imaging contrast. *ACS nano* **2017,** *11* (5), 4582-4592.
232. Greish, K., Enhanced permeability and retention (EPR) effect for anticancer nanomedicine drug targeting. In *Cancer Nanotechnology*, Springer: 2010; pp 25-37.
233. Miao, L.; Huang, L., Exploring the tumor microenvironment with nanoparticles. In *Nanotechnology-Based Precision Tools for the Detection and Treatment of Cancer*, Springer: 2015; pp 193-226.
234. Nel, A.; Ruoslahti, E.; Meng, H., New insights into "permeability" as in the enhanced permeability and retention effect of cancer nanotherapeutics. ACS Publications: 2017.
235. Prabhakar, U.; Maeda, H.; Jain, R. K.; Sevick-Muraca, E. M.; Zamboni, W.; Farokhzad, O. C.; Barry, S. T.; Gabizon, A.; Grodzinski, P.; Blakey, D. C., Challenges and key considerations of the enhanced permeability and retention effect for nanomedicine drug delivery in oncology. AACR: 2013.
236. Wakaskar, R. R., Passive and active targeting in tumor microenvironment. *Int. J. Drug Dev. Res* **2017,** *9* (2).
237. Lu, J.; Liong, M.; Li, Z.; Zink, J. I.; Tamanoi, F., Biocompatibility, biodistribution, and drug-delivery efficiency of mesoporous silica nanoparticles for cancer therapy in animals. *Small* **2010,** *6* (16), 1794-1805.
238. Liu, H.; Zhang, Z.; Linhardt, R. J., Lessons learned from the contamination of heparin. *Natural product reports* **2009,** *26* (3), 313-321.
239. Islam, T.; Butler, M.; Sikkander, S. A.; Toida, T.; Linhardt, R. J., Further evidence that periodate cleavage of heparin occurs primarily through the antithrombin binding site. *Carbohydrate research* **2002,** *337* (21), 2239-2243.
240. Casu, B.; Guerrini, M.; Guglieri, S.; Naggi, A.; Perez, M.; Torri, G.; Cassinelli, G.; Ribatti, D.; Carminati, P.; Giannini, G., Undersulfated and glycol-split heparins endowed with antiangiogenic activity. *Journal of medicinal chemistry* **2004,** *47* (4), 838-848.
241. Ni, M.; Elli, S.; Naggi, A.; Guerrini, M.; Torri, G.; Petitou, M., Investigating glycol-split-heparin-derived inhibitors of heparanase: A study of synthetic trisaccharides. *Molecules* **2016,** *21* (11), 1602.
242. Naggi, A., Glycol-splitting as a device for modulating inhibition of growth factors and heparanase by heparin and heparin derivatives. In *Chemistry and biology of heparin and heparan sulfate*, Elsevier: 2005; pp 461-481.
243. Wu, L.; Viola, C. M.; Brzozowski, A. M.; Davies, G. J., Structural characterization of human heparanase reveals insights into substrate recognition. *Nature structural & molecular biology* **2015,** *22* (12), 1016.

244. Jaseja, M.; Rej, R. N.; Sauriol, F.; Perlin, A. S., Novel regio-and stereoselective modifications of heparin in alkaline solution. Nuclear magnetic resonance spectroscopic evidence. *Canadian Journal of Chemistry* **1989,** *67* (9), 1449-1456.
245. Holme, K. R.; Liang, W.; Tyrrell, D. J.; Shaklee, P. N., Method for controlling O-desulfation of heparin. Google Patents: 1998.
246. Kennedy, T. P., Method of synthesis of 2-O-desulfated heparin and use thereof for inhibition of elastase and cathepsin G. Google Patents: 1998.
247. Vlodavsky, I.; Elkin, M.; Pappo, O.; Aingorn, H.; Atzmon, R.; Ishai-Michaeli, R.; Aviv, A.; Pecker, I.; Friedmann, Y., Mammalian heparanase as mediator of tumor metastasis and angiogenesis. *The Israel Medical Association journal: IMAJ* **2000,** *2*, 37-45.
248. Vlodavsky, I.; Korner, G.; Ishai-Michaeli, R.; Bashkin, P.; Bar-Shavit, R.; Fuks, Z., Extracellular matrix-resident growth factors and enzymes: possible involvement in tumor metastasis and angiogenesis. *Cancer and Metastasis Reviews* **1990,** *9* (3), 203-226.
249. Lee, K.; Lee, H.; Bae, K. H.; Park, T. G., Heparin immobilized gold nanoparticles for targeted detection and apoptotic death of metastatic cancer cells. *Biomaterials* **2010,** *31* (25), 6530-6536.
250. Freeman, C.; Parish, C. R., A rapid quantitative assay for the detection of mammalian heparanase activity. *Biochemical Journal* **1997,** *325* (1), 229-237.
251. Lakowicz, J. R., Introduction to fluorescence. In *Principles of fluorescence spectroscopy*, Springer: 1999; pp 1-23.
252. Alias, A.; Zabidi, Z.; Ali, A.; Harun, M.; Yahya, M., Optical characterization and properties of polymeric materials for optoelectronic and photonic applications. *International Journal of Applied Science and Technology* **2013,** *3* (5).
253. Arppe, R.; Hyppänen, I.; Perälä, N.; Peltomaa, R.; Kaiser, M.; Würth, C.; Christ, S.; Resch-Genger, U.; Schäferling, M.; Soukka, T., Quenching of the upconversion luminescence of NaYF 4: Yb 3+, Er 3+ and NaYF 4: Yb 3+, Tm 3+ nanophosphors by water: the role of the sensitizer Yb 3+ in non-radiative relaxation. *Nanoscale* **2015,** *7* (27), 11746-11757.
254. Förster, T., Zwischenmolekulare energiewanderung und fluoreszenz. *Annals of Physics* **1948,** *437* (1-2), 55-75.
255. Shrestha, D.; Jenei, A.; Nagy, P.; Vereb, G.; Szöllősi, J., Understanding FRET as a research tool for cellular studies. *International journal of molecular sciences* **2015,** *16* (4), 6718-6756.
256. Latt, S.; Cheung, H.; Blout, E., Energy transfer. A system with relatively fixed donor-acceptor separation. *Journal of the American Chemical Society* **1965,** *87* (5), 995-1003.
257. Stryer, L.; Haugland, R. P., Energy transfer: a spectroscopic ruler. *Proceedings of the National Academy of Sciences* **1967,** *58* (2), 719-726.
258. Freeman, R.; Willner, I., Optical molecular sensing with semiconductor quantum dots (QDs). *Chemical Society Reviews* **2012,** *41* (10), 4067-4085.
259. Guerry, A.; Bernard, J.; Samain, E.; Fleury, E.; Cottaz, S.; Halila, S., Aniline-catalyzed reductive amination as a powerful method for the preparation of reducing end-“clickable” chitooligosaccharides. *Bioconjugate chemistry* **2013,** *24* (4), 544-549.
260. Dale, R. E.; Eisinger, J.; Blumberg, W., The orientational freedom of molecular probes. The orientation factor in intramolecular energy transfer. *Biophysical journal* **1979,** *26* (2), 161-193.
261. Dos Remedios, C. G.; Moens, P. D., Fluorescence resonance energy transfer spectroscopy is a reliable" ruler" for measuring structural changes in proteins: dispelling the problem of the unknown orientation factor. *Journal of structural biology* **1995,** *115* (2), 175-185.
262. Wu, P.; Brand, L., Orientation factor in steady-state and time-resolved resonance energy transfer measurements. *Biochemistry* **1992,** *31* (34), 7939-7947.

263. Srinivas, G.; Bagchi, B., Effect of orientational motion of mobile chromophores on the dynamics of Förster energy transfer in polymers. *The Journal of Physical Chemistry B* **2001,** *105* (38), 9370-9374.
264. Lewis, F. D.; Zhang, L.; Zuo, X., Orientation control of fluorescence resonance energy transfer using DNA as a helical scaffold. *Journal of the American Chemical Society* **2005,** *127* (28), 10002-10003.
265. VanBeek, D. B.; Zwier, M. C.; Shorb, J. M.; Krueger, B. P., Fretting about FRET: Correlation between κ and R. *Biophysical journal* **2007,** *92* (12), 4168-4178.
266. Technologies, B., Real-time-pcr-dyes. In *2B Scientific*.
267. Li, H.; Rothberg, L. J., DNA sequence detection using selective fluorescence quenching of tagged oligonucleotide probes by gold nanoparticles. *Analytical chemistry* **2004,** *76* (18), 5414-5417.
268. Tutkus, M.; Marciulionis, T.; Sasnauskas, G.; Rutkauskas, D., DNA-Endonuclease Complex Dynamics by Simultaneous FRET and Fluorophore Intensity in Evanescent Field. *Biophysical journal* **2017,** *112* (5), 850-858.
269. Zeng, P.; Hou, P.; Jing, C. J.; Huang, C. Z., Highly sensitive detection of hepatitis C virus DNA by using a one-donor-four-acceptors FRET probe. *Talanta* **2018,** *185*, 118-122.
270. Wu, B.; Cao, Z.; Zhang, Q.; Wang, G., NIR-responsive DNA hybridization detection by high efficient FRET from 10-nm upconversion nanoparticles to SYBR green I. *Sensors and Actuators B: Chemical* **2018,** *255*, 2853-2860.
271. Artemyev, M. V.; Nabiev, I. R., Molecular beacons involving highly luminescent colloidal quantum dots. *Journal of Nanophotonics* **2012,** *6* (1), 060304.
272. Pei, H.; Zheng, Y.; Kong, R.; Xia, L.; Qu, F., Niche nanoparticle-based FRET assay for bleomycin detection via DNA scission. *Biosensors and Bioelectronics* **2016,** *85*, 76-82.
273. Kudr, J.; Richtera, L.; Xhaxhiu, K.; Hynek, D.; Heger, Z.; Zitka, O.; Adam, V., Carbon dots based FRET for the detection of DNA damage. *Biosensors and Bioelectronics* **2017,** *92*, 133-139.
274. Ha, T.; Ting, A. Y.; Liang, J.; Caldwell, W. B.; Deniz, A. A.; Chemla, D. S.; Schultz, P. G.; Weiss, S., Single-molecule fluorescence spectroscopy of enzyme conformational dynamics and cleavage mechanism. *Proceedings of the National Academy of Sciences* **1999,** *96* (3), 893-898.
275. Ting, A. Y.; Kain, K. H.; Klemke, R. L.; Tsien, R. Y., Genetically encoded fluorescent reporters of protein tyrosine kinase activities in living cells. *Proceedings of the National Academy of Sciences* **2001,** *98* (26), 15003-15008.
276. Taraska, J. W.; Puljung, M. C.; Olivier, N. B.; Flynn, G. E.; Zagotta, W. N., Mapping the structure and conformational movements of proteins with transition metal ion FRET. *Nature methods* **2009,** *6* (7), 532.
277. Dexter, D. L., A theory of sensitized luminescence in solids. *The Journal of Chemical Physics* **1953,** *21* (5), 836-850.
278. Mikhnenko, O. V.; Blom, P. W.; Nguyen, T.-Q., Exciton diffusion in organic semiconductors. *Energy & Environmental Science* **2015,** *8* (7), 1867-1888.
279. Dexter, D.; Schulman, J. H., Theory of concentration quenching in inorganic phosphors. *The Journal of Chemical Physics* **1954,** *22* (6), 1063-1070.
280. Adronov, A.; Fréchet, J. M., Light-harvesting dendrimers. *Chemical Communications* **2000,** (18), 1701-1710.
281. Demchenko, A. P., *Introduction to fluorescence sensing*. Springer Science & Business Media: 2008.
282. Buxbaum, E., *Biophysical chemistry of proteins: an introduction to laboratory methods*. Springer Science & Business Media: 2010.
283. Jameson, D. M., *Introduction to fluorescence*. CRC Press: 2014.
284. Didenko, V. V., *Fluorescent energy transfer nucleic acid probes: designs and protocols*. Springer Science & Business Media: 2006; Vol. 335.

285. Desai, U. R.; Wang, H. M.; Linhardt, R. J., Specificity studies on the heparin lyases from Flavobacterium heparinum. *Biochemistry* **1993,** *32* (32), 8140-8145.
286. Han, Y.-H.; Garron, M.-L.; Kim, H.-Y.; Kim, W.-S.; Zhang, Z.; Ryu, K.-S.; Shaya, D.; Xiao, Z.; Cheong, C.; Kim, Y. S., Structural snapshots of heparin depolymerization by heparin lyase I. *Journal of Biological Chemistry* **2009,** *284* (49), 34019-34027.
287. Hovingh, P.; Linker, A., The enzymatic degradation of heparin and heparitin sulfate III. Purification of a heparitinase and a heparinase from flavobacteria. *Journal of Biological Chemistry* **1970,** *245* (22), 6170-6175.
288. Dietrich, C. P.; Silva, M. E.; Michelacci, Y. M., Sequential Degradation of Heparin in Flavobacterium heparinum PURIFICATION AND PROPERTIES OF FIVE ENZYMES INVOLVED IN HEPARIN DEGRADATION. *Journal of Biological Chemistry* **1973,** *248* (18), 6408-6415.
289. Linker, A.; Hovingh, P., Isolation and characterization of oligosaccharides obtained from heparin by the action of heparinase. *Biochemistry* **1972,** *11* (4), 563-568.
290. Córdula, C. R.; Lima, M. A.; Shinjo, S. K.; Gesteira, T. F.; Pol-Fachin, L.; Coulson-Thomas, V. J.; Verli, H.; Yates, E. A.; Rudd, T. R.; Pinhal, M. A., On the catalytic mechanism of polysaccharide lyases: evidence of His and Tyr involvement in heparin lysis by heparinase I and the role of Ca 2+. *Molecular BioSystems* **2014,** *10* (1), 54-64.
291. Sasisekharan, R.; Shriver, Z.; Liu, D.; Venkataraman, G., Rationally designed heparinases derived from heparinase II. Google Patents: 2007.
292. Liu, D.; Shriver, Z.; Godavarti, R.; Venkataraman, G.; Sasisekharan, R., The Calcium-binding Sites of Heparinase I fromFlavobacterium heparinum Are Essential for Enzymatic Activity. *Journal of Biological Chemistry* **1999,** *274* (7), 4089-4095.
293. Shaya, D.; Zhao, W.; Garron, M.-L.; Xiao, Z.; Cui, Q.; Zhang, Z.; Sulea, T.; Linhardt, R. J.; Cygler, M., Catalytic mechanism of heparinase II investigated by site-directed mutagenesis and the crystal structure with its substrate. *Journal of biological chemistry* **2010,** *285* (26), 20051-20061.
294. Rivara, S.; Milazzo, F. M.; Giannini, G., Heparanase: a rainbow pharmacological target associated to multiple pathologies including rare diseases. *Future medicinal chemistry* **2016,** *8* (6), 647-680.
295. Dempsey, L. A.; Plummer, T. B.; Coombes, S. L.; Platt, J. L., Heparanase expression in invasive trophoblasts and acute vascular damage. *Glycobiology* **2000,** *10* (5), 467-475.
296. Hulett, M. D.; Freeman, C.; Hamdorf, B. J.; Baker, R. T.; Harris, M. J.; Parish, C. R., Cloning of mammalian heparanase, an important enzyme in tumor invasion and metastasis. *Nature medicine* **1999,** *5* (7), 803.
297. Graham, L. D.; Underwood, P. A., Comparison of the heparanase enzymes from mouse melanoma cells, mouse macrophages, and human platelets. *IUBMB Life* **1996,** *39* (3), 563-571.
298. Gilat, D.; Hershkoviz, R.; Goldkorn, I.; Cahalon, L.; Korner, G.; Vlodavsky, I.; Lider, O., Molecular behavior adapts to context: heparanase functions as an extracellular matrix-degrading enzyme or as a T cell adhesion molecule, depending on the local pH. *Journal of Experimental Medicine* **1995,** *181* (5), 1929-1934.
299. Fairbanks, M. B.; Mildner, A. M.; Leone, J. W.; Cavey, G. S.; Mathews, W. R.; Drong, R. F.; Slightom, J. L.; Bienkowski, M. J.; Smith, C. W.; Bannow, C. A., Processing of the human heparanase precursor and evidence that the active enzyme is a heterodimer. *Journal of Biological Chemistry* **1999,** *274* (42), 29587-29590.
300. FREEMAN, C.; PARISH, R. C., Human platelet heparanase: purification, characterization and catalytic activity. *Biochemical Journal* **1998,** *330* (3), 1341-1350.
301. Gong, F.; Jemth, P.; Galvis, M. L. E.; Vlodavsky, I.; Horner, A.; Lindahl, U.; Li, J.-p., Processing of macromolecular heparin by heparanase. *Journal of Biological Chemistry* **2003**.
302. Nasser, N.; Sarig, G.; Brenner, B.; Nevo, E.; Goldshmidt, O.; Zcharia, E.; Li, J.-P.; Vlodavsky, I., Heparanase neutralizes the anticoagulation properties of heparin and low-molecular-weight heparin. *Journal of Thrombosis and Haemostasis* **2006,** *4* (3), 560-565.

303. Mourier, P.; Anger, P.; Martinez, C.; Herman, F.; Viskov, C., Quantitative compositional analysis of heparin using exhaustive heparinase digestion and strong anion exchange chromatography. *Analytical Chemistry Research* **2015,** *3*, 46-53.
304. Ranjit, S.; Gurunathan, K.; Levitus, M., Photophysics of backbone fluorescent DNA modifications: reducing uncertainties in FRET. *The Journal of Physical Chemistry B* **2009,** *113* (22), 7861-7866.
305. Jensen, F., *Introduction to computational chemistry*. John wiley & sons: 2017.
306. Dykstra, C.; Frenking, G.; Kim, K.; Scuseria, G., *Theory and Applications of Computational Chemistry: the first forty years*. Elsevier: 2011.
307. Chatzieleftheriou, S.; Adendorff, M. R.; Lagaros, N. D., Generalized Potential Energy Finite Elements for Modeling Molecular Nanostructures. *Journal of chemical information and modeling* **2016,** *56* (10), 1963-1978.
308. Peng, C.; Ayala, P. Y.; Schlegel, H. B.; Frisch, M. J., Using redundant internal coordinates to optimize equilibrium geometries and transition states. *Journal of Computational Chemistry* **1996,** *17* (1), 49-56.
309. Dračínský, M., The chemical bond: The perspective of NMR spectroscopy. In *Annual Reports on NMR Spectroscopy*, Elsevier: 2017; Vol. 90, pp 1-40.
310. Callister, W. D.; Rethwisch, D. G., *Materials science and engineering*. John Wiley & Sons NY: 2011; Vol. 5.
311. Hettema, H., A note on Michael Weisberg's: challenges to the structural conception of chemical bonding. *Foundations of Chemistry* **2008,** *10* (2), 135-142.
312. Johansson, M. K.; Fidder, H.; Dick, D.; Cook, R. M., Intramolecular dimers: a new strategy to fluorescence quenching in dual-labeled oligonucleotide probes. *Journal of the American Chemical Society* **2002,** *124* (24), 6950-6956.
313. Bienkowski, M.; Conrad, H. E., Structural characterization of the oligosaccharides formed by depolymerization of heparin with nitrous acid. *Journal of Biological Chemistry* **1985,** *260* (1), 356-365.
314. Jacobsson, I.; Höök, M.; Pettersson, I.; Lindahl, U.; Larm, O.; Wirén, E.; Von Figura, K., Identification of N-sulphated disaccharide units in heparin-like polysaccharides. *Biochemical Journal* **1979,** *179* (1), 77-87.
315. Irvine, S. A.; Steele, T. W.; Bhuthalingam, R.; Li, M.; Boujday, S.; Prawirasatya, M.; Neoh, K. G.; Boey, F. Y. C.; Venkatraman, S. S., Quantification of aldehyde terminated heparin by SEC-MALLS–UV for the surface functionalization of polycaprolactone biomaterials. *Colloids and Surfaces B: Biointerfaces* **2015,** *132*, 253-263.
316. Oliveira, G.; Carvalho Jr, L.; Silva, M., Properties of carbodiimide treated heparin. *Biomaterials* **2003,** *24* (26), 4777-4783.
317. Wallace, B.; Atzberger, P. J., Förster resonance energy transfer: Role of diffusion of fluorophore orientation and separation in observed shifts of FRET efficiency. *PloS one* **2017,** *12* (5), e0177122.
318. Zhu, M.; Lerum, M. Z.; Chen, W., How to prepare reproducible, homogeneous, and hydrolytically stable aminosilane-derived layers on silica. *Langmuir* **2011,** *28* (1), 416-423.
319. Wang, Y.-P.; Yuan, K.; Li, Q.-L.; Wang, L.-P.; Gu, S.-J.; Pei, X.-W., Preparation and characterization of poly (N-isopropylacrylamide) films on a modified glass surface via surface initiated redox polymerization. *Materials Letters* **2005,** *59* (14-15), 1736-1740.
320. Williams, S. E.; Davies, P. R.; Bowen, J. L.; Allender, C. J., Controlling the nanoscale patterning of AuNPs on silicon surfaces. *Nanomaterials* **2013,** *3* (1), 192-203.
321. Bhat, R. R.; Genzer, J., Tuning the number density of nanoparticles by multivariant tailoring of attachment points on flat substrates. *Nanotechnology* **2006,** *18* (2), 025301.
322. Zhang, H.; He, H.-X.; Wang, J.; Mu, T.; Liu, Z.-F., Force titration of amino group-terminated self-assembled monolayers using chemical force microscopy. *Applied Physics A* **1998,** *66* (1), S269-S271.

323. Pick, C.; Argento, C.; Drazer, G.; Frechette, J., Micropatterned charge heterogeneities via vapor deposition of aminosilanes. *Langmuir* **2015,** *31* (39), 10725-10733.